

JOINT INSTITUTE FOR NUCLEAR RESEARCH

1

2



November 18, 2020

3

Conceptual design of the Spin Physics Detector

4

Draft version 2020.033

5

6

7

**This draft is the internal document
of the SPD working group
and must not be shown in public!**

8 Contents

9	1	Executive summary [A. Guskov]	6
10	2	Physics case	9
11	1	Gluons in proton and deuteron [A. Guskov, O. Teryaev]	9
12	1.1	Gluon probes at NICA SPD	10
13	1.2	Gluons at large x	13
14	1.3	Tests of TMD factorization with gluon probes	16
15	1.4	Linearly polarized gluons in unpolarized nucleon	16
16	1.5	Hadron structure and heavy charmonia production mechanisms	17
17	1.6	Non-nucleonic degrees of freedom in deuteron	19
18	1.7	Gluon polarization Δg with longitudinally polarized beams	20
19	1.8	Gluon-related TMD and twist-3 effects with transversely polarized beams	23
20	1.9	Gluon transversity in deuteron	25
21	1.10	Deuteron tensor polarization and shear forces	27
22	2	Quarks in proton and deuteron	29
23	2.1	Single-transverse spin asymmetries in the light mesons production	29
24	2.2	Drell-Yan pair production	30
25	2.3	Generalized parton distributions	31
26	2.4	Polarized fragmentation functions	32
27	3	Tests of QCD basics at low energies [U. Uzikov, A. Guskov]	33
28	3.1	Polarized pd elastic scattering within the Glauber model and pN spin amplitudes [Yu. Uzikov]	33
29			
30	3.2	Single-spin asymmetries at low energies [V. Abramov]	34
31	3.3	Exclusive hard processes with deuteron [M. Strikman]	35
32	3.4	Scaling behaviour of exclusive reactions with lightest nuclei and spin observables [Yu. Uzikov, V. Ladygin]	36
33			

34	3.5	Vector mesons and open charm near threshold [E. Tomasi]	37
35	3.6	Central nucleon-nucleon collisions [Komarov]	40
36	3.7	Onset of deconfinement in p - p and d - d central collisions [A. Korzenev]	41
37	3.8	Study of lightest neutral hypernuclei with strangeness -1 and -2 [Q. Zhao]	43
38	3.9	Multiquark correlations and exotic state production [V. Kim]	44
39	3.10	Yield of antiprotons in hadronic collisions for astrophysical dark matter search	
40		[R. El-Kholy]	45
41	3	Polarized beams [A. Kovalenko]	46
42	1	Available species and types of collisions	46
43	2	Beam structure, intensity and luminosity	46
44	3	Polarization control and monitoring	47
45	3.1	Transportation of polarized ions in the complex	47
46	3.2	Operation modes of the NICA collider at polarized ions	47
47	3.3	Specifications to the polarized beams in the collider	48
48	3.4	Spin flipping system	48
49	3.5	Online control of the polarization in the collider	49
50	3.6	Polarization control in the collider NICA in ST regime	50
51	3.7	Ion polarization control in ST regime by means of two snakes	51
52	3.8	Stability of spin motion	52
53	3.9	Polarized beams dynamics in Nuclotron	52
54	3.10	Operation modes of the NICA collider at polarized beams	53
55	3.11	Conclusion and outlook	54
56	4	Detector layout	55
57	1	General design [A. Guskov]	55
58	2	Magnetic system [A. Kovalenko]	57
59	3	Beam pipe [A. Guskov]	59
60	4	Vertex detector [N. Zamyatin]	60
61	4.1	General overview	60
62	4.2	Double-sided silicon detectors	62
63	4.3	Mechanical layout	62
64	4.4	MAPS option	63
65	4.5	Cost estimate	63

66	5	Straw tracker [T. Enik]	63
67	5.1	Straw technology	64
68	5.2	General layout of the ST	65
69	5.3	Front-end electronics	67
70	5.4	Cost estimate	68
71	6	Electromagnetic calorimeter [O. Gavrischuk]	68
72	6.1	Design of the calorimeter module	69
73	6.2	Multi-pixel photodiodes	69
74	6.3	MPPC readout and High Voltage control	70
75	6.4	Readout electronics	70
76	6.5	Cosmic ray test results	71
77	6.6	Dependence of calorimeter response on the number of photoelectrons	73
78	6.7	Long-term stability	74
79	6.8	Overview of the SPD calorimeter	76
80	6.9	Cost estimate	76
81	7	Range (muon) system [G. Alexeev]	77
82	7.1	General description	77
83	7.2	System layout	78
84	7.3	Mini drift tubes detector	79
85	7.4	Front-end electronics	81
86	7.5	Performance figures	83
87	8	Particle identification system	83
88	8.1	Time of flight system [A. Korzenev]	83
89	8.2	Aerogel counters [A. Kulikov]	90
90	9	Beam-beam counter [V. Ladygin]	91
91	9.1	Inner part of the BBC: MPC	91
92	9.2	Outer part of the BBC: scintillation tiles	94
93	10	Zero Degree Calorimeter [S. Shimansky]	95
94	5	Local polarimetry [V. Ladygin]	98
95	1	Asymmetry in inclusive production of charged particles	98
96	2	Inclusive π^0 production	98
97	3	Single transverse spin asymmetry for very forward neutron production	100

98	6	Detector control system [A. S. Chepurnov]	102
99	1	DCS concept	102
100	2	DCS architecture	104
101	3	SCADA for DCS	104
102	7	Data acquisition system [L. Afanasyev]	107
103	1	Introduction	107
104	2	DAQ structure	108
105	3	Data format	109
106	4	Cost estimate	109
107	8	Computing and Offline Software	114
108	1	SPD Computing Model	114
109	2	Online Filter	115
110	3	Computing System	115
111	3.1	The Computing Model	116
112	3.2	Computing services	117
113	4	Offline Software	118
114	5	Resource estimate	118
115	9	Physics performance	120
116	1	General performance of the SPD setup	120
117	1.1	Minimum bias events [A. Guskov]	120
118	1.2	Tracking [A. Guskov]	122
119	1.3	Vertex reconstruction [A. Guskov, V. Andreev]	123
120	1.4	Calorimetry [A. Guskov]	124
121	1.5	Particle identification with TOF [A. Guskov]	126
122	2	Accuracies of asymmetries measurement	127
123	2.1	Charmonia production [I. Denisenko]	129
124	2.2	Prompt photon production	132
125	2.3	Open charm production	134
126	10	Integration and services [OUT OF DATE]	137
127	1	Hall facilities and services	137
128	2	SPD integration	138

129	11 Beam test facilities [A. Baldin, A. Kovalenko]	140
130	1 Test zone with extracted Nuclotron beams	140
131	2 Tests at the SPD straight section of the collider	141
132	12 Running strategy	142
133	1 Accelerator [A. Kovalenko]	142
134	2 Spin Physics Detector [A. Guskov]	144
135	13 Cost estimate	145
136	14 Participating institutions and author list [In progress]	146
137	15 Conclusion	149

Chapter 1

Executive summary [A. Guskov]

The Spin Physics Detector (proto-)collaboration proposes to install a universal detector in the second interaction point of the constructing NICA collider (JINR, Dubna) to study the spin structure of the proton and deuteron and other spin-related phenomena with polarized proton and deuteron beams at the collision energy up to 27 GeV and the luminosity up to $10^{32} \text{ cm}^{-2} \text{ s}^{-1}$. In polarized proton-proton collisions the NICA SPD experiment will cover the cinematic gap between the low-energy measurements at ANKE-COSY and SATURNE and high-energy measurements at the Relativistic Heavy Ion Collider and the planned fixed-target experiments at LHC (see Fig. 1.1). Possibility for NICA to operate with polarized deuteron beams at such energies is unique.

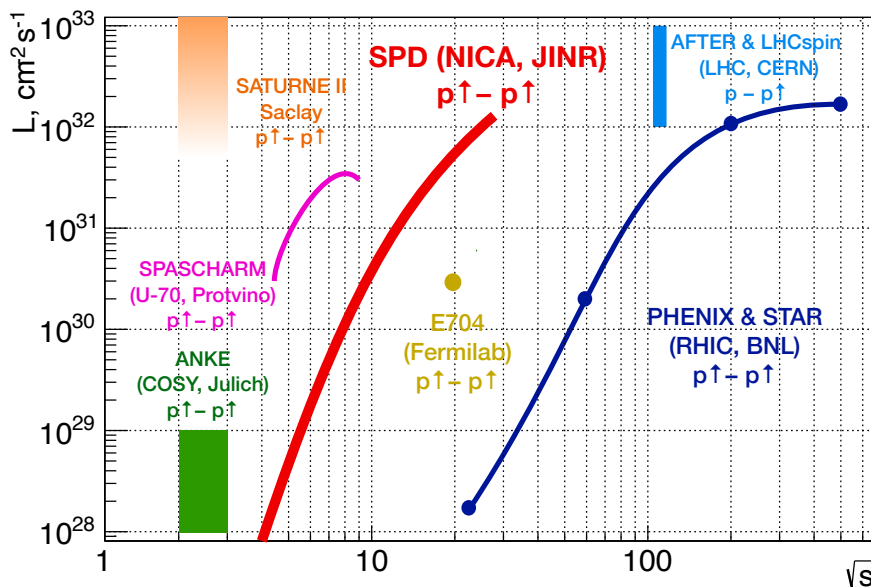


Figure 1.1: NICA SPD and other past, present, and future experiments with polarized protons.

The SPD is planned to operate as a universal facility for comprehensive study of the unpolarized and polarized gluon content of the nucleon at large Bjorken- x , using different complementary probes such as: charmonia, open charm and prompt photon production processes. The experiment aims to provide access to the gluon helicity, gluon Sivers and Boer-Mulders functions in the nucleon, as well as the gluon transversity distribution and tensor PDFs in the deuteron, via the measurement of specific single

153 and double spin asymmetries (see Tab. 1.1). The results expected to be obtained by the SPD will
 154 play an important role in the general understanding of the nucleon gluon content and will serve as a
 155 complementary input to the ongoing and planned studies at RHIC, and future measurements at the EIC
 156 (BNL) and fixed-target facilities at the LHC (CERN). Other polarized and unpolarized physics is possible
 157 especially at the first stage of NICA operation with reduced luminosity and collision energy of proton
 158 and ion beams.

Table 1.1: Gluon vector PDFs planned to be addressed at SPD. Columns represent gluon polarization
 while rows represent hadron polarization.

	Unpolarized	Circular	Linear
Unpolarized	$g(x)$ gluon density		$h_1^{\perp g}(x, k_T)$ gluon Boer-Mulders function
Longitudinal		$\Delta g(x)$ gluon helicity	
Transverse	$\Delta_N^g(x, k_T)$ gluon Sivers function		$\Delta_T g(x)$ gluon transversity (deuteron only)

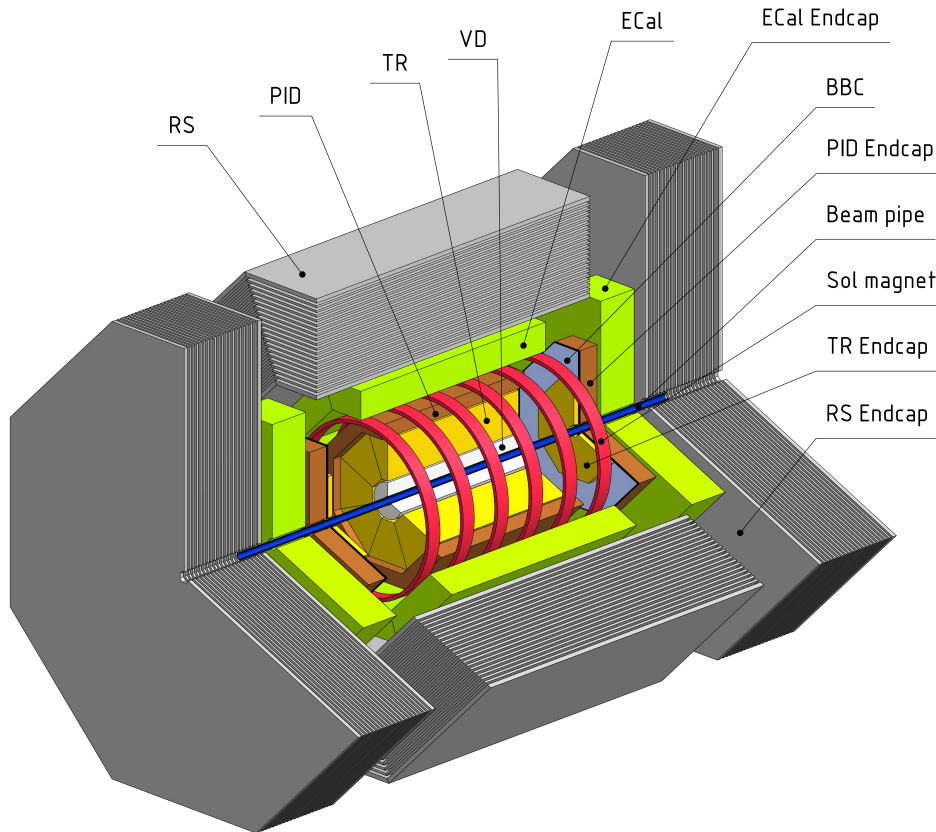


Figure 1.2: General layout of the SPD setup.

159 The physics goals dictate the layout of the detector. The SPD experimental setup is being designed as
 160 a universal 4π detector with advanced tracking and particle identification capabilities based on modern

161 technologies. A silicon vertex detector will provide resolution for position of primary and secondary
162 vertices on the level of XX μm that is needed for reconstruction of secondary vertices of D -mesons
163 decays. A straw tube-based tracking system placed within a solenoidal magnetic field up to 1 T at the
164 detector axis should provide transverse momentum resolution $\sigma_{p_T}/p_T \approx 2\%$ for a particle momentum 1
165 GeV/ c . A time-of-flight system with time resolution of about 60 ps will provide 3σ separation for π/K
166 and K/p up to about 1.2 GeV and 2.2 GeV, respectively. Possible use of an aerogel-based Cherenkov
167 detector could extend this range. Detection of photons will be provided by a sampling electromagnetic
168 calorimeter with energy resolution $\sim 5\%/\sqrt{E}$. To minimize multiple scattering and photon conversion
169 effects for photons, detector material will be kept to a minimum throughout the internal part of the
170 detector. A muon (range) system is planned for the muon identification. It can also act as a rough hadron
171 calorimeter. A pair of beam-beam counters and zero-degree calorimeters will be responsible for local
172 polarimetry and luminosity control. To minimize possible systematic effects the SPD will be equipped
173 with a triggerless DAQ system. High collision rate (up to 4 MHz) and a few hundred thousand detector
174 channels pose a significant challenge to the DAQ, the online monitoring, the offline computing system
175 and data processing software.

176 The proposed physics program covers at least 5 years of running.

177 The estimated cost of the Spin Physics Detector is XX M\$. This value does not cover the R&D expenses
178 and the construction of the SPD Test zone. Any expenses related with development and construction of
179 an infrastructure for polarized beams at NICA are also out of this estimation.

Chapter 2

Physics case

1 Gluons in proton and deuteron [A. Guskov, O. Teryaev]

Gluons, together with quarks, are the fundamental constituents of the nucleon. They play a key role in generation of its mass and carry about half of its momentum in hard (semi)inclusive processes. The spin of the nucleon is also built up from the intrinsic spin of the valence and sea quarks (spin-1/2), gluons (spin-1), and their orbital angular momenta. Notwithstanding the progress achieved during the last decades in the understanding of the quark contribution to the nucleon spin, the gluon sector is much less developed. One of the difficulties is the lack of the direct probes to access gluon content in high-energy processes. While the quark contribution to the nucleon spin was determined quite precisely in semi-inclusive deep-inelastic scattering (SIDIS) experiments like EMC, HERMES, and COMPASS, the gluon contribution is still not well-constrained even so it is expected to be significant.

In recent years, the three-dimensional partonic structure of the nucleon became a subject of a careful study. Precise mapping of three-dimensional structure of the nucleon is crucial for our understanding of Quantum Chromodynamics (QCD). One of the ways to go beyond the usual collinear approximation is to describe nucleon content in the momentum space employing the so-called Transverse-Momentum-Dependent Parton Distribution Functions (TMD PDFs) [1–6].

The most powerful tools to study TMD PDFs are the measurements of the nucleon spin (in)dependent azimuthal asymmetries in SIDIS [1, 4, 5, 7] and Drell–Yan processes [8, 9]. Complementary information on TMD fragmentation process, necessary for the interpretation of SIDIS data, is obtained from e^+e^- measurements [10]. Being an actively developing field, TMD physics triggers a lot of experimental and theoretical interest all over the world, stimulating new measurements and developments in TMD extraction techniques oriented on existing and future data from lepton-nucleon, electron-positron and hadron-hadron facilities at BNL, CERN, DESY, FNAL, JLab, and KEK. For recent reviews on experimental and theoretical advances on TMDs see Refs. [11–15]. While a lot of experimental measurements were performed (and are planned) and theoretical understanding was achieved for Leading Order (LO) (twist-2) TMD PDFs such as Sivers, transversity and Boer-Mulders functions of quarks, only few data relevant for the study of gluon TMD PDFs are available [16–21].

The simplest model of the deuteron is a weakly-bound state of a proton and a neutron mainly in the S-wave with a small admixture of the D-wave state. This approach is not much helpful in the description of the deuteron structure at large Q^2 ¹. Possible non-nucleonic degrees of freedom in deuteron could play an important role in the understanding of the nuclear modification of PDFs (the EMC ef-

¹We use Q^2 (or μ^2) as a generic notation for the hard scale of a reaction: the invariant mass square of lepton pairs in Drell-Yan processes, Q^2 , transverse momentum square p_T^2 of produced hadron or its mass square M^2 .

212 fect). Since the gluon transversity operator requires two-unit helicity-flip it does not exist for spin-1/2
 213 nucleons [22]. Therefore, proton and neutron gluon transversity functions can not contribute directly
 214 to the gluon transversity of the deuteron. A non-zero deuteron transversity could be an indication of a
 215 non-nucleonic component or some other exotic hadronic mechanisms within the deuteron.

216 Most of the existing experimental results on spin-dependent gluon distributions in nucleon are obtained
 217 in the experiments at DESY (HERMES), CERN (COMPASS), and BNL (STAR and PHENIX). Study of
 218 polarized gluon content of the proton and nuclei is an important part of future projects in Europe and the
 219 United States such as AFTER@LHC and LHCSpin at CERN, and EIC at BNL [23–25]. Notwithstanding
 220 the fact that the gluons in nucleon were successfully probed in SIDIS measurements, hadronic collisions
 221 have an important advantage since they probe the gluons at the Born-level without involving the EM
 222 couplings.

223 1.1 Gluon probes at NICA SPD

224 The polarized gluon content of proton and deuteron at intermediate and high values of the Bjorken x
 225 will be investigated using three complementary probes: inclusive production of charmonia, open charm,
 226 and prompt photons. Study of these processes is complementary to such proven approaches to access
 227 the partonic structure of the nucleon in hadronic collisions as the inclusive production of hadrons with
 228 high transverse momentum and the Drell-Yan process. Unfortunately, the latter one is unlikely to be
 229 accessible at SPD due to the small cross section and unfavourable background conditions. For effective
 230 registration of each aforementioned gluon probes, the SPD setup is planned to be equipped with a range
 231 (muon) system, an electromagnetic calorimeter, a time-of-flight system, straw tracker, and a silicon ver-
 232 tex detector. Nearly a 4π coverage of the setup and a low material budget in the inner part of the setup
 233 should provide a large acceptance for the detection of the desired final states. In Fig. 2.1(a) the kinematic
 234 phase-space in x and Q^2 to be accessed by the SPD is compared to the corresponding ranges of previ-
 235 ous, present and future experiments. Parameters of the experimental facilities planning to contribute to
 236 gluon physics with polarized beams are listed in Tab. 2.1. Figure 2.1(b) illustrates the behavior of the
 237 cross sections for the inclusive production of J/ψ , ψ' , D -mesons and high- p_T prompt photons in p - p
 238 collisions as a function of \sqrt{s} .

239 1.1.1 Charmonia production

240 From the experimental point of view, for considered energies, hadronic production of charmonia seems
 241 to be particularly suited to access gluon content in hadrons. Production of prompt J/ψ -mesons looks
 242 most attractive, since large data set of $J/\psi \rightarrow \mu^+ \mu^-$ ($BF = 0.06$) events is accumulated in beam-dump
 243 experiments with proton and pion beams at \sqrt{s} close to 20 GeV. However J/ψ -meson is not the cleanest
 244 probe of the proton structure, since a significant fraction (about 20% [30]) of J/ψ -mesons observed
 245 in hadronic collisions is produced indirectly through decays of χ_{cJ} and $\psi(2S)$ (the so-called feed-down
 246 contribution), and modeling of this contribution introduces additional uncertainties in theoretical calcu-
 247 lations. Hence, to provide additional constraints to production models, it is important to study production
 248 of χ_{cJ} and $\psi(2S)$ separately, through their decays $\chi_{cJ} \rightarrow \gamma J/\psi$ ($BF = 0.014, 0.343$ and 0.19 for $J = 0, 1$
 249 and 2) and $\psi(2S) \rightarrow \mu^+ \mu^-$ ($BF = 0.08$). The latter state is of special interest, because it is essentially free
 250 from feed-down contamination from higher charmonium states, due to the proximity of $D^0 \bar{D}^0$ -threshold.
 251 However, the separation of the $\chi_{c0,1,2}$ signals is a challenging experimental task due to the small mass
 252 difference between the states and low energy resolution of the electromagnetic calorimeters for soft pho-
 253 tons.

254 Besides, from the theoretical point of view the task of accessing gluon distributions using heavy quarko-
 255 nia is rather challenging. The heavy quark-antiquark pair couples directly to gluons from initial-state
 256 hadrons (Fig. 2.2(a)) and it's production can be calculated perturbatively, because the hard scale of the

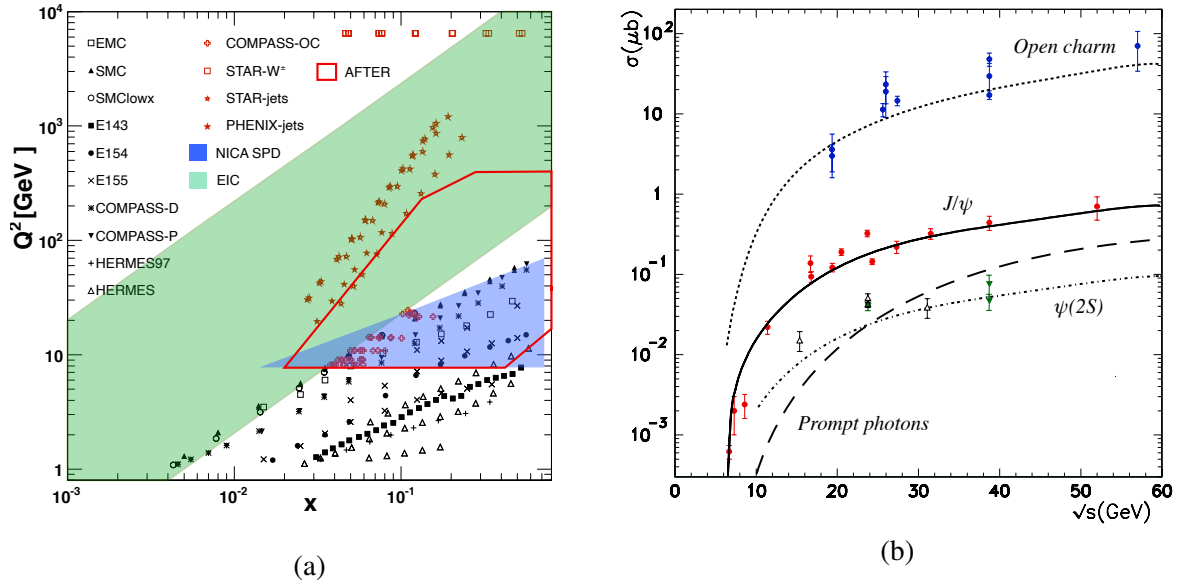


Figure 2.1: (a) The kinematic coverage, in the (x, Q^2) plane, of the hadronic cross section data for the processes commonly included in global QCD analyses of polarized quark (black) and gluon (red) PDFs [26]. The kinematic domain expected to be covered by NICA SPD by charmonia, open charm and prompt-photon production is shown in blue. (b) Cross section for the processes of open charm, J/ψ , $\psi(2S)$ and prompt photons ($p_T > 3$ GeV) production as a function of center-of-mass energy (based on [27]).

Table 2.1: Main present and future actors in gluon spin physics.

Experimental facility	SPD @NICA [29]	RHIC [28]	EIC [25]	AFTER @LHC [23]	SpinLHC [24]
Scientific center	JINR	BNL	BNL	CERN	CERN
Operation mode	collider	collider	collider	fixed target	fixed target
Colliding particles & polarization	$p^\uparrow-p^\uparrow$ $d^\uparrow-d^\uparrow$ $p^\uparrow-d, p-d^\uparrow$	$p^\uparrow-p^\uparrow$	$e^\uparrow-p^\uparrow, d^\uparrow, {}^3\text{He}^\uparrow$	$p-p^\uparrow, d^\uparrow$	$p-p^\uparrow$
Center-of-mass energy $\sqrt{s_{NN}}$, GeV	≤ 27 ($p-p$) ≤ 13.5 ($d-d$) ≤ 19 ($p-d$)	63, 200, 500	20-140 (ep)	115	115
Max. luminosity, $10^{32} \text{ cm}^{-2} \text{ s}^{-1}$	~ 1 ($p-p$) ~ 0.1 ($d-d$)	2	1000	up to ~ 10 ($p-p$)	4.7
Physics run	>2025	running	>2030	>2025	>2025

257 process is limited from below by the heavy quark mass, providing the direct access to polarized and un-
 258 polarized gluon distributions. However, the process of transition of the heavy quark-antiquark pair into a

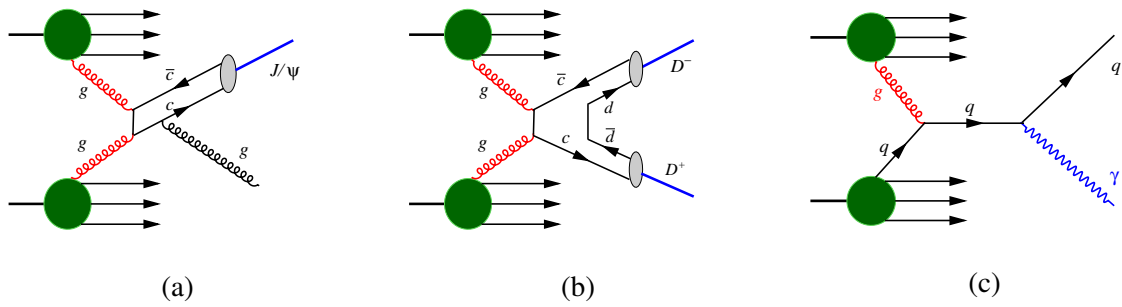


Figure 2.2: Diagrams illustrating three probes to access the gluon content of proton and deuteron in polarized collisions at NICA SPD: production of (a) charmonium, (b) open charm, (c) prompt photons.

259 physical bound-state is not well understood at present and can become a source of significant theoretical
 260 uncertainties. We review modern status of the theory of quarkonium production in more detail in Sec. 1.5
 261 to explain the latter point.

262 Therefore, quarkonium production can be used to study the structure of hadrons only with a great caution
 263 and only if the results consistent with other probes will eventually emerge. The studies of hadronic
 264 structure and heavy quarkonium production mechanism should become complimentary. But for now the
 265 most reasonable phenomenological strategy for measurements at SPD concerning quarkonia is to study
 266 yields and polarization of different quarkonium states in a wide kinematic range, at various energies, and
 267 in polarized as well as non-polarized hadronic collisions, to provide the development of the theory with
 268 more constraints allowing to exclude various models. When the theory of production of heavy quarkonia
 269 is firmly established – it will become an invaluable tool to study the details of hadronic structure.

270 1.1.2 Open charm production

271 It is well-known that the heavy flavor production offers direct probes of the gluon distributions in hadrons.
 272 The basic mechanism responsible for charm pair production in pp collisions is the gluon fusion (GF, see
 273 Fig. 2.2(b)). In the framework of pQCD, the GF contributes to the hadron cross section as $\mathcal{L}_{gg} \otimes \hat{\sigma}_{c\bar{c}}$,
 274 where the gluon luminosity \mathcal{L}_{gg} is a convolution of the gluon densities in different protons, $\mathcal{L}_{gg} = g \otimes g$.
 275 At leading order in pQCD, $\mathcal{O}(\alpha_s^2)$, the partonic cross section $\hat{\sigma}_{c\bar{c}}$ describes the process $gg \rightarrow c\bar{c}$.

276 The GF contribution to the charmonia production in pp collisions has the form $\mathcal{L}_{gg} \otimes \hat{\sigma}_{(c\bar{c})+X} \otimes W_{c\bar{c}}$.
 277 At the Born level, the partonic cross section $\hat{\sigma}_{(c\bar{c})+X}$ is of the order of α_s^3 because its basic subprocess
 278 is $gg \rightarrow (c\bar{c}) + g$. Moreover, the quantity $W_{c\bar{c}}$, describing the probability for the charm pair to form a
 279 charmonium, imposes strong restrictions on the phase space of the final state.² For these two reasons,
 280 the α_s -suppression and phase space limitation, the cross sections for charmonia production are almost
 281 two orders of magnitude smaller than the corresponding ones for open charm, see Figs. 2.1 (b).

282 To analyze the kinematics of a DD pair, each of D -mesons has to be reconstructed. The decay modes
 283 $D^+ \rightarrow \pi^+ K^- \pi^+$ (BF=0.094) and $D^0 \rightarrow \pi^+ K^- \pi^+$ (BF=0.04) can be used for that. To suppress a com-
 284 binatorial background SPD plans to use the search for a secondary vertex of a D -meson decay that is
 285 about 100 μm far from the interaction point (the $c\tau$ values are 312 and 123 μm for the charged and
 286 neutral D -mesons, respectively). Identification of a charged kaon in the final state by the time-of-flight
 287 system would also help to do that. Production and decay of D^* -mesons could be used as an additional tag
 288 for open-charm events. Singe-reconstructed D -mesons also carry reduced but still essential information
 289 about gluon distribution that is especially important in the low-energy region with a lack of statistics.

²To form a charmonium, the momenta of the produced quark and antiquark should be sufficiently close to each other.

290 1.1.3 Prompt photon production

291 Photons emerging from the hard parton scattering subprocess, the so-called prompt photons, serve as a
 292 sensitive tool to access the gluon structure of hadrons and hadron-hadron collisions. Inclusive direct pho-
 293 ton production proceeds without fragmentation, i.e. the photon carries the information directly from the
 294 hard scattering process. Hence this process measures a combination of initial k_T effects and hard scat-
 295 tering twist-3 processes. There are two main hard processes for the production of direct photons: gluon
 296 Compton scattering, $gq(\bar{q}) \rightarrow \gamma q(\bar{q})$ (Fig. 2.2(c)), which dominates, and quark-antiquark annihilation,
 297 $q\bar{q} \rightarrow \gamma g$. Contribution of the latter process to the total cross section is small.

298 Theoretical predictions for inclusive prompt photon production are shown in Fig. 2.3(a) as transverse
 299 momentum spectrum at the energy $\sqrt{s} = 27$ GeV. Calculations are performed in LO and NLO approx-
 300 imations of CPM, as well as in the Parton Reggeization Approach (PRA), which is a QCD and QED
 301 gauge-invariant version of k_T -factorization. They include direct and fragmentation contributions, the lat-
 302 ter one is about 15-30 %. The K-factor between LO and NLO calculations in the CPM slightly depends
 303 on $p_{T\gamma}$ and equals about 1.8 [31]. LO prediction of PRA coincides with the result of NLO CPM calcu-
 304 lation at moderate transverse momenta ($p_T < 4$ GeV) while at higher p_T PRA predicts somewhat harder
 305 p_T -spectrum.

306 In experiments prompt photons are detected alongside with a much larger number of photons from decays
 307 of secondary π^0 and η mesons (minimum-bias photons). The main challenge is to subtract these decay
 308 contributions to obtain the photons directly emitted from hard collisions. This kind of background is
 309 especially important at small transverse momenta of produced photons (p_T) and gives the lower limit
 310 of the accessible p_T range. Therefore the prompt-photon contribution with $p_T \leq 2 - 3$ GeV is usually
 311 unreachable in the experiment [32]. Figure 2.3(b) [33] presents the comparison of the p_T spectra ($x_T =$
 312 $2p_T/\sqrt{s}$) measured in a wide kinematic range of \sqrt{s} in different fixed-target and collider experiments
 313 and the theoretical NLO calculations performed within the JETPHOX package [34]. While high-energy
 314 collider results exhibit rather good agreement with expectations, situation at high- x_T is not pretty good.
 315 The results of the E706 ($\sqrt{s} = 31.6$ and 38.8 GeV) [35] and R806 ($\sqrt{s} = 63$ GeV) [36] experiments
 316 break out the trend and demonstrate some "slope". It could be an indication of possible systematic effects
 317 that have not been yet fully understood.

318 A pair of prompt photons can be produced in hadronic interactions in $q\bar{q}$ annihilation, quark-gluon scat-
 319 tering, and gluon-gluon fusion hard processes (at the leading, next-to-leading, and next-to-next-leading
 320 orders, respectively). The double prompt photon production in nucleon interactions at low energies is not
 321 yet well-studied experimentally. The production cross section for proton-carbon interaction at $\sqrt{s} = 19.4$
 322 GeV/c has been measured by the CERN NA3 experiment [37]. Based on this result we can expect the
 323 cross section of the double photon production with $p_T > 2$ GeV/c for each photon on the level of about
 324 0.5 nb.

325 Estimations of the expected event rates are evaluated for p - p collisions at $\sqrt{s} = 27$ and 13.5 GeV for the
 326 projected integrated luminosity 1.0 and 0.1 fb $^{-1}$, respectively that corresponds effectively to one year of
 327 data taking (10^7 s). The results are listed in Tab. 2.2.

328 1.2 Gluons at large x

329 The gluon PDF is one of poorly known parton distributions in the proton because available data con-
 330 strain weakly the quantity $g(x, Q^2)$, particularly for x greater than 0.5 [40, 41]. In the high- x region, the
 331 gluon density is usually parameterized as $g(x, Q^2) \sim (1-x)^L$, and values of L extracted from global fits
 332 differ considerably from each other. In particular, obtained results for L vary from 3 to 11 at $Q^2 = 1.9$
 333 GeV 2 [42].

334 To improve the situation with large x , one needs precise data on the heavy flavor production at energies

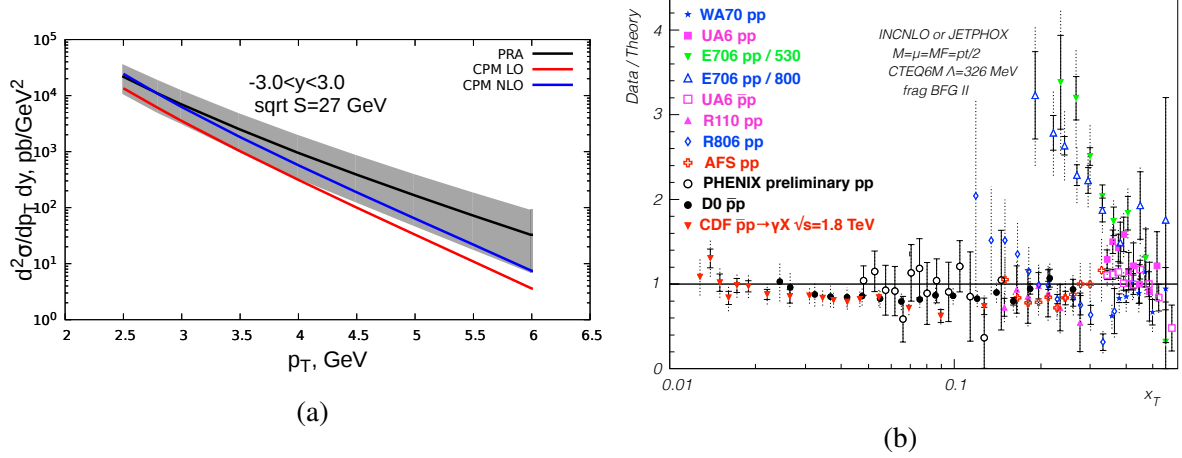


Figure 2.3: (a) Prediction for prompt photon transverse momentum spectrum at $\sqrt{s} = 27$ GeV obtained in LO (red line) and NLO (blue line) approximations of CPM and LO of PRA (black line). Uncertainty bands for PRA predictions are due to factorization/renormalization scale variation only. (b) Data-to-theory ratio for the fixed-target and collider experiments [33].

Table 2.2: Expected rates for each of the gluon probes (per one year of SPD running).

Probe	$\sigma_{27 GeV}$, nb (\times BF)	$\sigma_{13.5 GeV}$, nb (\times BF)	$N_{27 GeV}$, 10^6	$N_{13.5 GeV}$, 10^6
Prompt- γ ($p_T > 3$ GeV/c)	35	2	35	0.2
J/ψ $\rightarrow \mu^+ \mu^-$	200 12	60 3.6	12	0.36
$\psi(3686)$ $\rightarrow J/\psi \pi^+ \pi^- \rightarrow \mu^+ \mu^- \pi^+ \pi^-$ $\rightarrow \mu^+ \mu^-$	25 0.5 0.2	5 0.1 0.04	0.5 0.2	0.01 0.004
Open charm: $D\bar{D}$ pairs	1.5×10^4	1300	1.5×10^4	130
Single D -mesons $D^+ \rightarrow K^- 2\pi^+$ and $D^- \rightarrow K^+ 2\pi^-$ $D^0 \rightarrow K^- \pi^+$ and $\bar{D}^0 \rightarrow K^+ \pi^-$	1100 730	100 65	1100 730	10 6.5

335 not so far from the production threshold. Concerning the open charm production in pp collisions, the
 336 corresponding cross sections are poorly known for $\sqrt{s} < 27$ GeV [43, 44].³ Presently, the only available
 337 measurements for this region were performed by the E769 experiment, which corresponds three hundred
 338 events collected in pA collisions [45]. Unfortunately, E769 results have large uncertainties, which is
 339 enough to estimate only the order of magnitude for the $pp \rightarrow c\bar{c}X$ cross section at $\sqrt{s} \approx 20$ GeV. For this
 340 reason, future studies of the open charm production at SPD in pp and dd collisions for $\sqrt{s} \leq 27$ GeV are
 341 of special interest. In particular, they will allow to reduce significantly the present uncertainties in the
 342 gluon density (and α_s) at a GeV scale, especially for high x .

343 Detailed information on the gluon distribution at large x is very important for various phenomenological

³On the contrary, the J/ψ production cross section is known well enough practically down to the threshold, see Fig. 2.1(b).

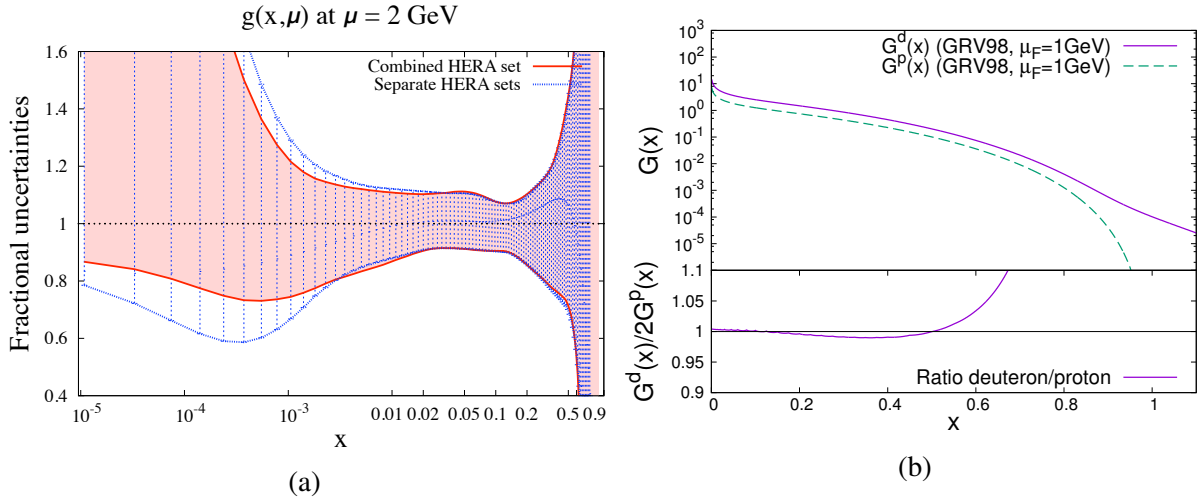


Figure 2.4: (a) Uncertainty of unpolarized gluon PDF based on HERA data ($\mu = 2 \text{ GeV}$) [38]. (b) Gluon PDF in the deuteron in comparison with the nucleon [39].

344 applications. For instance, it is of current interest to estimate the $b\bar{b}$ pair production cross section at
 345 NICA energies. Such predictions, however, are not presently reliable due to their strong dependence on
 346 the exponent L which is known poorly. Another example is the DGLAP evolution of the PDFs. Using
 347 precise data on $g(x, Q^2)$ (and α_s) at $Q^2 \sim m_c^2$ (m_c is the mass of the c-quark) as boundary conditions in
 348 DGLAP equations, one could reduce essentially the uncertainties in evolution of PDFs for higher values
 349 of Q .

350 From the theoretical point of view, the threshold behavior of cross sections is closely related to the so-
 351 called infrared renormalon problem. It is well known that radiative corrections to the production cross
 352 sections contain the mass (or threshold) logarithms whose contribution is expected to be sizable near the
 353 threshold. These logarithms are usually taken into account within the soft gluon resummation (SGR)
 354 formalism [46–50]. Formally resummed cross sections are, however, ill-defined due to the Landau pole
 355 contribution, and few prescriptions have been proposed to avoid the renormalon ambiguities [51–54].
 356 Unfortunately, numerical predictions for heavy quark production cross sections can depend significantly
 357 on the choice of resummation prescription. Undoubtedly, anticipated data from SPD on the charm pro-
 358 duction not so far from the production threshold will provide an excellent test for these prescriptions.

359 Another interesting problem for NICA SPD is to probe the intrinsic charm (IC) content of the proton [55,
 360 56]. The IC contribution to open charm production is expected to be sizable near the threshold because
 361 its PDF, $c(x, Q^2)$, is predicted to be harder than the gluonic one. As a result, the IC density in the proton
 362 can be dominant at sufficiently large x independently of its overall normalization [57]. To visualize the
 363 IC component, one needs to collect much enough events like $D\bar{D}$ pair produced in $pp \rightarrow D\bar{D}$ with a large
 364 overall x_F close to 1. That events are predicted to be very rare within the GF mechanism and would
 365 directly indicate the five-quark component in the proton, $|uudc\bar{c}\rangle$

366 Investigation of the open charm production in pp , pd and dd collisions might be one of the key points in
 367 the NICA SPD programme. The motivation is twofold. On the one hand, production of D -mesons in pp
 368 collisions is practically unmeasured at NICA energies. On the other hand, these presently unavailable
 369 data on open charm production rates are strongly necessary for determination of the gluon density $g(x, \mu)$
 370 at large x where this PDF is practically unknown.

371 Moreover, anticipated results on the open charm production are very important for many other current
 372 issues in particle physics: from infrared renormalon ambiguities in cross sections to intrinsic charm
 373 content of the proton.

1.3 Tests of TMD factorization with gluon probes

The description of hard inclusive processes in hadron collisions is based on factorization theorems. Formulation of factorization theorems in terms of the TMD PDFs of quarks and gluons is the most important step towards studying the 3D structure of hadrons and the nature of their spins. The conventional TMD-approach [58] can be applied for study of processes with colorless final states with transverse momenta much smaller than the relevant scale of hadron interactions, $q_T \ll Q$. In recent years a substantial success was achieved in the quark sector of TMD PDFs related with their correct theoretical definition and the connection with experimentally observed cross sections within the framework of factorization theorems [6]. In the case of unpolarized hadron collisions, in the leading twist approximation the production cross section is a function of two independent TMD PDFs, i.e. distribution functions of unpolarized quarks f_1^q and distribution functions of transversely polarized quarks $h_1^{\perp q}$ (referred to as Boer-Mulders function) in unpolarized nucleons. For description of cross sections in collisions of polarized hadrons, the number of TMD PDFs increases.

However, the situation with gluon TMD PDFs is significantly different. Until recently, gluon TMD PDFs were used only within the framework of phenomenological models of the type of the Generalized Parton Model (GPM), in which the factorization formula of the Collinear Parton Model is applied if small (non-perturbative-origin) transverse momenta of gluons from colliding hadrons are available.

The proof of the factorization theorem for processes with gluon TMD PDFs, as well as the formulation of evolution equations for them, have been presented relatively recently in [59], where it was applied to describe the Higgs boson production with small transverse momenta. However, hard processes in which detailed information on gluon TMD PDFs can be obtained primarily, include the processes of production of heavy mesons (D , B) and heavy quarkonia (J/ψ , Υ , η_c , η_b , ...). In these processes, there are two non-perturbative mechanisms to be factorized: the emission of soft gluons in the initial state and the formation of a colorless hadron in the final state. Even in the case of heavy meson production with small transverse momenta when their spectrum is determined only by a non-perturbative q_T -distribution of initial gluons, for factorization of hard and soft interactions it is not enough to use the TMD PDFs formalism, the introduction of new non-perturbative process-dependent hadron observables, the so-called TMDShFs (TMD shape functions) [60, 61] is needed. Moreover, the differential cross section for the process of production the state \mathcal{Q} in a collision of unpolarized hadrons is written as

$$\frac{d\sigma}{dyd^2q_T} \sim f_1^g \otimes f_1^g \otimes S_{\mathcal{Q}} - w_{UU} \otimes h_1^{\perp g} \otimes h_1^{\perp g} \otimes S_{\mathcal{Q}},$$

where $S_{\mathcal{Q}}$ is the polarization-independent TMDShFs of this process and w_{UU} is the universal contribution weight function of linearly polarized TMD PDFs.

The factorization theorem contains three or more non-perturbative hadronic quantities at low transverse momenta: gluon TMD PDFs and TMDShFs. Thus, the phenomenological extraction of gluon TMDs from quarkonium production processes is still possible, i.e., a robust factorization theorem can potentially be obtained in any particular case of heavy meson production. However one also needs to model and extract the involved TMDShFs.

1.4 Linearly polarized gluons in unpolarized nucleon

Search for the polarized quarks and gluons in unpolarized hadrons is of special interest in studies of the spin-orbit couplings of partons and understanding of the proton spin decomposition. The corresponding intrinsic transverse momentum \vec{k}_T dependent distributions of the transversely polarized quarks, $h_1^{\perp q}(x, \vec{k}_T^2)$, and linearly polarized gluons, $h_1^{\perp g}(x, \vec{k}_T^2)$, in an unpolarized nucleon have been introduced in Refs. [3] and [62]. Contrary to its quark version $h_1^{\perp q}$ the TMD density $h_1^{\perp g}$ is T - and chiral-even, and thus can directly be probed in certain experiments.

417 Azimuthal correlations in heavy quark pair production in unpolarized ep and pp collisions as probes
 418 of the density $h_1^{\perp g}$ have been considered in Refs. [63, 64]. For the case of DIS, the complete angular
 419 structure of the pair production cross section has been obtained in terms of seven azimuthal modulations.
 420 However, only two of those modulations are really independent; they can be chosen as the $\cos\varphi$ and
 421 $\cos 2\varphi$ distributions, where φ is the heavy quark (or anti-quark) azimuthal angle [65, 66].⁴

To probe the TMD distributions, the momenta of both heavy quark and anti-quark, \vec{p}_Q and $\vec{p}_{\bar{Q}}$, in the process $pp \rightarrow Q\bar{Q}X$ should be measured (reconstructed). For further analysis, the sum and difference of the transverse heavy quark momenta are introduced,

$$\vec{K}_\perp = \frac{1}{2}(\vec{p}_{Q\perp} - \vec{p}_{\bar{Q}\perp}), \quad \vec{q}_T = \vec{p}_{Q\perp} + \vec{p}_{\bar{Q}\perp}, \quad (2.1)$$

422 in the plane orthogonal to the collision axis. The azimuthal angles of \vec{K}_\perp and \vec{q}_T are denoted as ϕ_\perp and
 423 ϕ_T , respectively.

424 The angular structure of the $pp \rightarrow Q\bar{Q}X$ cross section has the following form:

$$d\sigma_{pp} \propto A(q_T^2) + B(q_T^2)q_T^2 \cos 2(\phi_\perp - \phi_T) + C(q_T^2)q_T^4 \cos 4(\phi_\perp - \phi_T). \quad (2.2)$$

425 Assuming factorization for the TMD distributions, the terms A , B and C can schematically be written as
 426 the following convolutions [64]:

$$\begin{aligned} A &\propto f_1^q \otimes f_1^{\bar{q}} \otimes A_q + f_1^g \otimes f_1^g \otimes A_g + h_1^{\perp g} \otimes h_1^{\perp g} \otimes A_g^\perp, \\ B &\propto h_1^{\perp q} \otimes h_1^{\perp \bar{q}} \otimes B_q + f_1^g \otimes h_1^{\perp g} \otimes B_g, \\ C &\propto h_1^{\perp g} \otimes h_1^{\perp g} \otimes C_g. \end{aligned} \quad (2.3)$$

427 The order α_s^2 predictions for the coefficients A_i , B_i and C_i ($i = q, g$) in Eqs.(2.3) are presented in Ref.[64].
 428 Using these results, one can, in principle, extract the densities $h_1^{\perp q}(x, \vec{k}_T^2)$ and $h_1^{\perp g}(x, \vec{k}_T^2)$ from azimuthal
 429 distributions of the $D\bar{D}$ pairs produced in pp collisions.

430 Another processes proposed to probe the linearly polarized gluons in unpolarized proton are: pseu-
 431 doscalar C -even quarkonia (such as η_c and χ_c) [68], di-gamma ($pp \rightarrow \gamma\gamma X$) [69] and J/ψ - pair ($pp \rightarrow$
 432 $J/\psi J/\psi X$) [70] production. These reactions are however strongly suppressed in comparison with
 433 $pp \rightarrow D\bar{D}X$.

434 1.5 Hadron structure and heavy charmonia production mechanisms

435 In this section we give a short review of modern status of the theory of heavy quarkonium production
 436 with an emphasis on possible applications of heavy quarkonium measurements for studies of the gluon
 437 content of hadrons.

438 Production of heavy quarkonia proceeds in two stages: first, a heavy quark-antiquark pair is produced
 439 at short distances, predominantly via gluon-gluon fusion but also with a non-negligible contribution
 440 of $q\bar{q}$ and qg -initiated subprocesses. The second stage is hadronization of quark-antiquark pair into a
 441 physical quarkonium state, which happens at large distances (low scales) and is accompanied by a com-
 442 plicated rearrangement of color via exchanges of soft gluons between the heavy quark-antiquark pair and
 443 other colored partons produced in the collision. Existing approaches, aimed to describe hadronization
 444 stage, such as Non-Relativistic QCD factorization (NRQCD-factorization) [71] and (Improved-) Color-
 445 Evaporation Model (CEM) [72–75] are currently facing serious phenomenological challenges (see e.g.

⁴The function $h_1^{\perp g}$ can also be determined from measurements of the Callan-Gross ratio in DIS [67].

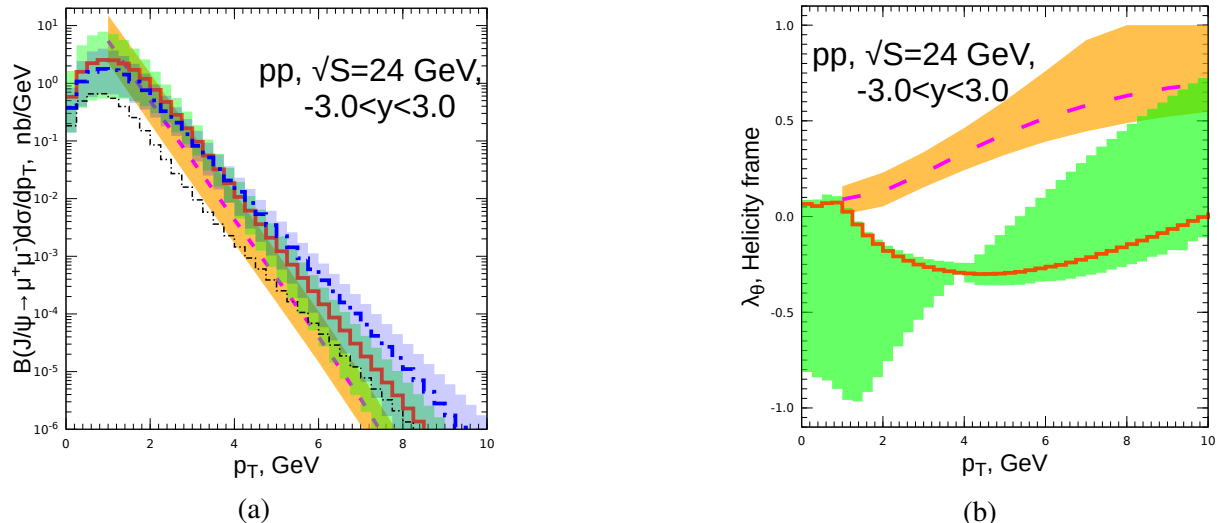


Figure 2.5: Theoretical predictions for inclusive J/ψ p_T -spectrum (a) and p_T -dependence of polarization parameter λ_θ (b) in various models: NLO of Collinear Parton Model + NRQCD-factorization (thick dashed line with orange uncertainty band) [88, 89], LO of PRA [90] + NRQCD-factorization (thick solid histogram with a green uncertainty band) [91, 92], and LO PRA [90] + Improved Color Evaporation Model (thick dash-dotted histogram with blue uncertainty band) [93]. The contribution of $q\bar{q}$ -annihilation channel to the central ICEM prediction is depicted by the thin dash-dotted histogram. Uncertainty bands are due to factorization/renormalization scale variation only.

446 recent reviews [76, 77]). NRQCD-factorization is challenged by the long-standing “polarization puzzle” [78, 79] and violation of Heavy-Quark Spin Symmetry relations between Long-Distance Matrix
 447 Elements (LDMEs) of η_c and J/ψ [80], while CEM usually rather poorly reproduces the detailed shapes
 448 of inclusive p_T -spectra of charmonia and bottomonia and, unlike NRQCD-factorization [81, 82], sig-
 449 nificantly under-predicts bulk of cross section for pair hadroproduction of J/ψ even at NLO in α_s [83].
 450 Presently, the study of the heavy-quarkonium production mechanism is an active field of research, with
 451 new approaches, such as subleading-power fragmentation [84] and Soft-Gluon Factorization [85–87],
 452 being proposed recently.
 453

454 Due to above-mentioned problems and multitude of competing theoretical approaches and models avail-
 455 able on the market, our lack of quantitative understanding of the mechanism of hadronization can become
 456 a source of significant theoretical uncertainties if quarkonium production is to be used as a tool to study
 457 the proton structure. The Fig. 2.5 provides an insight on this situation at NICA SPD. In this figure,
 458 predictions of three models for the p_T -spectrum (Fig. 2.5(a)) and p_T -dependence of the polarization pa-
 459 rameter λ_θ (Fig. 2.5(b)) are compared. The first one relies on the NLO calculation in Collinear Parton
 460 Model (with LO being $O(\alpha_s^3)$, see Fig. 2.2(a)) to describe short-distance part of the cross section and
 461 uses the NRQCD-factorization formalism for the long-distance part, with LDMEs of the latter tuned to
 462 charmonium production data in hadronic collisions, DIS and e^+e^- -annihilation [78, 79, 88, 89]. In the
 463 second prediction, the short-distance part of the cross section is calculated in the LO ($O(\alpha_s^2)$ for color-
 464 octet and P -wave contributions and $O(\alpha_s^3)$ for color-singlet S -wave ones) of PRA [90], while LDMEs
 465 in this calculation had been fitted to the charmonium hadroproduction data from RHIC, Tevatron and
 466 LHC [91, 92]. The third prediction is performed in the LO ($O(\alpha_s^2)$) of PRA with the same uninte-
 467 grated PDFs as for the second one, but interfaced with an improved Color-Evaporation Model (ICEM)
 468 of Ref. [93] for description of hadronization. Non-perturbative parameters of the ICEM had been taken
 469 from the Ref. [93] where they had been fitted to charmonium hadroproduction data at Tevatron and LHC
 470 energies. Predictions of all three models for inclusive J/ψ p_T -spectrum at NICA SPD appear to be

471 consistent within their uncertainty bands. However, the structure of this predictions is significantly dif-
 472 ferent, with NRQCD-based predictions being dominated by gluon-gluon fusion subprocess, while ICEM
 473 prediction containing significant contamination from $q\bar{q}$ -annihilation (thin dash-dotted histogram in the
 474 Fig. 2.5(a)), which reaches up to 50% at low $p_T < 1$ GeV and contributes up to 10% at higher $p_T > 3$
 475 GeV. Also ICEM tends to predict significantly harder p_T -spectrum at $p_T > 5$ GeV, than NRQCD-based
 476 PRA prediction which was performed with the same unintegrated PDFs.

477 Discussion above shows, that J/ψ p_T -spectrum can be reliably predicted only in the limited range of
 478 transverse momenta, approximately from 3 to 6 GeV at $\sqrt{s} = 24$ GeV. At higher p_T the shape of the
 479 spectrum becomes highly model-dependent and at lower $p_T < M_{J/\psi}$ the TMD-factorization effects (in-
 480 cluding possible violation of factorization, see [60, 61]) come into the game and the contribution of
 481 $q\bar{q}$ -annihilation subprocess becomes uncertain. Nevertheless, predictions and measurements of rapidity
 482 or x_F -differential cross-sections even in this limited p_T -range could help to further constrain the gluon
 483 PDF, e.g. to rule-out the extreme values of L in the $x \rightarrow 1$ asymptotics of the PDF $\sim (1-x)^L$.

484 Predictions of NLO CPM and LO of PRA for polarization parameter λ_θ (see the Fig. 2.5(b)) are sig-
 485 nificantly different, with PRA predicting mostly un-polarized production ($\lambda_\theta \simeq 0$) while CPM predicts
 486 transverse polarization ($\lambda_\theta = +1$) at high p_T . Disagreement of the predictions for polarization param-
 487 eters mostly reflects the difference of LDMEs obtained in two fits and their large uncertainty bands are
 488 due to significant uncertainties of LDMEs. Measurements of heavy quarkonium polarization at NICA
 489 energies will provide additional constraints on models, however due to well-known problems with de-
 490 scription of polarization at high energies [78, 79] constraints coming from polarization measurements
 491 should be interpreted with great care and one should try to disentangle conclusions for gluon PDF from
 492 the results related to heavy quarkonium polarization.

493 1.6 Non-nucleonic degrees of freedom in deuteron

494 The naive model describes the deuteron as a weakly-bound state of a proton and a neutron mainly in
 495 S-state with a small admixture of the D-state. However, such a simplified picture failed to describe the
 496 HERMES experimental results on the b_1 structure function of the deuteron [94]. Modern models treat
 497 the deuteron as a six-quark state with the wave function

$$|6q\rangle = c_1|NN\rangle + c_2|\Delta\Delta\rangle + c_3|CC\rangle, \quad (2.4)$$

498 that contains such terms as the nucleon $|NN\rangle$, Δ -resonance $|\Delta\Delta\rangle$ and the so-called hidden color compo-
 499 nent $|CC\rangle$ in which two color-octet baryons combine to form a color singlet [95]. Such configurations
 500 can be generated, for example, if two nucleons exchange a single gluon. The relative contribution of the
 501 hidden-color term varies from about 0.1% to 80% in different models [96]. The components other than
 502 $|NN\rangle$ should manifest themselves in the high- Q^2 limit. Possible contributions of the Fock states with a
 503 valent gluon like $|uuudddg\rangle$ could also be discussed [39, 97].

504 The unpolarized gluon PDF of the deuteron in the light-front quantization was calculated in the Ref. [39]
 505 under the approximation where the input nuclear wave function is obtained by solving the nonrelativistic
 506 Schrödinger equation with the phenomenological Argonne v18 nuclear potential as an input. Gluon PDFs
 507 calculated per nucleon are very similar for the proton one in the range of small and intermediate x values
 508 while for $x > 0.6$ the difference becomes large due to the Fermi motion (see Fig. 2.14(a)). A similar
 509 work was performed in Ref. [98] for determination of spatial gluon distribution in deuteron for low- x
 510 that could be tested in the J/ψ production at EIC. Today the gluon content of deuteron and light nuclei
 511 becomes the matter of interest for the lattice QCD studies [99]. Apart from the general understanding of
 512 the gluon EMC effect, the measurement of the gluon PDF at high- x for deuteron could provide a useful
 513 input for high-energy astrophysical calculation [39].

SPD can perform an explicit comparison of the differential inclusive production cross sections $d\sigma/dx_F$ for all three gluon probes: charmonia, open charm, and prompt photons using p - p and d - d collisions at $\sqrt{s_{NN}} = 13.5$ GeV and possibly below. Such results could be treated in terms of the difference of unpolarized gluon PDFs in deuteron and nucleon.

1.7 Gluon polarization Δg with longitudinally polarized beams

The gluon helicity distribution function $\Delta g(x)$ is a fundamental quantity characterizing the inner structure of the nucleon. It describes the difference of probabilities to find in the longitudinally polarized nucleon a gluon with the same and opposite spin orientations. The integral $\Delta G = \int \Delta g(x) dx$ can be interpreted as the gluon spin contribution to the nucleon spin. After the EMC experiment discovered that only a small part of proton spin is carried by the quarks [100], the gluon spin was assumed to be another significant contributor. So ΔG is a key ingredient of the nucleon helicity sum rule

$$\frac{1}{2} = \frac{1}{2}\Delta\Sigma + \Delta G + L_q + L_g, \quad (2.5)$$

where $\Delta\Sigma \approx 0.25$ [15] is the net contribution from the quark spin and L_q, L_g represent contribution of the orbital angular momenta of quarks and gluons, respectively.

The first attempt to measure the gluon polarization in the nucleon was made by the FNAL E581/704 Collaboration using a 200 GeV polarized proton beam and a polarized proton target [101]. They measured the longitudinal double-spin asymmetries A_{LL} for inclusive multi- γ and $\pi^0\pi^0$ production to be consistent with zero within their sensitivities. In the following years a set of SIDIS measurements was performed by the HERMES [102], SMC [103] and COMPASS [104–108] experiments. The production of hadron pairs with high transverse momenta and the production of the open charm where the photon-gluon fusion mechanism dominates were studied. It was figured out that with a large uncertainty the value of ΔG is close to zero. Nevertheless, for gluons carrying a large fraction x of the nucleon momentum, an evidence of a positive polarization has been observed, see Fig. 2.6(a). New results for ΔG were obtained from the measurement of the A_{LL} asymmetries in the inclusive production of high- p_T neutral pions [109–111], η -mesons [109], jets [112], heavy flavors [113] and, recently, J/ψ -mesons [114] in polarized p - p collisions at RHIC. The new data in general are in agreement with SIDIS measurements, which demonstrates the universality of the helicity-dependent parton densities and QCD factorization.

At the moment the most recent sets of polarized PDFs extracted in the NLO approximation are LSS15 [115], DSSV14 [116, 117], NNPDF-pol1.1 [26], and JAM17 [118]. To obtain them, different approaches, parameterizations, and sets of experimental data were used, see Ref. [119] for more details. Fit results for $\Delta g(x)$ from DSSV14 and NNPDF-pol1.1 are presented in Fig. 2.6(b) [117]. The RHIC p - p data put a strong constraint on the size of $\Delta g(x)$ in the range $0.05 < x < 0.2$ but cannot determine its sign as soon as they mainly probe Δg squared (see details below). The small x region remains still largely unconstrained and could be covered in future by measurements at EIC [25]. Region of high x is covered at the moment only by SIDIS measurements which still lack a proper NLO description [120]. The uncertainty of the contribution to Δg from the kinematic range $0.001 < x < 0.05$ vs. the corresponding contribution from the range $x > 0.05$ for the DSSV global fits is shown in Fig. 2.7(a) [116].

In case of the longitudinally polarized p - p collisions the asymmetry A_{LL} is defined as

$$A_{LL} = \frac{\sigma^{++} - \sigma^{+-}}{\sigma^{++} + \sigma^{+-}}, \quad (2.6)$$

where σ^{++} and σ^{+-} denote the cross sections with the same and opposite proton helicity combinations, respectively. For the prompt photons produced via the gluon Compton scattering

$$A_{LL}^\gamma \approx \frac{\Delta g(x_1)}{g(x_1)} \otimes A_{1p}(x_2) \otimes \hat{a}_{LL}^{gq(\bar{q}) \rightarrow \gamma q(\bar{q})} + (1 \leftrightarrow 2). \quad (2.7)$$

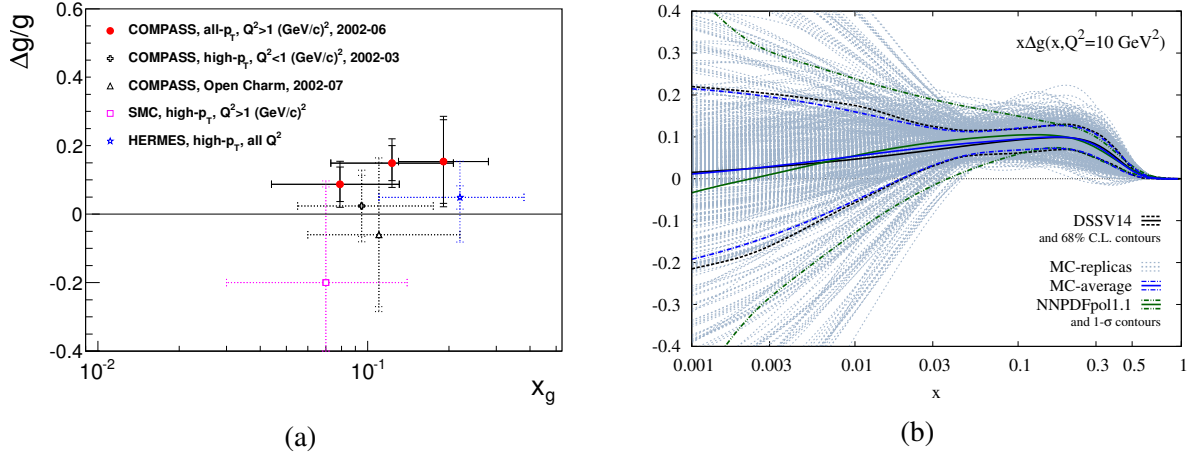


Figure 2.6: (a) SIDIS data on $\Delta g(x)/g(x)$ extracted in LO [108]. (b) Global fit results for the gluon helicity distribution $\Delta g(x)$ [117].

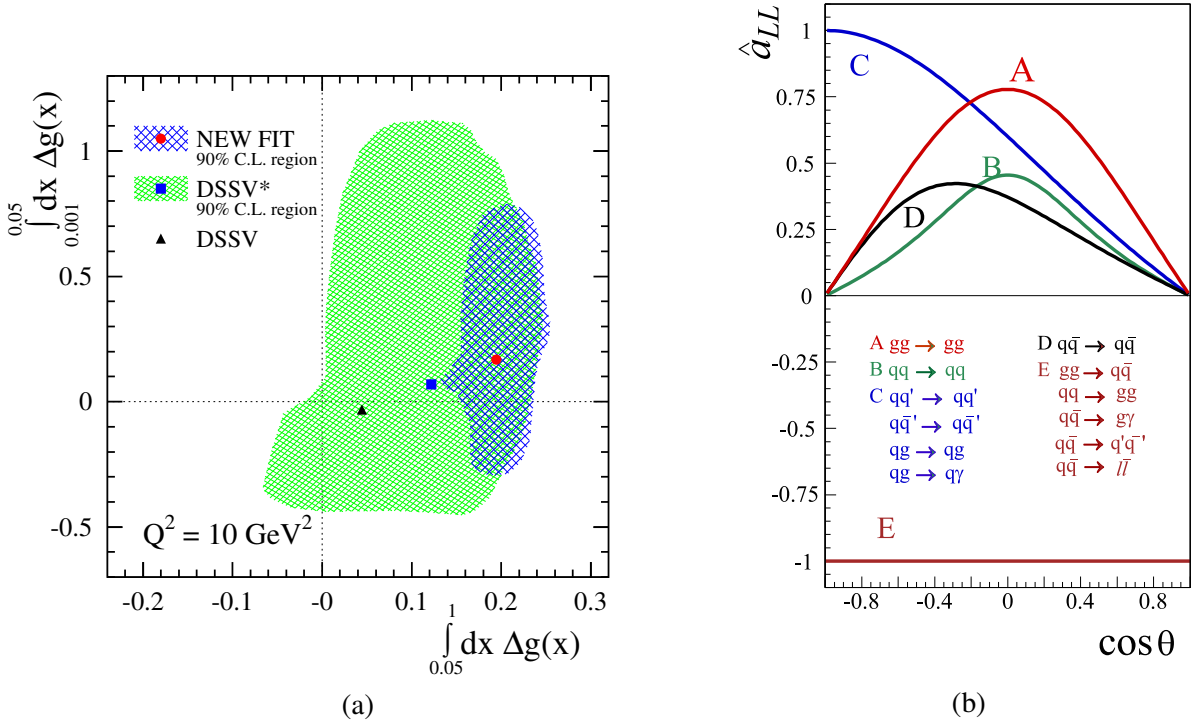


Figure 2.7: (a) Estimates of contributions of low- x and high- x kinematic ranges into ΔG for the DSSV series of the global fit. The 90% C.L. areas are shown [116]. (b) Partonic longitudinal double-spin asymmetries A_{LL} for different hard processes as a function of center-of-mass scattering angle [121].

553 Here $A_{1p}(x)$ is the asymmetry well-measured in a wide range of x and $\hat{a}_{LL}^{gq(\bar{q}) \rightarrow \gamma q(\bar{q})}$ is the asymmetry of
 554 the corresponding hard process. The Fig. 2.7(b) shows the behavior of \hat{a}_{LL} for different hard processes
 555 as a function of the center-of-mass scattering angle. For charmonia and open charm production via the
 556 gluon-gluon fusion process the expression for the corresponding asymmetry reads

$$A_{LL}^{c\bar{c}} \approx \frac{\Delta g(x_1)}{g(x_1)} \otimes \frac{\Delta g(x_2)}{g(x_2)} \otimes \hat{a}_{LL}^{gg \rightarrow c\bar{c}X}. \quad (2.8)$$

557 This asymmetry on the one hand is more sensitive to the gluon polarization than the corresponding one

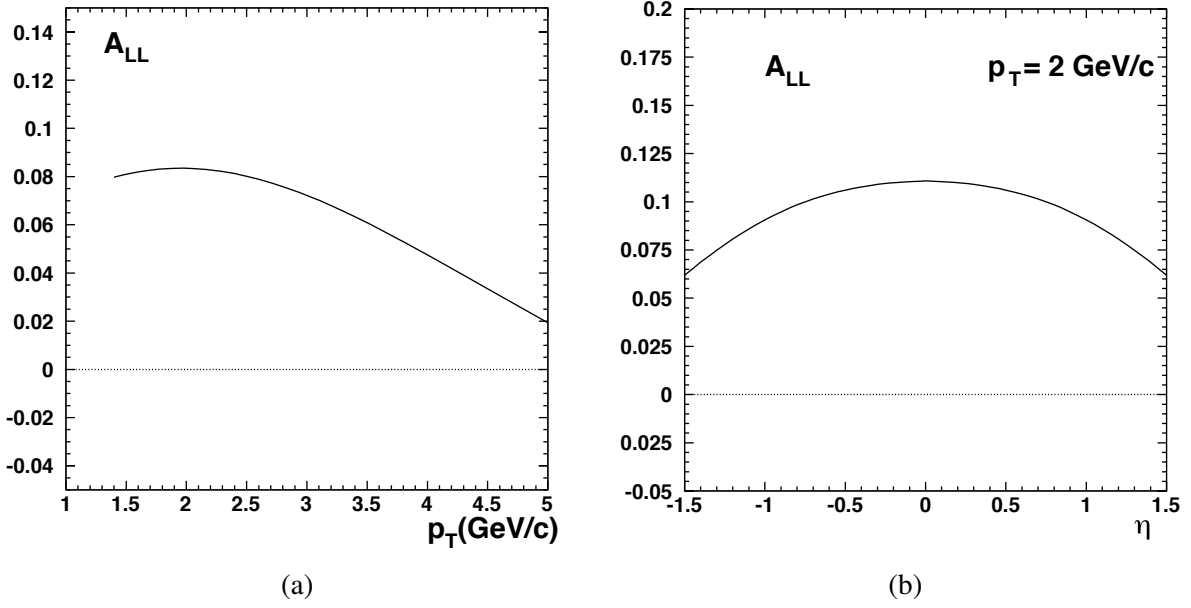


Figure 2.8: Longitudinal double spin asymmetry A_{LL} for inclusive J/ψ production calculated for p - p collisions at $\sqrt{s} = 39$ GeV in the LO approximation as a function of a) transverse momentum p_T and b) pseudorapidity η [122].

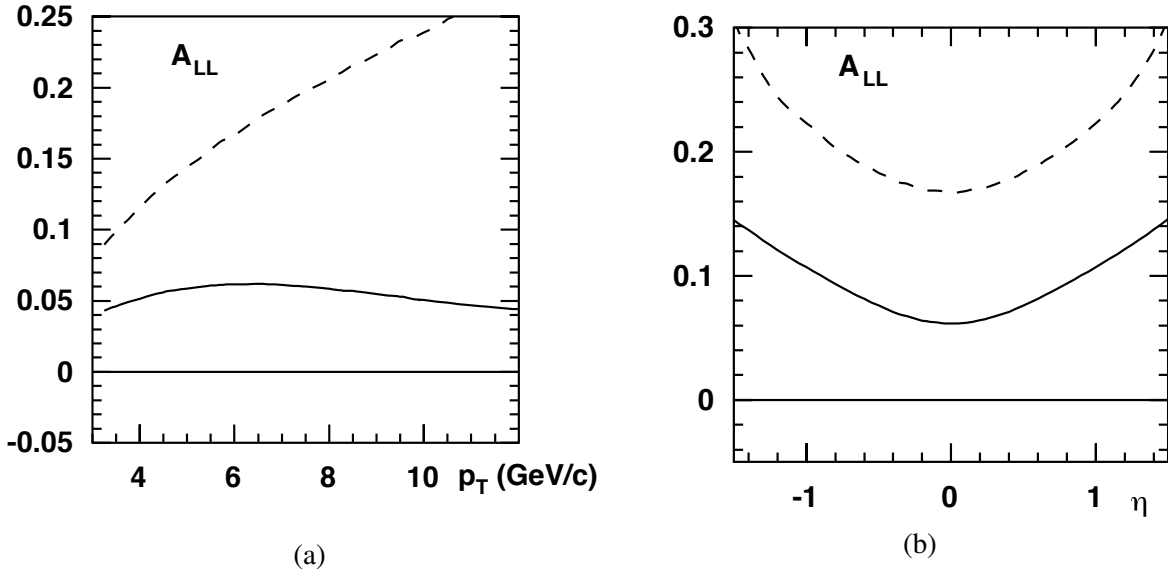


Figure 2.9: Longitudinal double spin asymmetry A_{LL} for inclusive prompt-photon production calculated for p - p collisions at $\sqrt{s} = 39$ GeV in the LO approximation as a function of a) transverse momentum p_T and b) rapidity η ($p_T = 6$ GeV/c) [122].

558 for the prompt photons due to the quadratic dependence on Δg . On the other hand the sign of the Δg
 559 value can not be determined from it. So the measurements with prompt photons and heavy-quark states
 560 are complementary. The contribution of $q\bar{q}$ annihilation processes to the above-mentioned asymmetries
 561 is negligible despite $\hat{a}_{LL} = -1$ because of the smallness of the sea-quark polarization in the nucleon.

562 It is important to emphasise that a sizable systematic uncertainty of A_{LL} measurements in the inclusive
 563 J/ψ production comes from our limited knowledge of charmonia production mechanisms including

564 the feed-down contribution. Each of them has different partonic asymmetries \hat{a}_{LL} [123]. For the Δg
 565 estimation in Ref. [114] the value of $\hat{a}_{LL}^{J/\psi}$ has been forced to -1 . The SPD setup will have the possibility
 566 to reconstruct $\chi_c J$ states via their radiative decays and resolve J/ψ and $\psi(2S)$ signals in a wide kinematic
 567 range and disentangle contributions of different production mechanisms. The quality of the Δg estimation
 568 could be significantly improved by measuring A_{LL} separately for each charmonium state.

569 Predictions for the longitudinal double-spin asymmetries A_{LL} in p - p collisions can be found in Refs. [124]
 570 (J/ψ) and [125] (prompt photons). They mostly cover the kinematic range of the RHIC experiments.
 571 Some estimates for A_{LL} in charmonia [122] and prompt-photon [122, 126, 127] production at $\sqrt{s} =$
 572 39 GeV (see Figs. 2.8 and 2.9, respectively) have been done in preparation of the unrealized HERA- \vec{N}
 573 project.

574 The authors of the Ref. [128] proposed to extract information about the gluon helicity Δg via studying
 575 of the production of high- p_T prompt photons accompanied by Σ^+ hyperons. To do that the single lon-
 576 gitudinal spin asymmetry $A_L^{\gamma\Sigma}$ and the polarization of the produced Σ^+ hyperons should be measured.
 577 However, further elaboration of this method is needed.

578 1.8 Gluon-related TMD and twist-3 effects with transversely polarized beams

579 One of the promising ways to investigate the spin structure of the nucleon is the study of transverse single-
 580 spin asymmetries (SSAs) in the inclusive production of different final states in high-energy interactions.
 581 The SSA A_N is defined as

$$A_N = \frac{\sigma^\uparrow - \sigma^\downarrow}{\sigma^\uparrow + \sigma^\downarrow}, \quad (2.9)$$

582 where σ^\uparrow and σ^\downarrow denote the inclusive production cross sections with opposite transverse polarization of
 583 one of the colliding particles. At the moment, more than forty years after the transverse spin phenom-
 584 ena were discovered, a wealth of experimental data indicating non-zero A_N in the lepton-nucleon and
 585 nucleon-nucleon interactions was collected. However, our understanding of the SSA phenomenon is not
 586 yet conclusive.

587 Theoretically two dual approaches are used to explain the transverse single-spin asymmetries: the collinear
 588 twist-3 formalism and the transverse momentum dependent (TMD) factorization approach. In the first
 589 one at large transverse momenta $p_T \gg \Lambda_{QCD}$ of a produced particle, the collinear factorization involving
 590 twist-3 contributions for three-parton (Efremov-Teryaev-Qiu-Sterman) correlations [129–132] are used.
 591 Here $\Lambda_{QCD} \approx 200$ MeV is the QCD scale. An alternative approach assumes the TMD factorization, valid
 592 for $p_T \ll Q$, where the SSAs come from the initial-state quark and gluon Sivers functions or the final-
 593 state Collins fragmentation functions. The Sivers function $f_{1T}^{\perp,q(g)}(x, k_T)$ is a TMD PDF that describes
 594 the left-right asymmetry in the distribution of the partons w.r.t. to the plane defined by the nucleon spin
 595 and momentum vectors. Originating from the correlation between the spin of the nucleon and the orbital
 596 motion of partons, it is an important detail of the three-dimensional picture of the nucleon. This func-
 597 tion is responsible for the so-called Sivers effect (for both quarks and gluons) that was first suggested
 598 in [133] as an explanation for the large single transverse spin asymmetries A_N in the inclusive production
 599 of the nucleon. More on the theoretical and experimental status of the transverse spin structure of the
 600 nucleon can be found in Refs. [13, 134]. The first attempt to access the gluon Sivers function (GSF)
 601 studying azimuthal asymmetries in high- p_T hadron pair production in SIDIS of transversely polarised
 602 deuterons and protons, was performed by COMPASS [20]. Using neural network techniques the contri-
 603 bution originating from Photon–Gluon Fusion (PGF) subprocess has been separated from the leading-
 604 order virtual-photon absorption and QCD Compton scattering subprocesses. The measured combined
 605 proton-deuteron PGF-asymmetry was found to be negative and more than two standard deviations below
 606 zero, which supports the possible existence of a non-zero Sivers function. In the meantime, COMPASS

607 did not see any signal for the PGF Collins asymmetry, which can analogously be related to the gluon
 608 transversity distribution. COMPASS studied GSF also through Siverson asymmetry in the J/ψ -production
 609 channel [21], again obtaining an indication of a negative asymmetry.

610 Recently, in Ref. [135] a first estimate of the GSF was obtained using the midrapidity data on the A_N
 611 SSA, measured in π^0 production at RHIC [16]. The extraction was performed within the GPM frame-
 612 work using GRV98-LO set for the unpolarized PDF and available parameterizations for the quark Siverson
 613 functions (SIDIS1 from Ref. [136] and SIDIS2 from Ref. [137]). The two parameterizations were ob-
 614 tained using different options for fragmentation functions, namely Kretzer [138] and DSS07 [139] sets,
 615 which give significantly different results for gluons. The latter point has a strong impact on the extracted
 616 GSF especially in low- x region. First k_T -moments of the GSF $\Delta_N^{q(g)}(x, k_T)$ for the SIDIS1 and SIDIS2
 617 sets are shown in Fig. 2.10 (a) and (b), respectively.

618 The gluon Siverson function is expected to satisfy the positivity bound defined as two time the unpolarized
 619 TMD gluon distribution. Although, some theoretical expectations are that the gluon Siverson function at
 620 relatively high x is about 1/3 of the quark one [134].

621 Several inclusive processes were proposed to access the gluon-induced spin effects in transversely po-
 622 larized p - p collisions. Single spin asymmetries for production of charmonia [140] (RHIC, AFTER),
 623 open charm [141–144] (RHIC) [144] (AFTER), and prompt photons [131, 145] (E704), [146] (RHIC)
 624 were estimated using both approaches for the experimental conditions of the past, present, and future
 625 experiments.

626 The SSA $A_N^{J/\psi}$ in the J/ψ production was measured by PHENIX in the p - p and p - A collisions at $\sqrt{s_{NN}} =$
 627 200 GeV/ c [17, 18]. The obtained values for $A_N^{J/\psi}$ are consistent with zero for negative and positive
 628 x_F . Theoretical predictions [140] based on the Color Evaporation Model with TMD approach and the
 629 gluon Siverson function from Ref. [147] for different center-of-mass energies are shown in Fig. 2.11(a) as
 630 functions of rapidity y . Since the J/ψ production mechanism is not well understood, the measurement
 631 of the $A_N^{J/\psi}$ may bring a valuable input to that matter as well. Predictions for $A_N^{J/\psi}$ in proton-proton
 632 collisions at NICA energy $\sqrt{s} = 27$ GeV, obtained in GPM + NRQCD approach, as function of x_F and
 633 p_T are shown in the Figure (2.12). For comparison, results are presented for SIDIS1 [136] and D’Alesio
 634 et al. [148, 149] parameterizations of proton Siverson function.

635 A measurement with open-heavy hadrons (both D - and B -mesons) was performed at RHIC (PHENIX,
 636 $\sqrt{s} = 200$ GeV) [19] using high- p_T muons from their semileptonic decays. Obtained results are affected
 637 by relatively large statistical uncertainties and do not exhibit any significant non-zero asymmetry. Never-
 638 theless, the results do not contradict the predictions of the twist-3 approach from Ref. [142]. The Siverson
 639 effect contribution to the A_N^D asymmetry calculated within the Generalized Parton Model for $\sqrt{s} = 27$
 640 GeV is presented in Fig. 2.11(b).

641 Measurement of the A_N^γ SSA with prompt photons provides a unique opportunity to study the Siverson PDF
 642 and twist-3 correlation functions, since the corresponding hard process does not involve fragmentation
 643 in the final state and thus is exempt from the Collins effect. The first attempt to measure A_N^γ at $\sqrt{s} = 19.4$
 644 GeV was performed at the fixed target experiment E704 at Fermilab in the kinematic range $-0.15 < x_F <$
 645 0.15 and $2.5 \text{ GeV}/c < p_T < 3.1 \text{ GeV}/c$. The results were consistent with zero within large statistical and
 646 systematic uncertainties [150]. Figure 2.13(a) shows the expected A_N^γ asymmetry as a function of x_F for
 647 $\sqrt{s} = 27$ GeV based on the SIDIS1 extraction of the gluon Siverson function. Quark and gluon contributions
 648 from the gluon Compton scattering, dominating at positive and negative values of x_F , respectively, are
 649 shown separately. The $q\bar{q}$ annihilation contribution is also presented. Dashed lines illustrate the twist-3
 650 predictions for $\sqrt{s} = 30$ GeV and $p_T = 4$ GeV/ c for negative [145] and positive [131] values of x_F . The
 651 p_T dependence of the A_N^γ asymmetry at $x_F = -0.5$ is shown for different values of \sqrt{s} in Fig. 2.13(b).

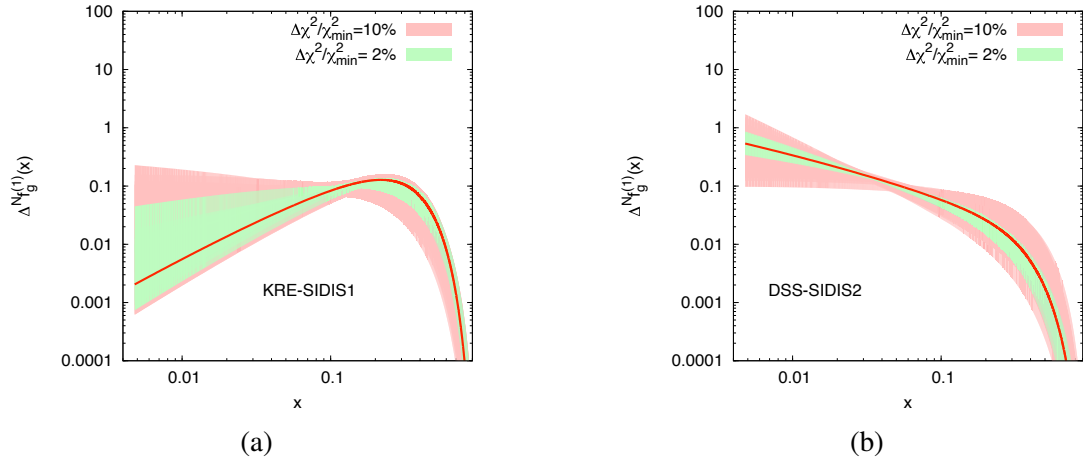


Figure 2.10: The first k_T -moment of the gluon Siverson function for SIDIS1 [136] and SIDIS2 [137] extractions of the quark Siverson functions [135].

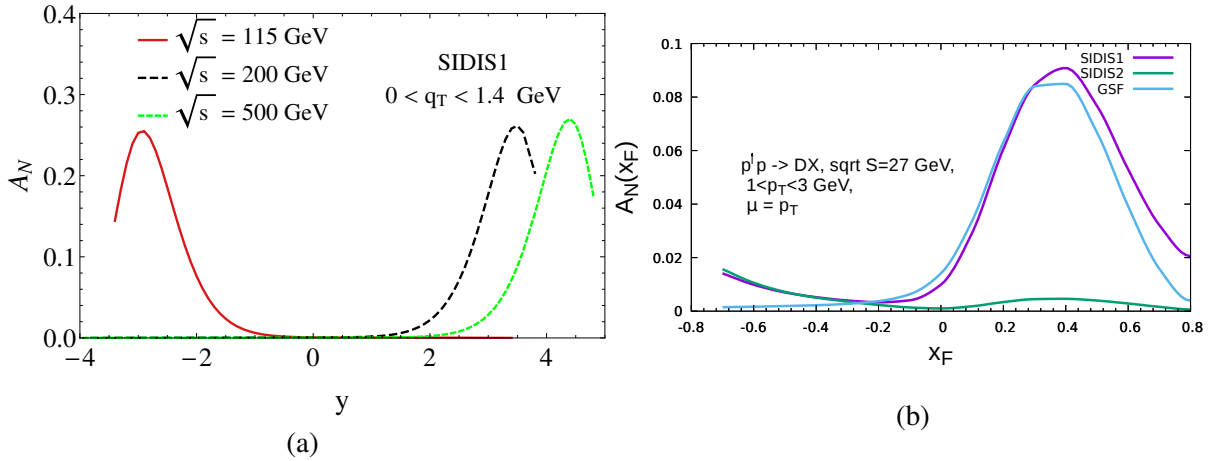


Figure 2.11: (a) Predictions for $A_N^{J/\psi}$ for $\sqrt{s} = 115$ GeV (AFTER), 200 GeV and 500 GeV (RHIC) as a function of rapidity y [140]. (b) Siverson effect contribution to the A_N^D asymmetry calculated within the Generalized Parton Model.

652 1.9 Gluon transversity in deuteron

653 The transversity function $\Delta_T q(x)$ is defined for partons as the difference of probabilities to find in a
 654 transversely polarized nucleon a parton with the same and opposite spin orientations. In spite of the
 655 definition is similar to the helicity function $\Delta q(x)$, the transversity describes a completely different aspect
 656 of the nucleon spin structure. This function is known quite well after a series of SIDIS and Drell-Yan
 657 experiments. As soon as the transversity is related with the spin flip, for the spin-1/2 nucleon only a
 658 quark contribution ($\Delta s = 1$) is possible while $\Delta s = 2$ for the spin-1 gluons is forbidden in the twist-2.
 659 Nevertheless, a tiny nonzero gluon transversity is allowed due to higher-twist effects and possible physics
 660 beyond the Standard model like electric dipole moment of the neutron [151]. The transverse double spin
 661 asymmetry A_{TT} defined for interaction of transversely polarized hadrons by the similar manner as A_{LL}
 662 is a way to access the transversity. But due to the absence of a gluonic contribution in the leading order
 663 in the case of the nucleon interactions $A_{TT} \ll A_{LL}$. As an example, the asymmetry A_{TT}^γ for the prompt-
 664 photon production at 200 and 500 GeV coming from the $q\bar{q}$ annihilation process calculated in LO [152]
 665 and NLO [153] is shown in Fig. 2.14(b).

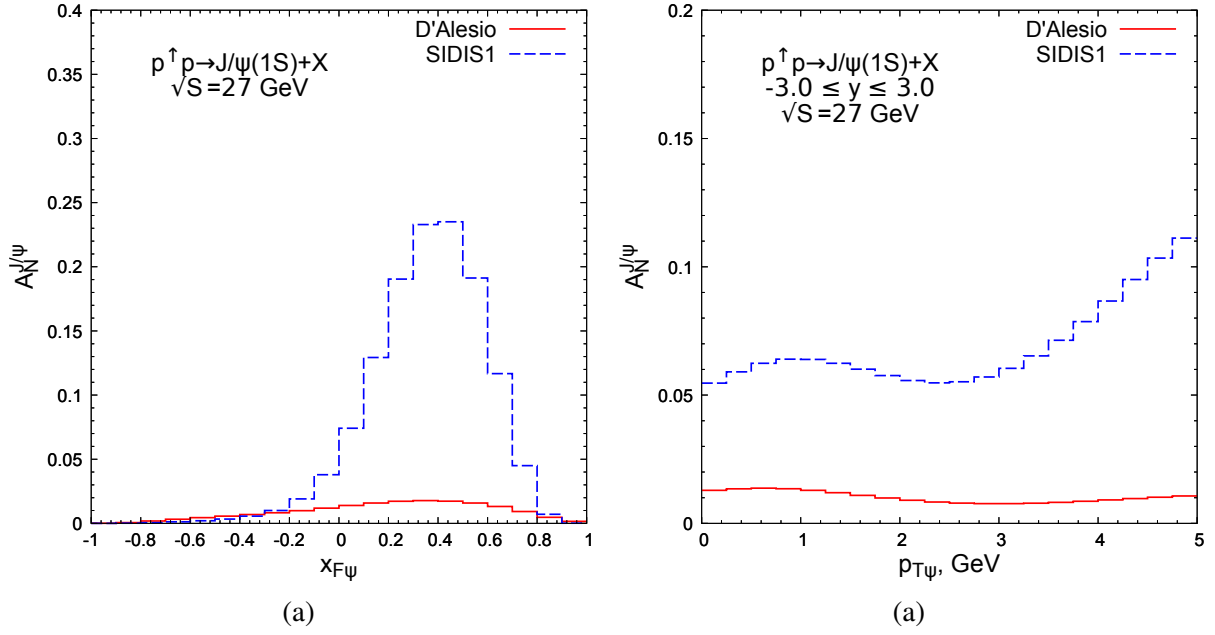


Figure 2.12: Predictions for $A_N^{J/\psi}$ as function of x_F (a) and p_T (b) in p - p collisions at the energy $\sqrt{S} = 27$ GeV obtained in GPM + NRQCD approach.

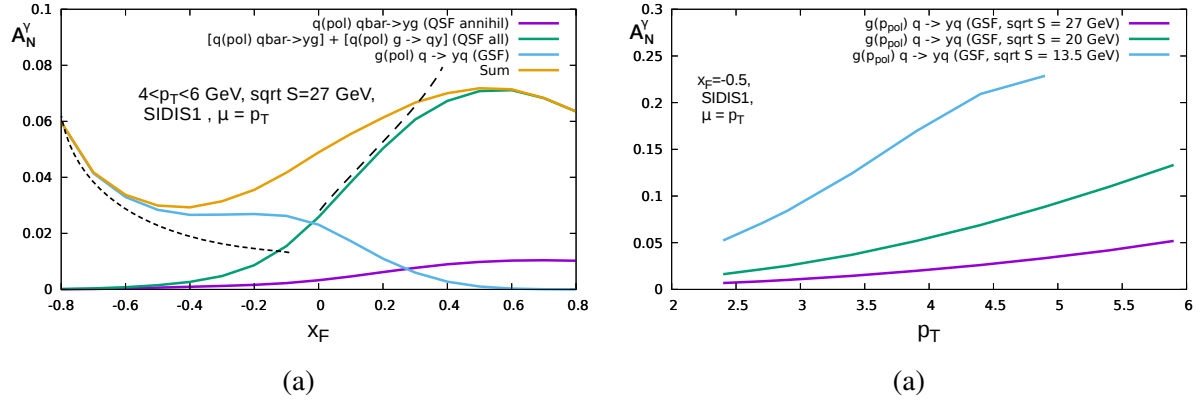
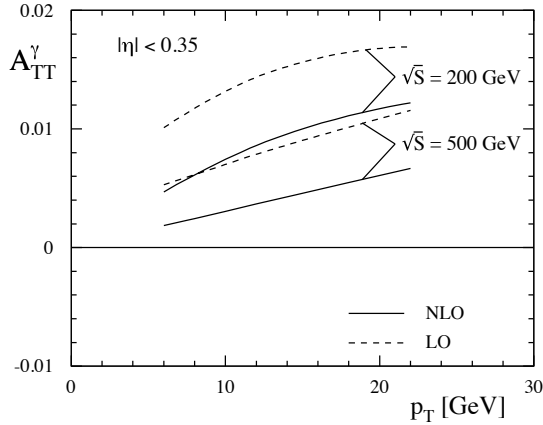


Figure 2.13: (a) x_F dependence of the asymmetry A_N^γ calculated basing on the SIDIS1 Siverts function for $\sqrt{s} = 27$ GeV and $4 < p_T < 6$ GeV. Gluon and quark contributions are shown separately by color solid lines. Dashed lines illustrate the twist-3 predictions for $\sqrt{s} = 30$ GeV and $p_T = 4$ GeV for negative [145] and positive [131] values of x_F . (b) p_T dependence of the A_N^γ asymmetry for different values of \sqrt{s} at $x_F = -0.5$.

666 Situation changes [154] for the spin-1 deuteron where a gluon component not embedded into the nucleons
 667 is possible. So in the collision of transversely polarized deuterons a nonzero contribution of the gluon
 668 transversity $\Delta_T g(x)$ to A_{TT} asymmetries is possible already in the twist-2. At the moment there is no any
 669 experimental data on the gluon transversity in the deuteron. The gluon-induced (NLO) Drell-Yan process
 670 $qg \rightarrow q\gamma^* \rightarrow q\mu^+\mu^-$ was proposed in Ref. [151] as a way to access it in the polarized p - d collisions at
 671 the SpinQuest experiment at Fermilab. A measurement of the double transverse spin asymmetries A_{TT}
 672 in the gluon-induced processes at polarized d - d collisions at NICA SPD could be an alternative way to
 673 access the $\Delta_T g(x)$.



(a)

Figure 2.14: (a) A_{TT}^{γ} asymmetry for the prompt-photon production at 200 and 500 GeV coming from the $q\bar{q}$ annihilation process calculated in LO [152] and NLO [153].

674 1.10 Deuteron tensor polarization and shear forces

675 The availability of tensor polarized deuteron beam opens a possibility to study shear forces generated
 676 by quarks and gluons [155]. The natural way to get the traceless part of the energy-momentum tensor
 677 related to shear is provided just by tensor polarization, as the relevant tensor $S^{\mu\nu}$ is a traceless one by
 678 construction. The contribution of the "tensor polarized" parton distribution C^T [156, 157] (introduced as
 679 an "aligned" one [158]) is constrained by the zero sum rule [158] for its second moment (complementing
 680 the Close-Kumano sum rule [157]) which may be decomposed into quark and gluon components [159]:

$$\sum_{i=q,\bar{q}} \int_0^1 C_i^T(x) x dx = \delta_T(Q^2), \quad (2.10)$$

$$\int_0^1 C_G^T(x) x dx = -\delta_T(Q^2). \quad (2.11)$$

681 As a result, the matrix elements of energy momentum tensors of quarks and gluons look like

$$\sum_i \langle P, S | T_i^{\mu\nu} | P, S \rangle_{Q^2} = 2P^\mu P^\nu (1 - \delta(Q^2)) + 2M^2 S^{\mu\nu} \delta_T(Q^2) \quad (2.12)$$

$$\langle P, S | T_g^{\mu\nu} | P, S \rangle_{\mu^2} = 2P^\mu P^\nu \delta(Q^2) - 2M^2 S^{\mu\nu} \delta_T(Q^2), \quad (2.13)$$

682 where the second terms describe the average (integrated over transverse distance) shear force. Here M is
 683 the nucleon mass.

684 The zero sum rules (2.10) were later interpreted [160] as yet another manifestation of Equivalence Prin-
 685 ciple (EP), as it was done earlier [161] for Ji sum rules. In turn, the smallness of δ_T , compatible with
 686 the existing HERMES data, was suggested [160] to be the new manifestation of Extended Equivalence
 687 Principle (ExEP) [162–164] valid separately for quarks and gluons in non-perturbative QCD due to the
 688 confinement and chiral symmetry violation. It was originally suggested for anomalous gravitomagnetic
 689 moments [162, 164]. In particular, it provides the rotation of spin in the terrestrial experiment with the
 690 angular velocity of Earth rotation. Let us stress, that it may seem trivial if spin is considered just as a
 691 vector. However, it became highly non-trivial if the measurement of spin by the device rotating together
 692 with Earth is taken into account. This is a particular example of the practical importance of the quantum

693 theory of measurement. Another example may be represented by the Unruh radiation in heavy-ion colli-
 694 sions [165], which implies that the particles production may be also considered as a quantum-mechanical
 695 measurement in the non-inertial hadronic medium.

696 Recently, ExEP was also discovered for the pressure [166].

697 To check ExEP for shear force one may use future studies of DIS at JLab and of Drell-Yan process with
 698 tensor polarized deuterons [167]⁵.

699 Note that tensor polarized parton distribution may be also measured in *any* hard process with the relevant
 700 combination of deuteron polarizations, in particular, for large p_T pions production, providing much better
 701 statistics. The correspondent quantity can be the P-even Single Spin asymmetry

$$A_T = \frac{d\sigma(+)+d\sigma(-)-2d\sigma(0)}{d\sigma(+)+d\sigma(-)+d\sigma(0)} \sim \frac{\sum_{i=q,\bar{q},g} \int d\hat{\sigma}_i C_i^T(x)}{\sum_{i=q,\bar{q},g} \int d\hat{\sigma}_i q_i(x)}, \quad (2.14)$$

702 where the differential cross section with definite polarization of deuteron appear.

703 Note that due to the tensor polarization tensor being traceless the sum rule for the three mutually orthog-
 704 onal orientations of coordinate frame is valid [158]:

$$\sum_i S_{zz}^i = 0. \quad (2.15)$$

705 As a result, the leading twist kinematically dominant "longitudinal" tensor polarization can be obtained
 706 by accelerating *transverse* polarized deuterons which will be accessible at NICA.

⁵Complementary probes are provided by vector mesons [163].

2 Quarks in proton and deuteron

2.1 Single-transverse spin asymmetries in the light mesons production

The single-transverse spin asymmetries (STSA) in the inclusive production of light mesons are the simplest spin observables in hadronic scattering and also related with the Sivers, Collins, and Boer-Mulders transverse momentum dependent functions discussed in the previous section. But unlike the case of charmonia, open charm and prompt photon production, quarks are the main contributors to the corresponding asymmetries. The first result for A_N was reported by the E704 collaboration for the production of the charged and neutral pions in $p \uparrow - p$ and $\bar{p} \uparrow - p$ collisions at $\sqrt{s} \sim 20$ GeV, which is up to 30% in the forward direction [168–171]. Similar values were reported by the RHIC experiments for higher energies [172–176].

Understanding of STSAs in the light mesons production is possible basing on the QCD factorization approach that separates the cross-sections into perturbatively calculable partonic-level cross-section and non-perturbative physics encoded in parton distribution functions (PDFs) and fragmentation functions (FFs). Being included into the global analysis together with other available data they are the important source of information about quark TMD functions. The JAM20 [177] is a recent example of such global QCD analysis where the available data for $p-p$ collisions have been combined with SSA data in SIDIS, Drell-Yan pair production, and e^+e^- annihilation.

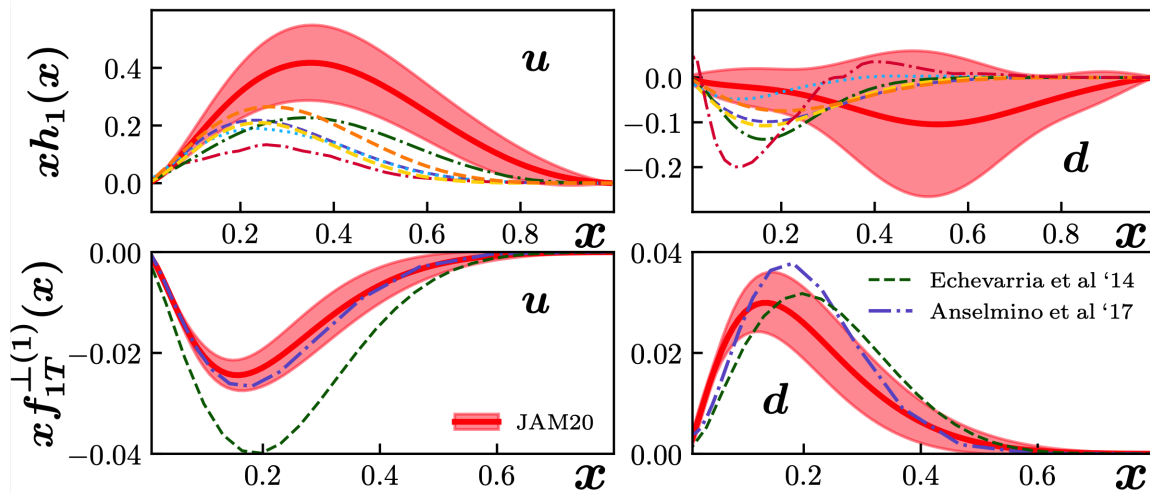


Figure 2.15: The extracted from the global analysis JAM20 (JAM collaboration) [177] functions $h_1(x)$ and $f_{1T}^{\perp(1)}(x)$ at $Q^2 = 4$ GeV² together with the corresponding results of other groups.

The first momenta $h_1(x)$ and $f_{1T}^{\perp(1)}(x)$ of the TMD pretzelosity $h_1(x, k_T)$ and Sivers $f_{1T}^{\perp(1)}(x, k_T)$ functions obtained from the global analysis JAM20 together with 1σ uncertainties at $Q^2 = 4$ GeV² are presented in Fig. 2.15. The so-called tensor charges

$$\delta q = \int_0^1 (h_1^q(x) - h_1^{\bar{q}}(x)) dx \quad (2.16)$$

for u and d quarks and $g_T = \delta u - \delta d$ are shown in Fig. 2.16. New data on the STSA in the light mesons production in the SPD energy range (and especially high- p_T data) are very much in demand for such kind of global analyses [178].

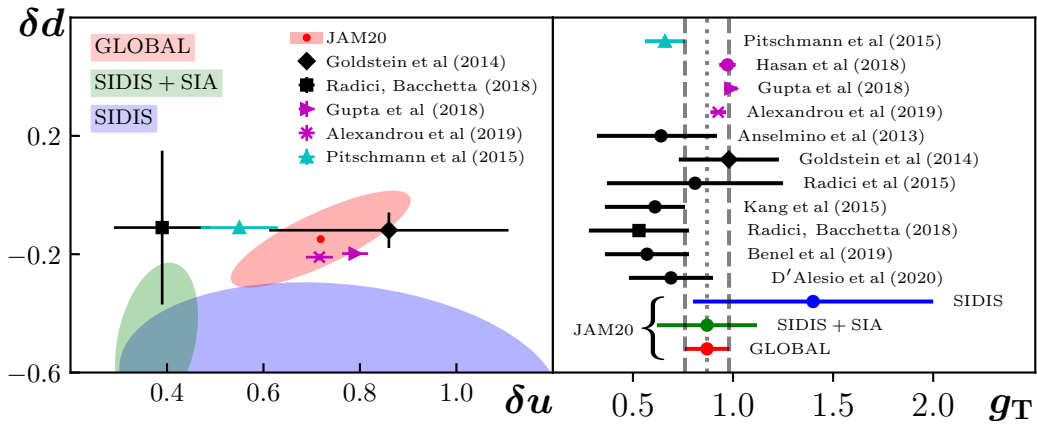


Figure 2.16: The results of the global analysis JAM20 (JAM collaboration) [177] along with others from phenomenology (black), lattice QCD (purple), and Dyson-Schwinger (cyan) for the tensor charges δu , δd and $g_T = \delta u - \delta d$ at $Q^2 = 4 \text{ GeV}^2$.

730 2.2 Drell-Yan pair production

731 Production of Drell-Yan (DY) pairs in polarized hadronic collisions $pp \rightarrow \gamma^* \rightarrow \mu^+ \mu^-$ is a promising
 732 way to touch the TMP PDFs of valence quarks and sea antiquarks by measuring the azimuthal asymme-
 733 tries. A tiny DY cross section and a huge combinatorial background coming from decays of secondary
 734 pions and kaons into muons make this task rather difficult. A typical detector configuration for such
 735 kind of studies at $\sqrt{s} \sim 20 \text{ GeV}$ is a fixed-target beam-dump setup where due to the Lorentz boost most
 736 of secondary pions and kaons are stopped in a thick absorber before decaying. At the moment only the
 737 COMPASS experiment at CERN has presented the results for the three azimuthal asymmetries measured
 738 in pion-induced polarized DY [179, 180]. The observed glimpse of the sign change in the Siv-
 739 ers asymmetries is found to be consistent with the fundamental prediction of QCD that the Siv-
 740 ers functions of \bar{u} and \bar{d} are expected from the SpinQuest experiment at Fermilab [181, 182].

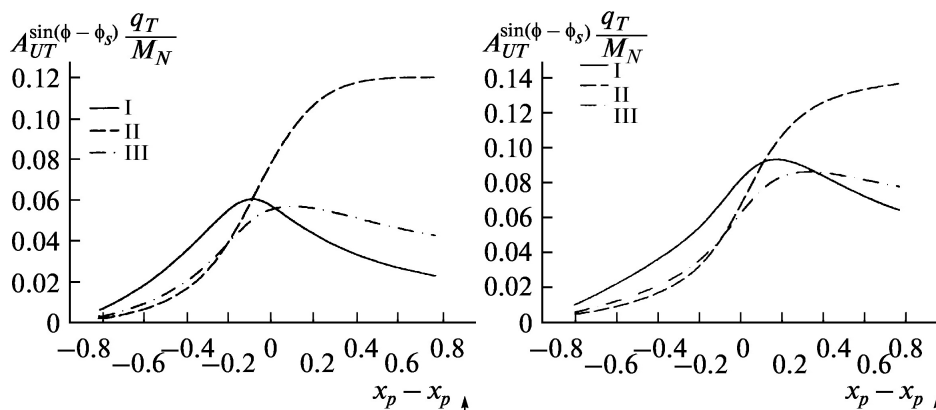


Figure 2.17: Estimated Siv-ers asymmetries for the NICA conditions $s = 20 \text{ GeV}$, $Q^2 = 4 \text{ GeV}^2$ (left) and $s = 20 \text{ GeV}$, $Q^2 = 15 \text{ GeV}^2$ (right). Fits for the Siv-ers functions are taken from [183].

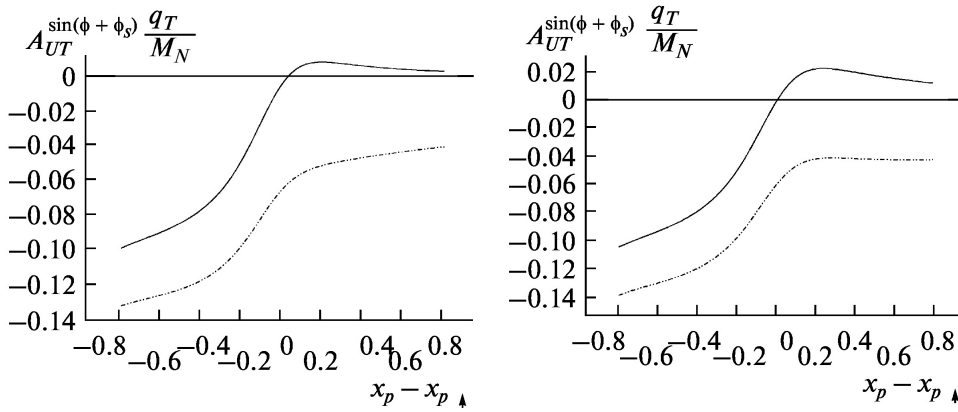


Figure 2.18: Estimated Boer-Mulders asymmetries for the NICA conditions.

742 Unfortunately, the Spin Physics Detector cannot use the advantage of fixed-target beam-dump setups
 743 and the expected background conditions for the Drell-Yan measurements are rather untoward. However,
 744 further improvement of the experimental techniques and analysis procedures could give a chance to
 745 access polarized DY at SPD. The estimated Sivvers and Boer-Mulders asymmetries for the SPD conditions
 746 are presented in Fig. 2.17 and 2.18, respectively.

747 2.3 Generalized parton distributions

748 The concept of Generalized Parton Distributions (GPDs) is a complementary to the TMD PDFs approach
 749 to describe the three-dimensional structure of hadrons. Study of the deeply virtual meson production
 750 (DVMP) is one of the proven ways to access GPDs. This process has been investigated in [] ... using
 751 lepton and photon beams. An exclusive electromagnetic process $pp \rightarrow ppM$ shown in Fig. 2.19(a), where
 752 the first proton radiates a photon with low virtuality that interacts with the other proton and produces a
 753 meson, could be used to access the Generalized Parton Distributions at SPD. At the SPD energies, the
 754 meson photoproduction amplitude can be presented in a factorized form as a convolution of the hard
 755 scattering part which can be calculated perturbatively and the GPDs [184, 185]. In the case of vector
 756 mesons production, the odderon exchange (that could be described as an exchange by at least 3 gluons)
 757 is also possible and the interference of these two channels is a matter of special interest. Ultrapерipheral
 758 p - A collisions at SPD, which enhance the photoproduction contribution by several orders of magnitude
 759 could also be considered. In addition, ultraperipheral processes could be used to test the most general
 760 non-perturbative concept of the Generalized Transverse Momentum dependent Distributions (GTMD).
 761 This possibility was explored for high energies in Ref. [186] but the approach could be extended down
 762 to the SPD energies.

763 The exclusive production of the J/ψ meson can be studied at SPD at energies $W = \sqrt{(q+p)^2} \sim 5 -$
 764 15 GeV. Here q and p are the 4-momenta of a virtual photon (odderon) and a proton, respectively. The
 765 large meson mass makes it possible to perform perturbative calculations at sufficiently low Q^2 , where
 766 the photon exchange should dominate. The corresponding cross section is estimated to be of about
 767 $\sigma_{J/\psi} \sim 10$ nb. The main contribution to the cross section is coming from the gluon GPDs.

768 The exclusive Drell-Yan (exDY) process was proposed for the study of GPDs in p - p collisions in Ref.
 769 [187]. The kinematics of this process is defined by convolution of two GPDs. Both quark and gluon
 770 GPDs contribute to the exDY cross section via the diagrams shown schematically in Fig. 2.19(b, c).

771 Investigation of the cross section determined by two-GPDs effects is in progress now [188]. It is shown

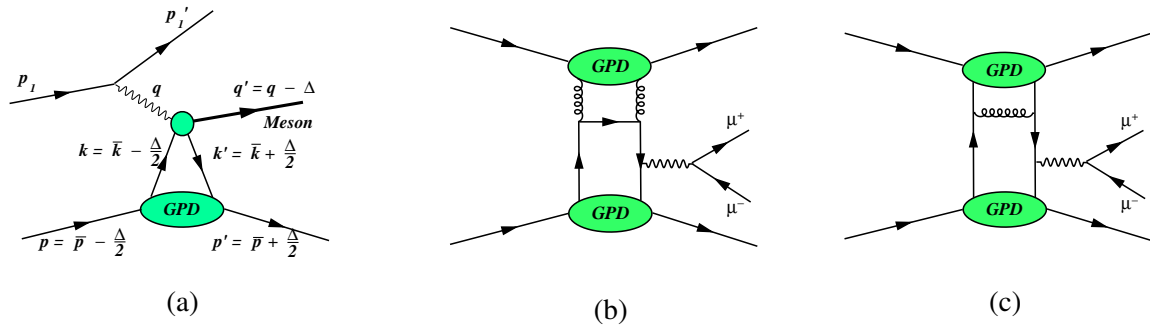


Figure 2.19: (a) Vector meson production at NICA via photoproduction mechanism or odderon exchange. (b, c) Drell-Yan process with gluon and quark GPDs.

772 that the gluon and sea quark GPDs lead to the cross section which does not decrease with the growth of
 773 energy. The exDY cross section $d\sigma/dQ^2$ at the NICA kinematics $\sqrt{s} = 24$ GeV and $Q^2 = 5$ (GeV/c) 2
 774 is estimated as 5 pb/(GeV/c) 2 which is much smaller with respect to the inclusive Drell-Yan cross sec-
 775 tion. Nevertheless, the exclusivity requirement applied in the analysis of the future SPD dimuon data
 776 could increase the signal-to-background ratio. It should be mentioned that J/ψ could also be produced
 777 exclusively in a similar way.

778 2.4 Polarized fragmentation functions

779 3 Tests of QCD basics at low energies [U. Uzikov, A. Guskov]

780 QCD has a remarkable success in describing the high energy and large momentum transfer processes,
 781 where the quarks in the hadrons behave, to some extent, as free particles and a perturbative approach can
 782 therefore be used. The QCD factorization theorem separates the cross-section into two parts: the pro-
 783 cess dependent perturbatively-calculable short-distance partonic cross-section, and the universal long-
 784 distance functions (PDFs and FFs). Nevertheless, the largest fraction of hadronic interactions involve
 785 low momentum transfer processes in which the effective strong coupling constant is large and a descrip-
 786 tion with a perturbative approach is not adequate. A number of (semi-)phenomenological approaches
 787 have been developed through the years to describe low-energy hadronic interactions starting from very
 788 basic principles. They describe such crucial phenomena as nuclear properties, hadronic spectra, decon-
 789 finement, various polarized and unpolarized effects in elastic and inelastic scattering of hadrons etc. In
 790 spite of a large set of experimental data and huge experience at the few-GeV region with fixed-target
 791 experiments worldwide, this energy range still attracts both experimentalists and theoreticians. Low-
 792 energy physics at SPD is a some kind of bridge to the physics program of the MPD, another experiment
 793 at NICA [189–191].

794 3.1 Polarized pd elastic scattering within the Glauber model and pN spin amplitudes [Yu. Uzikov]

795 Nucleon-nucleon elastic scattering contains fundamental information on the dynamics of the NN inter-
 796 action and constitutes a basic process in physics of atomic nuclei and hadrons. Full information about
 797 spin amplitudes of pp and pn elastic scattering can be obtained, in principle, from complete polarization
 798 experiment, which, however, requires to measure dozen independent observables at given collision en-
 799 ergy that constitutes too complicated experimental task. A systematic reconstruction of these amplitudes
 800 from scattering data is provided by the SAID data base [192] and covers laboratory energies up to 3 GeV
 801 ($p_{lab} \approx 3.8$ GeV/c) for pp and 1.2 GeV ($p_{lab} \approx 1.9$ GeV/c) for pn scattering. At higher energies there
 802 are only non-complete data on pp scattering, whereas information about the pn system is very scarce. In
 803 the literature there are several models and corresponding parametrizations for pN amplitudes. Some of
 804 them are obtained in the eikonal approach for the lab momentum 6 GeV/c [193] and for LHC energies
 805 [194]. Within the Regge phenomenology parametrization is obtained for 3-50 GeV/c (corresponding to
 806 $2.77 < \sqrt{s} < 10$ GeV)[195] and for values of s above 6 GeV² ($p_{lab} \geq 2.2$ GeV/c) in Ref. [196]. A possible
 807 way to check existing parametrizations is to study spin effects in proton-deuteron ($p-d$) and deuteron-
 808 deuteron (dd) elastic and quasi-elastic scattering. At high energies and small four-momentum transfer t ,
 809 $p-d$ scattering can be described by the Glauber diffraction theory of multistep scattering, which involves
 810 as input on-shell $p-N$ elastic scattering amplitudes. Applications of this theory with spin-dependent ef-
 811 fects included [197] indicate a good agreement with the pd scattering data at energies about 1 GeV if the
 812 SAID data on $p-N$ scattering amplitudes are used as input of the calculations [198–200].

813 The spin-dependent Glauber theory [197, 198] is applied recently [201, 202] to calculate spin observ-
 814 ables of $p-d$ elastic scattering at 3-50 GeV/c utilizing the pp elastic scattering amplitudes f_{pp} established
 815 and parametrized in Ref. [195] within the Regge formalism. The Regge approach allows one to con-
 816 struct $p-n$ (and $\bar{p}N$) amplitudes together with the pp amplitudes. This feature allows one to perform a
 817 test of broad set of $p-N$ amplitudes and applicability of the Regge model itself to $p-N$ elastic scattering.
 818 However, in view of the scarce experimental information about the spin-dependent $p-n$ amplitudes and
 819 taking into account that the spin-independent parts of the pp and pn amplitudes at high energies are ap-
 820 proximately the same, it was assumed in [201] as a first approximation, that $f_{pn} = f_{pp}$. The unpolarized
 821 differential cross section, vector (A_y^p, A_y^d) and tensor (A_{xx}, A_{yy}) analyzing powers and some spin corre-
 822 lation parameters $(C_{x,x}, C_{y,y}, C_{xx,y}, C_{yy,y})$ ⁶ of pd elastic scattering were calculated at $p_l = 4.85$ GeV/c

⁶We use here notations of Ref. [203]

and 45 GeV/c at $0 < -t < 2 \text{ GeV}^2$ using pN amplitudes from [195]. As shown in Ref. [201] available data on pd -elastic differential cross section in forward hemisphere are well described by this model. Most sensitive to the spin-dependent pN amplitudes are vector analyzing powers A_y and spin correlation parameters $C_{x,x}$ and $C_{y,y}$. So, even measurement of the ratio A_y^d/A_y^p at low t gives valuable information on the transverse spin-spin term in NN-amplitudes [204]. In contrast, the tensor analysing powers A_{xx} and A_{yy} are very weakly sensitive to those amplitudes and weakly changed with increasing energy. The calculated in [201] polarization observables can be measured at SPD NICA that will provide a test of the used p - N amplitudes. The corresponding differential cross section is rather large in the considered region $p_{lab} = 3 - 50 \text{ GeV}/c$ and $|t| = 0 - 2 \text{ GeV}^2$ being $d\sigma/dt > 0.1 \text{ mb}/\text{GeV}^2$. Expected counting rate N at $p_{lab} = 50 \text{ GeV}/c$ ($q_{pp}^{cm} = 5 \text{ GeV}/c$) for the luminosity $L = 5 \times 10^{30} \text{ cm}^{-2} \text{ s}^{-1}$ and for the solid angle $\Delta\Omega = 0.03$ is $N \geq 10^2 \text{ s}^{-1}$.

The pN helicity amplitudes ϕ_5 and $\phi_1 + \phi_3$, which can be tested in the above described procedure are necessary in search of time-reversal invariance effects in double-polarized pd scattering [205, 206]. Data of the spin-correlation parameters of pp elastic scattering being analyzed in the framework of the eikonal model [194] will allow one to obtain space structure of the spin-dependent hadron forces [207].

3.1.1 Elastic small angle pp scattering and periphery of the nucleon.

First evidence of the pion cloud effect in the diffractive scattering $|t| \sim 0.1 \text{ GeV}^2 \approx 4m_\pi^2$, have been found in the ISR measurements [208]. Theoretical study of the effect was provided by Anselm and Gribov [209] and recently in Refs. [210] and [211]). The observed at ISR oscillation effect was studied later on in Protvino and one more oscillation in the differential cross section was found there at $|t| \sim 0.5 \text{ GeV}^2$. Being located at higher t , it might be related with somewhat heavier mesons around the proton. The oscillation effect of the pp scattering amplitude at small momentum transfer was found also in the analysis of the recent high precision experimental data of the TOTEM collaboration at $\sqrt{s} = 13 \text{ TeV}$ [212]. The effect is related with the behavior of the hadron potential at large distances [213]. The future SPD experiment [214] can provide new precise data on small-angle elastic pp -scattering for exploring this phenomenon. For this aim measurements will be performed in the kinematic region of $|t| \sim 0.1 - 0.8 \text{ GeV}^2$ detecting in coincidence elastically scattered protons at angles $\theta \sim 3 - 10^\circ$ with accuracy of determination t better than $\Delta t \sim 0.02 \text{ GeV}^2$.

3.2 Single-spin asymmetries at low energies [V. Abramov]

A systematic study of such single-spin phenomena as the transverse single-spin polarization of hadrons (A_N) and the polarization of hyperons (P_N) in $p+p$, $d+d$, $C+C$ and $Ca+Ca$ collisions is proposed. A systematic study means a detailed study of the dependence of the observed A_N and P_N for dozens of reactions on variables such as collision energy (\sqrt{s}), Feynman variable (x_F), transverse momentum (p_T), the atomic weights of the colliding particles (A_1 and A_2), the multiplicity of charged particles (N_{ch}) in the event, and the centrality of collisions. The study of a large number of reactions will reveal the dependence of A_N and P_N on the quantum numbers (spin, isospin, flavor, etc.) of the hadrons participating in the reaction. A systematic study also implies a global analysis of all available single-spin data within a certain model in order to identify general behavior and the mechanism of the origin of polarization phenomena.

One of such models is the chromomagnetic quark polarization (CPQ) model [215]. The CPQ model assumes the presence of an inhomogeneous circular transverse chromomagnetic field \mathbf{B}^a in the interaction region of colliding hadrons. The interaction of the chromomagnetic moments of test quarks, which later form the observed hadron, with the field \mathbf{B}^a leads, as a result of the Stern-Gerlach effect, to the appearance of spin effects (with nonzero A_N and P_N). The spin precession of test quarks leads to the phenomenon of oscillations $A_N(x_F)$ and $P_N(x_F)$ depending on the Feynman variable x_F , and the frequency

868 of these oscillations depends on the number of spectator quarks, color charges of quarks and antiquarks,
 869 and the direction of their motion in the c.m. of reactions. The frequency of these oscillations is a linear
 870 function of the number of quarks and antiquarks - spectators interacting in pairs with each of the test
 871 quarks, taking into account the color state of the pair. The highest oscillation frequencies are expected in
 872 the case of antibaryon production in baryon collisions and in ion collisions.

873 The CPQ model also predicts for a number of reactions such a phenomenon as the resonance dependence
 874 of A_N and P_N on energy (\sqrt{s}), which occurs if the sign of the color charge of the test quark and spectators
 875 is opposite. The most interesting reaction in this respect is the production of anti-lambda in various initial
 876 states of the beams of the NICA collider, for which the resonance energy is close to 7 GeV in the c.m.s.

877 The threshold dependence of A_N on the hadron production angle in the c.m. is also predicted. An
 878 example of the manifestation of the threshold dependence A_N is the reaction $p^\uparrow p(A) \rightarrow \pi^- X$, for which
 879 the threshold angle is 74° , since the test quark is the d -quark, which is heavier than the u -quark.

880 An important advantage of hyperons is the ability to measure A_N and P_N for them, that makes it possible
 881 to compare them with each other and with model predictions.

882 The rate of pion production in pp collisions varies from $3 \cdot 10^7/s$ at 23 GeV to $2 \cdot 10^5/s$ at 7 GeV. In
 883 C + C and Ca + Ca collisions, it will be three orders of magnitude lower. The rate of production of
 884 hyperons is two orders of magnitude lower than that of pions. Antihyperones are produced 5 to 10 times
 885 less frequently than hyperons.

886 **3.3 Exclusive hard processes with deuteron [M. Strikman]**

887 Questions involved in studies of the short-range / high momentum nuclear structure and understanding
 888 microscopic nucleon structure and dynamics of large momentum transfer processes are delicately inter-
 889 twined: understanding of hard dynamics of two body processes is also necessary for precision studies of
 890 the short range nuclear structure. Exclusive large t reactions like $p^2H \rightarrow ppn$ process can address many
 891 of these questions. Advantages of such reaction is a good knowledge of the nonrelativistic deuteron
 892 wave function and ability to choose both kinematics sensitive to dynamics of elastic NN scattering and
 893 the kinematics sensitive to short range deuteron structure. The collider kinematics presents a number
 894 of advantages as all particles in the reactions in question have large momenta and hence can be easily
 895 detected.

896 **3.3.1 Probing dynamics of NN interaction**

897 The simplest kinematics is production of two nucleons approximately back to back large transverse
 898 momenta and spectator nucleon with longitudinal momentum $p \sim p_{2H}/2$ and transverse momentum \geq
 899 200 MeV/c [216, 217].

900 In the impulse approximation this process corresponds to elastic scattering of the projectile proton off
 901 a quasifree nucleon of the target. In this kinematics soft rescatterings of the initial and final nucleons,
 902 which accompany the hard $pp(pn)$ reaction are large. The eikonal approximation, which accounts for
 903 relativistic kinematics as dictated by the Feynman diagrams, reveals the important role played by the ini-
 904 tial and final state interactions in the angular and momentum dependences of the differential cross section
 905 in well defined kinematics. The condition for the applicability of the generalized eikonal approximation
 906 [218] is that the c.m. scattering angle and invariant mass of the two nucleon system are large enough so
 907 that $-t, -u \geq 2 \text{ GeV}^2$.

908 It was suggested in [219], [220] that nucleons in the elementary reaction interact in small size configura-
 909 tions with a small cross section - so called color transparency phenomenon. This effect is suppressed by
 910 the space - time evolution of nucleon wave packets [221, 222]. However effect of evolution is very small

911 for the deuteron where typical distances between nucleons in the rescattering amplitude are is ≤ 1.5 fm.
 912 Hence the discussed process allows to measure the wave packet size of a nucleon practically right in the
 913 interaction point.

914 It was pointed out that the hard dynamics in pp and pn elastic scattering may be rather different [223].
 915 Hence it would be instructive to compare the channels where pp and pn are produced with large p_t .

916 Experiments with polarized beams would greatly add to this program: due to a better separation of kine-
 917 matic domains where impulse approximation, double and triple scattering dominate, while the studies
 918 $\vec{p}\vec{d} \rightarrow pNN$ processes will allow both to study spin structure of pp and pn elastic scattering at large t (the
 919 later is practically not known). Also, it would be possible to find out whether the a strong difference be-
 920 tween the cross sections of elastic scattering of protons with parallel and antiparallel spins[224] involves
 921 collisions of protons in configurations with sizes depending on the spin orientation.

922 It would be possible also to study effects of coherence in the channels where exchange by gluons in
 923 t-channel is not possible, for example $pd \rightarrow \Delta NN$. In particular, it would be possible to test the effect of
 924 chiral transparency suggested in [225] - suppression of the pion field in the nucleons experiencing large
 925 $-t$ scattering.

926 3.3.2 Probing microscopic deuteron structure

927 It is established now that the dominant source of the short range/ high momentum correlations (SRC)
 928 in nuclei are proton - neutron correlations with the same quantum numbers as the deuteron and with
 929 high momentum tail similar to that in the deuteron, see review in [226, 227]. Hence the deuteron serves
 930 as a kind of the hydrogen atom of the SRC physics. Only after it would be tested experimentally that
 931 approximations currently used for the description of the p^2H reaction work well, it would be possible to
 932 perform high precision studies of SRC in heavier nuclei.

933 It was demonstrated in Ref.[216, 217] that under specific kinematical conditions (in particular low trans-
 934 verse momenta of a slow nucleons in the deuteron rest frame)) the effect of initial and final state inter-
 935 actions can be accounted for by rescaling the cross section calculated within the plane wave impulse
 936 approximation. In this kinematics it would be possible to check universality of the wave function - in
 937 particular its independence on the momentum transfer in the elementary reaction. Such factorization is
 938 expected to break down at sufficiently large $-t$ and $-u$ where scattering involves interaction of nucleons
 939 in the small size configurations (the color transparency regime) since the small size configurations are
 940 suppressed in bound nucleons with suppression growing with the nucleon off shellness [222].

941 Studies of the nonnucleonic configurations in the deuteron as well as relativistic effects. in the scattering
 942 off a polarized deuteron are of separate interest. In particular, it would be possible to a search for non-
 943 nucleonic degrees of freedom like 6 quark, two Δ isobars via production reaction $p^2H \rightarrow \Delta^{++} + p + \Delta^-$
 944 with Δ^{++} and proton back to back and Δ^- being slow in the deuteron rest frame.

945 3.4 Scaling behaviour of exclusive reactions with lightest nuclei and spin observables [Yu. Uzikov, 946 V. Ladygin]

947 The structure of the lightest nuclei at short distances $r_{NN} < 0.5$ fm or high relative momenta ($q > \hbar/r_{NN} \sim$
 948 0.4 GeV/c constitutes a fundamental problem in nuclear physics. One of the most important questions
 949 is related to search for onset of transition region from meson-baryon to quark-gluon picture on nuclei.
 950 A definite signature for transition to the valence quark region is given the constituent counting rules
 951 (CCR) [228, 229]. According the dimensional scaling the differential cross section of a binary reaction
 952 at enough high incident energy can be parametrized as $d\sigma/dt \sim s^{-(n-2)} f(t/s)$, where n is the sum of
 953 constituent quarks in all participants, s and t are Mandelstam variables. Many hard processes with free
 954 hadrons are consistent with CCR at energies of several GeV. The CCR properties of the reactions with

955 the lightest nuclei were observed in photodisintegration of the deuteron $\gamma d \rightarrow pn$ at $E_\gamma = 1 - 4$ GeV
 956 and ${}^3\text{He}$ nucleus ${}^3\text{He}(\gamma, pp)n$, $\gamma{}^3\text{He} \rightarrow dp$. More earlier data on the reaction $dd \rightarrow {}^3\text{He}p, dd \rightarrow {}^3\text{He}n$
 957 [230] and $pd \rightarrow pd$, as was show in Ref.[231] also follow CCR behavior s^{-22} and s^{-16} , respectively, at
 958 surprising low energies, 0.5 GeV. Recently the CCR behaviour of the reaction $pd \rightarrow pd$ was observed in
 959 [232, 233] at higher energies. On the other hand, the reaction with pion production $pp \rightarrow d\pi^+$ does not
 960 follow CCR rule demonstrating the differential cross section $\sim s^{-9}$ instead of s^{-12} . One possible way to
 961 explain this is a partial restoraion of chiral symmetry at enough high excitaion energy [234]. However,
 962 systematic study of these properties of the reactions with lightest nuclei are absent. So, important to
 963 know whether reaction $pn \rightarrow dp^0$ follows the CCR behavior and at what minimal energy there is the
 964 CCR onset. Assuming the model of the vector meson dominance and taking into account the observed
 965 CCR behavior of the $\gamma d \rightarrow pn$ reaction, one may expect the $\sim s^{-12}$ dependence of the cross section of
 966 the reaction $pn \rightarrow dp^0$. Furthermore, possible relation between CCR behavior of the upolarized cross
 967 section and spin observables of the same reaction are practically not known. The SPD NICA facility
 968 provides a good opportunity for this study using polarized beams in pp, dd and pd collisions.

969 The tensor A_{yy} and vector A_y analyzing power in dp - elastic scattering obtained at $60^\circ, 70^\circ, 80^\circ$ and 90°
 970 in cms versus transverse momentum p_T [235, 236] demonstrates the negative and positive asymptotics,
 971 respectively. Note, that negative sign of A_{yy} is observed also in deuteron inclusive breakup at large p_T
 972 [237],[238]. It would be interesting to extend the range of the measurements to larger p_T , where the
 973 manifestation of non-nucleonic degrees of freedom is expected. New precise measurements with small
 974 statistical and systematic uncertainties at the energies higher than $\sqrt{s} \geq 3.3$ GeV and at different scattering
 975 angles are required to make a conclusion about the validity of CCR [228, 229] in dp - elastic scattering.
 976 We propose to measure also different vector and tensor analyzing powers in dp - elastic scattering at SPD
 977 energies.

978 The measurements of dp - elastic scattering can be performed either with polarized deuterons and un-
 979 polarized protons, or with unpolarized deuterons and polarized deuterons. The dp - elastic scattering
 980 events can be selected using cuts on the azimuthal and polar scattering angles correlations. The vector
 981 A_y and tensor A_{yy} and A_{xx} analyzing powers will be measured simultaneously in the case of the ver-
 982 tically polarized deuteron beam. The precision on the tensor $\Delta A_{yy} \sim 0.09$ and $\Delta A_{xx} \sim 0.09$ and on the
 983 vector $\Delta A_y \sim 0.03$ analyzing powers can be achieved for the scattering angle $\sim 90^\circ \pm 5^\circ$ at $\sqrt{s} \sim 4.5$ GeV
 984 ($p_T \sim 1.7$ GeV/c) for 30 days of the beam time at the luminosity $\mathcal{L} \approx 10^{29} \text{ cm}^{-2} \cdot \text{s}^{-1}$. We assume $\sim 75\%$
 985 of the beam polarization from the ideal values of polarization for different spin modes. The counting rate
 986 has been estimated using dp - elastic scattering cross section parameterization from Ref.[233]. The spin
 987 correlations can be obtained in quasi-free dp - elastic scattering using dd - collisions.

988 3.5 Vector mesons and open charm near threshold [E. Tomasi]

989 The study of charm production (hidden and open) and backward vector meson production at SPD will
 990 take full advantage of the possibility to use polarized p, d beams (as well as heavier ions) in a kinematical
 991 region where data are scarce on cross sections and polarization effects are mostly unmeasured. In general,
 992 threshold meson production in NN -collisions gives deeper insight in the reaction mechanisms as it is
 993 shown by the experimental programs at different proton accelerators as SATURNE and COSY.

994 3.5.1 Charm production

995 The production mechanisms for charmonium and $D (D^*)$ mesons in nucleon-nucleon collision is poorly
 996 understood. Charm quarks are not preexisting in the nucleon as valence quarks: how they are formed
 997 and how they hadronize is an open question. To interpret the production and the propagation of charm
 998 in heavy ion collision as a probe of quark-gluon plasma (QGP), it is necessary to have a solid theoretical
 999 background based on the understanding of elementary processes.

1000 Experimental data and theoretical studies of J/ψ production in different processes and of its decays
 1001 exist: for a review, see [239] and for a most recent data collection [240]. In the threshold region, the
 1002 final particles are produced in S -state and the spin structure of the matrix element is largely simplified.
 1003 The effective proton size, which is responsible for charm creation, has to be small, $r_c \simeq 1/m_c \simeq 0.13$
 1004 fm, where m_c is the c -quark mass, selecting small impact parameters [241]. The S -wave picture can
 1005 therefore be applied for $q \leq m_c$, where q is the norm of the J/ψ - three-momentum in the reaction center
 1006 of mass (CMS). The momenta of the produced particles are small, but the mechanisms for the production
 1007 of charmed quarks must involve large scales. In Ref. [242], the near-threshold J/ψ - production in
 1008 nucleon-nucleon collisions was analyzed in the framework of a general model independent formalism,
 1009 which can be applied to any reaction $N + N \rightarrow N + N + V^0$, where $V^0 = \omega, \phi$, or J/ψ . Such reactions
 1010 show large isotopic effects: a large difference for pp - and pn -collisions, which is due to the different spin
 1011 structure of the corresponding matrix elements at threshold: $\sigma(np \rightarrow npJ/\psi)/\sigma(pp \rightarrow ppJ/\psi) = 5$.

1012 In Ref. [242] an estimation for the J/ψ production was suggested from the comparison of the cross
 1013 sections for the ϕ and J/ψ production in pp collisions. For the same value of the energy excess, $Q =$
 1014 $\sqrt{s} - 2m - m_V$, taking into account the different phase space volumes, coupling constants for the decay
 1015 $V \rightarrow \pi\rho$, monopole-like phenomenological form factor for the vertex $\pi^*\rho^*V$, with virtual π and ρ , one
 1016 finds the following simple parameterization for the cross section, holding in the near threshold region
 1017 only:

$$\sigma[nb] = 0.097(Q[\text{GeV}])^2. \quad (2.17)$$

1018 In Ref. [243] a parameterization of exponential form

$$\sigma[nb] = ae^{-bM_{J/\psi}/\sqrt{s}}; \quad (2.18)$$

1019 was suggested. The values $a = 1000$ [nb], and $b = 16.7$ GeV reproduce well the experimental data above
 1020 threshold.

1021 In Fig. 2.20(a) the data for $p + p \rightarrow J/\psi + p + p$ (red circles) and $p + A \rightarrow J/\psi + X$ (blue squares)
 1022 are plotted from the recollections in Refs. [239] (filled symbols) and [240] (open symbols). Different
 1023 symbols differentiate J/ψ production in pp or (extrapolated from) pA collisions. The data, mostly
 1024 collected at CERN, are reconstructed from the measurement using models and/or assumptions, and the
 1025 compiled total cross section for J/ψ production may differ up to a factor of two. For example, the
 1026 original reference for the measurement from Protvino at $\sqrt{s} = 11.5 \text{ GeV}$ [244] gives $\sigma(pp \rightarrow (J/\psi \rightarrow$
 1027 $\mu + \mu^-) + X) = 9.5 \pm 2.5$ nb, whereas the same experimental point is referenced as $\sigma = 11 \pm 3$ nb, in
 1028 Ref. [239] and $\sigma = 20 \pm 5.2$ nb, in Ref. [240]. The cross section from Ref. [242] is also plotted in Fig.
 1029 2.20(a) (solid line).

1030 Taking the value of luminosity $\mathcal{L} = 10^{30} \text{ cm}^{-2} \text{ s}^{-1}$, one expects 3 counts/hour for such a process with a
 1031 cross section of the order of 1 nb. This number is not corrected for the detector efficiency and reconstruc-
 1032 tion with identification, for example, in a missing mass. The reconstruction of J/ψ through its decay into
 1033 a lepton pair, that is the preferred mode, requires two additional orders of magnitude as the branching
 1034 ratio is $(\simeq 5.9 \pm 0.5)10^{-2}$.

1035 In Ref. [242] it was shown that only one polarization observable, the J/ψ -polarization, is identical for pp
 1036 and pn collisions: the J/ψ meson is transversely polarized, even in collisions of unpolarized nucleons.

1037 Open charm production, $N + N \rightarrow N + \bar{D} + \Lambda_C(\Sigma_C)$ gives information on scattering lengths, effective
 1038 radius, hadronic form factors, and coupling constants and is also related to the dynamics of charm crea-
 1039 tion in NN, NA, AA^* collisions. The spin and isospin structure of the matrix element for the reactions
 1040 $N + N \rightarrow \Lambda_C(\Sigma_C) + \bar{D} + N$ was derived for open charm in Ref. [248]. Detailed estimation of cross sec-
 1041 tions and the expressions of the polarization observables can be found there. Existing information and

1042 estimations indicate that near threshold cross section can be of the order of microbarns. The thresh-
 1043 old cross section, normalized at the lowest existing value is plotted in Fig. 2.20(b), where the insert
 1044 highlights the threshold region.

1045 The charm production near threshold cross section follows the behaviour:

$$\sigma[\mu b] = 0.03(Q[\text{GeV}])^2. \quad (2.19)$$

1046 It is plotted in Fig. 2.20(b) over a collection of data from Ref. [245] reanalyzed from several experiments
 1047 on charm production in pp and pA collisions at different facilities. We stress that these are difficult
 1048 measurements, with low counting rates and huge backgrounds, but that even setting upper limits will be
 1049 important, as no data at all are present in the threshold region.

1050 The understanding of charm production (open or hidden) should unify the different steps: parton-level
 1051 hard process with production of $c\bar{c}$ pairs, after hadronization of $c\bar{c}$ into J/ψ or into charmed hadrons
 1052 (mesons and baryons) including the final state interaction of the produced charmed hadrons with other
 1053 particles. The relatively large transferred momenta involved in most processes of J/ψ production in
 1054 hadron-hadron collisions allow to treat the first step in framework of perturbative QCD. But the applica-
 1055 bility of QCD is not so straightforward for the description of the c -quark hadronization. In this respect,
 1056 precise data collected in the SPD energy range will bring important information, especially if covering a
 1057 wide range above threshold.

1058 3.5.2 Backward meson production

1059 Larger counting rates are expected for light meson productions, since cross sections are of the order of
 1060 mb. The ρ^0 meson production in elementary collisions and on nuclei has been discussed for example
 1061 in Ref. [249] and references therein. The ρ^0 inclusive cross section has been measured at different
 1062 accelerators since the 70s, mostly at CERN [250], and more recently by the HADES collaboration [246].

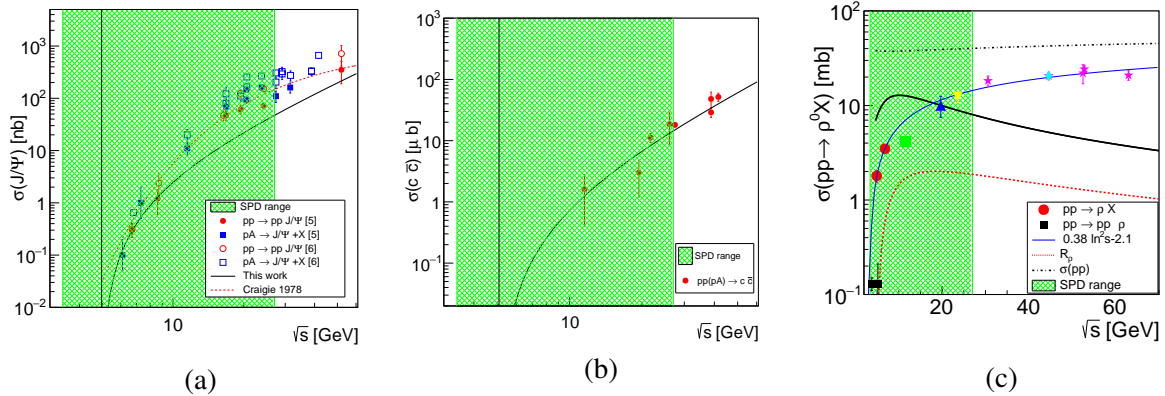


Figure 2.20: (a) Experimental data on $J\psi$ production in pp (red circles) and pA (blue squares) reactions, from the recollections in Refs. [239] (filled symbols) and [240] (open symbols). The solid line is the calculation from Ref. [242]. (b) Total charm production in pp and pA collisions. Data are from Ref. [245]. The line is a threshold parametrization (see text). (c) Cross section for ρ -meson production in pp collisions: inclusive (different symbols and colors from different experiments) and exclusive data from $pp \rightarrow pp\rho$ (black squares). The present calculation is shown as a black line. The red dashed line is the renormalization factor. The black dash-dotted line is the total pp cross section. The first red point is the inclusive measurement from Ref. [246]. The blue line is the parametrization from Ref. [247]. The green filled region represents the SPD range.

1063 In Ref. [247] the following parametrization was suggested

$$\sigma(pp \rightarrow \rho^0 X) = (0.38 \pm 0.02) \ln^2 s - (2.1 \pm 0.4). \quad (2.20)$$

1064 In Ref. [251] a specific kinematics, the backward light meson production in pp or pA collisions, was
 1065 discussed in similarity with the 'quasi real electron method', where a hard photon is produced on the
 1066 collision of electrons on any target [252]. Two important characteristics have been proved for the electron
 1067 case: (i) the collinear emission probability has a logarithmic enhancement; (ii) the cross section can be
 1068 factorized in a term related to the probability of the meson emission with a given energy at a given angle
 1069 from the beam particle, and a term related to the interaction of the beam remnant after emission on the
 1070 target.

1071 In hadron case the cross section can be written as:

$$\begin{aligned} d\sigma^{pT \rightarrow h_+ X}(s, x) &= \sigma^{nT \rightarrow X}(\bar{x}s) dW_{h_+}(x), \\ d\sigma^{pT \rightarrow h_0 X}(s, x) &= \sigma^{pT \rightarrow X}(\bar{x}s) dW_{h_0}(x), \end{aligned} \quad (2.21)$$

1072 where h is a hadron, x ($\bar{x} = 1 - x$) is the energy fraction carried by the meson (the beam remnant). $dW_\rho(x)$
 1073 can be inferred using the QED result, corrected by a renormalization factor in order to account for the
 1074 emission of n real soft neutral pions escaping the detection.

1075 The prediction of the model for backward ρ -meson production in pp collisions is shown in Fig. 2.20(c),
 1076 as a black solid thick line. The red dashed line is the renormalization factor, integrated over x . The total
 1077 pp cross section is the black dash-dotted line. The blue line is the parameterization of the inclusive ρ
 1078 cross section from Ref. [247]). The available data are also shown, as different symbols and colors for
 1079 inclusive measurements and as black squares for exclusive ρ production. Backward production can be
 1080 of the order of several mb, therefore accessible at SPD also with the initial lower luminosity. Collecting
 1081 precise, systematic data should help to refine the models and of great interest also for the collision on
 1082 heavy targets. Backward kinematics could constitute an original contribution to the field, offering an
 1083 alternative possibility to produce neutron beams.

1084 3.6 Central nucleon-nucleon collisions [Komarov]

1085 The main experimental basis for clarification of the non-perturbative QCD (NPQCD) baryon structure
 1086 is the baryon spectroscopy and the short-range nucleon-nucleon interaction. The more the nucleons
 1087 are overlapped during collision, the higher sensitivity of the latter to the NPQCD structure. Maximum
 1088 sensitivity can be reached in conditions of overlapping of the quark core of nucleons and sufficiently
 1089 long time of this overlapping. Unfortunately, these conditions practically are not met in the available
 1090 nucleon-nucleon experimental data: at relatively low energies the effective momentum transfers are not
 1091 sufficiently high, and at high energies the contents of colliding nucleons diverge too quickly. This cir-
 1092 cumstance explains why the region of the NN collisions at distances smaller than the radius of the nucleon
 1093 core still remains unexplored. Access to this area is possible through the central collisions (CC) of the
 1094 nucleons at adequate energies. The collisions are usually named central if the corresponding impact
 1095 parameter R is small, $R < r_{core} \approx 0.4 fm$.

1096 Overlapping of the nucleon cores can be achieved at the center-of-mass (CM) energies $\sqrt{s_{min}} = U_{rep}(0) +$
 1097 $2m_N$, where $U_{rep}(0)$ is the repulsive potential of the NN interaction at zero distance, $U_{rep}(0) \approx 1 GeV$.
 1098 Then the minimal energy of interest is $\sqrt{s_{min}} \approx 2.9 GeV$. At the energies less than 7.5 GeV (correspond-
 1099 ing the chiral symmetry breaking momentum $\Lambda_{\chi SB} \approx 1.2 GeV/c$ [253, 254]) the resulting intermediate
 1100 state is an excited (6q)* system of six chiral constituent quarks interacting via goldstone boson, gluon
 1101 exchange and confinement potential. This interaction is supposed to be much more intensive than in the
 1102 perturbative quark-gluon system, and provides therefore relatively long lifetime of the system, sufficient

1103 for manifestation of the NPQCD structure. In some conditions, it can even produce quasi-bound states,
 1104 resonance dibaryons. It should be stressed that the $(6q)^*$ system under consideration is characterized by
 1105 very high baryon and energy densities since two baryons and the whole CM energy is concentrated in a
 1106 small volume of about $4/3\pi(r_{core})^3$ size.

1107 Decay of the $(6q)^*$ system leads to reconstruction of hadronic states in the form

$$p + p \rightarrow (6q)^* \rightarrow N + N + Mesons, \quad (2.22)$$

1108 where *Mesons* denotes the system of light mesons, predominantly pions.

1109 Peripheral NN collisions proceed mainly via production of excited baryons N^* in the intermediate state

$$p + p \rightarrow \{(N + N^*) \text{ or } (N^* + N^*)\} \rightarrow N + N + Mesons \quad (2.23)$$

1110 and have, in general, the final states similar to that in the central collisions (2.22). Therefore, in order
 1111 to distinguish the central collision process (2.22) from the peripheral (2.23), one needs special centrality
 1112 criteria. According to [255, 256], there are two such criteria: A) using of the reaction

$$N + N \rightarrow d(90^\circ) + Mesons, \quad (2.24)$$

1113 where $d(90^\circ)$ is a deuteron emitted at the angle close to 90° ⁷; B) smallness of the interaction region size
 1114 $r_{int} < r_{core}$, where $r_{int} = 1/(-Q^2)^{1/2}$ with $Q = P_1 - D/2$. Here P_1 is the four-momentum of one of the
 1115 initial nucleons and D is the four-momentum of the final joined nucleon pair.

1116 Evaluation of feasibility of experiments with the above centrality criteria shows [256] that at the expected
 1117 luminosity [29] the event rate in SPD will be at the level of tens events per second. Hence, rather large
 1118 amount of information about the processes of interest can be obtained in a reasonable time.

1119 The following goals can be aimed, in particular, in experiments with central collisions:

- 1120 – study of known and search for new dibaryon resonances in the region of $\sqrt{s} \approx 2.5 - 7.5$ GeV;
- 1121 – search for the predicted dominance of the σ -meson production [257];
- 1122 – search for the expected effects caused by the chiral symmetry partial restoration (drop of mass and
 1123 width of mesons) [258, 259];
- 1124 – study of the energy dependence of the reaction (2.24) cross section, what is sensitive to the strength
 1125 of the confinement forces and the value of the chiral symmetry breaking momentum;
- 1126 – first measurement of the analyzing power of the reaction (2.24) for transverse and longitudinal
 1127 beam polarization.

1128 It is worth to mention that experiments of this kind have never been carried out systematically. There
 1129 exists a possibility to observe new unexpected effects that can induce new approaches in solving the
 1130 fundamental problems of the non-perturbative QCD.

1131 3.7 Onset of deconfinement in p - p and d - d central collisions [A. Korzeney]

1132 A study of the phase diagram of strongly interacting matter by varying interaction energy at central
 1133 collisions of heavy ions is a primary goal of the NICA MPD experiment [189]. A structures in the
 1134 energy dependence of several observables in the range of $\sqrt{s_{NN}} \approx 7$ -12 GeV had been predicted for the

⁷or reaction $N + N \rightarrow \{pp\}_{S_0}(90^\circ) + Mesons$, where $\{pp\}_{S_0}$ is a proton pair in the 1S_0 state

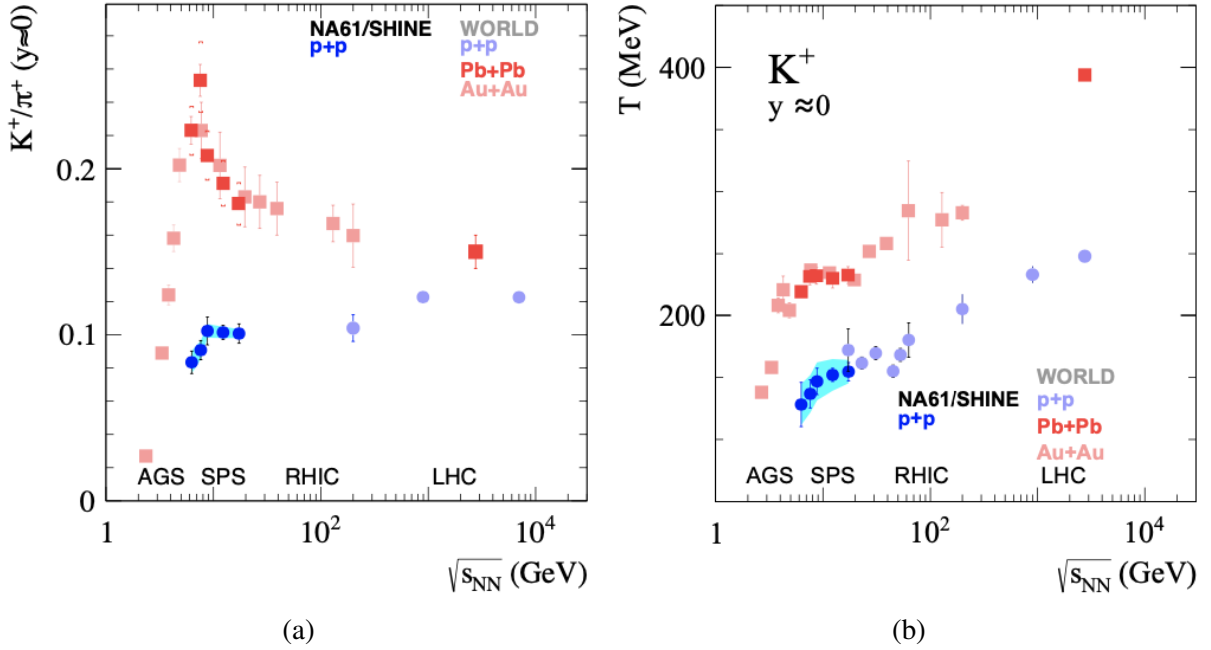


Figure 2.21: Energy dependence of the K^+/π^+ ratio (a) and the inverse slope parameter T of transverse mass spectra (b) at mid-rapidity. The NA61/SHINE results for inelastic p - p interactions are shown together with the world data [260].

1135 transition to a deconfined phase. However recently NA61/SHINE have found intriguing similarities in
 1136 p - p interactions where no deconfinement transition is expected [260]. It can be interesting to study this
 1137 effect in p - p and d - d interactions at the first phase of SPD when the beam polarization will not be yet
 1138 available. These measurements can serve as an important crosscheck for results of NA61/SHINE and,
 1139 potentially, results of MPD.

1140 The energy dependence of the K^+/π^+ ratio and inverse-slope parameters of transverse-mass spectra (so
 1141 called effective temperature T) of kaons at mid-rapidity are shown in Fig. 2.21. The results for heavy ion
 1142 collisions are plotted for comparison. The K^+/π^+ ratio in heavy ion collisions shows the so called horn
 1143 structure. Following a fast rise the ratio passes through a maximum at around 8 GeV and then settles to
 1144 a plateau value at higher energies. While the collision energy dependence of the T parameter shows the
 1145 so-called step structure at about the same value of $\sqrt{s_{NN}}$.

1146 The K^+ yield is proportional to the overall strangeness production and pions can be associated with
 1147 the total entropy produced in the reaction. Thus the K^+/π^+ production ratio can be a good measure
 1148 of strangeness-to-entropy ratio which is different in the confined phase (hadrons) and the QGP (quarks,
 1149 anti-quarks and gluons). The K^+ is a proper observable for this measurement because the anti-hyperon
 1150 yield is small and the main carriers of anti-strange quarks are K^+ and K^0 with $\langle K^+ \rangle \approx \langle K^0 \rangle$ due to
 1151 approximate isospin symmetry. Thus the K^+ (or K^0) yield counts about half of all $s\bar{s}$ pairs produced in
 1152 the collisions and contained in the reaction products. In contrast, the fraction of strange quarks carried
 1153 by K^- (or \bar{K}^0) and hyperons is comparable which makes the structure in the K^-/π^- distribution less
 1154 pronounced.

1155 A resonance-string models [261] in which the hydrodynamic expansion of the strongly interacting matter
 1156 created in nucleus-nucleus (A - A) collisions is replaced in p - p collisions by excitation of resonances or
 1157 strong fields between colour charges of quarks and di-quarks (strings) which makes them qualitatively
 1158 different. However the similarity of the transition energy in central heavy ion collisions and the break
 1159 energy in p - p interactions observed by NA61/SHINE provokes the question whether there is a common

1160 physics origin of the two effects. This makes the precision measurement of the kaon-to-pion ratio in p - p
 1161 and d - d interactions an interesting topic for the first phase of SPD when the beam polarization will not
 1162 be yet available.

1163 3.8 Study of lightest neutral hypernuclei with strangeness -1 and -2 [Q. Zhao]

1164 It is no doubt that the question of stability of the $A = 4$ double- Λ hypernuclei would be crucial for our
 1165 understanding of the role played by hyperons in nuclear matter [262–264]. While it is still controversial
 1166 for model calculations of such a four-body problem in the regime of weak binding [262, 265, 266],
 1167 [267], [267, 268], we propose that some general properties arising from the weakly binding systems
 1168 involving the 2-body and 3-body bound-state energies may provide a guidance for a possible stability of
 1169 ${}_{\Lambda\Lambda}^4\text{n}$ [269, 270]. Meanwhile, we propose a sensitive reaction process for the search for ${}_{\Lambda\Lambda}^4\text{n}$ in deuteron-
 1170 deuteron scatterings, i.e. $d + d \rightarrow K^+ + K^+ + {}_{\Lambda\Lambda}^4\text{n}$, which is accessible at NICA. After all, it would rely
 1171 on the experimental study to decide the dedicate dynamics for such an exotic system.

1172 The quantum numbers of the ground state ${}_{\Lambda\Lambda}^4\text{n}$ will favor $J^P = 0^+$, where the neutron pair and Λ pair have
 1173 spin 0, namely, their spins are anti-parallel, respectively. Meanwhile, the total isospin is $I = 1$. Thus, the
 1174 total wavefunction of the ground state is anti-symmetric under the interchange of the two nucleons or the
 1175 two Λ .

1176 The most ideal reaction for producing ${}_{\Lambda\Lambda}^4\text{n}$ should be $d + d \rightarrow K^+ + K^+ + T$ which is an extremely clean
 1177 process since the background processes involving the K^+K^- productions become irrelevant. It makes the
 1178 measurement of the missing mass spectrum recoiling against the K^+K^+ pairs sensitive to the existence
 1179 of any pole structure in the $nn\Lambda\Lambda$ system.

1180 In Ref. [269] we have shown that the energy region above $E_{cm} \simeq 5.2$ GeV is favored to produce ${}_{\Lambda\Lambda}^4\text{n}$ with
 1181 the total cross section of about 2.5 nb. Here, based on the same analysis we make a rough estimate of its
 1182 production rate at the kinematics of SPD.

1183 The c.m. energy at SPD starts at $E_{cm} = 6.7$ GeV with a luminosity of $L = 10^{27} \text{ cm}^{-2} \text{ s}^{-1}$. We estimate
 1184 that the total cross section at $E_{cm} = 6.7$ GeV will drop about one order of magnitude compared with the
 1185 peak value of about 2 nb. Thus, the events expected in one-year runtime (10^7 s) are

$$1186 N = \sigma_{total} \times L \times t = 0.2 \text{ nb} \times 10^{27} \text{ cm}^{-2} \text{ s}^{-1} \times 10^7 \text{ s} \simeq 2.0, \quad (2.25)$$

1187 which is a small event counting. It could be even smaller taking into account the detection efficiency
 1188 which generally will reduce the event counting by one order of magnitude. However, if the luminosity
 1189 can reach 10^{29} , which is an approximate average between the lower limit of $10^{27} \text{ cm}^{-2} \text{ s}^{-1}$ and the upper
 limit of $2 \times 10^{30} \text{ cm}^{-2} \text{ s}^{-1}$, the event counting can be significantly increased:

$$1190 N_m = \sigma_{total} \times L \times t = 0.2 \text{ nb} \times 10^{29} \text{ cm}^{-2} \text{ s}^{-1} \times 10^7 \text{ s} \simeq 200, \quad (2.26)$$

1191 which is sufficient for establishing the state. For the highest luminosity, one would expect about 4000
 1192 events in one-year runtime. Even though the detection efficiency will reduce the events, there will be
 tens to hundreds of events to count.

1193 Apart from the process of $d + d \rightarrow K^+ + K^+ + (n, n, \Lambda, \Lambda)$, it is also interesting to look at the proton-
 1194 proton collisions, $p + p \rightarrow K^+ + K^+ + \Lambda + \Lambda$, where the missing mass spectrum of K^+K^+ also provides
 1195 a clean and direct way to search for the di-baryon $\Lambda\Lambda$, or to study the $\Lambda\Lambda$ interactions. For the proton-
 1196 deuteron collisions, the double K^+ channel is $p + d \rightarrow K^+ + K^+ + n + \Lambda + \Lambda$. The recoiled part of the
 1197 double K^+ is $n\Lambda\Lambda$, which literally can produce the exotic H di-baryon. A direct measurement of such
 1198 a system would provide rich information about both $\Lambda\Lambda$ and $n\Lambda$ interactions [271, 272], [273, 274],
 1199 [275, 276]. Nevertheless, notice that the final states have access to the nK^+ invariant mass spectrum.
 1200 The exclusive measurement of this process can also tell whether the light pentaquark state $\Theta^+(1540)$
 1201 exists or not.

1202 **3.9 Multiquark correlations and exotic state production [V. Kim]**

1203 Multiquark correlations in the collisions of particles and nuclei play an important role in understanding
 1204 of QCD. Multiquark correlation phenomena may be divided into three classes. The first one can be
 1205 related with parton distribution functions (PDFs) of the colliding hadrons and nuclei. In the leading twist
 1206 approximation, in the nuclear PDFs there is a contribution at large $x > 1$, which is related with objects
 1207 known as fluctons [277] or few-nucleon short-range correlations [222]. Beyond the leading twist, two-
 1208 or three- quark correlations in parton distributions of hadron and nuclei are related with higher twist
 1209 contributions. The second one is related with parton subprocesses. Namely, when multiparton scattering
 1210 occurs, that is, e.g., when two partons from each colliding objects simultaneously scatter off each other.
 1211 The third class can be related with production of exotic multiquark resonance states, e.g., pentaquark and
 1212 tetraquark states. Below one can briefly outline possible studies at SPD, which can shed light on the all
 1213 three classes of multiquark phenomena mentioned above.

1214 **3.9.1 Multiquark correlations: fluctons and diquarks**

1215 Nuclear fluctons consist of the nucleons compressed in distances comparable with nucleon size, so the
 1216 flucton with five or six nucleons could be considered as a cold dense baryon matter since the effective
 1217 nuclear density [278] would be high as that in the core of neutron stars [226]. Fluctons are directly
 1218 connected with cumulative hadron production in the nuclear fragmentation region [279, 280]. The flucton
 1219 approach [281], which is based on hard QCD-factorisation and EMC-ratio constraints, predicts an extra
 1220 nuclear quark sea, which has rather hard momentum distribution: the extra nuclear sea x -slope is equal
 1221 to the x -slope of the valence quarks. It leads to "superscaling" for cumulative hadron production at
 1222 $x > 1$ in the nuclear fragmentation region: the x -slope of all cumulative hadron distributions including
 1223 "sea" ones [281, 282] are the same. The superscaling phenomenon was experimentally confirmed by
 1224 ITEP group [283, 284]. In high- p_T cumulative processes at the central region, other contributions should
 1225 be added to the contribution of the nuclear PDFs at $x > 1$, such as the contributions from the PDFs
 1226 of the other colliding object and possible intranuclear rescattering effects [285, 286]. So, beyond the
 1227 nuclear fragmentation region one should observe deviations from superscaling for cumulative production.
 1228 Another aspect of multiquark correlations is two-quark correlations (diquark states) in baryons [287].
 1229 This is an important source of high- p_T baryon production [288–290]. Being a higher-twist the diquark
 1230 contribution can describe the strong scaling violation for baryon production in hard processes at SPD
 1231 energies [289–291].

1232 **3.9.2 Multiparton scattering**

1233 Measuring few-particle correlation at SPD one can study multiparton scattering processes [291], which
 1234 are related with 2D- and 3D- PDFs. It is also significant for production of multiquarks systems [291,
 1235 292].

1236 **3.9.3 Multiquark exotic state production**

1237 Multiparton scattering [292] provide a unique opportunity to study production of various multiquark
 1238 states, such as, e.g., in Refs. [293–295] at SPD energies. For multiquark systems with possible diquark
 1239 structure [296, 297] it can be especially interesting issue [291, 292].

1240 Near the thresholds of heavy quarks production, where relative velocities of final particles are vanishing,
 1241 is expected formation of new type of resonances, like J/ψ - N [298–301]. This question became especially
 1242 interesting after pentaquarks observation at LHCb [302, 303] in the decay $\Lambda_b^0 \rightarrow J/\psi p K^-$.

1243 Enhancement effect was observed at the threshold of the reactions $e^+e^- \rightarrow p\bar{p}$ and $e^+e^- \rightarrow \Lambda\bar{\Lambda}$ [304]
 1244 and also in the decay $J/\psi \rightarrow p\bar{p}\gamma$ [305]. Furthermore, the double spin correlation A_{NN} measured in large

1245 angle ($\sim 90^\circ$) pp -elastic scattering [306] demonstrates an enhancement near the strange ($\sqrt{s} = 2.5$ GeV)
 1246 and charm ($\sqrt{s} = 5$ GeV) threshold, respectively, in the two-baryon system. According to [307], the ob-
 1247 served strong spin correlations are consistent with formation in the s -channel of “octoquark” resonances
 1248 $uuuds\bar{s}uud$ and $uuudc\bar{c}uud$. The SPD NICA has a possibility for search of such states.

1249 To summarise this section, SPD with study of the inclusive particle production and few-particle corre-
 1250 lations at different kinematic regions in pp -collisions as well as in the cumulative processes with light
 1251 nuclei has a unique opportunity to test various aspects of multiquark correlations: from the cold dense
 1252 baryon matter to the exotic multiquark resonance production.

1253 **3.10 Yield of antiprotons in hadronic collisions for astrophysical dark matter search [R. El- 1254 Kholly]**

1255 Dark matter (DM) is a long-standing mystery in cosmology. It makes up more than 26% of the Universe
 1256 [308], yet we still do not know its identity. Evidence of DM is mostly gravitational, *e.g.* the rotation
 1257 curves of spiral galaxies and the mass discrepancy in galaxy clusters [309]. The most favored candi-
 1258 date for DM is the WIMP (Weakly Interacting Massive Particle) [310]. Different search approaches are
 1259 employed to search for DM; each with its own underlying paradigm. The main approaches are collider
 1260 searches, direct detection (DD), and indirect detection (ID). The last approach include astrophysical
 1261 searches that seek to detect potential anomalous signatures, that hypothetically are produced via pair
 1262 annihilation and decay of DM particles, in the cosmic ray (CR) spectrum [310]. Naturally, these exper-
 1263 iments track different signal components. However, the chance of detection is thought to be higher for
 1264 rare antimatter components such as antiprotons. Recently, the AMS-02 experiment [311] has measured
 1265 the cosmic antiproton flux with unprecedented precision over a wide energy range (from 1 to 450 GeV)
 1266 [312]. However, we still cannot confirm or rule out an antiproton signature in these measurements due
 1267 to several sources of uncertainties [313].

1268 Secondary antiprotons are produced in collisions of primary CRs with interstellar medium (ISM). To
 1269 be able to detect any anomalous signal, we first need to subtract the flux of antiprotons produced by
 1270 these CR-ISM collisions. Even though there are several sources of uncertainty standing in the way of
 1271 pinpointing what this ordinary flux is—such as propagation parameters, solar modulation, and primary
 1272 spectra slopes—the most significant uncertainty, which ranges from 20% to 50% according to energy,
 1273 comes from antiproton-production cross sections [313]. Almost 70% of the secondary antiproton yield is
 1274 produced in pp collisions. However, existing datasets for this production channel is incredibly scarce, and
 1275 mostly date back to before 1980. Moreover, all old datasets did not account for hyperon decay or isospin
 1276 effect [314]. As for other production channels, data are almost non-existent. Thus, if we were to catch
 1277 up with the accuracy of AMS-02 measurements, we would have to perform new precision measurements
 1278 of antiproton-production cross sections in pp collisions as well as other production channels (*e.g.* pD ,
 1279 p^3He , p^4He , and $^4He^4He$). It is also hoped to study the contribution of different production mechanisms
 1280 such as hyperon (namely, $\bar{\Lambda}$ and $\bar{\Sigma}^-$) and neutron decays. The kinematic range that needs to be covered
 1281 to achieve that has already been outlined [315].

1282 Preliminary MC studies [316, 317] show that at SPD energy range, the production rate is $> 10^5$ s $^{-1}$,
 1283 which would minimize statistical uncertainty. In addition, the 4π angular acceptance will allow SPD to
 1284 access a wider kinematic range, in terms of transverse momenta, in comparison with fixed-target exper-
 1285 iments operating at the same energy level. With a precise TOF (time-of-flight) system ($\sigma_{TOF} \sim 70$ ps),
 1286 K^-/\bar{p} separation can be achieved with high purity up to ~ 3.5 GeV. SPD can also contribute to mea-
 1287 surement of hyperon-decay contribution via reconstruction of secondary vertices [317]. To summarize,
 1288 the SPD detector can make a sizable contribution to the search for physics beyond the standard model in
 1289 terms of the astrophysical search for DM.

Chapter 3

Polarized beams [A. Kovalenko]

1 Available species and types of collisions

Basic specification to available polarization states and combinations is the following:

- protons: vector polarization, longitudinal and transverse direction in respect to a particle velocity;
- deuterons (possibly helium-3 ions at the second stage): vector and tensor polarization, vertical direction of polarization, changing of the polarization direction at 90° up to about 4 GeV/c momentum;
- possibility to collide any available polarized particles: proton – deuteron, proton – helium-3, deuteron – helium-3 with the luminosity of $10^{30} \text{ cm}^{-2} \text{ s}^{-1}$ at the collision energy equivalent to the proton-proton collisions;
- possibility of asymmetric collisions should be considered as an option for the future development of the facility;
- for efficient estimates of systematic error it is desirable to realize a bunch-to-bunch polarization flipping at 90° within minimal time.

Technical realization of the above mentioned conditions is feasible [318].

2 Beam structure, intensity and luminosity

Beam structure of polarized proton and deuteron beams at the first stage will be corresponded to that was optimized for the NICA heavy ion regime. Some of the important, for the SPD, operation parameters in case of bunched beam are the following: bunch number 22, bunch length $\sigma = 60$ cm, the collider orbit length - 503 m, bunch velocity $v \approx c = 3 \times 10^8$ m/s, revolution time $\tau = 1.67 \times 10^{-6}$ s, bunch revolution frequency $f \approx 0.6$ MHz, time gap between bunches $\Delta\tau = 76.0 \times 10^{-9}$ s. The dependence of the pp-collision luminosity on the energy and number of protons is presented in Fig. 3.1.

As it is clear from the calculations the luminosity level of $1 \times 10^{30} \text{ cm}^{-2} \text{ s}^{-1}$ is reached at a bunch intensity of 10^{11} polarized protons, whereas to obtain the level of $1 \times 10^{32} \text{ cm}^{-2} \text{ s}^{-1}$ multi-bunch storage mode should be used [319].

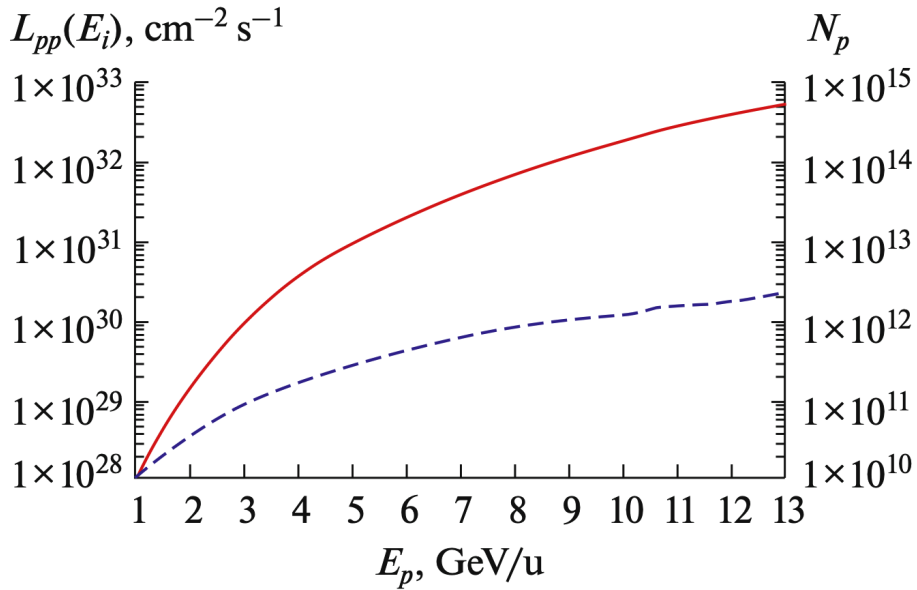


Figure 3.1: Normalized dependence of the pp-collision luminosity L and the beam intensity N on proton kinetic energy.

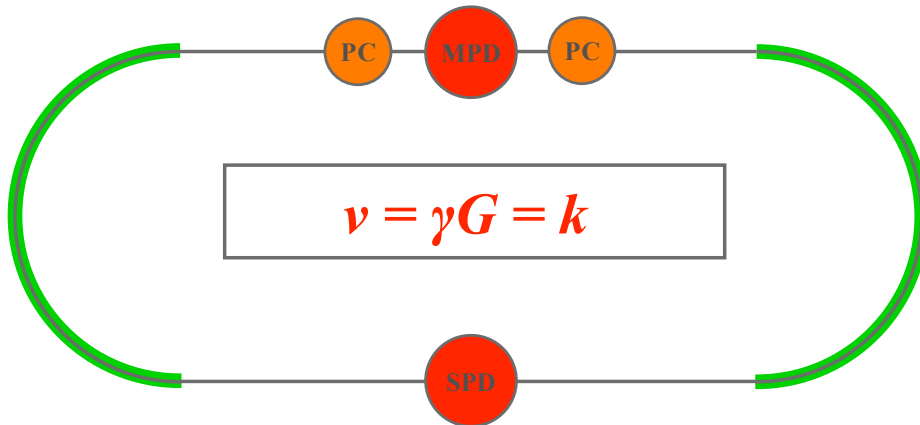


Figure 3.2: General scheme of the polarization control at integer spin resonance points.

1316 3 Polarization control and monitoring

1317 3.1 Transportation of polarized ions in the complex

1318 Polarized protons and deuterons from the source SPI are accelerated first in the linac LU-20M and after
 1319 that are injected and accelerated in the Nuclotron to the specified energy and extracted to the collider via
 1320 long transfer line. The main tasks at this stage are the following: i) preservation of the beam polarization
 1321 during acceleration in the Nuclotron (and in the collider also) and ii) the polarization control in the
 1322 collider mode. Moreover, it is necessary to adjust the polarization direction in the transfer line and the
 1323 other points of the collider orbit.

1324 3.2 Operation modes of the NICA collider at polarized ions

1325 From the spin dynamics point of view, NICA collider can operate in two regimes (modes), namely: in
 1326 a Preferred Spin mode (PS-regime) and in the Spin Transparency mode (ST-regime) In the PS - regime

1327 periodic motion of the spin along the particle orbit is the only possible, i.e. – stationary magnetic structure
 1328 select the only one stable direction of the polarization vector in any point of the particle orbit, non-integer
 1329 part of the spin tune is not equal to zero, whereas in the ST – regime the direction of the spin vector is
 1330 reproduced in any point at every turn, i.e. magnetic structure of the accelerator (or storage ring) is
 1331 transparent for the spin – non-integer part of the spin tune is equal to zero.

1332 The main difference between the PS- and ST- regimes is occurred at the manipulations of the spin di-
 1333 rection during physics data taken. In the ST- regime the spin motion is very sensitive to the magnetic
 1334 field changes, because particles are moved in the vicinity of the integer resonance In this case the use of
 1335 additional "weak" magnetic field, rotating spin at small angles $\Psi \sim 1$ provides the needed polarization
 1336 direction at any specified point of the collider. It is possible to use a pair of solenoids with the field
 1337 integral of $1 T \cdot m$, introduced negligible distortions of the particle closed orbit, to produce necessary
 1338 variation of the spin angle in the NICA collider over the momentum range up to 13.5 GeV/c. In the case
 1339 PS regime similar procedure will require spin rotators base on a strong fields, rotating the spins at the
 1340 angles of $\Psi \sim 1$. Thus, in the case of the changing the polarization direction from the longitudinal to
 1341 the transverse one, it would be necessary to apply the transverse field with the total integral of 20-30
 1342 $T \cdot m$, which would be resulted in a strong distortions of the particle close orbit. The amplitude of the
 1343 distortions can reach of tens of centimeters at low energies. Thus, efficient polarization control of ions,
 1344 deuterons especially, by means of quasi-stationary weak fields is possible the only if the ST- regime is
 1345 used.

1346 3.3 Specifications to the polarized beams in the collider

1347 Different experiments are planning with polarized proton, deuteron and helium-3 (in the future) particles
 1348 to identify and study different observables for different physics tasks: Drell-Yan, J/ψ , high hadron
 1349 physics, exotic states etc. The polarization control system should be satisfied to the following main
 1350 conditions:

- 1351 – to obtain both longitudinal and transverse polarization in the MPD and SPD detectors with the
 1352 polarization degree not less 70% and the polarization lifetime not less than the beam lifetime;
- 1353 – to provide the collision luminosity of $\sim 10^{30} - 10^{32} \text{ cm}^{-2}\text{s}^{-1}$ over the particle momentum range
 1354 from 2 to 13.5 GeV/c;
- 1355 – to provide the particle energy scan with a step of 1–2 GeV within the energy range 7–27 GeV and
 1356 0.3 MeV at lower energies;
- 1357 – to adopt operation in asymmetric on the particle momentum mode;
- 1358 – make simultaneous spin-flips for all bunches in the case of the Spin Flipping experiments (SF
 1359 system).

1360 3.4 Spin flipping system

1361 The spin flipping (SF) system makes it possible to carry out the spin physics experiments at much higher
 1362 level of the accuracy [320]. Being equipped by such system the SPD set-up will have real privileges, in
 1363 particular:

- 1364 – revers of the polarization direction at the polarized ion source is not necessary;
- 1365 – no necessity of a bunch-to-bunch luminosity measurements and bunch monitoring system;

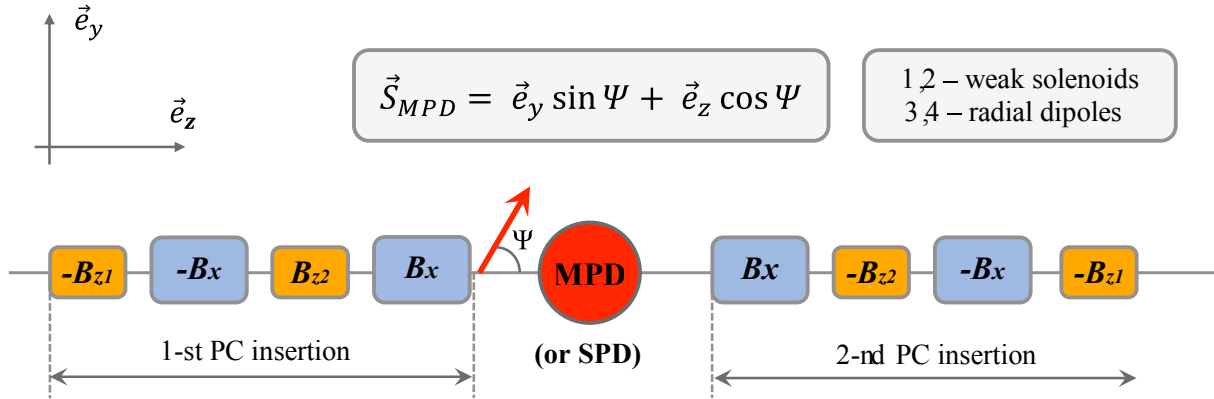


Figure 3.3: Detail scheme of the PC's insertions in the collider in the ST regime.

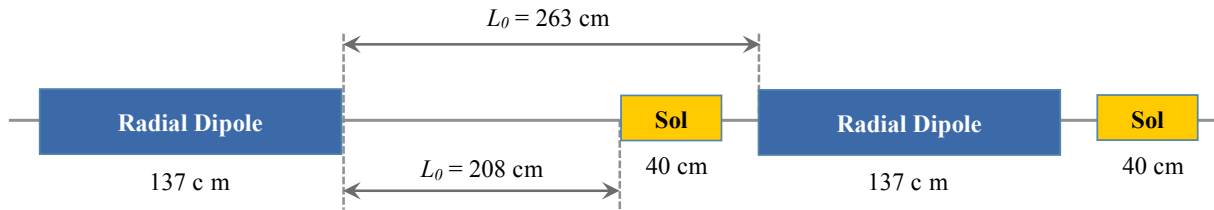


Figure 3.4: Placement of weak control solenoids in horizontal plane.

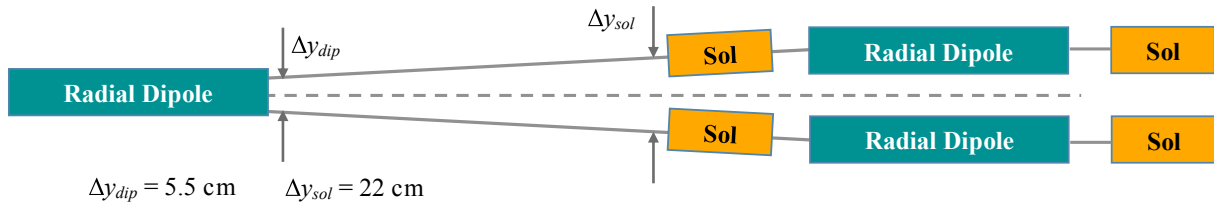


Figure 3.5: Placement of weak control solenoids in vertical plane together with radial dipoles.

- 1366 – the possibility of comparison collisions of bunches with any directions of the particle spin (vertical-
 1367 longitudinal, vertical – radial, radial – longitudinal, etc.). The SF system based on quasi-stationary
 1368 fields is naturally realized in the ST collider regime. The pair of "weak" controlled solenoids
 1369 provides simultaneous influence on the polarization direction and the spin tune. Thus, possibility
 1370 of the spin tune stabilization during the spin flipping is occurred, preventing both as the zero spin
 1371 tune and higher order spin resonances crossing. The polarization degree will be kept with an
 1372 exponential accuracy, if the field of "weak" controlled solenoids will be changed slowly. Typical
 1373 flipping time is estimated as about 1 ms and 10 ms for the proton and deuteron, respectively.
 1374 Realization of a SF system in the PS regime will require the inserting in the lattice RF-module of
 1375 a MHz's range and the field total integral of 1 T·m, that's not so simple technical problem.

1376 3.5 Online control of the polarization in the collider

1377 The unique possibility of the online polarization control is occurred if the collider operates in the ST-
 1378 regime. Because the field ramp in a "weak" solenoids ($t_{change} \sim 0.2$ s) is much larger of the spin pre-
 1379 cession period around the induced spin field ($t_{rev} \sim 10^{-4}$ s), any manipulations with the spin direction at
 1380 spin tune will be occurred adiabatically and the polarization degree during the experiment time will be
 1381 supported constant with the exponent accuracy. The direction of polarization vector will be a function
 1382 of the weak solenoids field and can be defined by mean of the field measurements. The comparison of

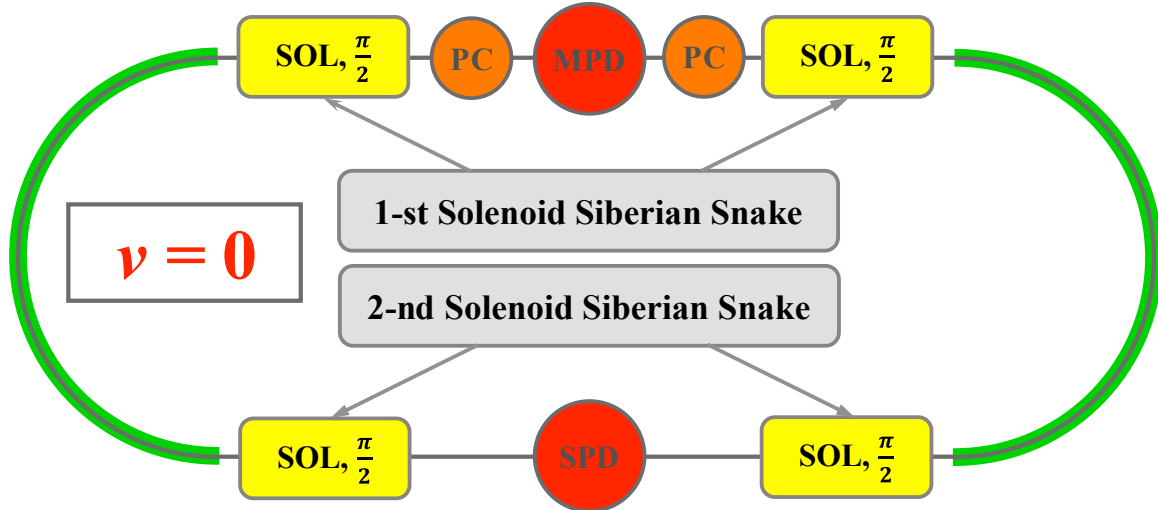


Figure 3.6: Scheme of realization ST regime in NICA collider.

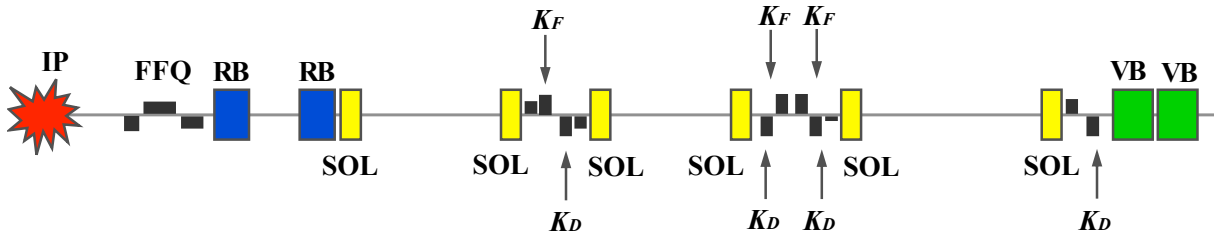


Figure 3.7: Distributed snake (one half) based on short 6 T SC solenoids.

1383 the ST- and PS- regimes in the NICA collider is presented in Table 3.1. Thus, the ST-regime makes it
 1384 possible to carry out the experiments at the NICA collider at the new level of the accuracy.

Table 3.1: Comparison of two regimes.

Possibility of realization	PS regime	ST regime
Stationary longitudinal/transverse polarization in the detectors	yes	yes
Polarization control in any point of the orbit	no	yes
Spin Flipping systems based on quasi- static fields	no	yes
on-line polarization control	no	yes

1385 3.6 Polarization control in the collider NICA in ST regime

1386 **Use of integer spin resonances in ST-regimes.** Stable polarization direction in the NICA collider is
 1387 vertical (orthogonal to the particle orbit), whereas the spin tune is proportional to the particle energy:
 1388 $\nu = \gamma G$, where G is anomalous part of the gyromagnetic ratio. The collider is operated in the PS-
 1389 regime practically over the total energy range because $\gamma \neq k/G$, where k is an integer. The ST regime is realized
 1390 at discrete energy points corresponding to integer spin resonances: $\gamma = k/G$. For protons the number of
 1391 points corresponding to ST- regime is 25 starting from minimal energy $E_{kin}^{min} = 108$ MeV with the step of
 1392 $\Delta E = 523$ MeV. There is only one point $E_{kin} = 5.63$ GeV/u, corresponding to the momentum 13 GeV/c
 1393 i.e. the ST-regime for deuterons in the Nuclotron/NICA complex.

1394 Possible scheme of ion polarization control in the collider at the integer spin resonances is presented

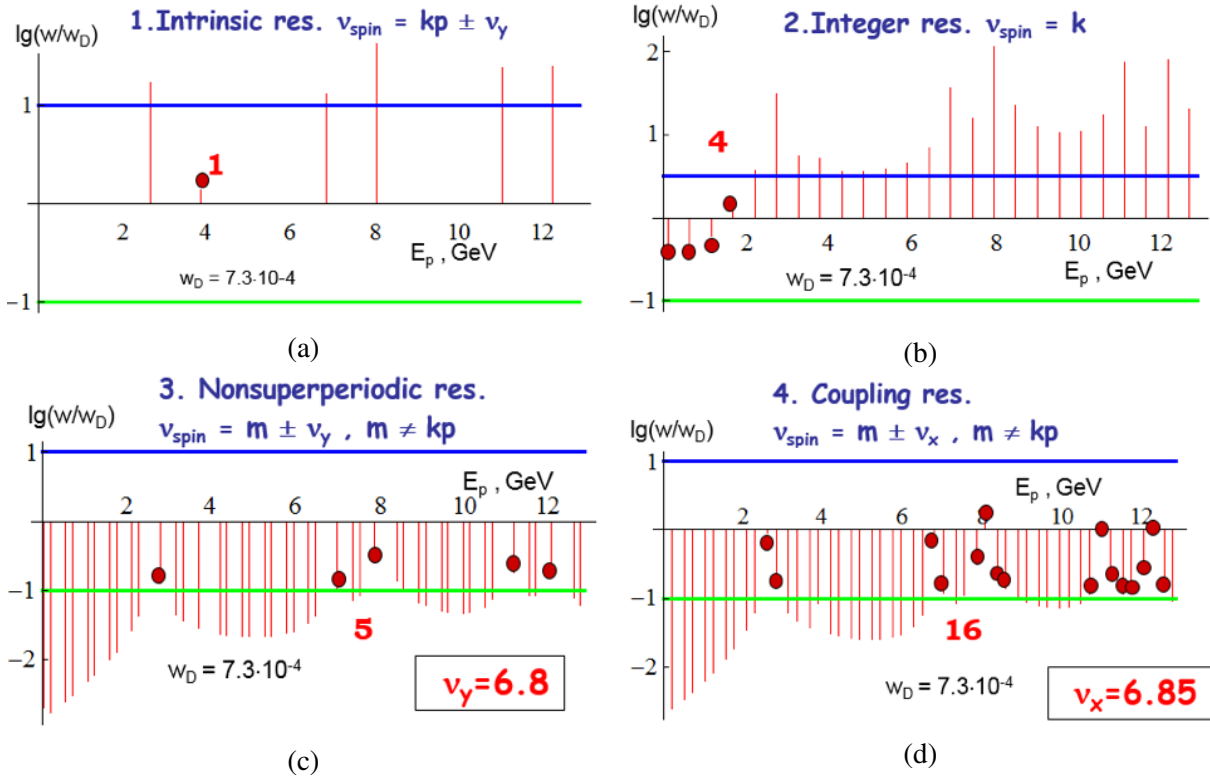


Figure 3.8: Linear spin resonances in the Nuclotron at polarized proton mode.

1395 in Fig. 3.2. Two PC-insertions (marked with orange circles in Fig. 3.2) placed near MPD are used
 1396 to stabilize the needed polarization direction at any point of the collider ring, including the collision
 1397 points, at injection, etc. Detail scheme of the PC's is presented in Fig. 3.3. Weak solenoids (B_{z1} and B_{z2}
 1398 generated longitudinal magnetic field $\pm B_{z2}$ are placed between the collider structural magnets, generated
 1399 radial field $\pm B_x$ (marked as 3 and 4), providing deflection the beams to the collision plane of the MPD.

1400 The scheme make it possible the ion polarization control in vertical plane (yz) in the MPD (or SPD) (Ψ
 1401 is angle between polarization and particle velocity vectors). The scheme provides necessary spin rotation
 1402 for all discrete points over NICA energy range if integral magnetic field will reach $0.6 \text{ T} \times \text{m}$ in each of
 1403 four solenoids. If we limit the field maximum to 1.5 T, the magnetic length of the solenoid unit of 40
 1404 cm. Real relative scale of the control solenoid (40 cm long), radial dipole and distances between them is
 1405 shown in Fig. 3.4.

1406 The scheme of installation weak control solenoids in vertical plane together with the collider lattice
 1407 elements is presented in Fig. 3.5. The beam convergence angle in vertical plane, defined by the dipoles
 1408 with transverse to the beam axis magnetic fields is: $a_x = 0.04 \text{ rad}$. The distance between the collider
 1409 rings in vertical is 32 cm. The distances in vertical plane between the particle closed orbits are $\Delta y_{dip} =$
 1410 $L_x a \approx 5.5 \text{ cm}$. and $\Delta y_{sol} = \Delta y_{dip} + 2L_1 a \approx 22 \text{ cm}$. at the output of common radial dipole and at the exits
 1411 of control solenoids respectively.

1412 3.7 Ion polarization control in ST regime by means of two snakes

1413 Two solenoidal snakes installed symmetrically in respect to both MPD and SPD set-ups will provide ST
 1414 regime in NICA collider (Fig. 3.6).

1415 The configuration make it possible to turn the spin in vertical plane (yz) of MPD or SPD detector,
 1416 whereas in the collider magnet arcs the polarization vector is moving in the median plane (xz) [321].

1417 The ST scheme with two snakes provides the zero spin tune at any point of the particle energy. It is
 1418 very important for optimization of the NICA effective operation at the highest possible luminosity of
 1419 pp - collisions, due to necessity of the particle store at an energy level that gives proper conditions for
 1420 electron cooling of stored beam. Only in this case it is possible to form particle bunches with high number
 1421 of particles and high degree of the polarization at low energy (about 1 GeV) with further acceleration up
 1422 to the experiment energy. The total integral of longitudinal solenoidal field should reach 4×25 T·m per
 1423 ring at the proton momentum of 13.5 GeV/c and 4×80 T·m for deuterons respectively. The distributed
 1424 system consisting of a short solenoids is possible, i.e. In the case of 6 T solenoids the total length of 4.2
 1425 m is sufficient to form a half-length snake. It is possible to adopt the collider lattice structure optimized
 1426 for heavy ion beam for the case of ST regime at the protons mode over the total energy range. Weak
 1427 control solenoids don't disturb practically orbital motion in the collider whereas, strong solenoids of
 1428 the snakes led to a strong betatron tunes coupling. Because longitudinal field of the snakes is changed
 1429 proportionally to the particle momentum, the collider magnetic optics will stay adequate to the polarized
 1430 particle stable motion during the beam acceleration phase. Matching of the solenoids with the collider
 1431 structure is provided by means of proper choice of the work point by means of structural KF (focusing)
 1432 and KD (defocusing) quadrupole lenses. Possible scheme of the distributed snake (one half) based on
 1433 short 6T superconducting solenoids (SC) is shown in Fig. 3.7. The elements are the following: SOL-SC
 1434 solenoid, FFQ - final focus triplet of the collider, VB - structural dipole magnets; RB - bending dipoles
 1435 with transverse field for converging the bunches in the collision point IP.

1436 3.8 Stability of spin motion

1437 In the ST regime precession of the polarization vector is caused by the field of solenoids, by the field
 1438 imperfections of the collider lattice elements, by a finite beam emittance and depends on a power of
 1439 zero spin tune resonance. To stabilize the polarization during acceleration process or during control
 1440 the polarization direction in the ST regime it will be necessary to provide spin tune level caused by the
 1441 control solenoids much higher of a power of zero spin tune resonance: The calculations have showed that
 1442 the level of 10^{-2} for protons and 10^{-4} for deuterons would be sufficient. These values put limitations on
 1443 the minimum field integral in each of weak control solenoids – 0.6 T·m.

Table 3.2: Polarization in the SPD and MPD detectors in PS and ST regimes.

Snake SPD	Snake MPD	Spin tune	Control regime	Polarization in SPD	Polarization in MPD
off	off	$\nu \neq \gamma G$	PS	vertical	vertical
off	off	$\nu = \gamma G$	ST	any	any
off	on	1/2	PS	longitudinal	in the collider median plane, direction angle depends on energy
on	off	1/2	PS	in the collider median plane, direction angle depends on energy	longitudinal
off	off	$\nu = \gamma G$	ST	any	any

1444 3.9 Polarized beams dynamics in Nuclotron

1445 Stable polarization direction in the Nuclotron is vertical, and the spin tune is proportional to the beam
 1446 energy: $\nu = \gamma G$ (G is anomaly part of the gyromagnetic ratio of the particle, γ is Lorentz factor) that
 1447 definitely lead to crossing of spin resonances during the particle acceleration and, as consequence, to

Table 3.3: Polarization in the SPD and MPD detectors in PS and ST regimes.

Snake SPD	Snake MPD	Spin tune	Control regime	SF system	Online polarization control	Possibility of acceleration in collider	Influence of RF modulation on polarization lifetime
off	off	$\nu \neq \gamma G$	PS	no	no	no	reduce
off	off	$\nu = \gamma G$	ST	yes	yes	no	reduce
off	on	1/2	PS	no	no	yes	no influence
on	off	1/2	PS	no	no	yes	no influence
off	off	$\nu = \gamma G$	ST	yes	yes	yes	no influence

1448 resonance depolarization of the beam. There is no problem with deuterons: the only one integer spin
 1449 resonance can be excluded by means of weak solenoid (~ 0.1 T·m) inserted into the accelerator lattice.
 1450 The number of different spin resonances in the proton mode is much larger. Logarithmic graphs of
 1451 linear spin resonances power scaled to the specific power corresponding to complete depolarization of
 1452 the beam are presented in Fig. 3.8 [322, 323]. The proton energy range E_p corresponds to the available
 1453 at Nuclotron. Each graph is divided into three areas that correspond to intermediate crossing (between
 1454 horizontal lines), fast crossing (below green line) and adiabatic crossing (upper blue line). The lines of a
 1455 fast and adiabatic crossing are corresponding to 1% loose of the polarization degree.

1456 The parameters taken for calculation of the resonances power were the following: the magnetic field ramp
 1457 - 1 T/s; beam emittance (horizontal and vertical) at the injection energy - 45π mm×mrad; quadrupole
 1458 misalignment errors – 0.1 mm; errors of angular alignment of structural dipole and quadrupole magnets
 1459 - 0.01 rad; and the relative error of the quadrupole gradients - 0.001. The resonances marked with red
 1460 circles are dangerous and lead to the beam depolarization after their crossing. To keep the polarization
 1461 of proton beam at proper level, partial Siberian snake based at a solenoid will be used. Two options
 1462 have been considered: 1) The use of a weak 5% snake with the field integral of 0.65 T·m, which can
 1463 save the proton beam polarization up to 3.4 GeV/c and 2) The use of 25% snake (~ 12 T·m). The first
 1464 one is efficient if the collider operates in the ST regime with two snakes and injection of the beam is
 1465 provided at low energy (around 1 GeV), whereas strong enough snake that is used in option 2 could save
 1466 the polarization over the total energy range in the Nuclotron and is suitable to the operation at integer
 1467 resonances. The choice of energy points is limited to the points of integer resonances.

1468 3.10 Operation modes of the NICA collider at polarized beams

1469 Collider NICA with two solenoidal snakes will make it possible the following operation configurations
 1470 (see Table 3.2) [324].

1471 If the snakes installed in SPD and MPD sections are switched off, the PS regime with vertical polarization
 1472 at any point of the collider orbit is occurred. Some narrow energy gaps which the ST regime at integer
 1473 resonances is exists in, gives possibility to have any direction of the polarization in the both detectors.
 1474 After switching one of the snakes on, the collider will operate in PS regime with the spin tune 1/2. The
 1475 snake transform completely spin motion providing stable longitudinal direction of the polarization in
 1476 opposite respect to the snake section of the collider orbit.

1477 If two dynamic solenoid snakes are switching on, the unique spin transparency (ST) regime is realized.
 1478 The spin tune don't depend on particle energy and equal to zero that's gives possibility to obtain any
 1479 direction of the polarization at any point of the collider orbit. The features of the collider operation in
 1480 polarized modes are shown in Table 3.3.

1481 It is very important to realize the possibility of polarized beam acceleration in the NICA collider without
1482 loose the polarization degree. The problem of reaching the highest possible luminosity of polarized
1483 proton collisions is connected with the particle multi-bunch storage in the collider and electron cooling
1484 of the stored beam during the process. The optimal proton beam kinetic energy at the beam injection into
1485 the collider is about 1 GeV [325, 326].

1486 **3.11 Conclusion and outlook**

1487 The proposed scheme of the ion polarization control in the NICA collider is adopted easily to the collider
1488 magnetic optics at any regimes of the polarization control. Important advantages could be obtained with
1489 the applying spin transparency regime. Polarization degree of about 70% is provided at the collision
1490 points. The polarization life time is expected to be at the level of hours comparable with the beam life
1491 time. We didn't describe some specific measurement and monitoring systems should be designed at the
1492 stage of preparation technical project. In particular: precise measurement of the luminosity (bunch-to-
1493 bunch?), absolute polarimeter based on a gas jet, targeting stations etc.

Chapter 4

Detector layout

1 General design [A. Guskov]

The physics tasks presented in Chapter 2 impose general requirements on the concept of the Spin Physics Detector. Unlike the case of high-energy collisions where the collision energy \sqrt{s} is a few orders of magnitude higher than a typical hard scale Q of the studied reactions, at the SPD energies for all the probes planned to be used to access the gluon content of the colliding particles $Q \sim M_{J/\psi} \sim 2M_D \sim p_{T\gamma \text{ min}}$ is just a few times less than $\sqrt{s}/2$. Therefore, one should expect quite a uniform distribution of all signal particles (muons from the J/ψ decay, prompt photons, products of D -mesons decay, etc.) over the kinematic range. In other words, there is no preferable range in rapidity, which could be specified for each probe for the optimal overall performance. Together with relatively small cross sections of the discussed probes, this fact leads one to a requirement of $\sim 4\pi$ coverage of the SPD setup.

The Spin Physics Detector must have sufficient tracking capabilities and a magnetic system for spectrometric purposes for the most of the addressed physics tasks. It has to be equipped with a muon system thick enough for effective separation of muons and hadrons to make it possible to deal with the decay $J/\psi \rightarrow \mu^+ \mu^-$. A precision vertex detector is needed for recovering of the secondary vertices from the decays of $D^{\pm/0}$ mesons and other short-lived particles. An electromagnetic calorimeter ensures capability to detect signal and background photons. A low material budget and general transparency of the setup should also provide favorable conditions for the photon physics. Hadron identification capability is needed for any physics task with protons and/or kaons in the final state, in particular, to enforce a signal-to-background ratio for D -mesons selection, and also to improve tracking at low momenta. Since tiny effects are intended to be investigated, a triggerless DAQ system is planned in order to minimize possible systematic uncertainties of the measurements.

Strict limitations to the SPD detector layout arise from the external conditions, such as the maximal possible load to the floor of the SPD experimental hall (1500 tons together with the lodgement and the detector moving system). Together with the requirement to have the overall thickness of the muon system not less than 4 nuclear interaction lengths (Λ_I), this limits the outer size of the SPD detector and the size of the inner part of the detector. The location of the collider infrastructure, in particular, focusing elements, also defines the size of the SPD setup along the beam axis. More details could be found in Chapter 3.

The general layout of the SPD is shown schematically in Fig. ???. The detailed description of each subsystem could be found below. Table 4.1 brings together the elements of the SPD physics program and the requirements to the experimental setup.

Table 4.1: Required setup configuration for each point of the SPD physics program. (+++) - absolutely needed, (++) - extremely useful, (+) - useful, (-) - not needed.

Program	Vertex detector	Straw tracker	PID system	Electromagnetic calorimeter	Beam-beam counter	Range system
Gluon content with:						
charmonia	+	++	-	++	-	+++
open charm	+++	++	++	-	-	+
prompt photons	+	+	-	++	-	-
SSA for π and K	+	++	+++	++	-	-
Light vector meson production	+	++	-	+	-	-
Elastic scattering	+	++	-	-	+++	-
\bar{p} production	+	++	+++	++	-	-
Physics with light ions	++	+++	+	++	+	-

2 Magnetic system [A. Kovalenko]

The SPD Magnetic System (MS) should satisfy the following criteria:

- minimization of the material inside the detector inner part;
- a magnetic field integral of (1-2) T m along the particle tracks, whereas the peak value of the field should be limited to 0.8 T over the straw tracker volume;
- minimization of the total weight, the cross section of the current coil (coils), and the overall amount of the MS material, i.e. the MS should have perfect mechanics.

Several options of MS's were considered:

1. Solenoid – a uniform multi-turn coil placed between the ECAL and the muon range (RS) systems;
2. Toroidal MS (inside ECAL): $3 \times 8 = 24$ coils forming a toroidal distribution of the field in the detector volume only,
3. Hybrid system consisting of a combination of toroidal coils in the barrel and solenoidal ones in the front/rear parts. Both room and cryogenic temperatures were considered;
4. System of 4 separate coils inside the ECAL: a) all coils are connected in series, and b) right and left hand pairs are connected opposite to each other;
5. Hybrid system consisting of a combination of 8 toroidal coils in the barrel and 2 pairs of separate solenoidal coils in the front/rear parts. Both room and cryogenic temperatures were considered;
6. System of 6 separate coils placed between the ECAL and the RS system of the reduced diameter.

Thus, more than 10 different options of the 3D magnetic field configurations were analyzed. The calculated field maps were used for the SPD simulation [...]. Conceptual analysis of the considered MS systems was performed also. Certain data were reported at the European Conference on Applied Superconductivity EUCAS2019 [...]. The general conclusions are briefly summarized below.

- 1549 1. The most well-known system is a classical solenoid. Experience in design and construction of
 1550 superconducting solenoids has been collected by numerous groups worldwide, including the NICA
 1551 MPD. The MPD solenoid manufacturing is completed and the assembling has been started in the
 1552 experimental hall. The main disadvantage for SPD of a solenoid similar to the MPD MS would be
 1553 a lot of material in front of the ECAL as well as its high cost. Moreover, the fixed geometry of the
 1554 field gives no universality of the SPD experimental program.
- 1555 2. The toroidal MS was considered in its “warm” and “cold” options. The warm one was rejected due
 1556 to the material budget: the necessary ampere-turns led to an unacceptable cross section of the coils
 1557 and hence the amount of copper. The problem is solved partially in the case of superconducting
 1558 coils. Nevertheless, the complexity of design of the coil system is very high in any case. The most
 1559 important negative effect can occur due to concentration of the coil material closer to the bunch
 1560 crossing area.
- 1561 3. The MS consisting of separated coils is absolutely transparent for the particles passing through
 1562 the inner volume of the detector and contains “target” material for the secondary particles in the
 1563 limiting volume at the ECAL inner part. The amount of material depends directly on the necessary
 1564 ampere-turns of the coil and the achievable current density. The last point gives evidence in favor
 1565 of the superconducting approach. The magnetic field radial and axial distribution is not so uniform
 1566 in comparison with a solenoid, especially in the area close to the coils. Nevertheless, the accuracy
 1567 of modern 3D calculation codes for non-linear magnetic fields and precise magnetic measurements
 1568 can guarantee the necessary accuracy of real field mapping. Optimization of the coil cross section
 1569 is also very important.
- 1570 4. The hybrid MS consisting of a toroidal system in the barrel part of the SPD and two pairs of
 1571 separate coil was considered as a compromise, and namely: minimization of the magnetic field
 1572 near the polarized particles interaction zone and a solenoidal-type distribution in the front and rear
 1573 parts of the detector. The MS scheme is shown in Fig. 4.2.

1574 More advanced analysis of the detector and the collider system has shown that partial compensation of
 1575 the magnetic field at the axis will give not so many advantages. However, it would be more beneficial,
 1576 somehow, if there was no the spin control system in the collider lattice. The NICA collider will be
 1577 equipped with such a system. The elements aimed at the particle spin control at the NICA collider were
 1578 proposed and are under technical design now. The general description of the spin control system is
 1579 presented in section 3. Thus, the condition of a “zero” magnetic field along the beam axis is not a critical
 1580 issue in our case. An updated choice of the SPD MS was made in favor of a separate 6-coil design. The
 1581 geometrical model of the coil system is presented in Fig. ??, and the field calculation data in Fig. 4.4.

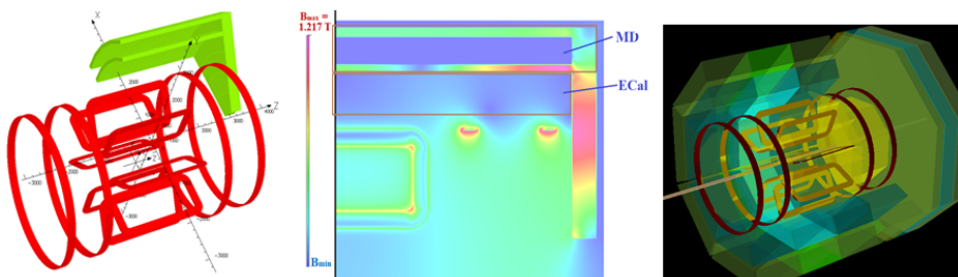


Figure 4.2: Hybrid MS: toroidal magnet consisting of 8 coils in the barrel part and a double-coil system in the front and rear parts of the detector.

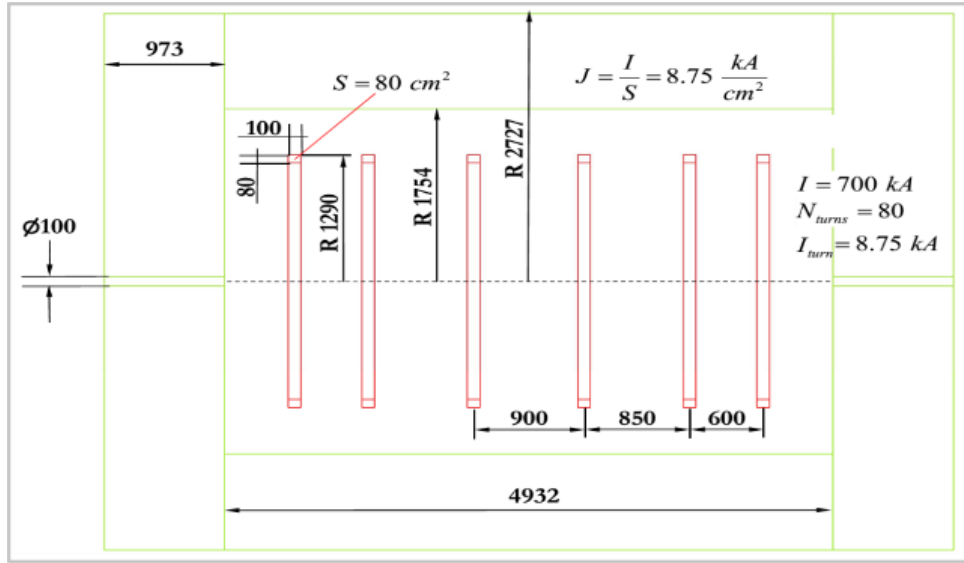


Figure 4.3: Geometrical model of the 6-coil magnetic system

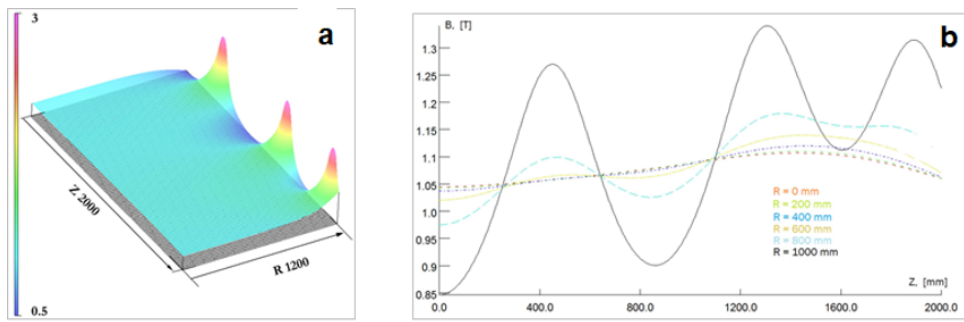


Figure 4.4: Field calculation results: (a) B_z as function of r, z ; (b). B_z as function of z at different r .

1582 As it is clear from Fig. 4.4, the longitudinal variation of an axial magnetic field is varied from about 5% at
 1583 the beam axis to about 12% at a radial distance of 2 cm from the coil inner turns. The number of 12% can
 1584 be further improved by the coils system optimization. We consider the technology of superconducting
 1585 coils manufacturing based on a hollow high-current cable similar to the one used for the Nuclotron
 1586 magnet or the one used in the ITER systems. The manufacturing technology of a hollow cable made of
 1587 NbTi/Cu composite wires cooled at 4.5 K with a forced helium flow is well developed at the Laboratory.
 1588 The magnets of the NICA booster and collider are being manufactured at the Laboratory magnet facility
 1589 (VBLHEP JINR). The coil containing 80 turns will provide $800 \text{ kA} \times \text{turns}$ and generate the necessary
 1590 magnetic field in the detector volume. Some of the SPD 6-coil MS are presented in Table 4.2 ??? in
 1591 comparison with the other detectors.

1592 3 Beam pipe [A. Guskov]

1593 A beam pipe separates the detector and high vacuum of the accelerator. It must be mechanically sturdy on
 1594 the one hand and thin enough in terms of the number of radiation lengths to minimize multiple scattering
 1595 and radiation effects, on the other. The diameter of the beam pipe is a compromise between the radial
 1596 size of the beams and the requirement to put coordinate detectors as close to the interaction point as
 1597 possible for better reconstruction of the primary and secondary vertices. A beryllium beam pipe of 6 cm

Table 4.2: Comparison of the SPD (NICA) and CMS (LHC) [] magnetic systems.

Parameter	SPD/NICA	CMS/LHC
Size (diam./length), m/m	2.9/6.0	6.5/12.7
Magnetic system	6 coils	solenoid
Peak magnetic field, T	1.0 (axis)	4.5
Coil average diam., m	~2.5	~ 6.5
Field volume, m ³	~45	~414
Stored energy, MJ	~40	~2800
Coil turns	80	2112
Operating current, kA	8.75	20
Total inductance, H	~0.2	12.6

1598 in diameter and 0.5 mm thick is proposed to be used.

1599 The schematic view of the beam pipe and its positioning inside the SPD is shown in Fig. 4.5. ...

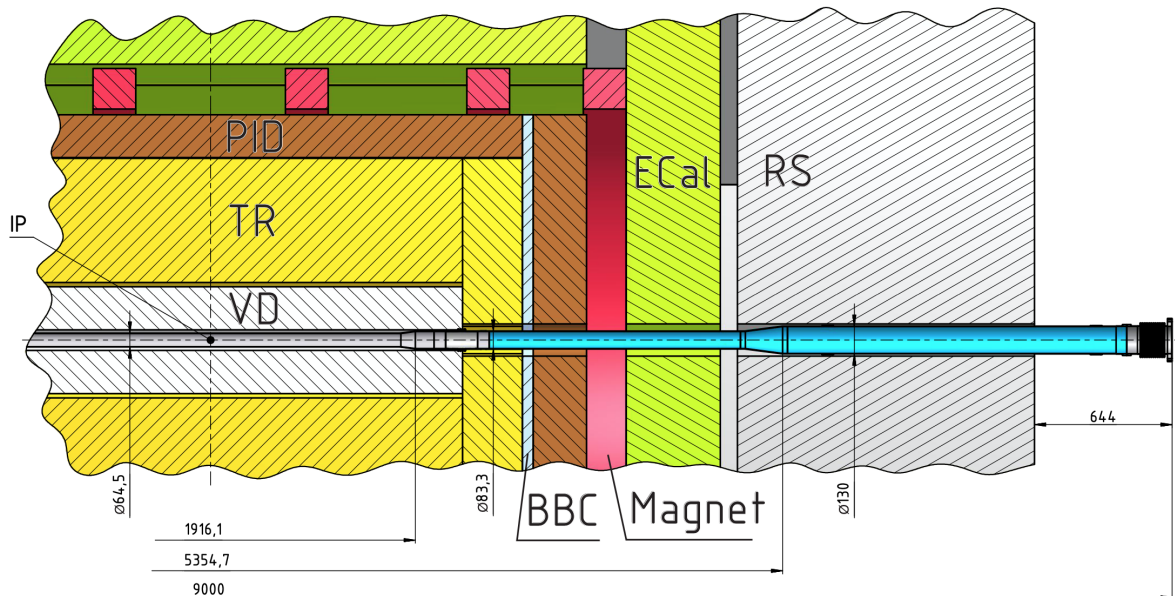


Figure 4.5: SPD beam pipe inside the setup.

1600 At the first stage of the SPD running a cheap steel beam pipe could be used.

1601 4 Vertex detector [N. Zamyatin]

1602 4.1 General overview

1603 The SPD Vertex Detector (VD) is a silicon-based part of the spectrometer responsible for precise de-
 1604 termination of the primary interaction point and measurement of secondary vertices from the decays
 1605 of short-lived particles (first of all, *D*-mesons). The Vertex Detector is divided into the barrel and two
 1606 end-cap parts (Fig. 4.6). Two different versions of the VD design are discussed: 1) five layers based
 1607 on double side silicon detectors (DSSDs) and 2) three inner layers based on Monolithic Active Pixel
 1608 Sensors (MAPS) and two outer layers based on DSSDs. The VD Barrel consists of five layers based

1609 on double side silicon detectors (approximately 4.2 m^2). The end-cap regions consist of five disks each
 1610 (approximately 7 m^2). The VD Barrel covers a radius $96 - 500 \text{ mm}$ (Fig. 4.7). All five cylindrical layers
 1611 are set with rectangular two-coordinate silicon strip detectors and give information on the coordinates
 1612 of the tracks (r, ϕ, z) (which makes it possible to measure a point in each layer). The end-cap regions
 1613 detect particles in the radial region between 96 mm and 500 mm . Each of the five disks is set with a
 1614 DSSD with concentric (r) strips and radial (ϕ) strips. The VD has a length of about 1.1 m and covers
 1615 the region of pseudo-rapidity up to $|\eta| < 2.0$. Each DSSD has a $300\text{-}\mu\text{m}$ thickness and a strip pitch in
 1616 the range from $95 \mu\text{m}$ to $281.5 \mu\text{m}$. The DSSDs are assembled into detector modules by two detectors
 1617 per module, forming 18-cm long strips. The detectors and the front-end electronics boards (FEE-PCB)
 1618 connected via low-mass polyimide microcables and assembled on low-mass mechanical supports with a
 1619 cooling system.

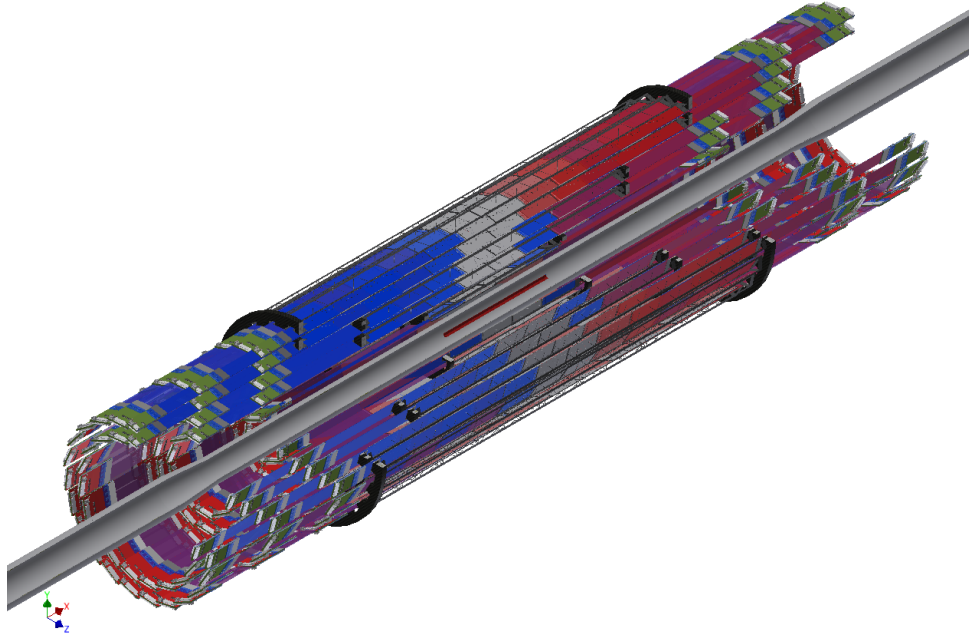


Figure 4.6: General layout of the SPD Vertex Detector.

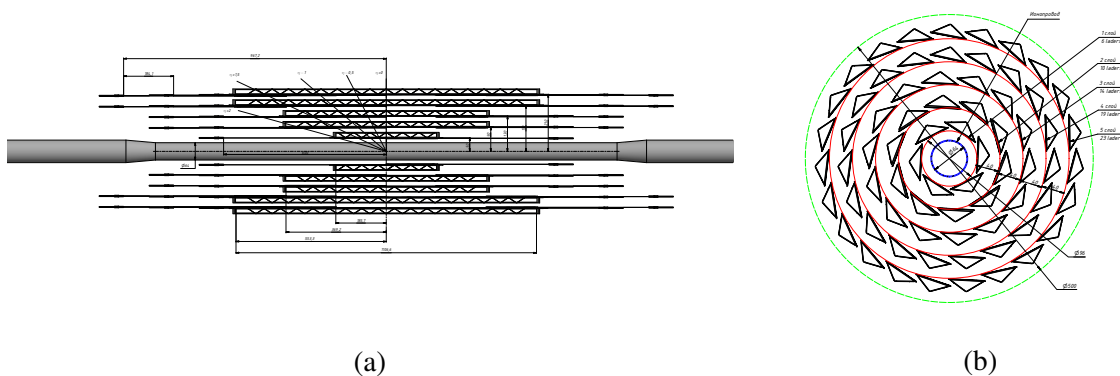


Figure 4.7: Longitudinal (a) and transversal (b) cross-sections of the barrel part of the Vertex Detector.

1620 From the general conditions of the SPD setup the VD performance requirements are i) geometry close to
 1621 4π ; ii) track reconstruction efficiency for muons greater than 99% at $p \leq 13 \text{ GeV}/c$ (for $0 \leq |\eta| \leq 2.5$); iii)
 1622 low material budget of less than $2X_0$ per layer; iv) coordinates resolutions for vertexing: $\sigma_{r,\phi} < 50 \mu\text{m}$,
 1623 $\sigma_z < 100 \mu\text{m}$. The lifetime of the Vertex Detector is required to be not less than 10 years of NICA

1624 running.

Table 4.3: Relevant numbers for the barrel VD.

Parameter	Layer 1	Layer 2	Layer 3	Layer 4	Layer 5	Total
N_{DSSD}/module	2	2	2	2	2	
$N_{\text{modules}}/\text{ladder}$	2	4	4	6	6	
$N_{\text{ladders}}/\text{layer}$	6	10	14	19	23	72
N_{DSSD}/layer	24	80	112	228	276	720
$N_{\text{chip}}/\text{module}$	10	10	10	10	10	
$N_{\text{chip}}/\text{layer}$	120	400	560	1140	1380	3600
$N_{\text{channel}}/\text{layer}$	15360	51200	71680	145920	176640	460800

1625 4.2 Double-sided silicon detectors

1626 The concept of the barrel DSSD module is shown in Fig. 4.8. The module consists of two silicon
1627 detectors wire bonded strip to strip for the $p+$ side (to reduce the number of readout channels), glued to
1628 the plastic frame and connected with two front-end electronic boards via a low-mass polyamide cable.

1629 The Silicon Detector is made using a planar double-side technology based on the n-type conductivity
1630 6-inch float-zone Silicon wafers (produced by ZNTC, Zelenograd, Russia). Its size is $63 \times 93 \text{ mm}^2$ and its
1631 thickness is $300 \mu\text{m}$ thickness. The pitch for the $p+$ side is $95 \mu\text{m}$ and for the $n+$ side $281.5 \mu\text{m}$. The
1632 number of strips is 640 and 320 for the $n+$ and $p+$ side, respectively. The stereo angle between the strips
1633 is 90 degrees. **The expected spatial resolution for such a detector topology is $\text{pitch}_{p(n)+}/\sqrt{12} = 27.4$**
1634 **(81.26) μm for $r - \phi$ and $r - z$ projections, respectively.** As mentioned before the barrel DSSD module
1635 contains two DSSDs ($p+$ strips wire bonded strip to strip) and has 640 strips at each side.

1636 To bring the front-end electronics out of the tracker volume, two thin polyimide cables with aluminum
1637 traces (for each side of the module) will be used. The cable consists of several layers: signal, perforated
1638 or solid dielectric (polyimide), and a shielding layer. Cable pins were designed for the tape-automated
1639 bonding with the detector and the pitch adapter sides. The maximum cable length is 60 cm, and the total
1640 thickness of all cable layers is less than $0.15\% X_0$.

1641 Since the DSSDs have a DC topology, it is necessary to supply bias voltage to the detector and electrically
1642 decouple the DC current from the ASICs electronics inputs. For this purpose, an integrated RC circuit
1643 (sapphire plates with Si-epitaxial layer Silicon On Insulator (SOI)) Pitch Adapter (PA) will be used for
1644 each side of the module (produced by ZNTC, Zelenograd) designed with different topologies for each
1645 side. After the pitch adapter the detector signal goes to ASIC. Table 4.4 shows a possible ASIC readout
1646 solution. The optimal choice should be done after the ongoing R&D.

1647 4.3 Mechanical layout

1648 The concept of the barrel DSSD ladder is shown in Fig. 4.9. The silicon modules are laying on a carbon
1649 fiber support from center to edge. The detectors are connected with the FFE via thin low-mass cables.
1650 The front-end electronics is located at the edges of the ladder and is placed in the conical caves as shown
1651 in Fig. 4.10 to provide a connection to the voltage supply, DAQ, and the cooling ASIC chips subsystems.

Table 4.4: Possible ASIC readout solution for the Vertex Detector.

ASIC	APV25	VATAGP7.3	n-XYTER	TIGER
Number of channels	128	128	128	64 (128?)
Dynamic range	-40fC – 40fC	-30fC – 30fC	Input current 10nA, polarity + and –	1–50fC
Gain	25mV/fC	20 μ A/fC		10.35mV/fc
Noise	246 e ⁻ +36 e ⁻ /pF	70e ⁻ +12 e ⁻ /pF	900 e ⁻ at 30pF	2000 e ⁻ at 100pF
Peaking time	50ns	50ns/500ns	30ns/280ns	60ns/170ns
Power consumption	1.15mW/ch.	2.18mW/ch.	10mW/ch.	12mW/ch.
ADC	No	No	16fC, 5 bit	10-bit Wilkinson ADC
TDC	No	No		10-bit Wilkinson ADC

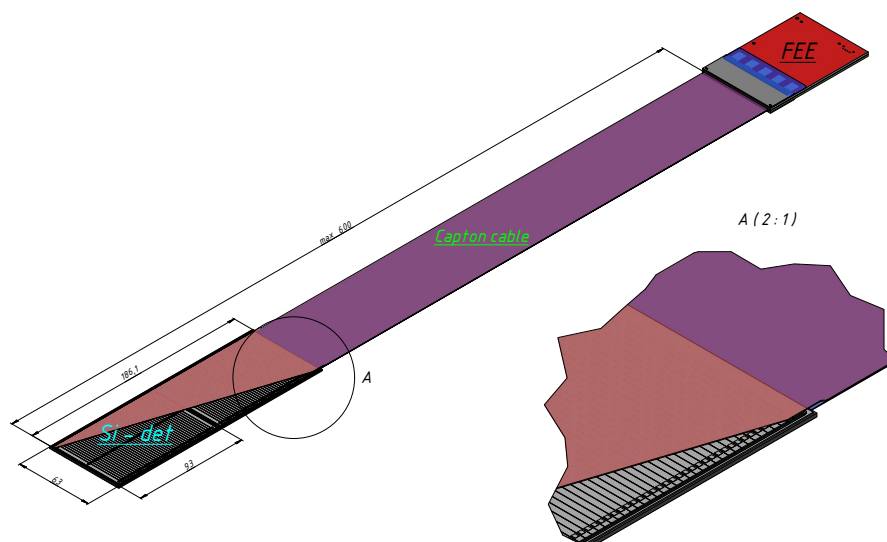


Figure 4.8: Concept of the barrel DSSD module.

1652 4.4 MAPS option

1653 4.5 Cost estimate

1654 5 Straw tracker [T. Enik]

1655 The purpose of a spectrometer is to reconstruct with high efficiency the tracks of primary and secondary
 1656 particles and to measure their momenta with high precision basing on a track curvature in a magnetic
 1657 field. The SPD Straw tracker (ST) with expected spatial resolution of about $150\mu\text{m}$ is planned to be
 1658 built of low-mass straw tubes similar to the ones used in many modern experiments such us NA62 [327],
 1659 COMET [328], SHiP [], Mu2e [329], COMPASS [330, 331], and NA64 [332]. The technology is quite
 1660 well established and a detailed R&D is not needed. The concept of the SPD ST is similar to the ATLAS
 1661 TRT [333? , 334] and PANDA [335] straw trackers.

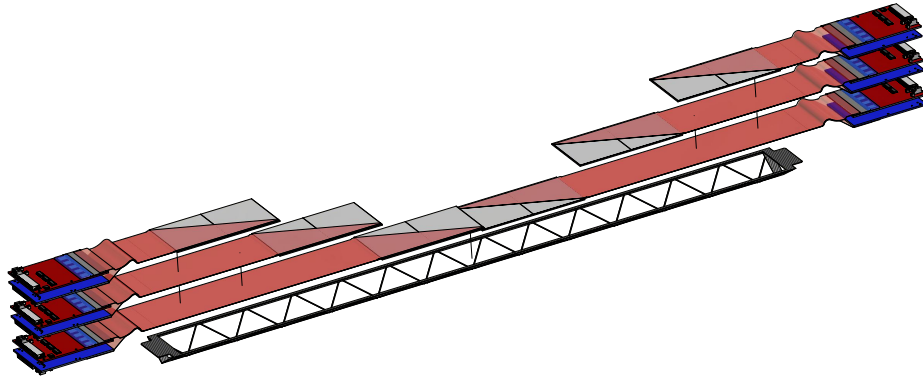


Figure 4.9: Conceptual layout of the barrel ladder.

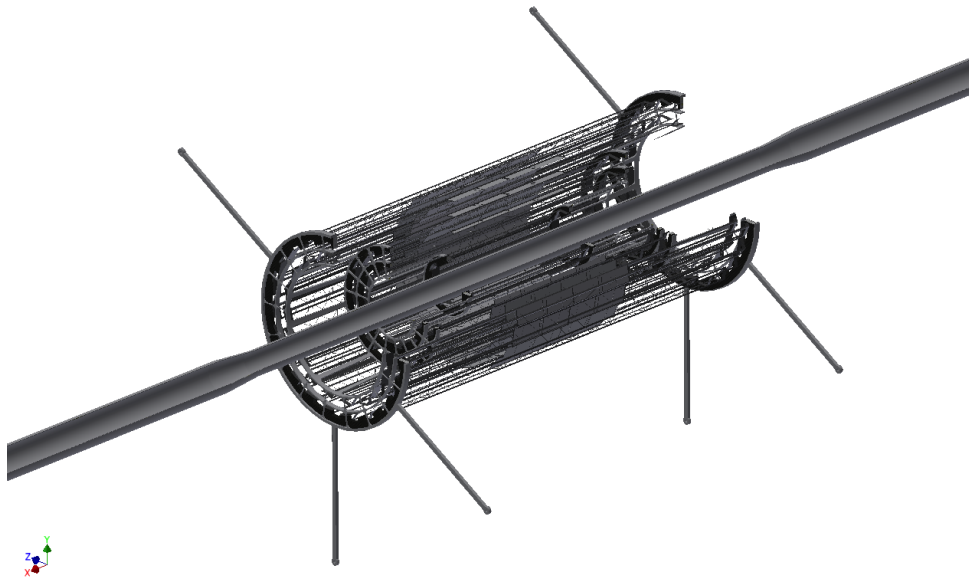


Figure 4.10: Concept of the VD mechanical support structure with conical caves for FEE.

1662 5.1 Straw technology

1663 Straw diameter for SPD ST is chosen to be 10 mm. Straws for SPD prototype are based on the same
1664 technology and mylar type like for the NA62 [336]. The straw tubes are manufactured from 36 μm thin
1665 PET foil, coated on one side with two thin metal layers (0.05 μm of Cu and 0.02 μm of Au) to provide
1666 electrical conductivity on the cathode and to improve the straw tube gas impermeability. NA62[12] has
1667 demonstrated that these straws can be operated in vacuum. A leak rate of about 7 mbar/min for the full

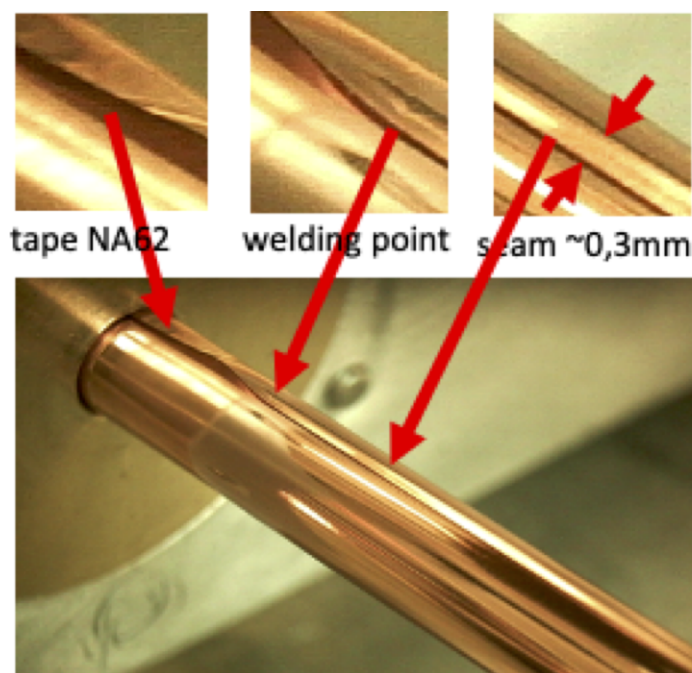


Figure 4.11: Individual straw tube of the SPD ST.

1668 detector (7168 straws) was measured [130]. A few straws are used for dedicated mechanical tests. They
 1669 are cut in 20 segments of about 25 cm length and tested under overpressure until the breaking point. The
 1670 other straws are cut to 5.3 m and the cut ends are stored for further analysis.. The breaking pressure is
 1671 9 bar on average and no sample broke under 8.5 bar. The quality control procedure is the same as for
 1672 NA62 straws. During the ultrasonic welding process the seam quality is verified by a digital microscope
 1673 (recorded to file for each straw). The seam quality is checked in real-time by the operator. Of the 50 tubes
 1674 produced so far, all had a good seam. Post-fabrication, several measurements and tests are performed.
 1675 The seam width and straw inner diameter are measured by an optical method. The cathode electrical
 1676 DC resistance is measured. The elongation and breaking force are both measured on the test samples
 1677 (cut straw ends). The straws undergo a long-term overpressure test with temporary end-plugs glued into
 1678 both ends of each straw. An overpressure test to $\Delta P \approx 2$ bar is performed for a period of about 1 h.
 1679 Subsequently, the straw is subjected to a long term overpressure test at $\Delta P \approx 2$ bar for a period of at least
 1680 30 days. Gas leak estimation is obtained by measuring the loss of pressure over time. The local straw
 1681 deformation is measured under an applied weight of 300 g, and the pressure is derived from the calibrated
 1682 relation between loss of pressure and deformation. Design of an individual straw tube is shown in Fig.
 1683 4.11.

1684 5.2 General layout of the ST

1685 The mechanical construction of the SPD Straw Tracker is based on engineering solutions which were
 1686 already efficiently used in ATLAS and PANDA experiments. The ST consists of three parts: a barrel
 1687 part and two end-caps. The barrel part has the external diameter of 850 mm and the internal hole with
 1688 diameter of 400 mm. The barrel part is divided into two parts along the beam axis. Azimuthally the
 1689 barrel part is subdivided into 8 modules with 24(?) layers of straw tubes.

1690 Each module is concluded into the 400- μ m carbon fiber capsule. The capsule provides also the posi-
 1691 tioning of individual straw tubes with 50 μ m accuracy. The side and the ends of the cylinder capsule
 1692 have 5-mm holes where straw end plugs are supposed to be fixed (Fig.). An FE electronic board on
 1693 one side of an edging side is used as a cover for generating a closed gas volume (of a working gas) for

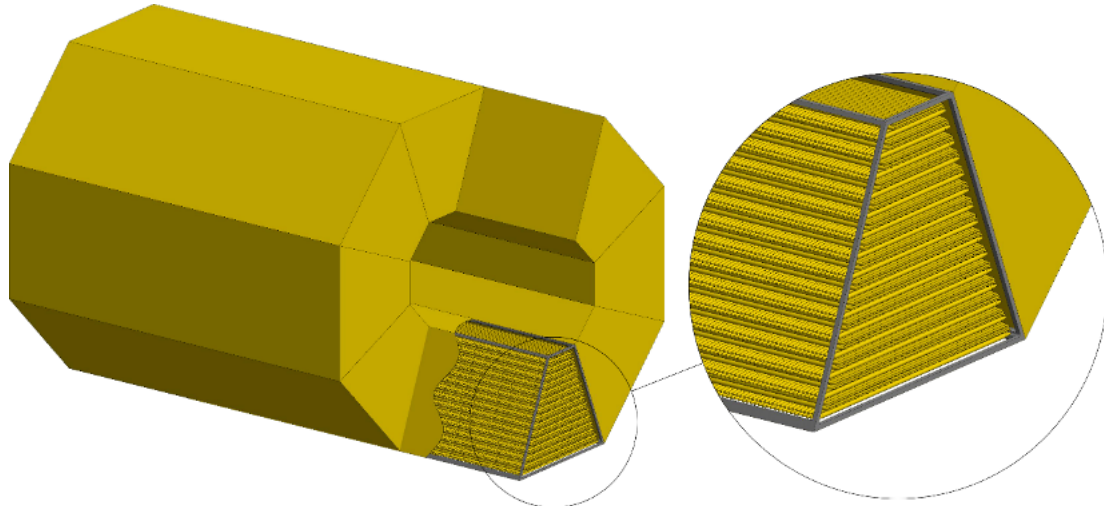


Figure 4.12: Layout of the barrel part of the ST.

1694 straws located along the beam line (NA62). As an option, it is also possible to install an FE electronic
 1695 board from the opposite side to get additional coordinates along the straw. (Pic.4.Mu2e). There are also
 1696 FE electronic boards for straw located along one lateral side of a capsule which are perpendicular to
 1697 the beam line. To achieve the rigidity of the construction is possible due to the low overpressure of gas
 1698 inside the detector [see PANDA] and straw fixation inside a closed volume. The anode wires positioning
 1699 accuracy is achieved by their fixation in the carbon fiber covers [see ATLAS]. The capsule provides also
 1700 thermostabilization of the gas mixture inside straws and protection of the straw surface from humidity.
 1701 It is also minimize the influence of an oscillating humidity quantity on a straw material. Figure 4.12
 1702 presents the layout of the barrel part of the Straw Tracker.

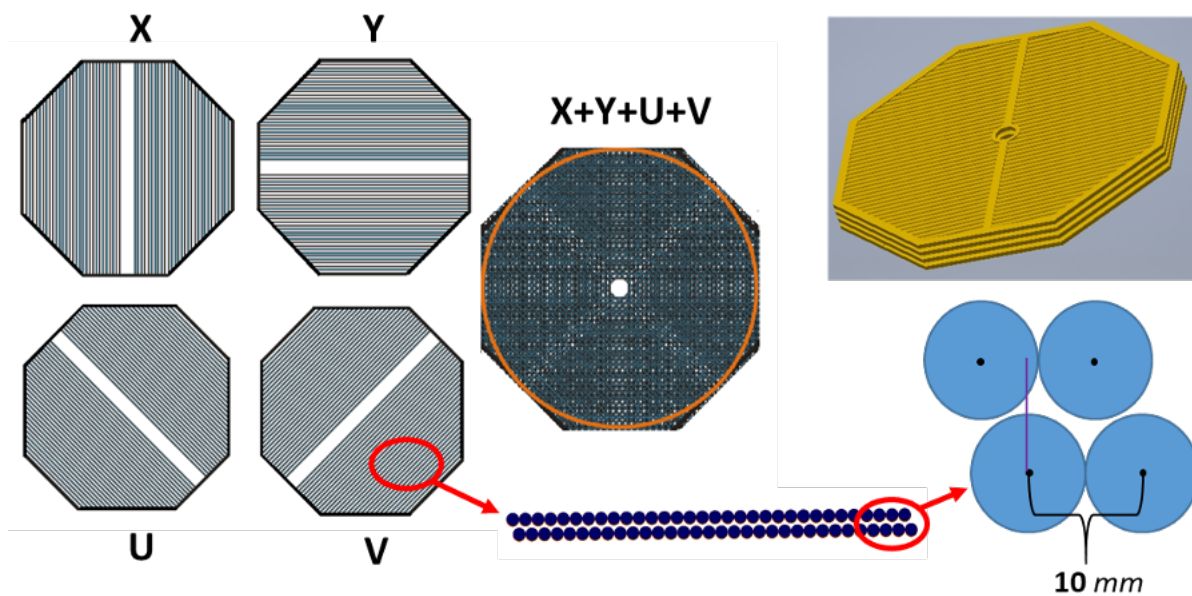


Figure 4.13: Layout of the end-cup part of the ST.

1703 Each capsule contains 30 double layers of straw with parallel (~ 1500 channels) and perpendicular
 1704 (~ 6000 channels) orientation in respect to the beam axis. The total number of electronic channels per
 1705 capsule is about 7500, so, the the total number of channels in the barrel part of the ST is 60 000.

1706 The entire construction is packed into the cylindric carbon fiber frame which consists of two individual
1707 semicylinders. Such a design provides a possibility to assemble and disassemble the ST in the presence
1708 of the beam pipe.

1709 Each end-cap part of the ST has 3 modules along the beam axis. Each module consists of 4 identical
1710 hexadecimal cameras (for measurement of the 4 coordinates: X, Y, U and V). In construction, the cameras
1711 are divided into halves. Each module has the technological hole $d=160$ mm for the beam pipe. The
1712 mechanical support is provided by the carbon fiber frames. The total amount of channels of electronics
1713 in both end-cups is 7200. The layout of the end-cup part of the ST is shown in Fig. 4.13.

1714 **5.3 Front-end electronics**

1715 The Straw Tracker is designed for precise measurements. It requires excellent spacial, angular and timing
1716 resolution to meet physics goals.

1717 Requirements for the straw readout electronics are:

- 1718 – to measure energy deposit (dE/dx) and time;
- 1719 – time resolution better than 1 ns;
- 1720 – low threshold to identify a charge from primary electron-ion clusters;
- 1721 – dynamic range about 1000;
- 1722 – low power consumption to reduce heating.

1723 Two options of electronics are under consideration now. The first one is the front-end electronics de-
1724 signed for NA64 experiment [11]. It is a 32-channel amplifier-discriminator board based on AST-1-1
1725 chip, developed by the Institute of Nuclear Problems of the Belarusian state University. The ampli-
1726 fier sensitivity is $K=100$ mV/ μ A (20 mV/fC). The discriminator threshold is adjustable in the range
1727 (2÷20) fC. The delay of LVDS output signal is 6 ns. The amplifier has an ion tail compensation (BLR).
1728 The LVDS output signals sent to 64-channel time-to-digital converters (TDC).

1729 The second option is to take the front-end electronics designed for DUNA experiment [], which is based
1730 on 64 channel VMM3 a custom Application Specific Integrated Circuit (ASIC), developed by BNL for
1731 the LHC experiments at CERN.

1732 A low power consumption and a low per-channel cost (about 0.9 \$/ch) of the chip are valuable futures for
1733 a compact multichannel detector readout. Each channel has ADC and TDC circuits. Fast serial outputs
1734 are used for readout. Each of the 64 ASIC channels is highly configurable and combines a preamplifier
1735 shaping circuit with an ADC to allow independent digitization of triggered input signals. These digitized
1736 signals can be output with four different data readout options, which provides flexibility to accommo-
1737 date different detector requirements and data rates. Each input channel has an individual preamplifier
1738 and dedicated digitizing logic. Each channel can be configured to accommodate a variety of input sig-
1739 nal sizes, polarity and capacitance. The preamplifier shaping circuit can be configured to use one of
1740 four different peaking times (25, 50, 100, and 200 ns) and eight gain settings (0.5, 1, 3, 4.5, 6, 9, 12,
1741 16 mV/fC). A channel-specific discriminator triggers on input signals above a configurable threshold to
1742 initiate digitization of the amplified pulse with a 10-bit Analogue to Digital Converter (ADC). Discrim-
1743 inator thresholds are adjusted by a global 10-bit Digital to Analogue Converter (DAC) with additional
1744 channel-specific 5-bit trimming DACs. These features allow the VMM3 to satisfy the SPD TR require-
1745 ment of measuring the collected charge and signal time in each channel. An equivalent noise charge of

1746 better than $1000e^-$ can be achieved with input capacitance less than 100 pF. On the basis of this perfor-
 1747 mance, it is reasonable to expect that VMM3 can meet the SPD TR requirement of low charge threshold
 1748 for the straw tube gain greater than $G = 10^4$ and the input capacitance less than 100 pF.

1749 It was shown that for 6 pF input capacitance and input charge greater than 1 fC the time resolution
 1750 better than 1 ns was obtained and a much better time resolution can be achieved for higher input signal
 1751 amplitudes. This suggests that VMM3 can satisfy the SPD TR requirements for the time resolution with
 1752 sufficiently high gain and appropriate input capacitance. The channel thresholds are individually adjusted
 1753 by a global 10-bit Digital to Analogue Converter (DAC) and an individual channel 5-bit trimming DAC.
 1754 This suggests that the required low charge threshold can be achieved.

1755 **5.4 Cost estimate**

1756 2M\$

1757 **6 Electromagnetic calorimeter [O. Gavrishuk]**

1758 The calorimeter should meet the criteria imposed by the physical goals of the SPD experiment of different
 1759 nature and importance. The most important criteria arise from physical requirements on accuracies of
 1760 measurement of energies, trajectories, and timings of photons and electrons. Technological possibilities
 1761 of modern experimental physics should be taken into account when choosing the calorimeter setup. Price
 1762 factors should also be considered to ensure the feasibility of the project. High multiplicity of secondary
 1763 particles leads to a requirement of high segmentation and dense absorber medium with small Molière
 1764 radius. It is needed in order to have sufficient spacial resolution and the ability to separate overlapping
 1765 showers. The transverse size of calorimeter cell should be of the order of Molière radius. A reliable
 1766 reconstruction of photons and neutral pions is possible only for small shower overlaps. Occupancy
 1767 should not exceed 5%, so that it is possible to determine photon reconstruction efficiency with high
 1768 precision.

1769 The SPD experiment imposes the following requirements on the calorimeter characteristics:

- 1770 1. reconstruction of photons and electrons in the energy range from 50 MeV to 10 GeV;
- 1771 2. energy resolution for the above-mentioned particles: $\sim 5\%/\sqrt{E}[\text{GeV}]$;
- 1772 3. good separation of two-particle showers;
- 1773 4. operation in the magnetic field;
- 1774 5. long-term stability: 2–3% in a six month period of data taking.

1775 The energy range requirement follows from the kinematic range of secondary particles, which are pro-
 1776 duced in collision of protons with energy up to 27 GeV and emitted into 4π sr. Good energy resolution is
 1777 required for identification and quantitative measurement of energies of single photons and neutral pions.
 1778 Good two-particle separation is needed to separate photon showers from π^0 decay in order to suppress
 1779 background events in measurements with prompt photons. Long-term stability is necessary for polariza-
 1780 tion measurements featuring π^0 reconstruction in the calorimeter, especially in the end-caps. Calorimeter
 1781 instability may result in false asymmetry values. While it is essential to meet the physics requirements
 1782 imposed on the calorimeter design, one should also take into account the cost estimate and technical
 1783 feasibility when choosing its granularity, as larger number of cells leads to larger costs of manufacturing
 1784 technology and readout electronics.

1785 6.1 Design of the calorimeter module

1786 The initial version of the module, which was made for testing purposes, consisted of alternating layers
 1787 of polystyrene scintillator and lead with thickness of 1.5 mm and 0.3 mm respectively. The selected
 1788 number of layers is 220, setting the number of radiation lengths to $12.6X_0$. The lead plates are intended
 1789 to absorb particle energy and develop the electromagnetic shower, whereas scintillator plates produce
 1790 an amount of light proportional to energy of particles. The properties of absorber and scintillator define
 1791 Molière radius, which is equal to 3.5 cm for the selected structure. Energy resolution for 1 GeV photons
 1792 is assumed to depend on the calorimeter sampling fraction and is expected to be 4.15%. The test results
 1793 of the present work are given for this particular design of the module.

1794 Scintillator plates are made of polystyrene beads with added luminophore admixture of 1.5% p-Terphenyl
 1795 and 0.05% POPOP ($C_{24}H_{16}N_2O_2$) [337]. It has scintillation time of about 2.5 ns and light output of
 1796 60% of anthracene, which are good results. The radiation hardness of the scintillator is sufficient for
 1797 radiation doses up to about 10 Mrad, which is important for operating the calorimeter in radiation field
 1798 of secondary particles in the vicinity of the interaction point.

1799 The luminophore admixtures re-emit the energy of excitations in polystyrene in the form of visible light.
 1800 The first admixture (p-Terphenyl) emits light with the wavelength of maximum emission at 340 nm. This
 1801 light is absorbed by the second admixture (POPOP) and is re-emitted into a spectrum with the wavelength
 1802 of maximum emission of 420 nm, which is seen as a light blue glow.

1803 Light from scintillator plates is gathered using wavelength shifting fibers (WLS) [338]. Fibers of type
 1804 Y-11(200), manufactured by KURARAY, are used. The fibers absorb light from POPOP and re-emit it
 1805 into a spectrum with the wavelength of maximum emission of 490 nm. 36 WLS fibers go along each
 1806 cell, gather in one bundle and transmit light to one multi-pixel photodiode (multi-pixel photon counter, or
 1807 MPPC) of size $6 \times 6 \text{ mm}^2$. In this prototype, counters of types S13160-6025, S13160-6050, S14160-6050
 1808 and FC-6035 [339] are used.

1809 The size of the cell for cosmic ray testing with the purpose of estimating signals from MIP was chosen
 1810 to be $55 \times 55 \text{ mm}^2$. It consists of 220 layers of scintillator and lead with widths of 1.5 mm and 0.3 mm
 1811 respectively.

1812 The module consists of 4 cells with cross section of $55 \times 55 \text{ mm}^2$, combined into one tower with cross
 1813 section of $110 \times 110 \text{ mm}^2$ and length of 440 mm. 9 modules of the calorimeter, each consisting of 4 cells,
 1814 were manufactured for testing at experimental stands in VBLHEP and outside. Four of them were tested
 1815 on cosmic rays. Test results are shown in Section 6.5.

1816 In the photo (Fig.4.14) a module of trapezoidal shape is shown, which is obtained after milling a rect-
 1817 angular parallelepiped at 2 degrees angle. The cell size of $40 \times 40 \text{ mm}^2$ at the front face and 55×55
 1818 mm^2 at the back face allows to implement projective geometry (if necessary) in the SPD electromagnetic
 1819 calorimeter.

1820 6.2 Multi-pixel photodiodes

1821 All of the MPPC that are used in this prototype have the same size of $6 \times 6 \text{ mm}^2$, but have different
 1822 dynamic and time characteristics. The S13160-6025 series has the best response speed, low capacitance
 1823 and large number of pixels, but the largest temperature coefficient of $K_T \sim 0.054 \text{ V}/^\circ\text{C}$. Temperature
 1824 coefficient shows linear dependence of breakdown voltage on temperature and leads to change in signal
 1825 amplification of several per cent per degree. To achieve calorimeter stability of about 2%, one needs to
 1826 ensure the stability of the surrounding environment, or use the breakdown voltage compensation scheme
 1827 $U_{OP} = U_{BR} + \Delta U - K_T \times \Delta T$, where U_{OP} and U_{BR} are the operation and the breakdown voltages, respec-
 1828 tively, ΔU is a voltage bias and ΔT is a deviation of the current temperature from the nominal one, e.g.

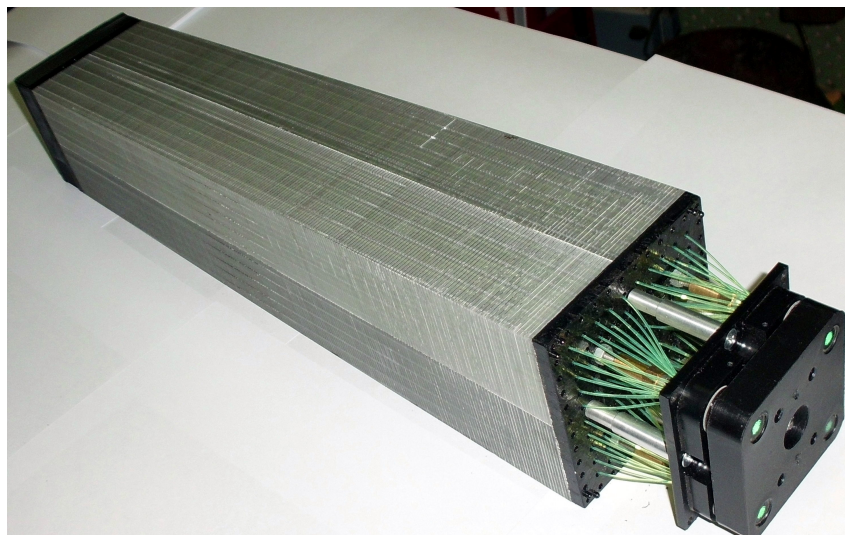


Figure 4.14: Photo of a single module, consisting of 4 cells with 220 layers of scintillator and absorber with thickness of 1.5 mm and 0.3 mm respectively. 4 bundles of fibers for guiding the light to the multi-pixel photon counters (MPPC) can be seen.

1829 20 °C.

1830 The S14160-6050 series has high photo detector efficiency, but fewer pixels, which is worse in terms
 1831 of dynamic range. This series has a small temperature coefficient. An optimal solution would be to
 1832 manufacture a similar photodiode series, but with smaller pixel size of 15 - 20 μm , which would make
 1833 them more suitable for a calorimeter.

1834 **6.3 MPPC readout and High Voltage control**

1835 Four MPPC are surface mounted on a circuit board, as shown in Fig.4.15. A thermistor is also installed
 1836 to measure the photodiode temperature. The circuit board is connected to a module such that the photodi-
 1837 odes are placed at the positions of fiber bundles. There is no optical contact between the photodiode and
 1838 WLS, instead there is an air gap of about 0.1 mm. Optical grease is not used in order to avoid instability
 1839 in the conditions of light guiding. A light insulating basket made of black plastic is installed on top of
 1840 the circuit board.

1841 The MPPC are connected to the amplifier board (Fig.4.16) using 17-pair flat twisted-pair cable of length
 1842 1 m. 5 pairs of wires transmit signals to the amplifiers[340]. Two wires are used to send base voltage
 1843 of ~ 40 V and connect the thermistor. Channel voltages are transmitted via signal wires as a small bias
 1844 from 0 to 5 V. This way, bias voltage can be precisely set in a small range, but with 10-bit precision (i.e.
 1845 about 5 mV).

1846 Voltage control is implemented on a software level, taking into account the temperature from thermistor
 1847 installed on the circuit board. This allows operation without special equipment for temperature stabiliza-
 1848 tion. Signal stability of the order of 0.1-0.2% is achieved during measurement over an extended period
 1849 of time.

1850 **6.4 Readout electronics**

1851 Readout electronics consist of analog-to-digital converter ADC-64 [341] (Fig.4.16(a)). ADC receives
 1852 continuous-time samples of input signal with a fixed frequency and provides full digital representation
 1853 of signals in time. Samples are received at a 64 MHz frequency, which corresponds to the time period
 1854 of 15.625 ns. Each sample is measured with a 12-bit precision. At present time, there is ADC-64-Ecal

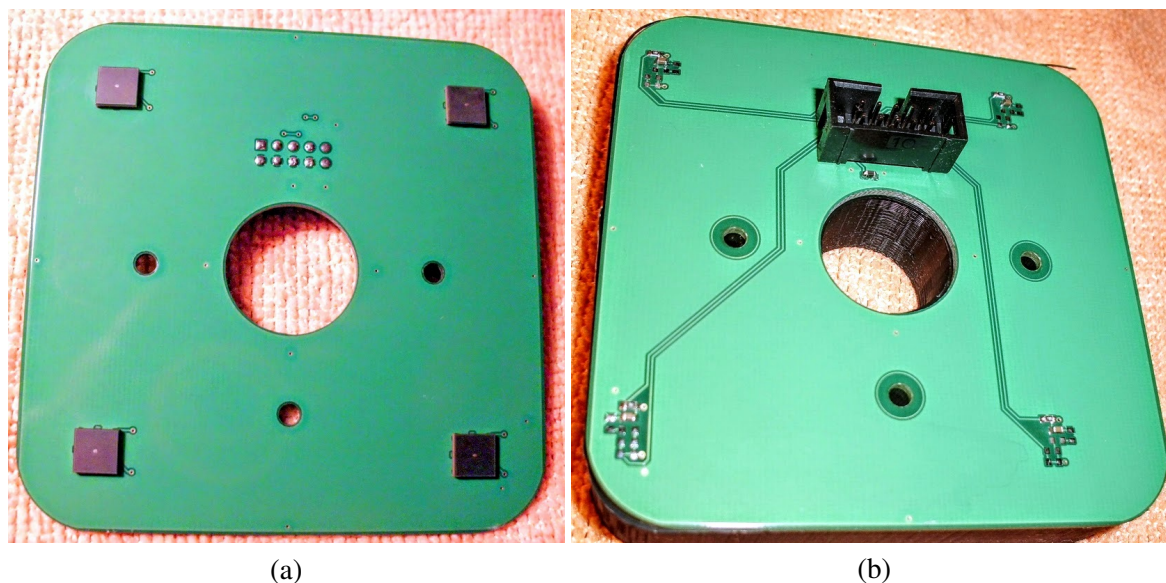


Figure 4.15: Printed circuit board with 4 MPPC diodes: front (a) and back (b) sides.

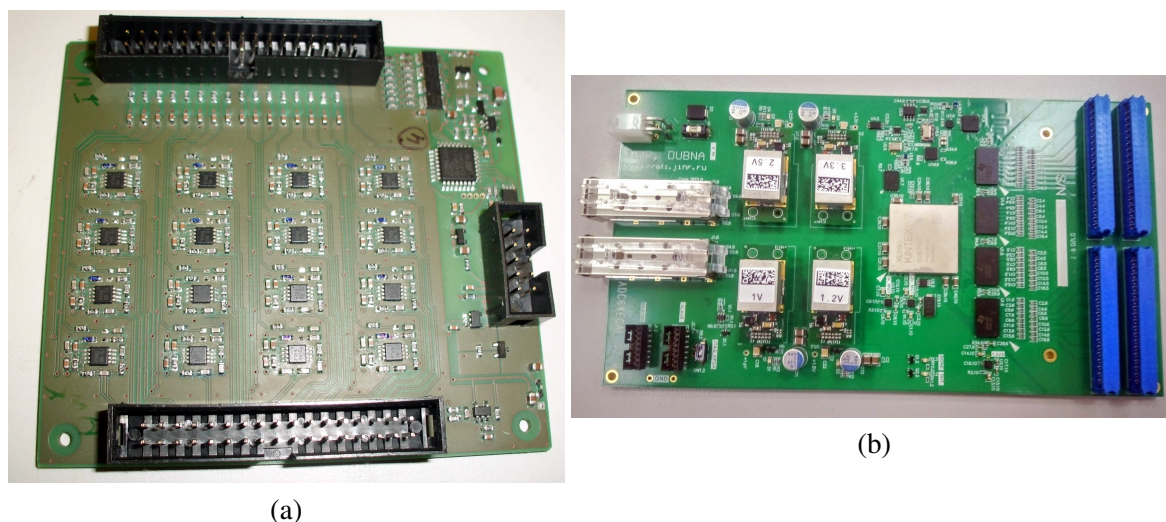


Figure 4.16: (a) The 16-channel amplifier board is used to control MPPC High Voltage and transmit signals to ADC-64. Power consumption is about 16 mW per 16 channels. (b) 64-channel ADC-64-Ecal, specifically designed for calorimeter operation in magnetic field. Power consumption is about 120 Watt per one board (64 channels).

1855 modification, which improves the precision to 14-bit and significantly extends the range of the measured
 1856 amplitudes. The new ADC modification also allows for operation in strong magnetic fields, which is
 1857 necessary for experiments at NICA accelerator complex.

1858 An Ethernet connector for data transfer can be seen in Fig.4.16(b), as well as a coaxial input for readout
 1859 synchronization, which serves as a trigger. The ADC can also operate in streamer mode due to dedicated
 1860 firmware. Usage of White Rabbit technology provides sub-nanosecond synchronization accuracy.

1861 6.5 Cosmic ray test results

1862 For testing on cosmic rays, a small setup of 4 (Fig.4.17) modules (each $11 \times 11 \text{ cm}^2$), of total cross
 1863 section $22 \times 22 \text{ cm}^2$, was used. The cells, each $55 \times 55 \text{ mm}^2$, are assembled in 4×4 setup. The modules



Figure 4.17: Photo of the calorimeter test setup, consisting of 4 modules of size $11 \times 11 \text{ cm}^2$, with total cross section of $22 \times 22 \text{ cm}^2$.

1864 are placed vertically, while the direction of registered cosmic rays is determined by trigger counters.
 1865 The counters are multi-pixel photodiodes of type FC6035 and size $6 \times 6 \text{ mm}^2$. All the photodiodes are
 1866 included in a coincidence trigger for ADC. The trigger includes signal from generator, which starts the
 1867 LEDs for control, calibration of calorimeter cells using estimates of light yield, and long-term stability
 1868 control. Data acquisition is conducted at ADC using software provided by the developer. During data
 1869 taking period of 5-6 days, statistics of the order of million triggers was obtained.

1870 The setup allows to measure energy depositions and trajectories of cosmic ray particles. Relativistic
 1871 muons with energy above 250 MeV pierce through the calorimeter and form a peak in deposited energy.
 1872 In order to select straight tracks of particles, which pass vertically through one module, only those events
 1873 are selected, where number of hits is equal to 1.

1874 Signals, obtained on cosmic muons, are used for amplitudes alignment and calorimeter energy calibra-
 1875 tion. Only events with exactly one cell hit were selected. The bordering cells have more events with
 1876 smaller amplitudes due to angled tracks. We perform calorimeter calibration using only vertical tracks.
 1877 Each maximum value in terms of ADC units is mapped to corresponding energy deposition. The energy
 1878 scale is determined from Monte-Carlo simulation as the scale factor between energy deposition of an
 1879 electron with 1 GeV energy, and a relativistic muon with energy above 1 GeV, in scintillator plates for
 1880 the given structure. From this proportion we estimate the MIP signal in this calorimeter to be 240 MeV.
 1881 This value, divided by the position of the muon peak maximum, is used as a calibration coefficient for
 1882 each cell. This calibration procedure involving MIP energy deposition is not absolute or conclusive.

1883 Primarily, it aligns the amplification coefficients in each cell to ensure equal response of each cell. The
 1884 measured electron or photon energy can be further revised by reconstructing neutral pions or calibrating
 1885 the calorimeter using electron or photon beams of given energy.

1886 The electromagnetic calorimeter measures electron or photon energy by summing up signals from all 16
 1887 cells. Each cell can only contain a fraction of energy, deposited by the particle in the calorimeter (if the
 1888 particle is not a relativistic muon, or MIP). If the calorimeter is calibrated with a precision of several per
 1889 cent, the total energy weakly depends on the particle angle and resolution increases only by 1.4%.

1890 Energy resolution of the calorimeter for vertical cosmic ray particles is 9.6% (Fig.4.18(a)). This number
 1891 corresponds to energy deposition of 240 MeV. Assuming resolution depends on energy as $E^{-1/2}$, the
 1892 energy resolution at 1 GeV is estimated to be 5%.

1893 Time resolution for calorimeters of such types is about 175 ps for MIP (Fig.4.18(b)) and can be improved
 1894 for high-energy electrons. This can be applied to identify particles in the energy range of 50–1550 MeV.

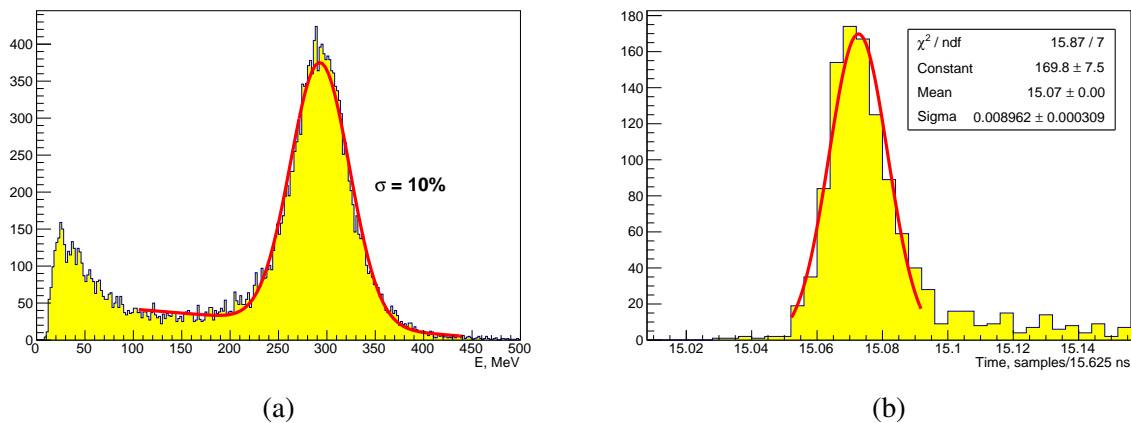


Figure 4.18: (a) Total energy deposition in the calorimeter for MIP obtained by summing up signals from 16 cells while selecting 1-hit events. (b) Time resolution for calorimeter cell #11 is equal to 175 ps.

1895 6.6 Dependence of calorimeter response on the number of photoelectrons

1896 Cosmic ray testing allows to obtain dependences of energy and time resolution on the number of pho-
 1897 toelectrons (NPE), produced during MIP passing through a cell. For each channel, time is calculated
 1898 as zero intersection of the waveform. This method, Constant Fraction Discriminator, is used for deter-
 1899 mining a time value on a constant fraction of pulse leading edge. Energy and time resolution of the
 1900 calorimeter depend on NPE as $1/\sqrt{NPE}$.

1901 Different conditions of light guiding were used in this 4-module calorimeter. These conditions included
 1902 forming of reflective surfaces on edges of WLS, or using the fibers as U-shaped loops. Differences in
 1903 light guiding conditions lead to large variations in NPE in the range between 1000 and 3000 photoelec-
 1904 trons per MIP for different cells. In terms of amount of deposited energy, this corresponds to 4000-12000
 1905 NPE/GeV .

1906 Information on number of photoelectrons for each cell allows to obtain dependence of energy and time
 1907 resolution on NPE . The presented dependences of energy and time resolution are displayed in Fig.4.19
 1908 and show that the limit for large values of NPE is 6.2% and 197 ps for energy and time resolutions
 1909 respectively.

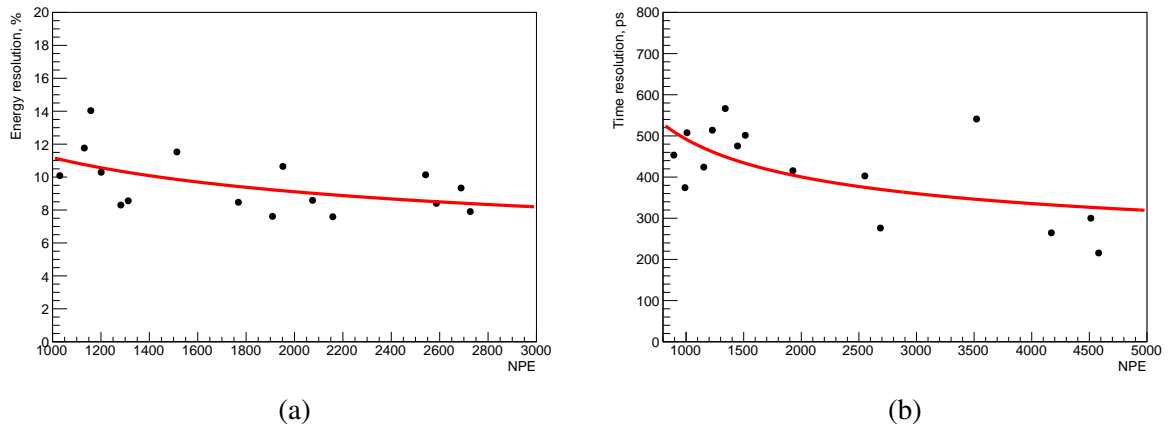


Figure 4.19: Dependence of time (a) and energy (b) resolution for different calorimeter cells on the number of photoelectrons (NPE).

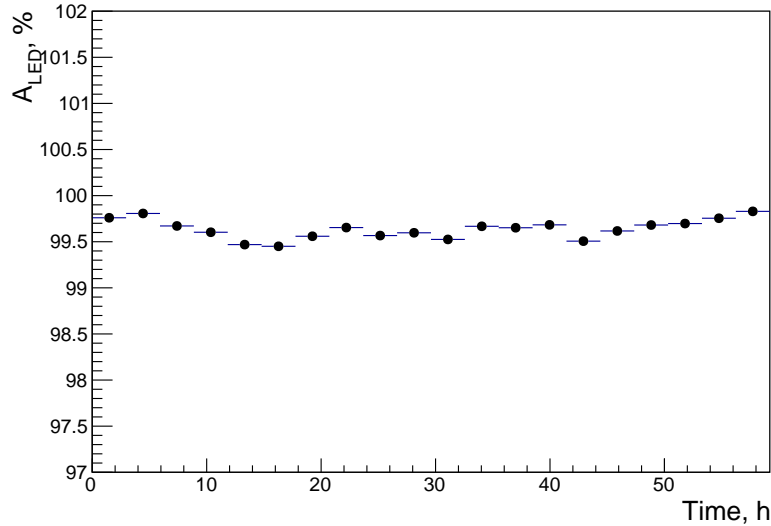


Figure 4.20: Dependence of sum (average value) of signals from calorimeter (in % with respect to the first 5 minutes of measurement period) on the time of measurement (in hours) with temperature-dependent voltage compensation.

1910 6.7 Long-term stability

1911 Temperature dependence of calorimeter stability was investigated using daily temperature variations in
 1912 the range of 18-22 °C. During the measurement of signals from cosmic ray particles over 5 days, signals
 1913 from LEDs of 1 Hz frequency were also measured. Photodiode temperature is constantly monitored using
 1914 high-voltage system. The voltage bias on photodiodes is corrected during temperature measurement
 1915 using a linear dependence: $U_{out} = U_{bias} - k \times (20 - T)$.

1916 Daily temperature variations during the measurement were about 5°C. Temperature coefficient of $k =$
 1917 $0.034 \text{ V}/^\circ\text{C}$ is used for temperature compensation of operating voltage. After compensation, variations in
 1918 signal amplitude are constrained within $\pm 0.4\%$. The plots are normalized to the start of the measurement.
 1919 First 300 signals (5 min) are used to normalize the full measurement period. The calorimeter can operate
 1920 with the stability of $\sim 0.8\%$ if the temperature compensation of operating voltage is maintained, as it can
 1921 be seen from these results and is shown in Fig. 4.20.

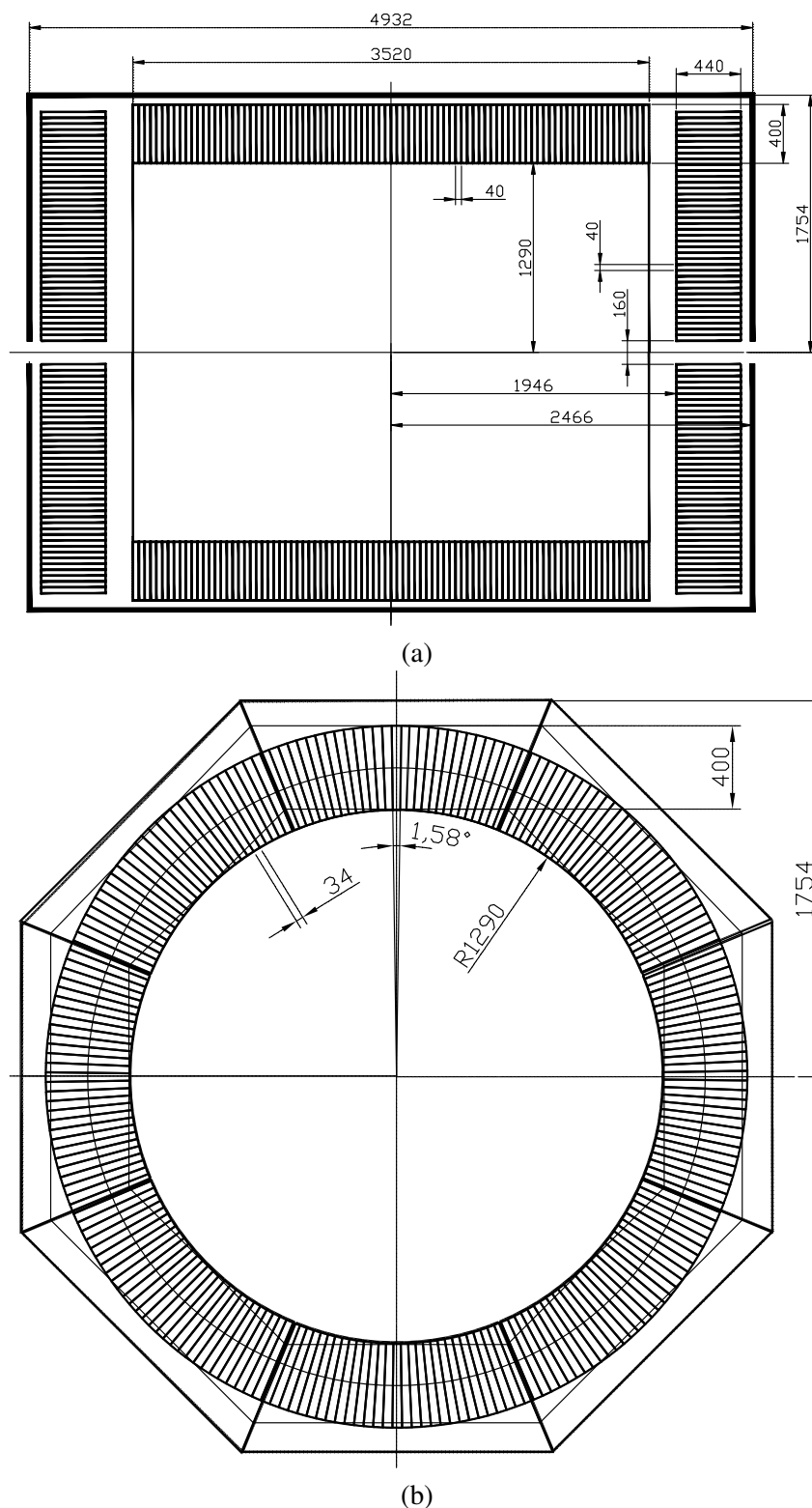


Figure 4.21: (a) Barrel and end-cap parts of the calorimeter. Holes of size $160 \times 160 \text{ mm}^2$ for beam pipe can be seen in the centers of the end-caps. (b) Schematic drawing of a cross section of the barrel part of the calorimeter. It is sectioned into 224 azimuthal sectors (8 sections, 28 cells per section) with vertex angle of 1.58° .

6.8 Overview of the SPD calorimeter

The SPD electromagnetic calorimeter is placed between the Range System and the magnet coils, as shown in Figs.1.2 and ???. It consists of a barrel and two end-caps, covering 4π solid angle. The outer dimensions of the calorimeter are determined by the inner size of the muon system. The thickness of the calorimeter is determined by the required thickness of the active part and size of the readout block, consisting of photodiode and amplifier boards, as well as size of the flexible part of the fibers.

For efficient absorption of electrons and photons with energies up to 10 GeV, calorimeter thickness, which is defined by the number of sampling layers, should be at least 18–20 X_0 in terms of radiation lengths X_0 . For sampling structure of 1.5 mm scintillator and 0.5 mm lead, 200 layers are required for thickness of 18.6 X_0 , which sets the length of the active part to 400 mm. The period of the structure is set to 2 mm in order to avoid optical contact between lead and scintillator, and because of connection technique involving special «Lego» spikes. Flexible parts of the fibers take up 8 cm. Transverse size of calorimeter cell should be of the order of Molière radius of calorimeter medium, which is in turn defined by the scintillator-to-lead sampling ratio. The selected structure has Molière radius of 2.4 cm. Separation efficiency of two photons with energies from 200 MeV to 500 MeV depends on the cell size and reaches a plateau at the cell size of 40 mm, as was determined in MC simulation. Therefore we have selected 40 mm cell granularity for both barrel and end-caps. Cells in the barrel part of the calorimeter have trapezoidal shape in azimuthal direction to minimize gaps between modules. The vertex angle of the trapezoid equals to 1.58° .

A schematic drawing of the calorimeter, which is limited in size by the muon system, is shown in Fig.4.21(a). The limits of the calorimeter zone are shown as a thick line. Holes of size $160 \times 160 \text{ mm}^2$ in the centers of end-caps for the beam pipe are shown.

The inner size of the barrel part is limited by radius of magnetic coils, whereas the outer size is limited by the dimensions of the muon range system. The thickness of the active part is 400 mm, which corresponds to 18.6 X_0 . This corresponds to 200 layers of scintillator and lead of width 1.5 mm and 0.5 mm respectively.

Barrel part of the calorimeter has 19712 cells of trapezoidal shape in azimuthal direction with vertex angle of 1.58° and front face size of 34 mm, and rectangular shape in polar angle direction with size of 40 mm (Fig.4.21(b)). The total weight of the barrel part is 40 tons.

The end-caps, one of which is shown in Fig.4.22, each consist of 4 sectors of 1308 cells per sector. The cell cross section is $40 \times 40 \text{ mm}^2$. There is a hole for beam pipe in the center of each end-cap. The hole has size of $160 \times 160 \text{ mm}^2$, which is equivalent to 16 cells. Each end-cap has 5232 cells. The thickness of the active part of an end-cap cell is 440 mm (Fig.4.21), which corresponds to 20.4 X_0 . The weight of one end-cap is 14 tons. The total weight of two end-caps is therefore 28 tons. In total, there are 10464 cells in both end-caps, each with dimensions of $40 \times 40 \times 440 \text{ mm}^3$.

The total weight of the calorimeter is $68 = 40 + 28$ tons, composed of barrel and two end-caps. The total number of cells of size about $40 \times 40 \text{ mm}^2$ is $30176 = 19712 + 10464$ for barrel and end-caps respectively.

6.9 Cost estimate

The cost of the calorimeter is proportional to the number of channels. Mechanical assembly of a calorimeter cell from scintillator and lead plates costs \$300 per channel. Another expensive element are the wavelength shifting fibers. For a $40 \times 40 \text{ mm}^2$ cell, 9 fibers of total length of 54 m are used. Assuming average price of \$5/m, the price per channel amounts to \$270. The cost of photodiodes depends on the quantity. For purchases of tens of thousands of units, their price is about \$30 per unit. Electronics

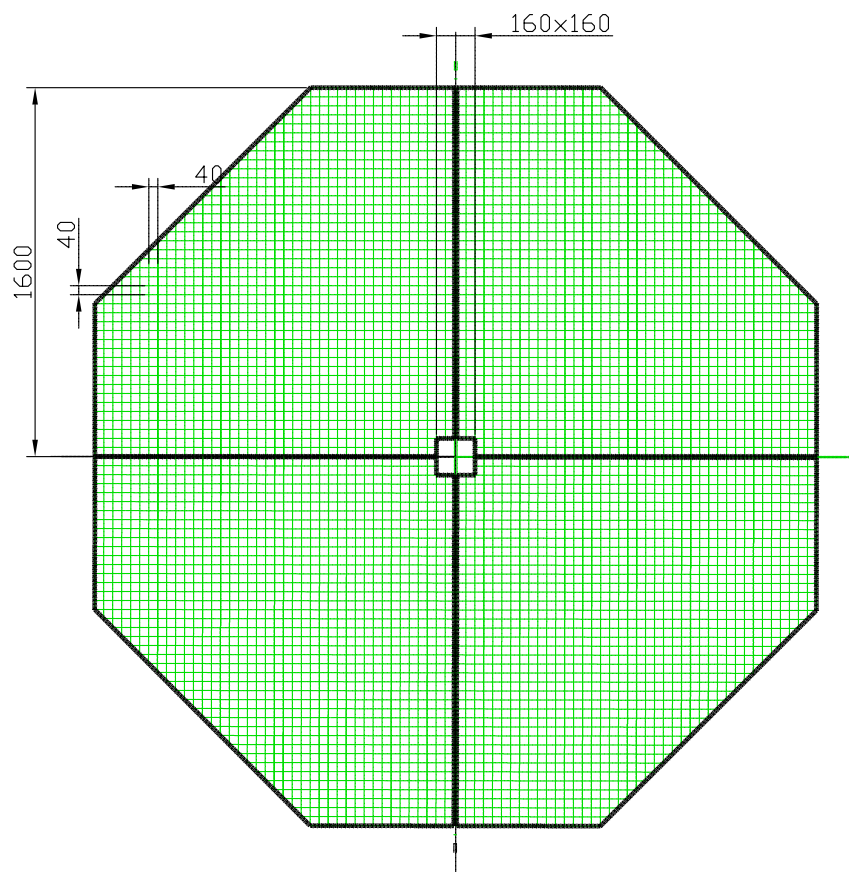


Figure 4.22: The endcap part of the calorimeter consists of 4 sectors, 1308 cells each. In total, there are 5232 cells in one end-cap, and 10464 cells in both end-caps.

Table 4.5: Contributions of separate elements to the cost of the ECAL.

	ECAL cell	WLS	ADC	HV	MPPC	Total
Cost per 1 cell [USD]	300	270	80	20	30	700 USD
Cost for 30.176 cells [MUSD]	9.1	8.1	2.4	0.6	0.9	21.1 MUSD

1966 also contributes significantly to the total cost, especially ADC with price of \$80 per channel. Cost of
 1967 supply and voltage control systems is \$20 per channel. The total cost of a calorimeter cell is about \$700.
 1968 So, the total cost of 30176-cell calorimeter is \$21.1 million.

1969 **7 Range (muon) system [G. Alexeev]**

1970 **7.1 General description**

1971 The Range System of the SPD detector serves for the following purposes: (i) identification of muons
 1972 in presence of a remarkable hadronic background and (ii) estimation of hadronic energy (coarse hadron
 1973 calorimetry). It is important to stress that the system is the only device in the SPD setup, which can
 1974 identify neutrons (by combining its signals with the electromagnetic calorimeter and the inner trackers).
 1975 Muon identification (PID) is performed via muonic pattern recognition and further matching of the track
 1976 segments to the tracks inside the magnets. The precise muon momentum definition is performed by the
 1977 inner trackers in the magnetic field. The Mini Drift Tubes [342, 343] are used in the Range System as
 1978 tracking detectors providing two-coordinate readout (wires and strips running perpendicularly). Such
 1979 readout is mostly needed for the events with high track multiplicity and also for the reconstruction of the

1980 neutron space angle.

1981 As for the design and construction of the present system, we assume to capitalize on the experience
 1982 gained by the JINR group in the development of the PANDA (FAIR, Darmstadt) Muon System [?].
 1983 These two systems (PANDA and SPD), dealing with muons of comparable momentum ranges and solv-
 1984 ing the same PID tasks, should look very similar in their design and instrumentation.

1985 7.2 System layout

1986 The Range System serves as an absorber for hadrons and a ‘filter’ for muons. It also forms the magnet
 1987 yoke. It consists of a Barrel and two End Caps. Each End Cap, in its turn, consists of an End Cap Disk
 1988 and a Plug. The schematic 3D view of the system and its main sizes are shown in Fig.4.23 (a). The
 1989 absorber structure is shown in Fig.4.23 (b). The outer 60-mm Fe layers are used for bolting the modules
 1990 together. The interlayer gaps of 35 mm are taken for reliable mounting of the detecting layers comprising
 1991 the MDTs proper, the strip boards and the front-end electronic boards on them. The 30-mm thickness
 1992 of the main absorber plates is selected as comparable with muon straggling in steel, thus giving the best
 1993 possible muon-to-pion separation, and also providing rather good sampling for hadron calorimetry.

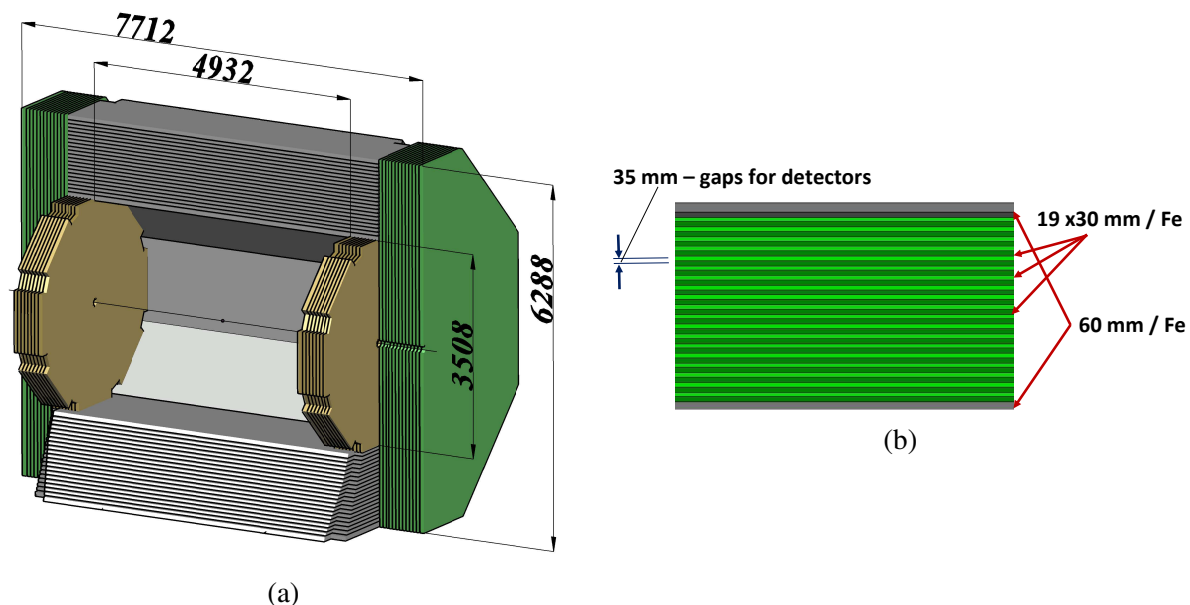


Figure 4.23: 3D view (half cut) of the Range (muon) system: (a) Barrel is shown in grey, End Cap Disks – in green, and End Cap Plugs – in yellow; (b) absorber structure.

1994 The Barrel consists of eight modules, and each End Cap Disk consists of two halves divided vertically.
 1995 Such subdivision of the system (14 pieces in total) is chosen to optimize its further assembly and to
 1996 satisfy the constructional requirements of the SPD experimental hall (cranes capability and floor load).
 1997 The total weight of the system is about 810 tons, including 30 tons of detectors. The total number of
 1998 MDT detectors is about 8000 units. The MDTs are deployed in the following way: along the beam
 1999 direction in the Barrel, and perpendicular to the beam (horizontally) in the End Caps.

2000 The absorption thicknesses of Barrel and End Caps are selected to be equal - to 4 nuclear interaction
 2001 lengths (λ_I) each. It provides uniform muon filtering in all directions. Together with the thickness of the
 2002 electromagnetic calorimeter ($\sim 0.5 \lambda_I$) the total thickness of the SPD setup is about $4.5 \lambda_I$.

2003 7.3 Mini drift tubes detector

2004 The Mini Drift Tubes (MDT) detector was initially developed and produced at JINR for the Muon System
 2005 of the D0 experiment at FNAL [344]. Later on, an MDT-based muon system was also produced for the
 2006 COMPASS experiment at CERN [345]. Developed two-coordinate readout modification of the MDT
 2007 with open cathode geometry and external pickup electrodes was proposed to and accepted by the PANDA
 2008 collaboration at FAIR for the muon system of their experimental setup. This new version of the MDT
 2009 is proposed for the SPD project, as it has all the necessary features – radiation hardness, coordinate
 2010 resolution and accuracy, time resolution, robustness, as well as advanced level of already conducted
 2011 R&D within the PANDA project.

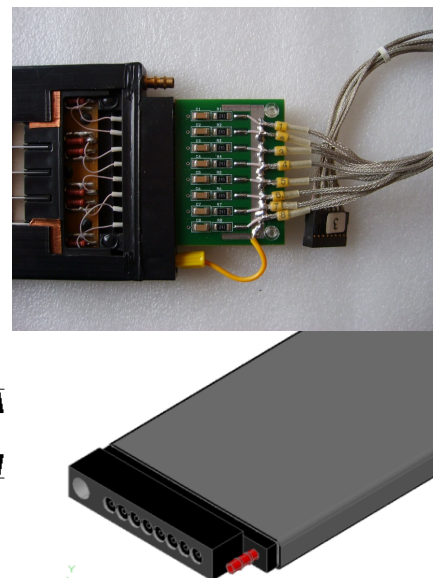
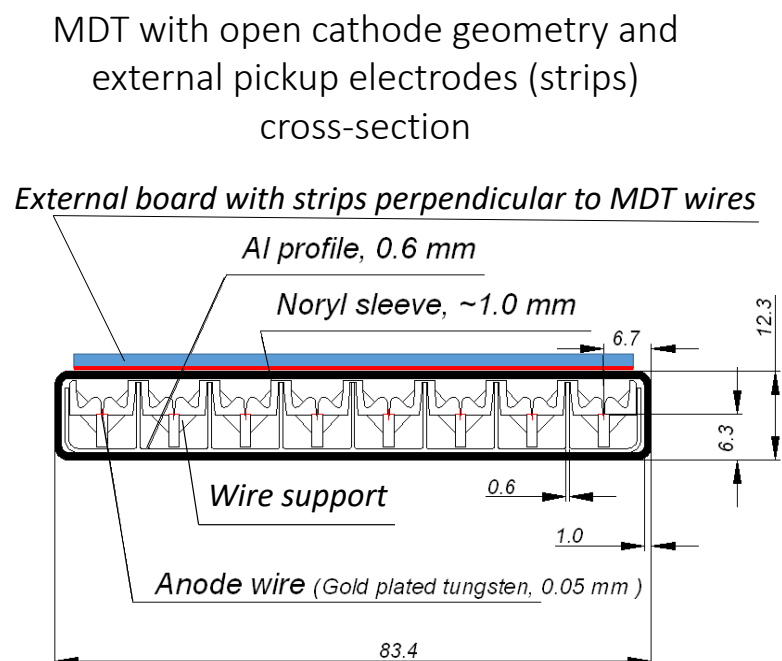


Figure 4.24: Mini Drift Tube with open cathode geometry cross-section (left) and layout (right).

2012 The cross-section and layout of the MDT with open cathode geometry are shown in Fig.4.24. The detec-
 2013 tor consists of a metallic cathode (aluminum extruded comb-like 8-cell profile), anode wires with plastic
 2014 supports, and a Noryl envelope for gas tightness. The comb-like profile of the cathode provides each wire
 2015 with an opening left uncovered to induce wire signals on the external electrodes (strips) perpendicular to
 2016 the wires. The strips are applied to obtain the second coordinate readout. The shape of the induced signal
 2017 repeats the initial one, having the opposite polarity, but the amplitude is about 15% of the wire signal (see
 2018 Fig.4.25). Thus, the strip signal readout requires higher signal amplification and proper electromagnetic
 2019 shielding.

2020 Application of an open cathode leads to the loss of the electric field symmetry in each of the 8 detec-
 2021 tor cells, resulting in lower gas gain for the applied voltage comparing to the standard MDT (cathode
 2022 openings closed with stainless steel lid). The conducted R&D proved that the MDT with open cathode
 2023 geometry easily achieves the parameters of the one with a closed cathode at higher voltages. The compar-
 2024 ative plots of the counting rate, efficiency, and gas gain for both detector types (see Fig.4.26) show
 2025 that the MDT with open cathode geometry repeats the standard MDT performance at a high voltage shift
 2026 of + 100V. The drift time and the amplitude spectra of both detector variants also match, if we set this
 2027 voltage shift between their operating points.

2028 According to the results of the MDT (open cathode geometry) ageing tests, accumulation of a 1 C/cm

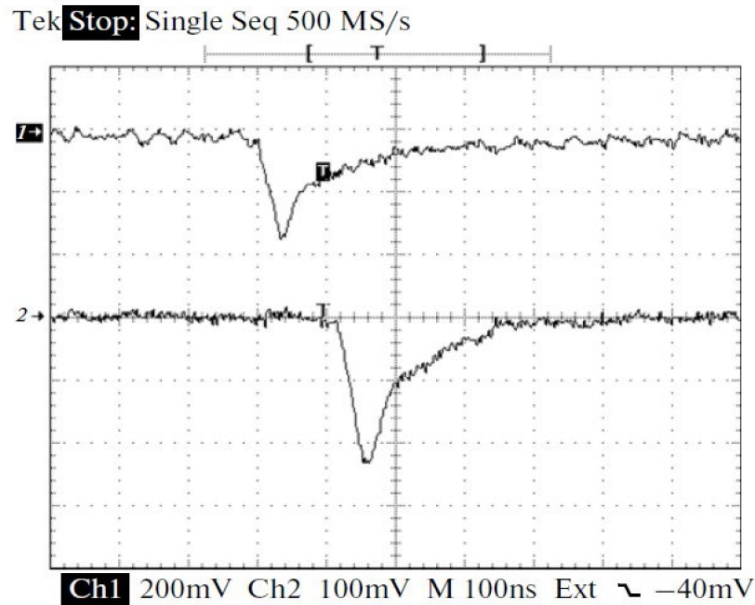


Figure 4.25: Oscillograms of single signals: from the anode wire (1) and the strip (2, inverted); the conversion factors are 60 and 480 mV/ μ A, respectively.

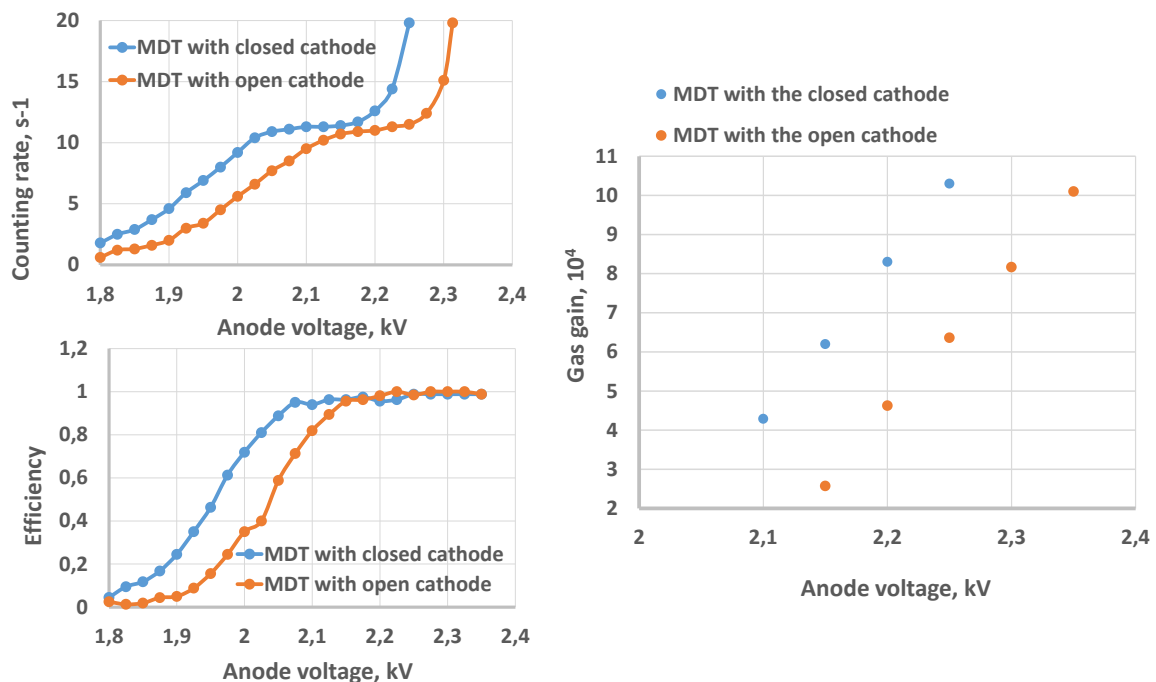


Figure 4.26: Comparative plots of the counting rate, efficiency, and gas gain versus the supply voltage for the MDT with closed and open cathode geometry.

2029 total charge does not produce any significant effect on the detector performance. To monitor the ageing
 2030 effects, measurements of the counting rate curves (Co-60 source) together with oscilloscopic observa-
 2031 tions of the MDT average signals (256 events) for Co-60 and X-rays were made twice a week over the
 2032 whole period of intense irradiation (see Fig.4.27). Later on, this measurement (with X-rays) was con-
 2033 ducted up to 3.5 C/cm of irradiation without any visible degradation of the MDT performance. It should
 2034 ensure stable MDTs performance for the lifetime of the SPD project.

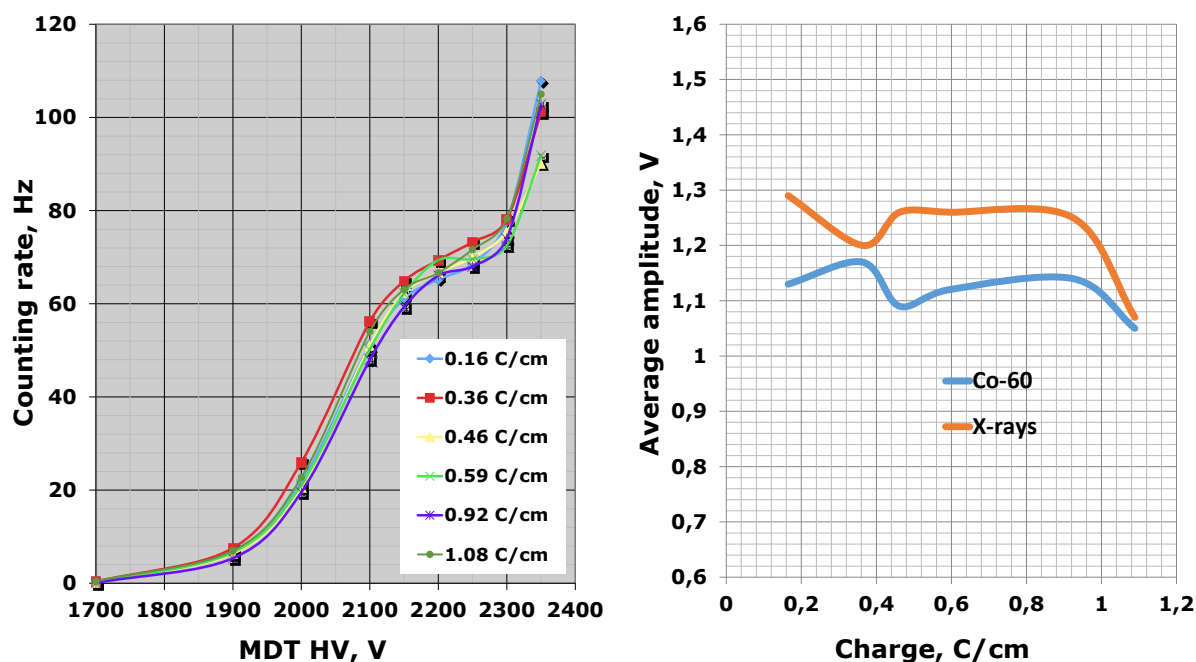


Figure 4.27: Counting rate curves for different accumulated charges (0.16÷1.08 C/cm) (left); average wire signal amplitudes vs accumulated charge for Co-60 and X-ray sources (right).

2035 All R&D studies were made with a gas mixture of 70% Ar + 30% CO₂ at atmospheric pressure, the one
 2036 to be used in the proposed SPD Muon System. It is inflammable, radiation hard and fast enough (150-
 2037 200 ns drift time). The wire pitch in the present design equals 1 cm, and a 3-cm strip width is selected
 2038 for the second coordinate. These spatial parameters provide the Range System with coordinate accuracy
 2039 well enough for identification of muons and give the system the features of a digital hadron calorimeter.

2040 7.4 Front-end electronics

2041 We plan to use the analog front-end electronics (with probable minor modifications) developed for
 2042 the D0/FNAL and COMPASS/CERN experiments and also accepted by PANDA/FAIR. It is based on
 2043 two ASIC chips: 8-channel amplifier Ampl-8.3 [346] and 8-channel comparator/discriminator Disc-8.3
 2044 [347].

2045 The HVS/A-8 card serves for two purposes - as an MDT high voltage distributor and a signal amplifier
 2046 designed to be the first stage of the Barrel and the End Cap Plugs wire signal readout. It is followed by
 2047 Disc-8.3 based discriminating electronics (design in process) to fulfill the readout.

2048 The ADB-32 card (initially designed for D0/FNAL) [348] is used for the End Cap Disks wire readout.
 2049 It amplifies and discriminates the MDT signal, shaping it to the LVDS standard for further treatment by
 2050 the digital front-end electronics.

2051 An A-32 preamplifier card is used to start the strip signal readout in the whole system. It should be
 2052 terminated (similarly to wire readout) by Disc-8.3-based discriminating electronics. In case of the End
 2053 Cap Disks an ADB-32 card will be used for this purpose. The view of the basic FEE cards is shown in
 2054 Fig.4.28.

2055 Totally, the Range System has 106000 readout channels (65000 of which are wires and 41000 strips).

2056 After having been shaped to the LVDS standard, the signals from the analog electronics go to the digital
 2057 front-end electronics for further treatment.

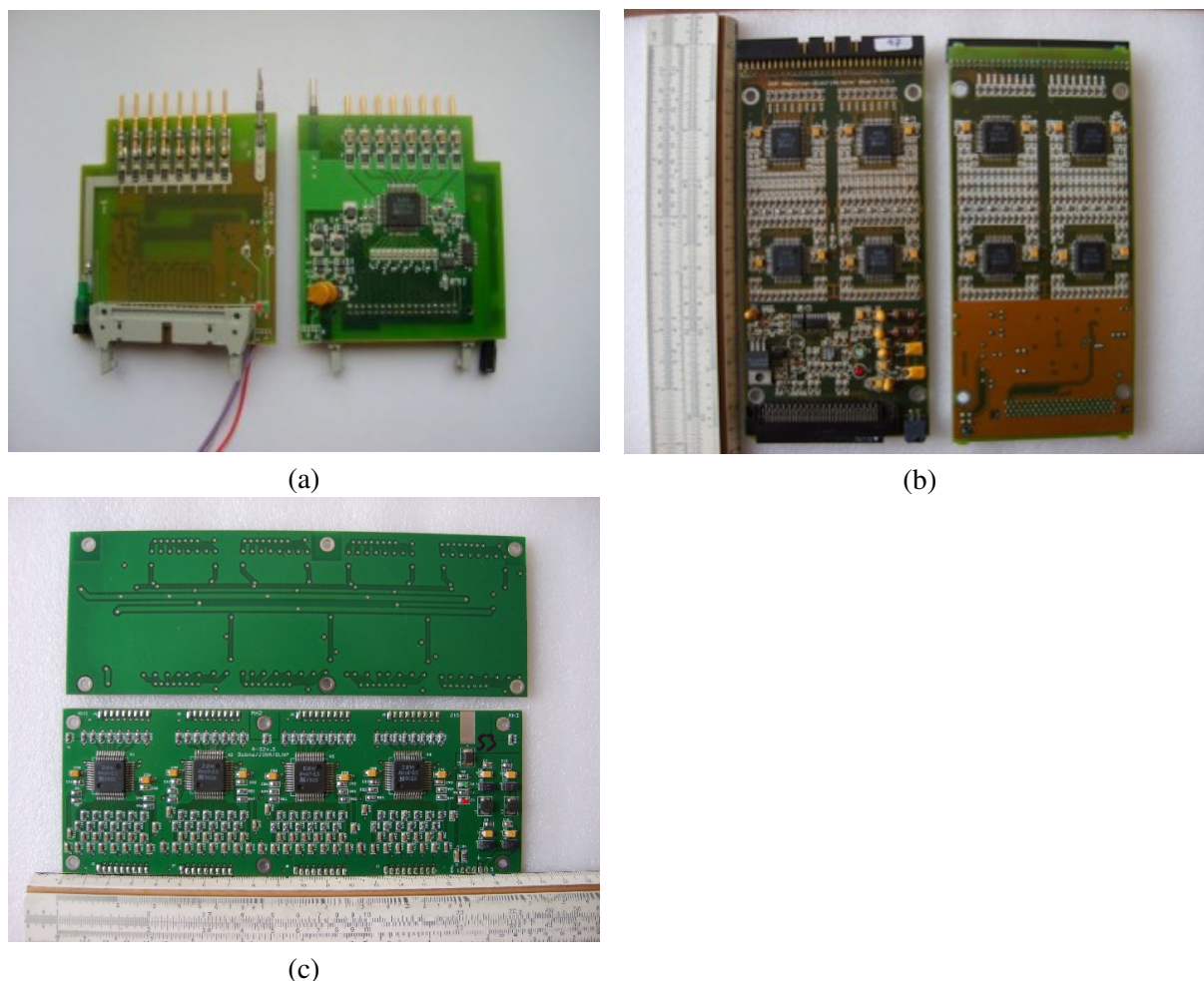


Figure 4.28: Front-end analog electronics cards: HVS/A-8 (a), ADB-32 (b) and A-32 (c).

2058 The digital electronics being created for the Muon System is based on the use of FPGA chips. The
 2059 prototype of the digital 192-channel MFDM module (Muon FPGA Digital Module) that we have devel-
 2060 oped includes a XC7A200T chip of the Xilinx Artix 7 family. This unit is functionally, mechanically, in
 2061 data format and DAQ interface, compatible with the previously developed MWDB (Muon Wall Digital
 2062 Board) unit [?] made on the basis of TDC F1 (ASIC) and successfully used for data readout from the
 2063 Muon System of the COMPASS experiment (CERN). This approach allows both types of units to be
 2064 used in the same readout system, thus making it possible for the new MFDBs cards to be tested under
 2065 actual operating conditions.

2066 The unit includes three electronic boards (Fig.4.29): motherboard, mezzanine card, and interface card.
 2067 The motherboard accepts 96 LVDS signals from the analog electronics through 3 high-density connec-
 2068 tors, converts them to LVTTTL levels and writes to the FPGA, and also communicates with two other
 2069 boards. The mezzanine card also accepts 96 LVDS signals through 3 connectors, converts them to
 2070 LVTTTL levels and transmits through the 120-pin board-to-board connector to the motherboard. The in-
 2071 terface card is designed to connect the MFDM module with the DAQ via the HotLink interface (RJ45
 2072 connector), to download the firmware to the FPGA from a local computer, as well as to download the
 2073 firmware via the RS-485 interface (RJ45 connector) from a remote computer.

2074 Tests performed at CERN with the Muon System prototype on cosmic muons gave encouraging results.
 2075 The further tests will be conducted with a prototype of the SPD range system (~ 1200 channels of wire
 2076 and strip readout) at the Nuclotron test beam area.

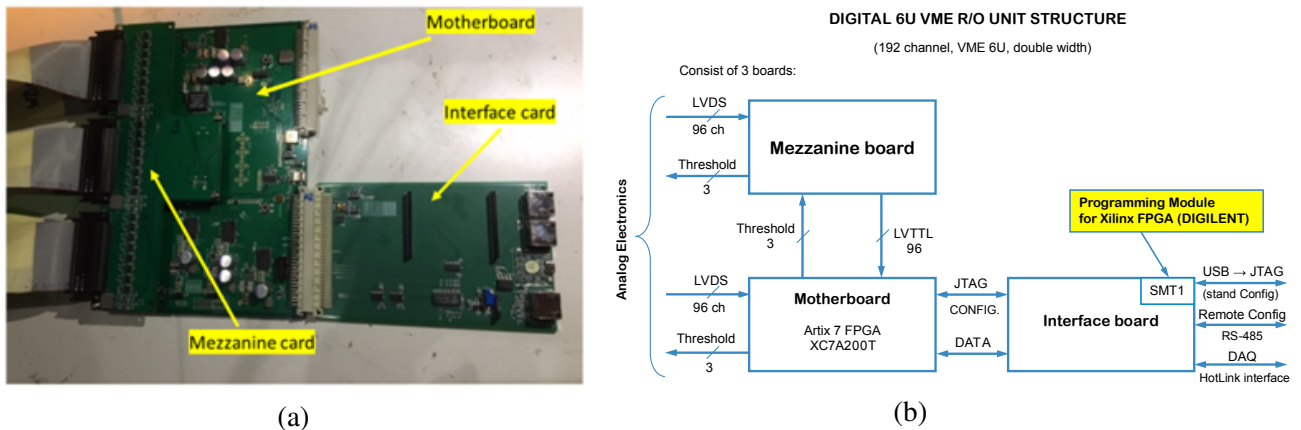


Figure 4.29: Digital 192-channel MFDM module (a) and its block-diagram (b).

2077 In the future, after the final tuning of the unit, we are planning to replace the HotLink interface in the
 2078 MFDM module with the S-Link interface for direct connection of the Muon System digital electronics
 2079 to the FPGA-based SPD DAQ. A general view of the data flow structure for the Muon System is shown
 2080 in Fig.4.30.

2081 7.5 Performance figures

2082 The evaluation of the main parameters of the proposed Range System is being performed with big pro-
 2083 totype installed at CERN within the PANDA program. The prototype (Fig.4.31) has a total weight of
 2084 about 10 tons (steel absorber and detectors with electronics) and comprises 250 MDT detectors with
 2085 4000 readout channels (2000 for the wires and 2000 for the strips, 1 cm wide). It has both samplings
 2086 (3 cm and 6 cm) present in the system (Barrel and End Caps), thus providing an opportunity for direct
 2087 calibration of the response to muons, pions, protons, and neutrons.

2088 Fig.4.32 gives the examples of the prototype response to different particles. The patterns demonstrate
 2089 excellent PID abilities of the Range System. The data were taken during the May and August runs of
 2090 2018 at the T9/PS/CERN test beam. The beam particles hit the prototype from the top of the picture.
 2091 The beam momentum for all the particles is 5.0 GeV/c. Neutrons were generated by a proton beam on a
 2092 carbon target placed in the very vicinity of the first detecting layer. The points on the pictures represent
 2093 hit wires, thus giving the impression of a typical device response with an accuracy ~ 1 cm.

2094 8 Particle identification system

2095 8.1 Time of flight system [A. Korzenev]

2096 The purpose of the time-of-flight (TOF) system is to discriminate between charged particles of different
 2097 masses in the momentum range up to 3 GeV/c. The system will be located inside the magnet coils which
 2098 will limit the radial flight distance for particles to 108 cm. The system will occupy a distance of 20 cm
 2099 radially to the straw station. The space will potentially be shared with an aerogel detector which will
 2100 be described in the next section. This short distance between the collision point and TOF dictates the
 2101 requirement for the time resolution of TOF to be better than 70 ps. In view of uncertainty related to the
 2102 bunch length (about 60 cm), the time which can be assigned to the collision vertex will only be on the
 2103 order of 1 ns, so it is useless for identification purposes. Therefore the particle identification can only be
 2104 done for multi-track events, where several particles emerged from a primary vertex hit active elements
 2105 of TOF. A certain mass hypothesis will have to be applied in this procedure. For details of this analysis
 2106 see the section ???. In addition to the particle identification, the detector will also provide a start time to

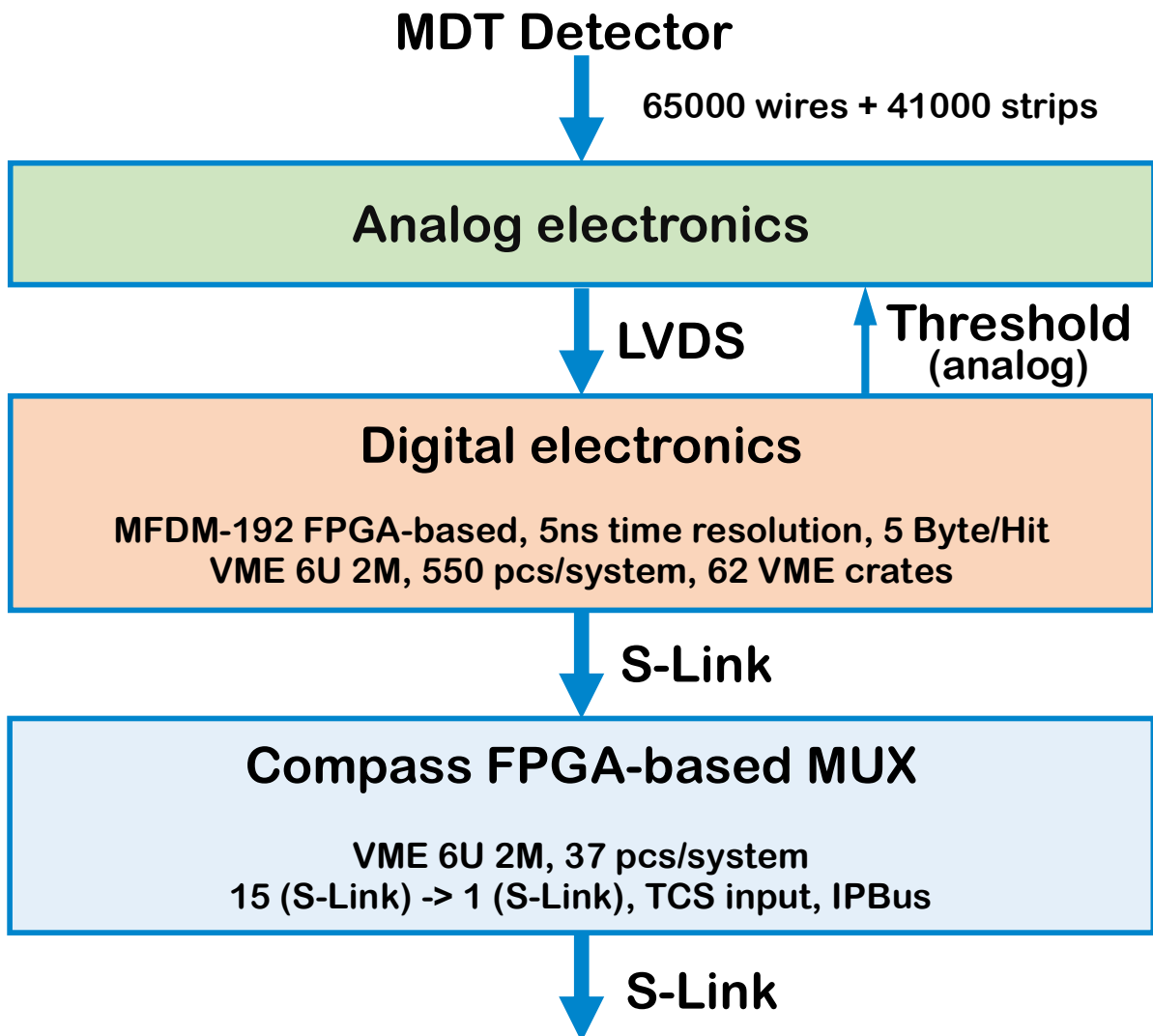


Figure 4.30: Data flow diagram – from detector to DAQ.

2107 the straw drift tubes.

2108 The TOF system will consist of a barrel and two end-cap parts with an overall active area of 27.1 m^2 . The
 2109 charge particle rate that detector will have to withstand is 0.1 kHz/cm^2 for the barrel. The rate increases
 2110 rapidly when moving closer to the beam axis. Thus, for TOF elements located in end-caps 20 cm from
 2111 the beam axis, the rate will be 1 kHz/cm^2 (see Fig. ?? for details). Two alternative technologies are being
 2112 considered for the detector: a multigap Timing Resistive Plate Chamber (mRPC) and a plastic scintillator
 2113 with Silicon Photomultiplier (SiPM) reading. Both are shown in Fig. 4.33. These two technologies, in
 2114 general, can provide about the same efficiency and time resolution, require similar readout electronics
 2115 and have about the same cost per channel. Main features as well as pros and cons of both options are
 2116 listed below:

2117 – *The multigap Timing Resistive Plate Chamber (mRPC)*. It is a stack of resistive glass plates with
 2118 high voltage applied to external surfaces. Pickup electrodes are located inside the chamber sep-
 2119 arating two stacks, 6 gas each. A fast signal induced on the pickup electrodes by an electron
 2120 avalanche is further transported to FEE located nearby. Schematic cross-section of MRPC is
 2121 shown in Fig. 4.34. All aspects of this technology are well tested and are deployed in a num-

PANDA Muon System Prototype @ PS/T9/CERN Beam Line

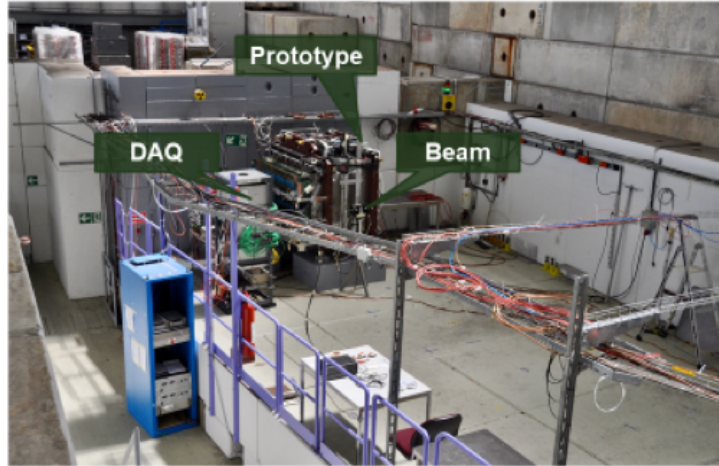


Figure 4.31: Range System prototype (10 ton, 4000 readout channels) at CERN.

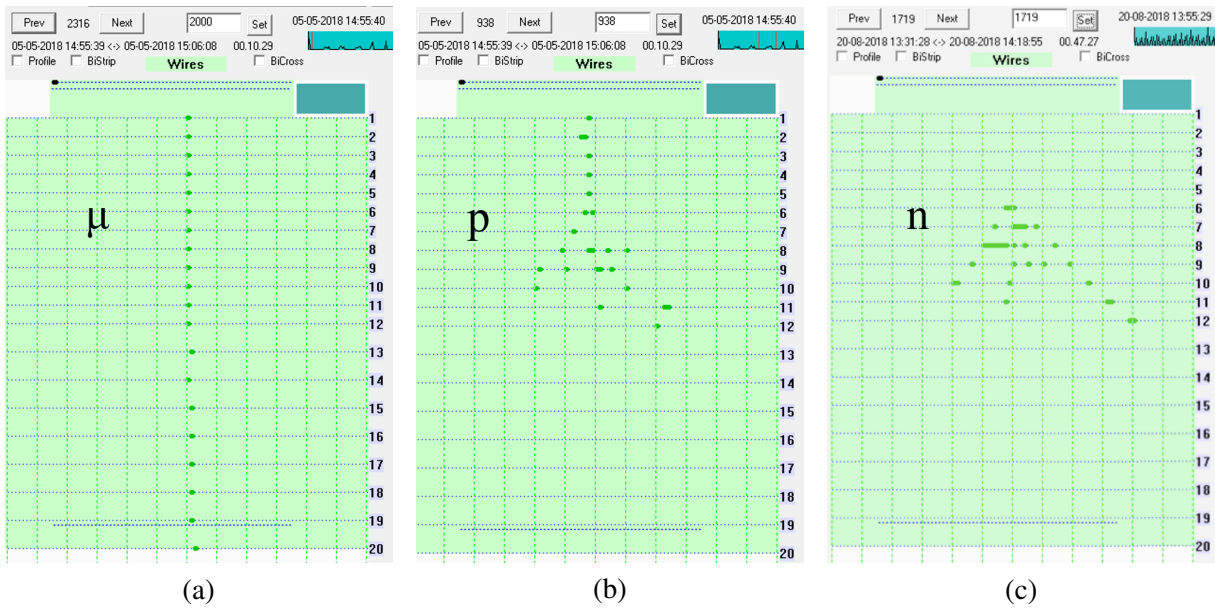


Figure 4.32: Demonstration of PID abilities: patterns for - (a) muon, (b) proton and (c) neutron.

2122 ber of projects like MPD [349] and BM@N which is described later. Overall dimensions of one
 2123 mRPC is $400 \times 330 \times 25 \text{ mm}^3$ which corresponds to a PCB with 24 readout strips, each 10 mm
 2124 wide and 400 mm long. The detector is composed of 220 chambers: 160 and 30 chambers for
 2125 the barrel and each end-cap, respectively. Adjacent MRPCs will be positioned in such a way as
 2126 to create an overlap of 1 strip at the edge of the active area. This will ensure the inter-calibration
 2127 of the MRPCs using tracks crossing both chambers. A rectangular shape of chamber, which is
 2128 quite large and can not be modified, creates a certain inconvenience for covering the end-cap parts
 2129 of detector. Contributions of all parts of TOF to the radiation length is about $0.14 X_0$ on average
 2130 [349].

2131 – *The plastic scintillator option.* The basic element of the detector is a plastic scintillator tile with

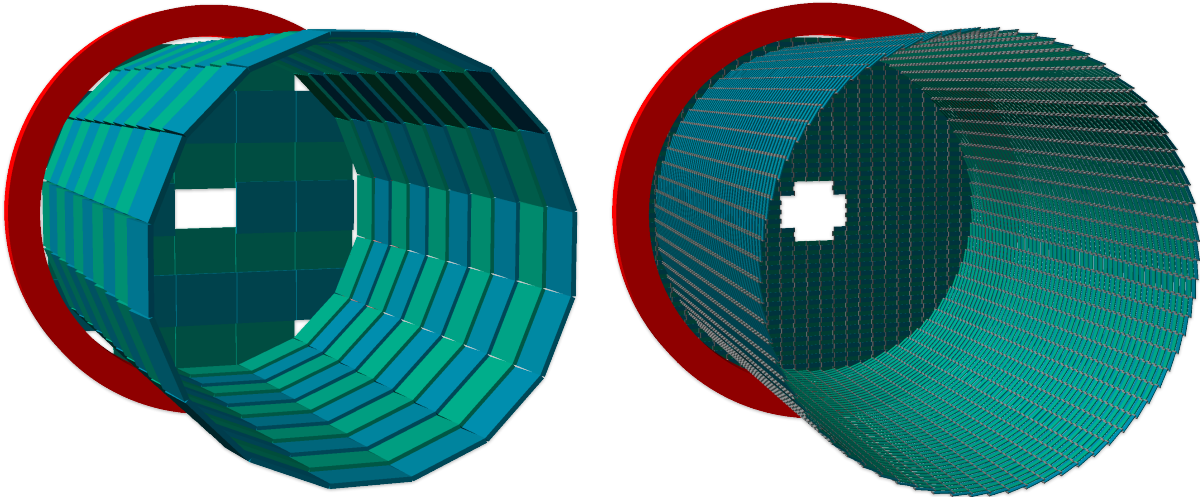


Figure 4.33: Two technologies are being considered for the time-of-flight system of SPD: the multigap Timing Resistive Plate Chamber, mRPC (left) and the plastic scintillator option (right). Barrel and one of two end-cap parts are shown for both options. One of six magnet coils limiting the volume of TOF is shown in red.

2132 dimensions of $90\text{ mm} \times 30\text{ mm} \times 5\text{ mm}$. Scintillation photons produced by an ionizing particle are
 2133 read out on two ends of tile by an array of 4 SiPMs soldered to custom pre-amplifier PCBs.
 2134 A schematic view to the plastic scintillator tile of TOF/PANDA is presented in Fig. 4.37. The
 2135 TOF/SPD detector will be composed of 10.1k staggered tiles: 7.3k and 1.4k tiles for the barrel
 2136 and each end-cap, respectively. Heaving much smaller size of a single element of detector, it can
 2137 easier adopt the cylindrical shape of magnetic coils and the beam hole. Furthermore, the system
 2138 is much lighter in weight than the one of mRPC and the number of radiation lengths for particle
 2139 crossing the detector is smaller by a factor of 5. The system manufactured with this technology
 2140 is easier to maintain than the one of MRPC since it does not require gas circulation, neither high
 2141 voltage is needed (no trips due to sparks). This kind of setup, however, was not used in JINR
 2142 experiments before and will require detail R&D. The resistance of scintillator to the radiation level
 2143 to be studied.

2144 Dimensions and numbers of TOF elements for two options are given in Tab. 4.6. The choice of the
 2145 technology for the baseline option will be made after more detailed studies of the actual particle rates,
 2146 comparing the respective performances, the calibration strategy and the costs.

2147 **8.1.1 ToF system based on MRPC**

2148 The estimated time resolution of such a TOF system should not be worse than (60?) ps. The efficiency of
 2149 particle registration at high rate (few kHz/cm^2) must be above 98%. Based on the experience of building
 2150 similar systems in experiments as ALICE [?], HARP [?], STAR [?], PHENIX [?] and BM@N, a
 2151 glass multigap Timing Resistive Plate Chamber (mRPC) could be proposed as base time detector. For
 2152 example, ToF-700 wall in BM@N experiment provides us with the pion/kaon separation up to $3\text{ GeV}/c$
 2153 and proton/kaon separation up to $5\text{ GeV}/c$. In an assumption that time resolution of start timing detector
 2154 will be $<40\text{ ps}$.

2155 Design of the BM@N ToF-700 wall was based on experimental results obtained during multiple tests
 2156 of various modifications of glass mRPC exposed in charge particles beam [?]. The counting rate for
 2157 standard glass mRPC is limited to several hundreds Hz/cm^2 due to the use of conventional float glass
 2158 plates with a bulk resistivity in the range $10^{12} - 10^{13}\ \Omega \cdot \text{cm}$. Therefore, the extension of the counting

	MRPC	Plastic scintillator
Active area: Barel + 2×End-cap	$19.8 \text{ m}^2 + 2 \times 3.7 \text{ m}^2 = 27.1 \text{ m}^2$	
Area of readout element: pitch × length	strip $1.25 \text{ cm} \times 40 \text{ cm} = 50 \text{ cm}^2$	tile $2.9 \text{ cm} \times 9 \text{ cm} = 26.1 \text{ cm}^2$
Size of chamber or tile: W × L × H	chamber (24 strips) $33 \text{ cm} \times 40 \text{ cm} \times 2.5 \text{ cm}$	tile $3 \text{ cm} \times 9 \text{ cm} \times 0.5 \text{ cm}$
Number of chambers or tiles: Barel + 2×End-cap	chambers $160 + 2 \times 30 = 220$	tiles $7.3\text{k} + 2 \times 1.4\text{k} = 10.1\text{k}$
Number of DAQ channels	10.6k	20.2k

Table 4.6: Dimensions and numbers of TOF elements for two technologies: MRPC and plastic scintillator.

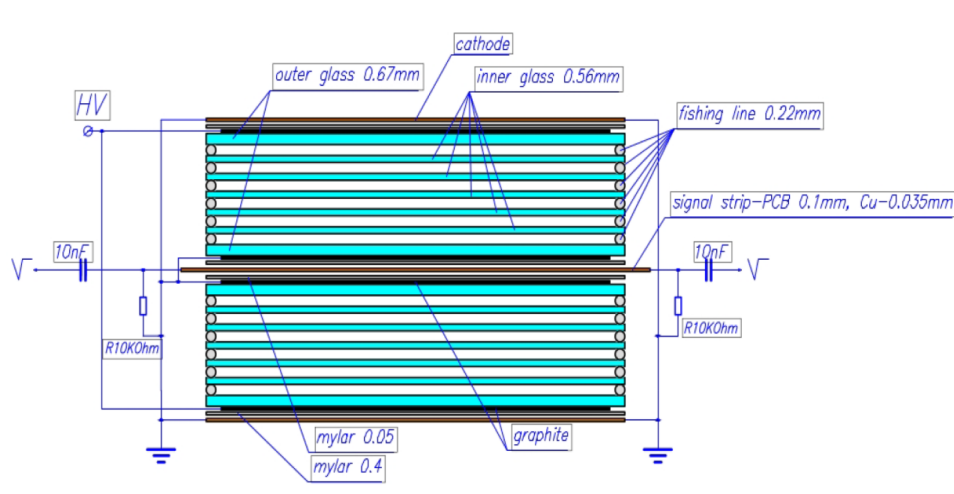


Figure 4.34: Schematic cross-section of the twelve gap MRPC.

2159 rate capabilities of mRPC has become an important issue.

2160 One of the way to increase the mRPCs performance at high rates is to use the low resistivity glass (less
 2161 than $10^{10} - 10^{11} \Omega \cdot \text{cm}$) [? ? ? ?] or ceramics [?] as the electrode materials. For instance,
 2162 time resolutions below 90 ps and efficiencies larger than 90% were obtained for particle fluxes up to 25
 2163 kHz/cm^2 for the 10-gap mRPC [?]. An alternative method is to reduce the glass stack resistance by
 2164 minimizing the used electrode thickness and increasing a temperature of the glass [? ?]. It was shown
 2165 that such method can provide high time resolution at continuous rate up to $20 \text{ kHz}/\text{cm}^2$ [?].

2166 **8.1.1.1 Warm mRPC for BM@N** Schematic cross section of mRPC is shown in Fig. 4.34. It con-
 2167 sists of two identical 6-gap stacks with anode strip readout plate in between. The size of mRPC is
 2168 $473 \times 279 \times 17 \text{ mm}^3$ with the working area of $351 \times 160 \text{ mm}^2$. Each mRPC has 32 $10 \times 160 \text{ mm}^2$ readout
 2169 strips with 1 mm gaps between them.

2170 Each stack is formed by seven glass plates with the $2 \times 10^{12} \Omega \cdot \text{cm}$ bulk resistivity. The gap between the
 2171 glasses 0.22 mm is fixed by spacers – usual fishing-lines, which ran directly through the RPC working
 2172 area. Graphite conductive coating with surface resistivity of $\sim 1 \text{ M}\Omega$ is painted to outer surfaces of
 2173 external glass plates of each stack to distribute both the high voltage and its separate ground and thus to
 2174 form the uniform electrical field in the stack sensitive area. The anode readout strips plate is a one-sided
 2175 printed PCB with the thickness of 100 mm, the thickness of the copper is 35 microns. Signals are taken

2176 from the both ends of anode strips. The entire mRPC assembly is put into a gas-tight box. Bottom of box
 2177 is made of a double side PCB (motherboard) with a thickness of 2.5 mm, side frame of the box is made
 2178 of aluminum profile, the top of box is closed by aluminum cover having thickness of 1.5 mm. Paper
 2179 [?] presents the performance of 12-gap mRPC in the range of the counting rate from 0.45 kHz/cm²
 2180 up to 10 kHz/cm² obtained using secondary muon beam from U70 at Protvino. The measurements at
 2181 different rates were performed in the mRPCs temperature range 25-45 °C with the step of 5 °C. The time
 2182 resolution is reached up to 50-60 ps with good and stable efficiency under temperature of 40-45 °C.

2183 **8.1.1.2 Chamber for SPD** Particle flux in the SPD experiment is expected to be up to few kHz/cm²
 2184 (at end-caps, 20 cm from the beam axis). Therefore the high-speed performance of TOF system is
 2185 important parameter. In order to increase the high-speed performance of mRPC now is decided to make
 2186 new chamber using of glass plate with less thickness and cover each plate by graphite (Fig. 4.35). It
 2187 should decrease the time dissipation of charge inside glass. Using such structures we expect to increase
 2188 high-speed performance twice with time resolution better than 50 ps.

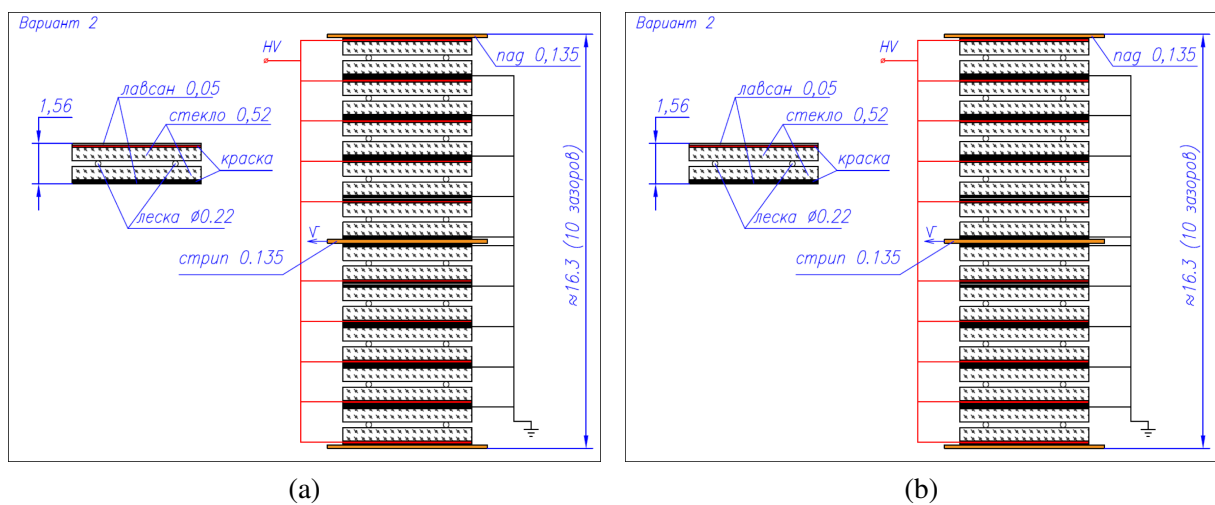


Figure 4.35: Schematic cross-section of the new MRPC.

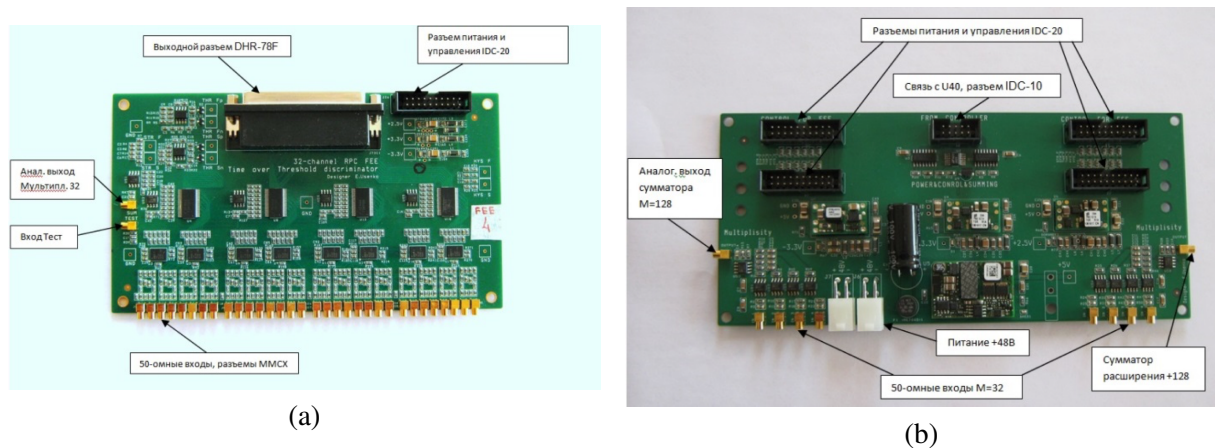


Figure 4.36: The 32RPC (a) and PWR&CTRL (b) modules used for readout of MRPC.

2189 **8.1.1.3 FEE of mRPC** The 32-channels FEE module (32RPC board) designed for our mRPCs bases
 2190 on a NINO chip. The output signal of NINO amplifier-discriminator is the time-over-threshold pulse
 2191 whose leading edge provides with the time of the hit while its pulse width is proportional to the input
 2192 signal charge [?]. The signals from mRPC to the module 32RPC are coming by 50Ω coaxial cables

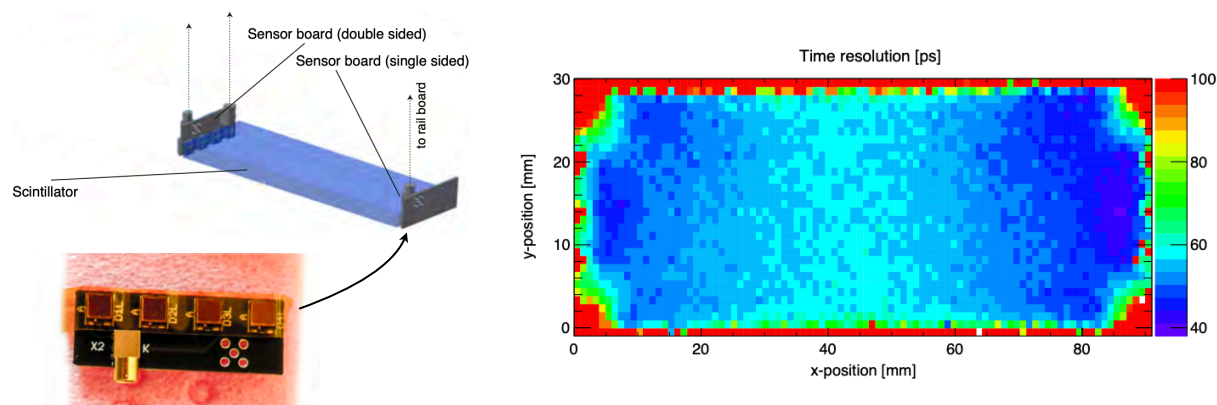


Figure 4.37: Left: schematic view to the plastic scintillator tile and a photo of the 4 SiPM board of PANDA [350]. Right: time resolution obtained from a position scan of a $90 \times 30 \times 5 \text{ mm}^3$ EJ-232 scintillator tile read out by Hamamatsu SiPMs attached to opposite sides, 4 SiPMs in series per side [350].

2193 with use MMCX connectors. Output LVDS signals are transmitting to the module of digitization with
 2194 use of DHR-78F sockets. At present a 64-channel VME time-to-digital converter TDC64VHLE based
 2195 on the HPTDC chip is used for digitization [?]. Power supply, threshold settings, stretch time settings
 2196 and hysteresis settings of the four 32RPC boards are made by a special designed module power and
 2197 control (PWR&CTRL). PWR&CTRL module is controlled by the U-40 VME module [?] via digital
 2198 SPI interface.

2199 8.1.2 TOF system based on plastic scintillator

2200 This option was inspired by the TOF system of MEGII [351] and PANDA [?] experiments. The surface
 2201 of TOF is segmented into many small scintillator tiles made of a fast scintillating organic material.
 2202 The optical readout is performed by Silicon Photomultipliers (SiPM) attached to the ends of every tile.
 2203 A typical number of optical photons released by a minimum-ionising particle crossing a 1 cm plastic
 2204 scintillator is $\sim 10^4$. A resulting number of detected photons depends on a signal propagation and photo-
 2205 sensor efficiencies. Nowadays, large-area SiPMs have appeared on the market at relatively moderate
 2206 cost and offer several advantages over PMTs: magnetic field tolerance, a much smaller volume and
 2207 footprint allowing a compact design for bars without light-guides, low operation voltage and high photon
 2208 detection efficiency (PDE). Thus, they ideally meet the requirements dictated by a thousand tile system
 2209 of TOF/SPD.

2210 The choice of scintillator material is primarily driven by the requirement for a short emission time.
 2211 Organic scintillators based on a plastic matrix of polyvinyl-toluene, such as EJ-228 (BC-420) or EJ-232
 2212 (BC-422), have an attenuation length of about 10 cm, rise time of 0.5 ns and wavelength of maximum
 2213 emission in UV region of 391 nm. They are commonly used for applications as the one discussed in
 2214 this section. Note that, contrarily to MRPC, the time resolution of a plastic scintillator detector degrades
 2215 exponentially with increase of distance between the interaction point and photosensor. It is especially
 2216 crucial for UV photons. Therefore the choice of scintillator is all the time a compromise between the
 2217 attenuation length (visible light) and fast emission (UV region).

2218 In the case of TOF/PANDA, a scintillator tile with dimensions of $90 \times 30 \times 5 \text{ mm}^3$ was read out by 4
 2219 Hamamatsu SiPMs coupled to opposite sides as shown in Fig. 4.37 (left). Each SiPM has its sensitive
 2220 area of $3 \times 3 \text{ mm}^2$, thus the array of four can detect about a quarter of photons reaching the end of tile.
 2221 This configuration was chosen as a baseline for estimates for the TOF system of SPD. The time resolution
 2222 obtained from a position scan is shown in Fig. 4.37 (right). One can see that the resolution varies from

2223 50 ps in the near-to-SiPM region to 60 ps in the center of tile. The resolution of 100 ps around the edge
 2224 of tile is, presumably, due to tracks only partially crossing the volume of scintillator.

2225 Summarizing the advantages of the plastic scintillator option versus MRPC, one can say that the assem-
 2226 bling is faster, easier and does not require clean environment; it is easier to maintain the detector (no gas
 2227 flow, only LV); the detector can be squeezed within 5 cm radially, thus leaving space for aerogel which
 2228 will be described in the next section; the circular cross section of barrel can be approximated exactly
 2229 matching the magnet coils from the outside; the radiation length is only 2% of X_0 . Weak points of the
 2230 plastic option are: an exponential drop of the resolution vs distance, which will require larger number
 2231 of SiPMs for the case of longer tile; a smaller surface of a single tile, 26 cm² vs 50 cm² of a MRPC's
 2232 strip, doubles the number of read channels; the organic material is sensitive to radiation. Although this
 2233 option is promising it will require detailed study before being accepted.

2234 8.2 Aerogel counters [A. Kulikov]

2235 Another option for the system of particle identification is aerogel Cherenkov counters. Aerogel is a syn-
 2236 thetic porous ultralight material which has found an application, in particular, as a radiator in Cherenkov
 2237 counters. Aerogel may have a refractive index in the range between 1.0006 and 1.2, the exact value of
 2238 the refractive index being specified at the production stage. In fact, aerogel fills the gap in the refrac-
 2239 tive index values between gases and liquids. This feature of aerogel allows one to use it in Cherenkov
 2240 counters for particle identification in conditions when other Cherenkov radiators are not applicable, for
 2241 instance, for π/K separation at the momenta from few hundred MeV/c to about 3 GeV/c. Selection of the
 2242 refractive index value defines the region of momenta where separation is effective.

2243 There exists a good experience of using threshold aerogel Cherenkov counters, in particular, in exper-
 2244 iments KEDR (BINP, Novosibirsk) [352], [353], BELLE (KEKB, Tsukuba) [354]. In the BELLE ex-
 2245 periment a threshold aerogel Cherenkov counter with refractive index from 1.010 to 1.030 provided π/K
 2246 separation in the momentum region up to 3.5 GeV/c. In the KEDR detector the aerogel counters with
 2247 refractive index 1.05 provided π/K separation in the range from 0.6 to 1.5 GeV/c.

2248 Aerogel has a short scattering length of light, 12-40 mm depending on wavelength. Therefore, directivity
 2249 of Cherenkov light cannot be used because directivity disappears soon after emission. For this reason
 2250 diffusive reflectors are used at the walls. No scintillation has been observed in aerogel. Aerogel samples
 2251 suffered from hygroscopicity for a long time, but in the 1990ties the technology of hydrofobic aerogel
 2252 has been developed.

2253 In KEDR, the aerogel counters received the name ASHIPH (Aerogel, SHifter, PHotomultiplier). In

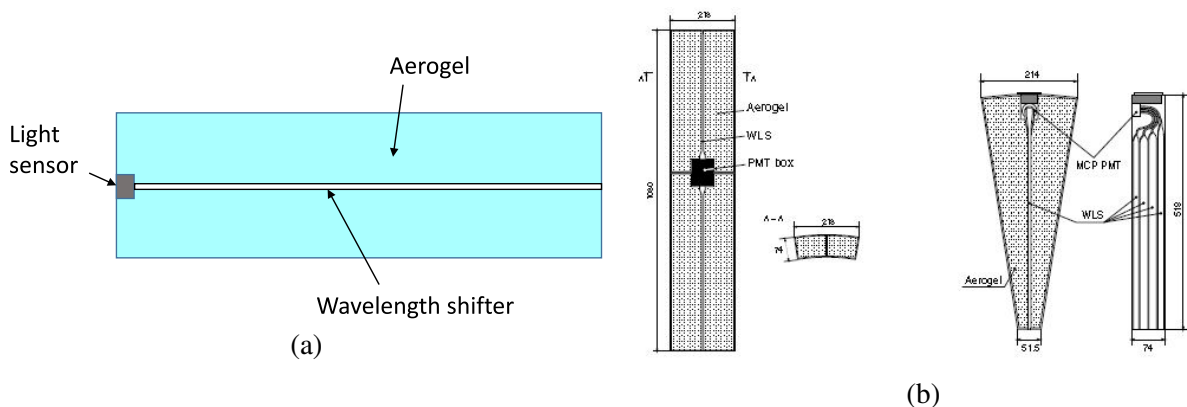


Figure 4.38: (a) Principle of ASHIPH operation. (b) KEDR aerogel counters: two barrel counters in a single housing (left), end-cup counter (right).

2254 Fig. 4.38(a) a principle scheme of the counter is shown. Cherenkov light from aerogel is captured by a
 2255 wavelength shifter (WLS). PMMA light guide doped with BBQ dye is used as wavelength shifter, cross
 2256 section of WLS is $3 \times 17 \text{ mm}^2$. WLS absorbs Cherenkov photons at short wavelengths where Cherenkov
 2257 radiation is more intensive and re-emit photons at large wavelength bringing them to a light sensor. In
 2258 Fig. 4.38(b) the counters of KEDR are shown. The microchannel plate photomultipliers served as light
 2259 sensors in KEDR, but for later developments the APD were used (BELLE-II), also SiPM are proposed
 2260 for aerogel detectors in PANDA (GSI) and FARICH (for $c\tau$ -factory in Novosibirsk).

2261 If a particle crosses WLS, it produces the signal much higher than the particle traversing aerogel. To
 2262 avoid misidentification, two-layer structure is used with shifted layers with respect to WLS position, so
 2263 that a particle cannot cross WLS in both layers. The thickness of one layer in KEDR is 74 mm, a total
 2264 amount of material in both layers is $0.24\%X_0$.

2265 For relativistic cosmic muons that cross both counter layers of KEDR the average number of photo-
 2266 electrons was 9.3 ± 0.4 , and the detection efficiency $99.3 \pm 0.1\%$ at the threshold equal to 2 p.e. For
 2267 under-Cherenkov-threshold muons ($200 < p_\mu < 300 \text{ MeV}/c$) the efficiency was $3 \pm 1\%$.

2268 In SPD aerogel counters *a la* ASHIPH can be inserted between the Straw tracker and ECAL. The value
 2269 of refractive index can be selected for the momentum region where πK separation is the most important.
 2270 The detector is thin (in X_0), fast and rather simple in operation.

2271 **9 Beam-beam counter [V. Ladygin]**

2272 Two Beam-Beam Counters are located just in front of the PID system end-cups. The main goal of the
 2273 Beam-Beam Counter is the local polarimetry at SPD, using the measurements of the azimuthal asymme-
 2274 try in inclusive production of charged particles in collisions of transverse polarized proton beams.

2275 Another purpose of the BBC is fast selection of different types of events. The Monte Carlo simulation
 2276 performed at $\sqrt{s}=27 \text{ GeV}/c^2$ for minimum bias p - p - collisions proves that at least one BBC will have
 2277 a signal for 72% of events (only 41% in both BBCs). However, in the case of hard processes at least
 2278 one BBC will hit in 96.5% of events, while both BBCs will have signals in 67% cases. Therefore, the
 2279 requirement of the BBC signals allows one to select hard processes.

2280 The concept of the BBC is shown in Fig.4.39. The detector consists of two major parts: the inner and
 2281 the outer one, which are based on different technologies. The BBC inner part will be based on fast
 2282 segmented Micro Channel Plate(MCP) detectors, while the BBC outer part will be produced from fast
 2283 plastic scintillator tiles. The inner part covers 30-60 mrad and should be separated into 4 layers consisting
 2284 of 32 azimuthal sectors. The outer part the range of the polar angle from 60 to 500 mrad divided into 5-6
 2285 layers on the polar angle each of them has 16 azimuthal sectors. The final segmentation will be obtained
 2286 from the optimization of the polar angle granularity for the entire energy range of NICA.

2287 **9.1 Inner part of the BBC: MPC**

2288 Two compact detector systems are proposed to meet the challenges of the fast beam-beam collisions
 2289 monitoring, event selection, and the precise timing determination in proton-proton and nucleus-nucleus
 2290 collisions at NICA. The Beam Position Monitor (BPM) and the Fast Beam-Beam Collision (FBBC)
 2291 monitor can to provide information for each bunch crossing both the beams location and the intensity of
 2292 collisions, as well as the azimuthal distribution of the particles in the event. The systems use fast Micro
 2293 Channel Plate detectors (MCPs). The ultra-high vacuum (UHV) compatibility and low-mass compact
 2294 design of the BPM and FBBC components allow one to consider their application inside the vacuum
 2295 beam line of the NICA collider. The BPM is based on the effect of the residual gas ionization and
 2296 provides high accuracy, and fast bunch-by-bunch measurements of the beam position. The FBBC uses

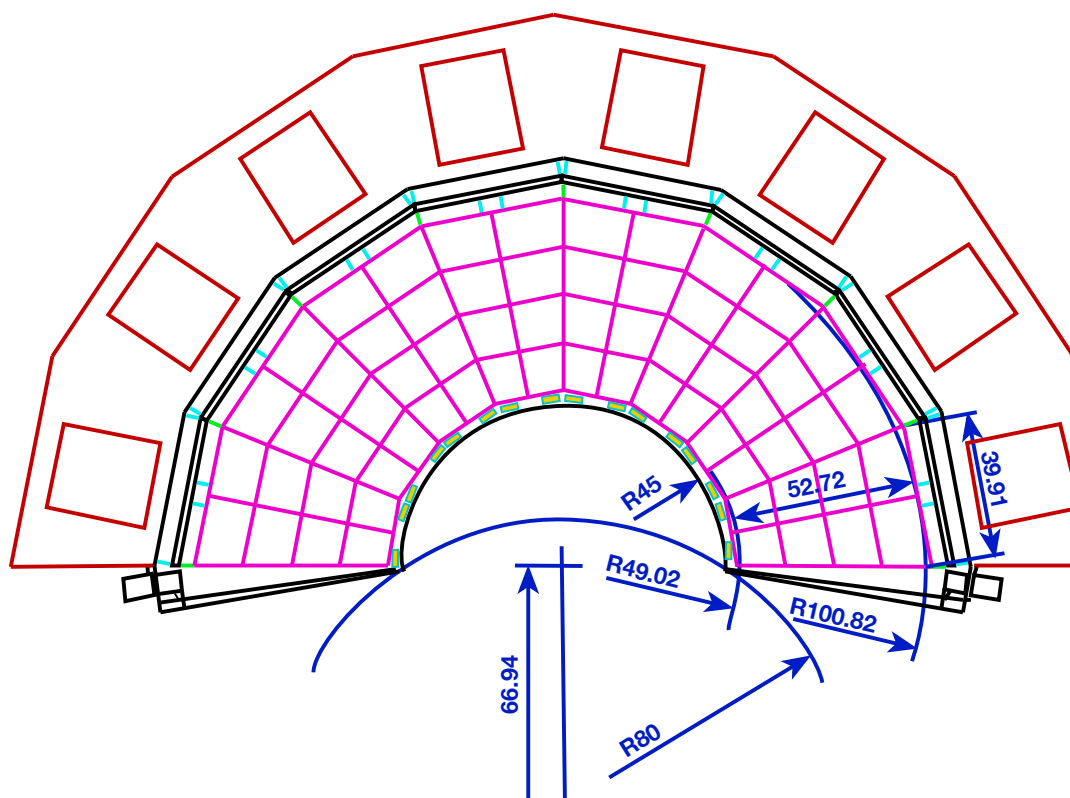


Figure 4.39: Beam-beam counter azimuthal and polar angle segmentation.

2297 the concept of the fast isochronous timing for the multi-pad readout of short (~ 1 ns) MCP signals
 2298 produced by the particles in the collisions of the beams. Studies of the polarization phenomena in light-
 2299 and intermetiate-ion interactions at SPD is another goal of research at NICA, and the FBBC is also
 2300 considered for the local polarimetry at SPD.

2301 One of the promising directions of beam diagnostics is the registration of residual gas ionization prod-
 2302 ucts by a fast MCP-based detector. Such detectors work in high-vacuum conditions and are used for
 2303 registration of beam profile at many accelerators, including Nuclotron (JINR), and heavy ion colliders.

2304 To meet the challenges of fast monitoring of beam-beam collisions for high-intensity NICA beams, the
 2305 MCP-based Fast Beam-Beam Collisions (FBBC) detector with high timing properties is proposed in
 2306 combination with the Beam Position Monitor (BPM). This will provide monitoring of bunch-by-bunch
 2307 crossing, the beams location and their profiles, the collision intensity, and the azimuthal distribution of
 2308 produced particles.

2309 Two compact systems based on the application of Micro Channel Plates (MCPs) are proposed (see
 2310 Fig.4.40) to meet the challenges of the fast beam-beam collisions monitoring, event selection, and de-
 2311 termination precisely the collision time t_0 for events where other detectors can not be used for that (p - p
 2312 elastic scattering, for instance). These systems of monitor detectors consist of 2D position-sensitive beam
 2313 imaging detectors (BPM) and two ring beam-beam collision detectors (FBBC-left and FBBC-right) that
 2314 are located inside the vacuum beam line. The ultra-high vacuum (UHV) compatibility and low-mass
 2315 compact design of the Fast Beam-Beam Collisions (FBBC) monitor in combination with the Beam Po-
 2316 sition Monitor (BPM) allow their application inside the vacuum beam line of the NICA collider. The
 2317 FBBC uses the concept of the isochronous multi-pad fast readout and the precise timing determination
 2318 of short (~ 1 ns) MCP signals. New MCPs with the improved characteristics, such as small diameter

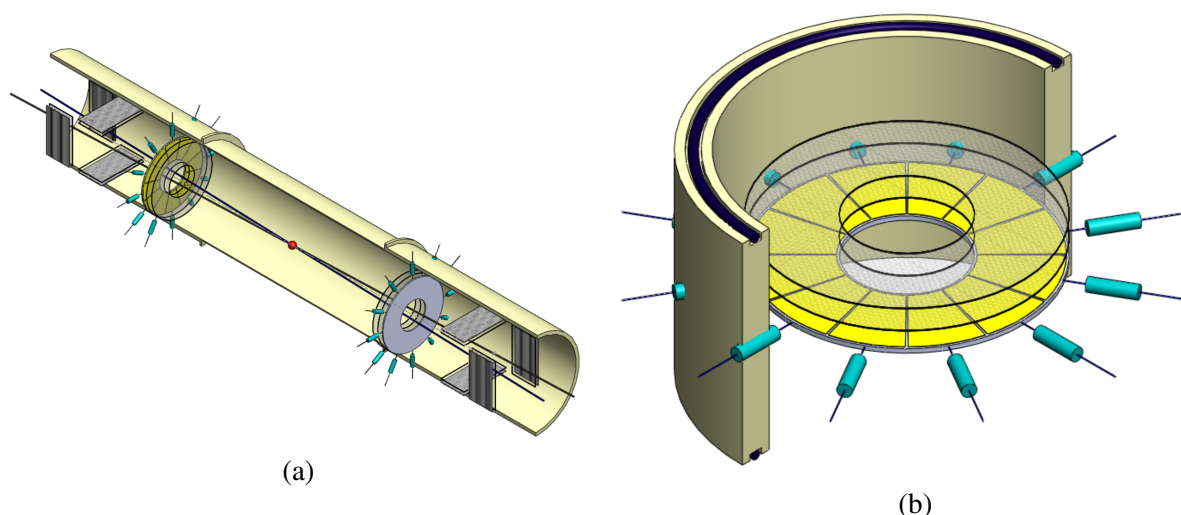


Figure 4.40: (a) General layout: the Fast Beam-Beam Collision (FBBC) monitor composed of MCP discs (1 and 2) in combination with the Beam Position devices (BPM) (3 and 4) are situated symmetrically to the Interaction Point (5) inside the vacuum beam pipe of the NICA collider. (b) Compact module of the Fast Beam-Beam Collision Monitor (FBBC) based on circular MCPs. Sector cathode readout pads and two MCP setups are embedded into a separate flange with a hermetic 50-Ohm signal and HV feedthroughs (the latter are not shown).

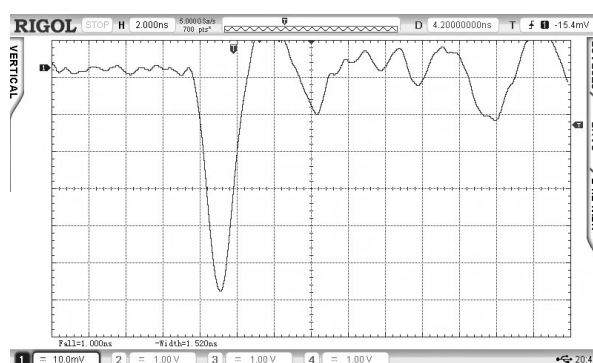


Figure 4.41: A typical MCP signal from the testing of the prototype detector.

2319 ($8\mu\text{m}$) channels, low resistivity (100-500 MOhm), high gain ($\sim 10^7$), short fast rise-time ($\sim 0.8\text{ns}$) sig-
 2320 nals, will be used.

2321 Fig.4.41 shows a typical MCP signal from the testing of the prototype detector. The colliding beams
 2322 pass through the central opening of the MCP, and the outer edges of the MCP capture secondary particles
 2323 flying a definite distance from the interaction point. The signals are recorded at the 12-sector cathode
 2324 and their arrival times are digitized along with the multiplicity information.

2325 The main feature of the new MCP is a high secondary emission coefficient and fast fronts of the output
 2326 signal. The new MCPs have a fast leading edge and high gain.

2327 A compact setup of two detectors with high timing capabilities based on the MCP applications – the Fast
 2328 Beam-Beam Collision counters (FBBC) and the Beam Position Monitor (BPM), is proposed to meet
 2329 a wide set of requirements including those of the future physics program with the polarized beams at
 2330 NICA SPD. The feasibility of the event-by-event monitoring of the beam-beam interactions at NICA
 2331 is confirmed both by the previous developments of the UHF-UHV technology and by the beam tests

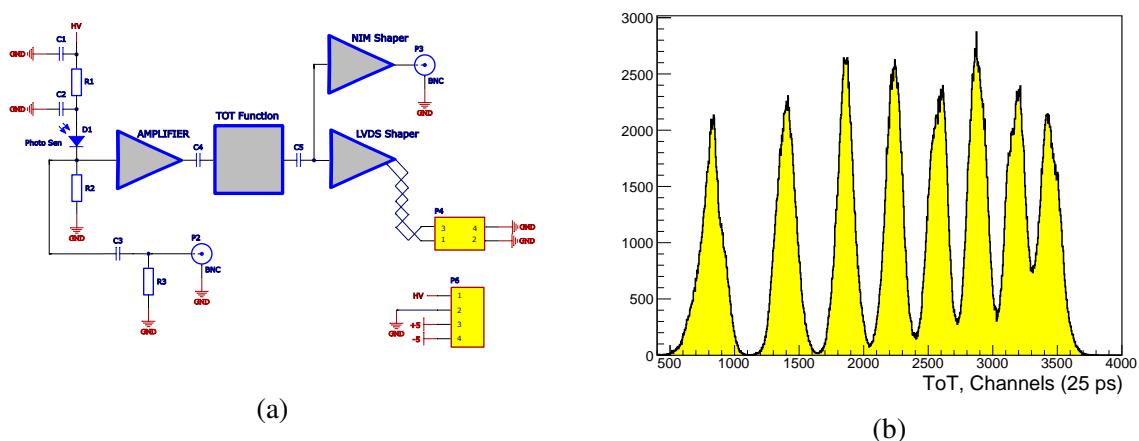


Figure 4.42: (a) Schematic view of the front-end electronics with a ToT function, (b) Distribution of the ToT for LED signal.

2332 (at JINR and CERN) of the prototype detectors and electronics, as well as by the in-lab tests of new
 2333 8-channel MCPs with the improved characteristics.

2334 9.2 Outer part of the BBC: scintillation tiles

2335 The scintillation part of the BBC will consist of tiles viewed by the SiPMs. The measurement of the
 2336 signal amplitude is required for time-walk correction to improve the time resolution.

2337 With a single-channel prototype of the detector we will have the ability to measure the amplitude using
 2338 developed FEE based on the Time-over-Threshold (ToT) technique. This technique is a well-known
 2339 method that allows us to measure the energy deposited in the material by reconstructing the given prop-
 2340 erty of the output current pulse – the total charge collected, the pulse amplitude, etc. The ToT method
 2341 converts the signal pulse height into a digital value in the early stage of the FEE, which greatly simplifies
 2342 the system in comparison to analog detectors with serial readout through ADCs. The measurement of the
 2343 ToT is composed of two measurements of time for the signal going above (leading) and returning below
 2344 (trailing) the given threshold. The first version of the prototype includes a power supply and electronics
 2345 (Fig.4.42(a)) made on a separate PCB. This PCB is used for each cell of the SiPM. The power supply
 2346 for the SiPM provides a voltage of up to 65 V with an individual channel adjustment within 0-10 V,
 2347 manual tuning, and a built-in voltmeter for the voltage monitoring. It is possible to connect eight cells
 2348 simultaneously. The amplifiers used for that do not change the leading edge of the signal. This allows us
 2349 to get a time stamp of the event. Afterwards, the signal is integrated and transmitted to the comparator.

2350 The response of the Hamamatsu S12572-010P SiPM [355] with the FEE to the LED has been studied.
 2351 The electrical signal from a lomo output of the LED was used as a trigger. The illumination was per-
 2352 formed by uniform light in a light-isolated box. In addition to the ToT information (Fig.4.42(b)), the time
 2353 stamp of the event for each SiPM cell was investigated. The distribution (Fig.4.43(a)) shows the correla-
 2354 tion of these values and that the signal in the region of small amplitudes comes later in time. This is due
 2355 to signal latency (the so-called time-walking effect). This delay occurs due to the difference between the
 2356 time when a photon or a charged particle passes through the detecting element and the time when the
 2357 electronics registers this signal. This leads to deterioration in the time resolution. After performing the
 2358 correction (see Fig.4.43(b)), the time-walking effect has been removed [356].

2359 The time resolution was defined as the RMS and was approximately 600ps. Taking into account the
 2360 non-Gaussian waveform (Fig.4.44(a)) and the fact that the time resolution is not the maximum allowed
 2361 for this type of the detector, the time-walk correction has been applied. The most important result of the

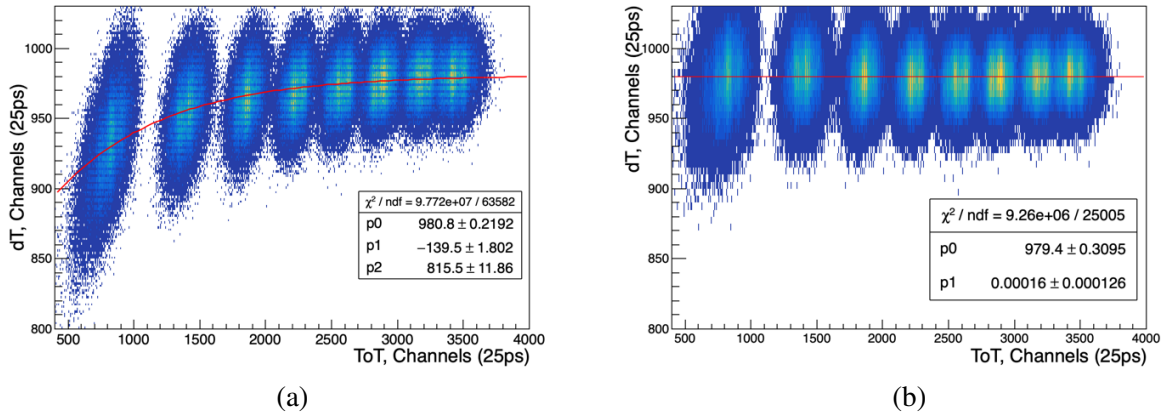


Figure 4.43: (a) dT ($T_{SiPM1} - T_{SiPM2}$) correlation on the ToT. (b) Result after the time-walk correction for the dT ($T_{SiPM1} - T_{SiPM2}$) correlation on the ToT.

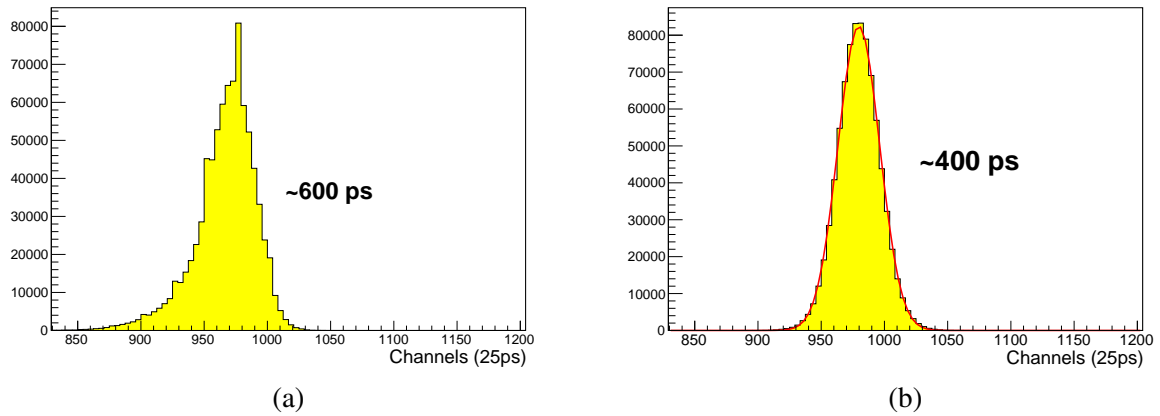


Figure 4.44: (a) dT ($T_{SiPM1} - T_{SiPM2}$). (b) Result after the time-walk correction for the dT ($T_{SiPM1} - T_{SiPM2}$).

2362 correction was a time resolution of approximately 400 ps (Fig.4.44(b)), which is 1.5 times better than the
2363 resolution before the correction.

2364 The first version of the prototype using developed front-end electronics based on the Time-over-Threshold
2365 method was tested. After the time-walk correction, the time resolution improved up to 400 ps. Taking
2366 into account the SiPM suboptimal for precise time measurements, the result is promising. Further devel-
2367 opment of the FEE with a ToT function allows using standard TDCs for timing measurements.

2368 10 Zero Degree Calorimeter [S. Shimansky]

2369 A zero degree calorimeter (ZDC) will be installed in the beam separation areas on both sides of the SPD
2370 interaction point, where all charged particles originating from the interaction region are swept out by the
2371 strong magnetic field. Main goals of the ZDC are:

- 2372 – luminosity measurement;
- 2373 – local polarimetry with forward neutrons (see Chapter 5);
- 2374 – spectator neutron tagging;

2375 – time tagging of the events for event selection.

2376 ZDC is a standard system used for the purposes mentioned above in many collider experiments. Strong
 2377 magnetic field before a ZDC cleans very well all charged particles allowing clean measurement of neu-
 2378 trals, so the device can work till very high luminosities. Scattering at zero angle is insensitive to trans-
 2379 verse polarization and provides offset-free luminosity measurement, very useful for luminosity cross-
 2380 checks. The device could provides an additional time stamp for an event. Standard usage of ZDC
 2381 includes local polarimetry with forward neutrons [357]. The main purpose is verification of longitudinal
 2382 polarization settings. One can expect 1-2% asymmetry for very fast neutrons at the position of the de-
 2383 tector. Precise tagging of very forward spectator neutrons provides a range of opportunities in study of
 2384 diffractive processes. To accomplish these tasks following performance parameters should be met:

2385 – time resolution 150-200 ps;

2386 – energy resolution for neutrons $50 - 60\%/\sqrt{E} \oplus 8 - 10\%$;

2387 – neutron entry point spatial resolution 10 mm.

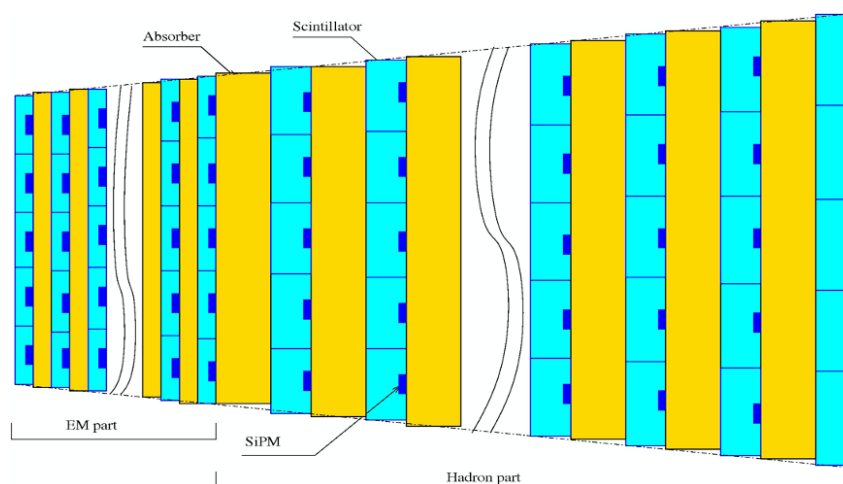


Figure 4.45: Schematic view of the ZDC.

2388 The design of the zero degree calorimeter was optimized basing on the Monte Carlo simulation to ob-
 2389 tain the necessary energy, spatial and time resolution. We propose to use a fine segmented calorimeter
 2390 based on plastic scintillator active tiles with direct SiPM readout and tungsten absorber plates similar to
 2391 calorimeter proposed for the CALICE [358]. A schematic view of the calorimeter is shown in Fig. 4.45.
 2392 In order to achieve good energy resolution for photons the first 10 layers will have smaller thickness
 2393 compare to the rest of the calorimeter. This allows to get reasonable energy resolution for photons, while
 2394 keeping reasonable number of readout channels. Each scintillator layer has 25 tiles arranged in 5×5 grid
 2395 with tile size growing from $17 \times 17 \text{ mm}^2$ for the first layer to $28 \times 28 \text{ mm}^2$ at the last layer. Each tile is
 2396 covered by a chemically produced thin white reflective layer with a small transparent window for optical
 2397 readout, done by HAMAMATSU SiPMs S13360-3050PE directly coupled to the tiles. Output signals
 2398 are digitized by 500 MHz flash ADC 16 channel boards. A fast output for SPD trigger system is also
 2399 produced. The ZDC will be placed inside the beam separation magnet and its size is limited to 88×88
 2400 mm^2 at front side and $140 \times 140 \text{ mm}^2$ at rear side. The length is limited to 650 mm.

2401 The expected energy resolution for neutrons is about $50\%/\sqrt{E} \oplus 30\%$ while the energy resolution for
 2402 photons is about $20\%/\sqrt{E} \oplus 9\%$. Spatial resolution for photons is estimated to be below 3 mm for 1 GeV

Table 4.7: The parameters of the ZDC layers.

Parameter	Electromagnetic part	Hadron part
Number of layers	10	26
Scintillator thickness, mm	5	10
Absorber thickness, mm	5	10
Total absorber thickness, mm	45	260
Part thickness, X_0	13	75
Part thickness, λ_I	0.5	2.9
Number of channels	250	650

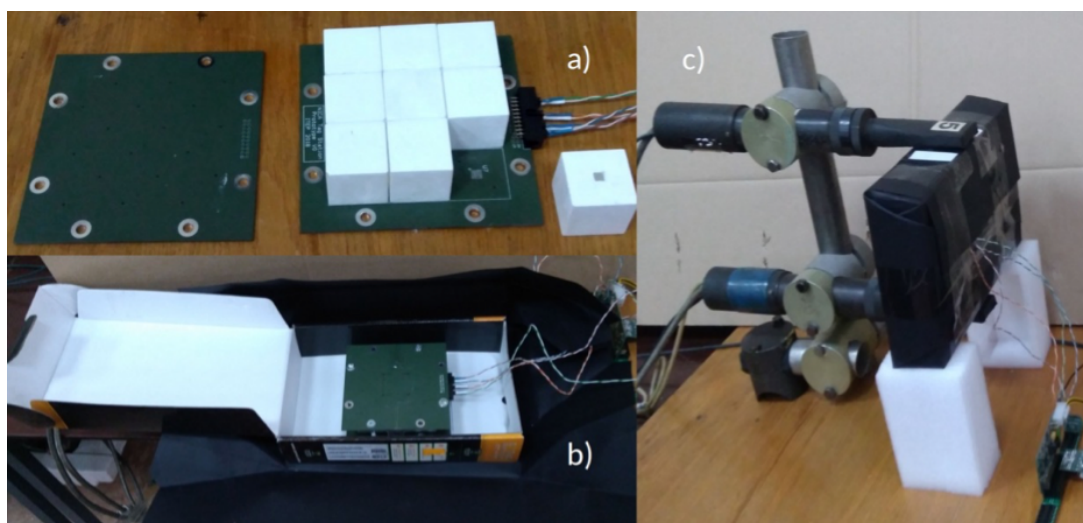


Figure 4.46: One layer prototype: a) 9 cubes of $30 \times 30 \times 30 \text{ mm}^3$ plastic, SiPM board and support board; b) the prototype assembly in a box before wrapping in black paper; c) the box in place for cosmic muon tests.

2403 and about 1.8 mm for 12 GeV which corresponds to 0.3 and 0.18 mrad for the $L \sim 10 \text{ m}$ distance from the
 2404 interaction point. For neutrons space resolution is 10-13 mm within energy range 1-12 GeV. Longitudinal
 2405 energy distributions for photons and neutrons are very different and can be used for neutron/photon
 2406 separation.

2407 For experimental estimates of the time resolution an assemblage of 9 plastic cubes laid on a printed
 2408 circuit board with mounted SiPMs and fixed with a support board (see Fig. 4.46) was tested with cosmic
 2409 muons. Each cube was of $30 \times 30 \times 30 \text{ mm}^3$ in size and is chemically covered with a thin light reflecting
 2410 layer. A numerical simulation has shown the mean number of cells hit in an event is more than 20 for
 2411 both photons and neutrons. It means the total thickness of scintillator plates of the order of 15 cm (5
 2412 times more than for tested prototype). The test results obtained for the prototype were extrapolated to the
 2413 full ZDC. Thus the expected time resolution has to be about 150 ps.

2414 The proposed design of the ZDC calorimeter satisfies most of its physics goals in the limited space inside
 2415 the magnet. The exception is the energy resolution for neutrons, which is reached by larger calorimeter
 2416 only. Nevertheless even this goal could be achieved by more elaborated analysis taking advantage from
 2417 the calorimeter fine granularity.

Chapter 5

Local polarimetry [V. Ladygin]

The main goal of the local polarimetry at SPD is the permanent monitoring of the beam polarization during data taking to reduce the systematic error coming from the beam polarization variation. Another task is beam polarization monitoring independent on the major polarimeters (CNI and the absolute one), as well as possible usage of this tool to tune the beam polarization axis. Since the SPD energy range is relatively new for spin physics, there is a lack of precise polarization data allowing one to find the explicit solution for the local polarimetry.

1 Asymmetry in inclusive production of charged particles

One of the tools to control the proton beam polarization is measurements of the azimuthal asymmetry in inclusive production of charged particles in collisions of transverse polarized proton beams. Such a method is well adopted at the STAR detector. Two Beam-Beam Counters (BBCs) are used for this purpose. Each BBC consists of two zones corresponding to different rapidity range. The inner and outer zones cover $3.3 < |\eta| < 5.0$ and $2.1 < |\eta| < 3.3$, respectively. The BBCs detect all the charged particles produced in the forward direction within their acceptance.

The correlation of the beam asymmetries measured by the RHIC pC CNI polarimeter [359, 360] and the STAR BBCs is demonstrated in Fig.5.1. One can see that the measurements by BBCs are sensitive to the transverse polarization of the colliding beams. The value of the effective analyzing power A_N for inclusive production of charged particles at $\sqrt{s} = 200$ GeV is about $(6 \div 7) \times 10^{-3}$. At NICA energies it will have, in principle, the same magnitude, or even a larger one due to a larger analyzing power for the p - p elastic scattering. Therefore, the BBCs can be used for the local polarimetry at SPD. The design of the SPD BBCs is described in the previous section.

2 Inclusive π^0 production

One of the reactions to measure and to monitor the vertical component of the polarized proton beam is the inclusive $pp \rightarrow \pi^{\pm,0} X$ reaction. Fig.5.2(a) demonstrates the single transverse spin asymmetries A_N obtained in the p - p collision for π^+ , π^0 and π^- inclusive production at 200 GeV ($\sqrt{s} \sim 20$ GeV)[168, 169]. The data demonstrate large values of the single transverse spin asymmetries with their signs following to the polarization of the valence quarks in the pions. This regime occurs already at 22 GeV [361] corresponding to $\sqrt{s_{NN}} \sim 7$ GeV for the collider option. Therefore, the inclusive neutral pion production can be used for the polarimetry over the full energy range of the SPD experiment.

The value of the single transverse spin asymmetry in the $pp \rightarrow \pi^0 X$ reaction is almost twice smaller than

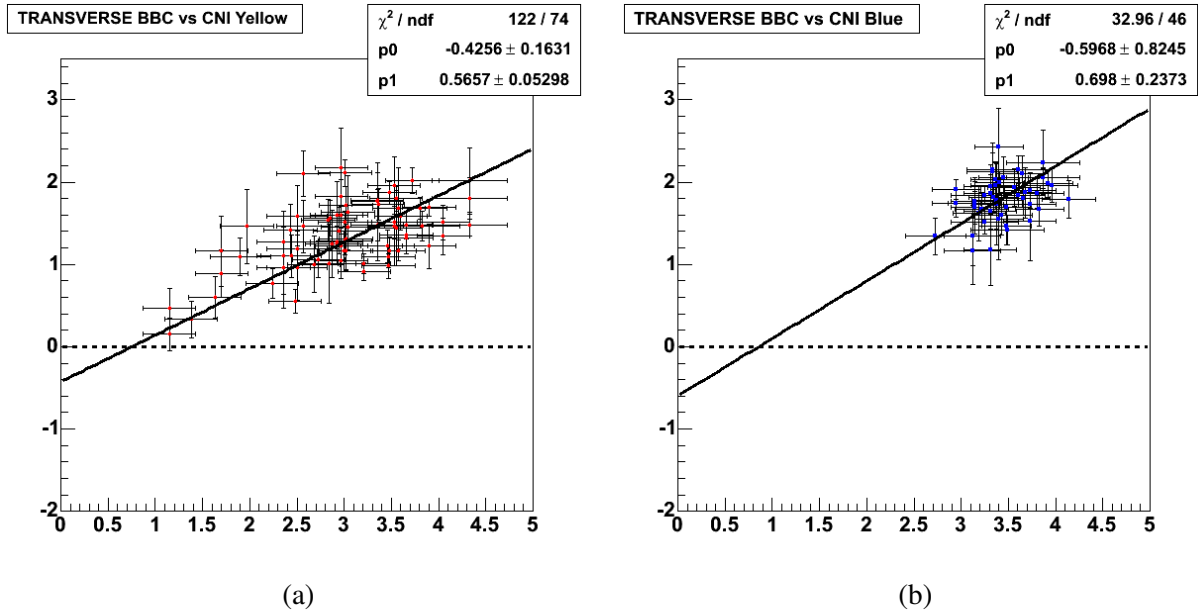


Figure 5.1: Correlation of the beam asymmetries measured by the RHIC pC CNI polarimeter [359, 360] and left (a) and right (b) STAR BBCs.

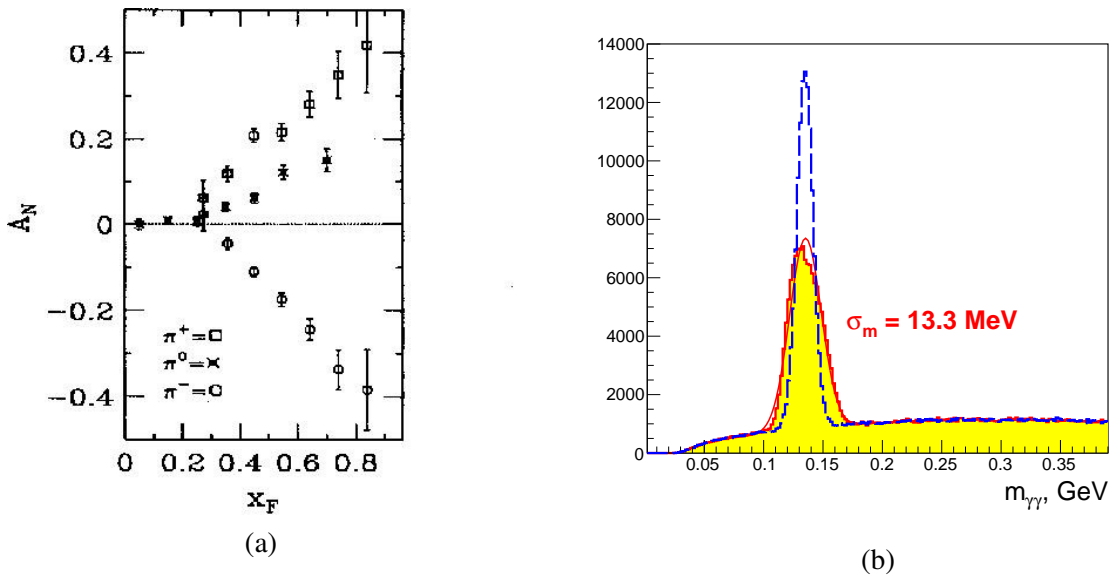


Figure 5.2: (a) Single transverse spin asymmetry A_N for inclusive pion production in p - p collisions at 200 GeV [168, 169]. (b) The π^0 reconstruction in the SPD ECAL end-cup with (red) and without (blue) vertex position information.

2449 for the charged pions production. However, the π^0 selection can be done more easily, since it does not
 2450 require track reconstruction.

2451 For online local polarimetry one can use the parts of the ECAL end-cups placed around the beam pipe.
 2452 Fast π^0 reconstruction algorithms will not include the information on the vertex position along the beam
 2453 axis, therefore, the width of the π^0 peak will increase. The Monte-Carlo results obtained for $\sqrt{s_{NN}} \sim 27$
 2454 GeV and presented in Fig.5.2(b) demonstrate such enlargement. However, one can see that the selection
 2455 of π^0 is good enough for the local polarimetry purposes. An effective analyzing power $\langle A_N \rangle$
 2456 for the kinematic range of produced π^0 $p_T > 0.5$ GeV/ c and $x_F > 0.5$ is about 0.1. The rate of π^0

2457 decays reconstructed in the end-caps of the calorimeter provides statistical accuracy of the beam polar-
 2458 ization estimation at a few-percent level after 10 minutes of data taking at $10 \text{ GeV} < \sqrt{s} \leq 27 \text{ GeV}$. The
 2459 corresponding accuracy of the spin direction reconstruction is about a few degrees.

2460 **3 Single transverse spin asymmetry for very forward neutron production**

2461 The energy dependence of the single transverse spin asymmetry, A_N , for neutron production at very
 2462 forward angles was measured in the PHENIX experiment at RHIC for the polarized p - p collisions at
 2463 $\sqrt{s}=200 \text{ GeV}$ [357]. The neutrons were observed in the forward detectors covering an angular range
 2464 of up to 2.2 mrad. The observed forward neutron asymmetries are large, reaching $A_N=-0.08\pm 0.02$ for
 2465 $x_F=0.8$; the measured backward asymmetries, for negative x_F , are consistent with zero. The results
 2466 of x_F dependence of A_N for neutron production in the (upper) ZDC trigger sample and for the (lower)
 2467 ZDC \otimes BBC trigger sample are shown in Fig.5.3(a). The error bars show statistical uncertainties, and the
 2468 brackets show the p_T -correlated systematic uncertainties. The data were obtained for 2 types of triggers:
 2469 the first one is the ZDC trigger for neutron inclusive measurements, requiring an energy deposit in the
 2470 ZDC to be greater than 5 GeV. The other one was a ZDC \otimes BBC trigger, a coincidence trigger of the ZDC
 2471 trigger with the BBC hits defined as one or more charged particles in both of the BBC detectors.

2472 The observed large asymmetry for forward neutron production was discussed within the pion exchange
 2473 framework, with interference between the spin-flip amplitude due to the pion exchange and the non-flip
 2474 amplitudes from all Reggeon exchanges. The numerical results of the parameter-free calculation of A_N
 2475 are in excellent agreement with the PHENIX data (see Fig.5.3(b)). One can see that A_N is increasing
 2476 almost linearly as a function of neutron transverse momentum q_T . One can expect the A_N value of \sim -
 2477 0.02 at $\sqrt{s}=27 \text{ GeV}$. Therefore, the $pp \rightarrow nX$ reaction with the neutron emission at very forward angles
 2478 can be used at SPD at least at a higher energy.

2479 Very forward neutrons are detected by two zero-degree calorimeters (ZDCs) [363] placed in the gaps
 2480 between the ion tubes of the colliding beams on the left and right from the center of the detector. Two
 2481 ZDCs will be also placed at SPD. These ZDCs can be considered as an additional tool for the local
 2482 polarimetry for pp-collisions at the highest NICA energy.

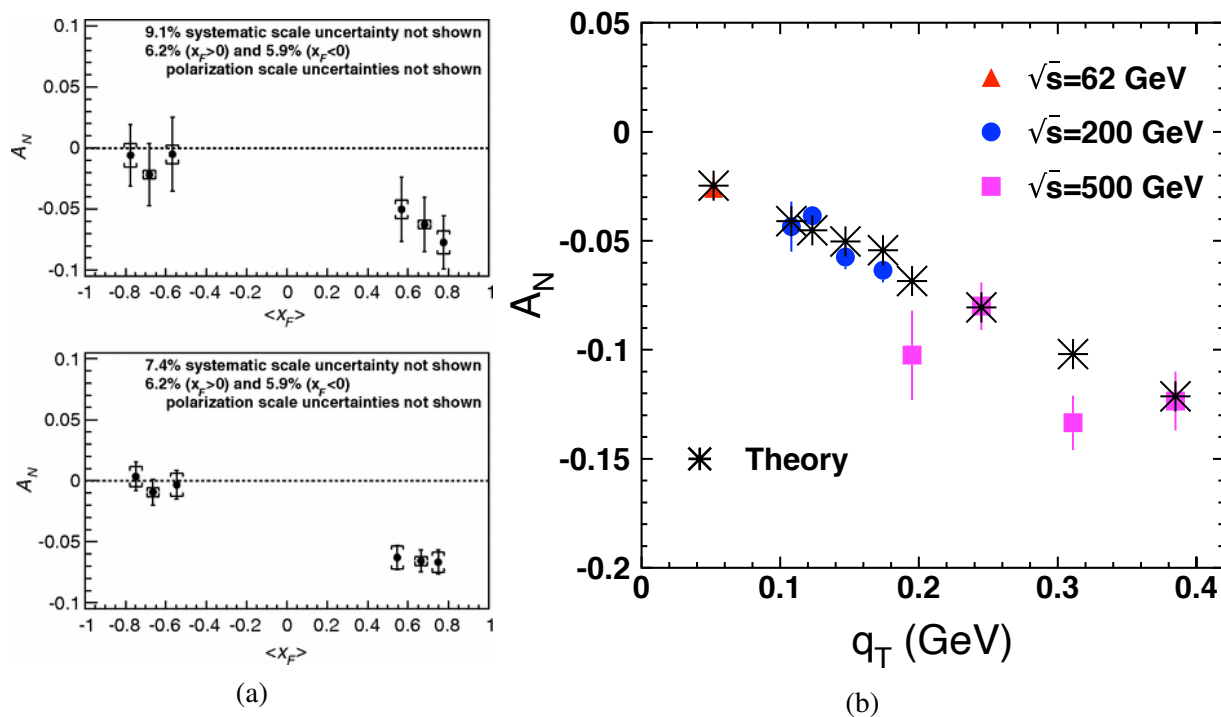


Figure 5.3: (a) x_F dependence of A_N for neutron production in the (upper) ZDC trigger sample and for the (lower) ZDC \otimes BBC trigger sample. (b) Single transverse spin asymmetry A_N in the reaction $pp \rightarrow nX$ measured at $\sqrt{s} = 62, 200, 500$ GeV at PHENIX. The asterisks show the result of the theoretical calculations [362].

Chapter 6

Detector control system [A. S. Chepurnov]

SPD detector control system (DCS) is designed to control the basic operating modes of the detector parts and the entire detector as a whole, for continuous monitoring of slowly changing parameters, of the detector itself, of engineering means which provide the detector operation and of the environment. DCS is synchronized with the basic operating modes of the NICA accelerator complex by means of synchronization subsystem shared between DCS and SPD DAQ. DCS provides parameterization of the managed object (i.e. SPD detector), implements algorithms for normalization, parameters measurement and control based on these parameters and generates necessary sets of abstractions and options for presenting these abstractions to the operator in intuitive manner. Critical values parameters going beyond the predefined limits in predetermined situations cause emergency events and initiate procedures for handling such events, including the procedure for automatically detector shutdown in order to prevent its damage. Parameter values are being archived in a database for long-term monitoring of the detector operation and identify possible failures in the operation of the equipment and emergency situations. The configurations of the detector parameters saved in the database make it possible to start the detector promptly and use it with various preset parameters and in various operating modes in accordance with the requirements of the particular physics experiment. DCS allows the autonomous operation of each detector subsystem at the stage of initial start-up, periodic maintenance, calibration sessions and planned upgrades. The number of parameters in the system is expected to be significant, so it is assumed that the system should be extendable and flexibly configurable. Architectural and software solutions based on the event-driven model [364] and client-server and producer-consumer [365] interaction models should be preferred for communication when building general DCS and control systems of each part of the detector. Centralized systems operating in the master-slave polling mode should be avoided.

1 DCS concept

Most of high-energy physics detectors include parts consisting of similar systems built from devices, sensors and actuators with similar or identical functionality. This determines parameterization of the entire detector as a managed object. Such systems include: 1) High voltage (HV) power supply system for powering gas detectors and light (photon) sensors (PMT and SiPM); 2) Low voltage (LV) power supplies for powering of magnets, digital and analog electronics; 3) Cryogenic systems; 4) Gas supply and mixing systems; 5) Vacuum systems; 6) Front-end electronic LV powering control and temperature monitoring; 7) Different cooling and temperature control systems; 8) DAQ system; 9) Accelerator interface and synchronization; 10) General external electricity and water cooling stations, etc.

The SPD detector is no exception and includes almost all of these systems spread among different parts of the detector as shown at layout diagram Fig. 6.1. Each part of the detector refers to one or more

2517 subsystems. The composition of the systems will be refined as the individual parts of the detector are
 2518 developed.

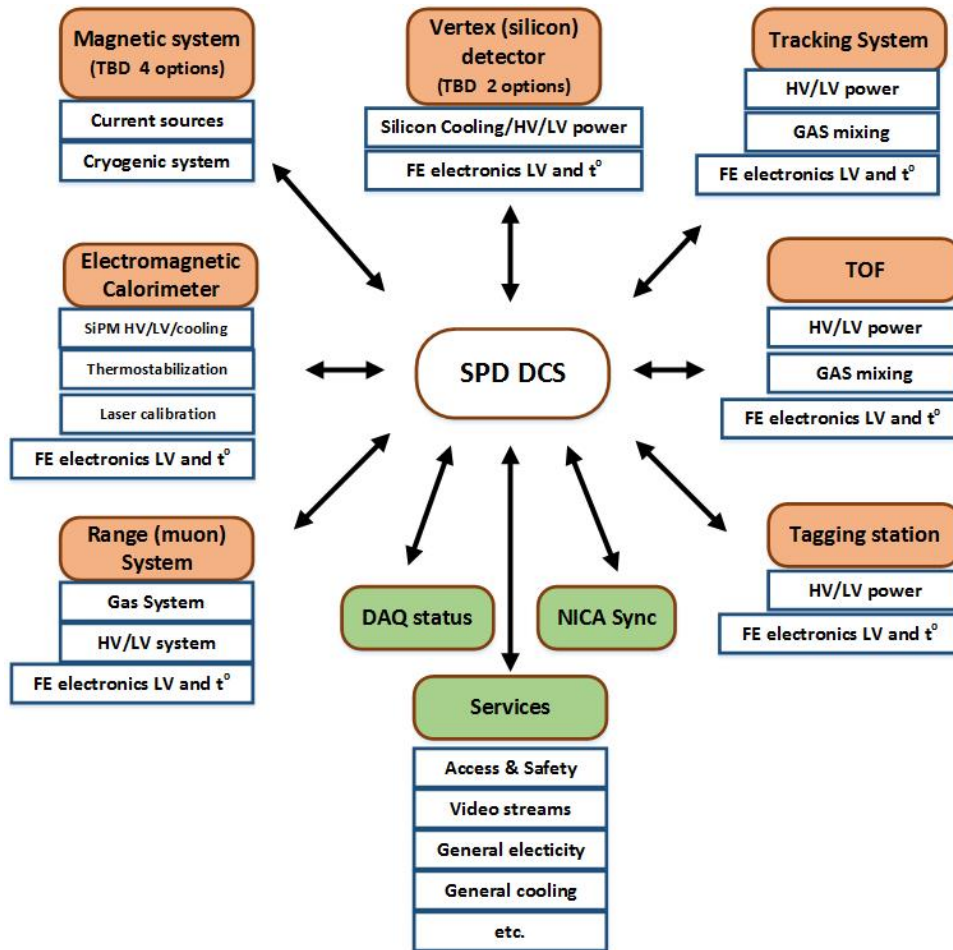


Figure 6.1: SPD detector control system layout.

2519 All the systems can be similarly parameterized and shown to the operator in an intuitive presentation in
 2520 order to simplify the operator’s decision-making algorithm. However, the physical implementation at the
 2521 hardware level of these elements may vary significantly in different parts of the SPD, because of: - the
 2522 parts inherit the experience of their developers gained in previous experiments, - hardware and software
 2523 components are selected based on their cost and availability, - parts of the detector are manufactured at
 2524 different times. Nevertheless, in order to optimize financial and human resources costs for the creation
 2525 of the entire detector and DCS in particular, it is necessary to recommend the developers of the detector
 2526 parts to strive for standardization of the used hardware and embedded software. This will significantly
 2527 reduce the efforts for developing, deploying and operating the detector and will result in significant cost
 2528 savings. To achieve these goals, it is advisable to work out at the stage of prototyping detector systems
 2529 not only the detector itself, front-end electronics and DAQ, but also slow control systems. This work can
 2530 be carried out in the Beam Test Zone (BTZ), for which the BTZ slow control system must be made as
 2531 similar as possible to the final DCS version.

2 DCS architecture

The detector control system is divided into three logical levels (Fig. 6.2). The lower layer includes measurement channels built into the Front End Electronics (FEE) and Data Acquisition (DAQ) of the detector parts, various stand-alone sensors, I/O devices, and low and high voltage power supplies. The middle level is represented by programmable logic controllers and integrated ready-made and custom made subsystems (vacuum posts, gas consoles, multichannel ready-made power subsystems etc.). Interfaces to the FEE and DAQ that provide data for the detector control system are also at this level. The upper level is designed to provide a human-machine interface for operators, implement a database of detector parameters and configurations, communicate with the external world (accelerator, engineering support systems, access system, etc.) and implement macro-control algorithms common for the entire detector. All these levels are connected in a hierarchical network using fieldbuses between the first and second level, for example CAN-bus with CANopen protocol. Ethernet LAN is used between the middle and upper levels. At the top level, special software such as SCADA (Supervisory Control And Data Acquisition) is used, which provides control, collection and storage of data in real time. It is proposed to use the WinCC OA system widely used in CERN as a SCADA system. We understand that for smooth and reliable communication with Nuclotron's control system, a gateway to the Tango Controls [366, 367] system should be developed and deployed.

3 SCADA for DCS

WinCC OA (ex PVSS-II) [368, 369] is a commercial SCADA system. It is a software component constructor that allows to use both preinstalled prototypes and templates, and software modules and system components developed in C. This system is actively used in many experiments at CERN and has support and safety certificates in the Russian Federation. The following properties make WinCC OA an attractive solution for use in DCS SPDs:

- object-oriented approach built into the system ensures an efficient development process and the ability to flexibly expand the system;

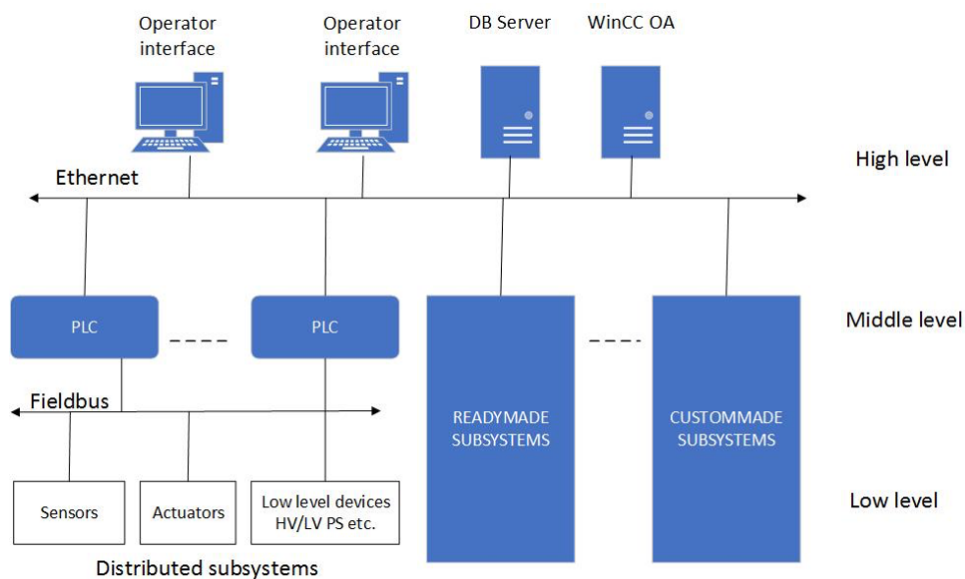


Figure 6.2: SPD detector control system architecture.

- 2557 – capability to create distributed systems - up to 2048 WinCC OA servers;
- 2558 – scalability from a simple single-user system to a distributed redundant network system with 10
2559 million tags (physical and synthetic parameters);
- 2560 – platform independent system is available for Windows, Linux;
- 2561 – event-driven system;
- 2562 – hot standby and 2x2 redundancy (DRSystem), the required level of availability and reliability;
- 2563 – wide range of drivers and options for communication OPC, OPC UA, S7, Modbus, IEC 60870-5-
2564 101/104, DNP3, XML, JSON, SOAP...;
- 2565 – support by major manufacturers of electronic devices for building automation systems in high
2566 energy physics.

2567 Each functional unit of the system that is software implemented as a separate process is called manager.
2568 A set of managers forms a system. Data exchange and communications between managers are done via
2569 TCP. The data is exchanged by means of passing events. The system allows parallelizing processes (man-
2570 agers) by running them on different computers with different OS. The system is scalable and balances
2571 load on control computers. The required managers start only if necessary and multiple instances may
2572 run simultaneously. Managers can be distributed across multiple computers/servers. The WinCC OA
2573 block diagram is shown in figure 6.3. The main process is the Event Manager, it contains and manages
2574 the process image (current values of all process variables), receives and qualifies data (central message
2575 manager), distributes data across other managers, acts as a data server for others, manages users autho-
2576 rization, manages the generation and status of alarm messages. The Database Manager receives data
2577 from the Event Manager and handles it according to its own algorithm. Historical database can use ei-
2578 ther proprietary database (HDB) or Oracle DBMS (the Oracle Real Application Clusters configuration is
2579 also supported). Parallel archiving in Oracle and HDB databases is possible. It is also possible to record
2580 user-defined data and log system events and messages in external relational database (MS SQL, MySQL,
2581 Oracle, etc).

2582 The WinCC OA Report Manager supports different ways of generating reports:

- 2583 – in Microsoft Excel format;
- 2584 – in xml format with the ability to display in any external tool for working with reports (Eclipse
2585 BIRT, Crystal Reports, SYMATIC Information Server etc.), SOAP protocol is also supported
2586 (Simple Object Access Protocol).

2587 Project development for the WinCC OA system is based on an object-oriented approach. In the WinCC
2588 OA data model, objects are represented as data points that characterize the image of a specific physical
2589 device or process. For each data point (called tag) element, properties and actions can be defined in
2590 accordance to it, such as signal processing (smoothing, setting limits, etc.), communication with external
2591 systems, archiving, generation of alarm messages (alarms), etc. Typing and inheritance are supported,
2592 due to which arbitrary hierarchical data structures can be created. Similarly, the principles of inheritance
2593 and reusability are implemented for graphical objects. The WinCC OA IDE includes the PARA configu-
2594 ration editor and the GEDI graphical editor of User Interface Manager (UI) (includes a data model editor,
2595 mass configuration tools, administration tools, an interface to version control systems, a debugger, etc.).
2596 Changes to data structures and graphics are applied without restarting the project. Writing custom scripts
2597 can be done using CONTROL ++ (a programming language, whose syntax is similar to C / C ++). Such

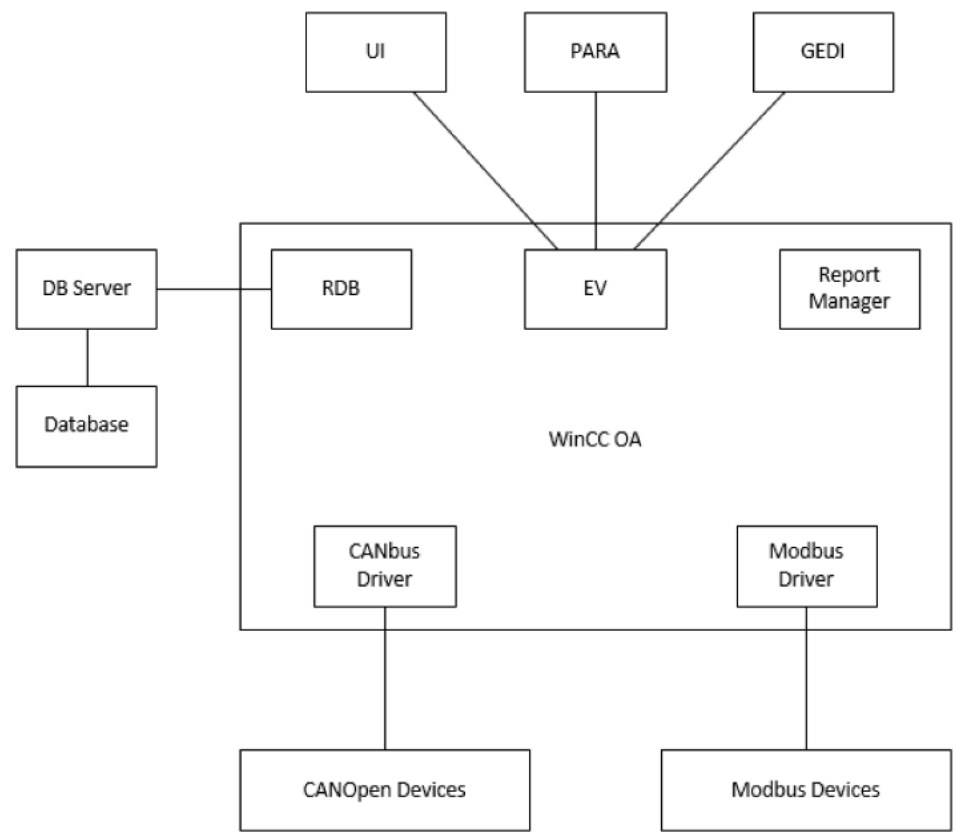


Figure 6.3: SCADA structural scheme of WinCC OA software.

2598 scripts can be both event handlers associated with elements of the graphical interface, and data process-
 2599 ing procedures. The system includes standard graphical objects library; it can be extended by developing
 2600 user objects or using the Qt Toolkit widgets. It is also possible to use the JavaScript libraries available
 2601 on the market or included JavaScript scripts. Thanks to the open API (C++ / C# API), it is possible to
 2602 create managers, drivers, widgets and CONTROL++ extensions. A new set of tools is available for the
 2603 concept of High Speed Programming implementation, which supports documentation build-up from the
 2604 source code, unit testing and autocompletion of program structures.

2605 It is also planned to provide data exchange between WinCC OA and Tango Controls which is used aon
 2606 upper level of NUCLOTORN's control system. This can be implemented using standard OPC technolo-
 2607 gies using a client-server architecture, or it can be implemented using SQL tools as a common database
 2608 for both SCADA systems used for accelerator and detector. The final choice of a suitable solution will
 2609 be made at the stage of system implementation. .

Chapter 7

Data acquisition system [L. Afanasyev]

1 Introduction

The data acquisition system of the SPD should provide continuous data taking, including data readout from the front-end electronics, data consistency check, event building and writing events to a storage. The system should have no dead time or minimal dead time. *These features will be implemented with the DAQ operating in a free-running (trigger-less) mode.*

Other important tasks of the DAQ are:

- initialization of hardware;
- control and monitoring of the data taking process: control of the status of all hardware devices including front-end electronics, status of software, quality of collected data;
- monitoring of the parameters characterizing the detector performance (accumulation of time, amplitude and hit distribution histograms, detector rates, etc.);
- logging of information and errors;
- distribution of data over computing nodes for further online analysis;
- etc.

The data acquisition system of SPD should withstand the data flux from p - p , p - d or d - d interactions at the extreme conditions of high luminosity. At the highest NICA energy and luminosity, $\sqrt{s} = 27$ GeV and $L = 10^{32} \text{ cm}^{-2} \text{ s}^{-1}$, the interaction rate within the SPD aperture will be 4 MHz, and the average multiplicity **about 20** ????. This drastically differs from the conditions of another NICA experiment, MPD, where the collision rate of heavy ions is orders of magnitude less, but the multiplicity is much higher.

The structure of DAQ will be similar to recently modernized DAQ of the COMPASS experiment at CERN [370–376]. The COMPASS DAQ extensively uses logical programmable integrated circuits FPGA at different levels of the system. This allows one to handle large data streams with minimal latency and provides very good flexibility. Unlike the COMPASS experiment, which uses the beam of the CERN SPS with a spill time structure, the SPD DAQ will deal with a continuous beam.

The DAQ of SPD will operate in a free-running mode, when the readout is not controlled by a trigger system, but occurs with a fixed frequency. It requires all front-end electronics running in a self-triggered

Table 7.1: Summary of detectors outputs to DAQ. Information type: T means time, A – amplitude (or charge).

Sub-detector	Information type	Number of channels	Channels per FE card	Number of outputs
Vertex detector	T + A	460800	640	720
Straw tracker	T / T+A	25000	64	391
Calorimeter	T + A	30176	64	472
PID??	T			
BBC				
Range system	T	106000	192	553
ZDC				
Total		621976		2136

mode, and the readout happens synchronously with a common clock distributed by the precise timing system. All the data received between the acts of readout are accumulated in the memories implemented in the front-end electronics modules and are stored there until the next readout. The readout frequency value will be chosen depending on the detector rates and memory depths available in the front-end cards. The width of the time slice between the successive readouts should be much larger than the response time of the sub-detectors in order to minimize the probability of separating an event into two slices.

Digitization of data and zero suppression occur in the front-end electronics. It is expected that the so-called "feature extraction algorithm" will be implemented in the front-end electronics of the Vertex detector and the Calorimeter. This algorithm, which is under development in several collaborations (in particular, PANDA [377], COMPASS [378–380]), allows transferring only the extracted time and amplitude, instead of many samples of the digitizer, thus greatly decreasing the amount of data to be transferred.

For now the expected data flux in the hardest conditions of the experiment (maximum energy and luminosity) has been estimated without detailed simulations, but using the current knowledge of the sub-detector structure, particle multiplicity per event, hit multiplicity in different detectors, expectations about the front-end electronics parameters and, where relevant, results of the beam tests at other experiments (MPD, PANDA). The total number of channels to be read out is about 700 thousand, with the major part coming from the Vertex Detector (~ 460 thousand for the VD strip option). The full numbers are given in Table 7.1. Preliminary estimation for the data flow is about 20 GB/s including some margin of safety.

2 DAQ structure

The scheme of the DAQ is presented in Fig. 7.1. The data from the front-end electronics cards come to the detector interface cards (FE concentrators). Now the existing electronics card with 12 input is considering as FE concentrators [372]. The Data-Handler multiplexers (UDHmx) are configured on the base of FPGA. The multiplexer has 48 high speed input and up to 8 output interfaces. They verify the consistency of data and store them until receiving the readout signal.

The two Data-Handler Switches (UDHSw) function as a 10×10 switch and perform event building with a maximum throughput rate of 10 GBytes/second. The UDHSw's perform the final level of event building and distribute the assembled events to 20 readout computers. The Data-Handler Switches and Data-Handler multiplexers are implemented on the same electronics cards by means of different firmware.

2669 Each readout computer is equipped with a dedicated PCIe buffer card for data collection. These cards are
2670 built on a FPGA chip and are commercially available. The current version of the card used in COMPASS
2671 has a bandwidth close to 1 GB/s [375]. Finally, the continuous sequence of slices is formed below the
2672 Network Switch in each of on-line computers to be used for on-line filtering and event monitoring.

2673 The slow control software accesses the front-end electronics via the FE concentrators using the UDP-
2674 based IPBus protocol [381]. The interface cards retransmit control and clock signals provided by the
2675 time distribution system to the corresponding front-end electronics, and convert the detector information
2676 from the detector specific interfaces to a common high-speed serial interface running over optical fiber.
2677 It is foreseen to use UCF [382] as a standard high speed link protocol within the DAQ.

2678 The White Rabbit system [383, 384] is planned to be used at NICA for time synchronization. It provides
2679 synchronization for large distributed systems with a time-stamping of 125 MHz, sub-nanosecond accu-
2680 racy and ~ 10 ps precision. Signals from the White Rabbit system will be used as an input for the Time
2681 Control System (TCS) [385] which will distribute clock signals through the whole electronic system.

2682 **3 Data format**

2683 The time structure of the expected data flow during a run is shown in Fig. 7.2. All processes are syn-
2684 chronized with a 125-MHz clock coming from the White Rabbit system. A Run is started after the reset
2685 procedure which includes all initialization processes. Afterwards, the continuous data flow is divided
2686 into a sequence of time slices. The proposed time slice duration can be selected in the range from 1 μ s to
2687 8.3 ms and will be chosen according to the data flux and capacity of the whole chain of data collection.
2688 Longer slices are preferable, because the longer the slice, the less the probability an event falling into
2689 two adjacent slices is. The slices have a continuous numbering within a frame, a wider time interval,
2690 which can extend from 65 ms to 549.7 s. The slice numbering is reset every Frame by the Start of the
2691 Frame signal.

2692 The proposed formats of the collected data are shown in Figs. 7.3–7.7. The data are formatted at all
2693 stages of transfer from the Front-End Concentrators to the Data-Handler Switches. The required headers
2694 and checksums are added at all stages.

2695 In Fig. 7.3, the structure of a Run is shown. The Run consists of a sequence of Frames (Fig. 7.4)
2696 numbered from 0 to N, where N, the maximum number of frames in the Run, is assigned by the TCS
2697 controller. The Frame consists of a sequence of slices numbered from 0 to K, the maximum number of
2698 slices in the Frame, which is also assigned by the TCS controller.

2699 Fig.7.5 shows the structure of the Slice. The Slice contains a sequence of Data Blocks from the Data
2700 Concentrators (Fig. 7.6). Finally, the lowest unit in the Data Format chain is the Data Block of FE
2701 Concentrators (Fig. 7.7) which contains Physical Data from several ports the amount of which depends
2702 on the FE card type.

2703 The proposed format provides a unique connection of the physical information to the detectors geometry
2704 and the event time.

2705 **4 Cost estimate**

2706 The numbers of modules and their preliminary cost estimation are summarized in Table 7.2.

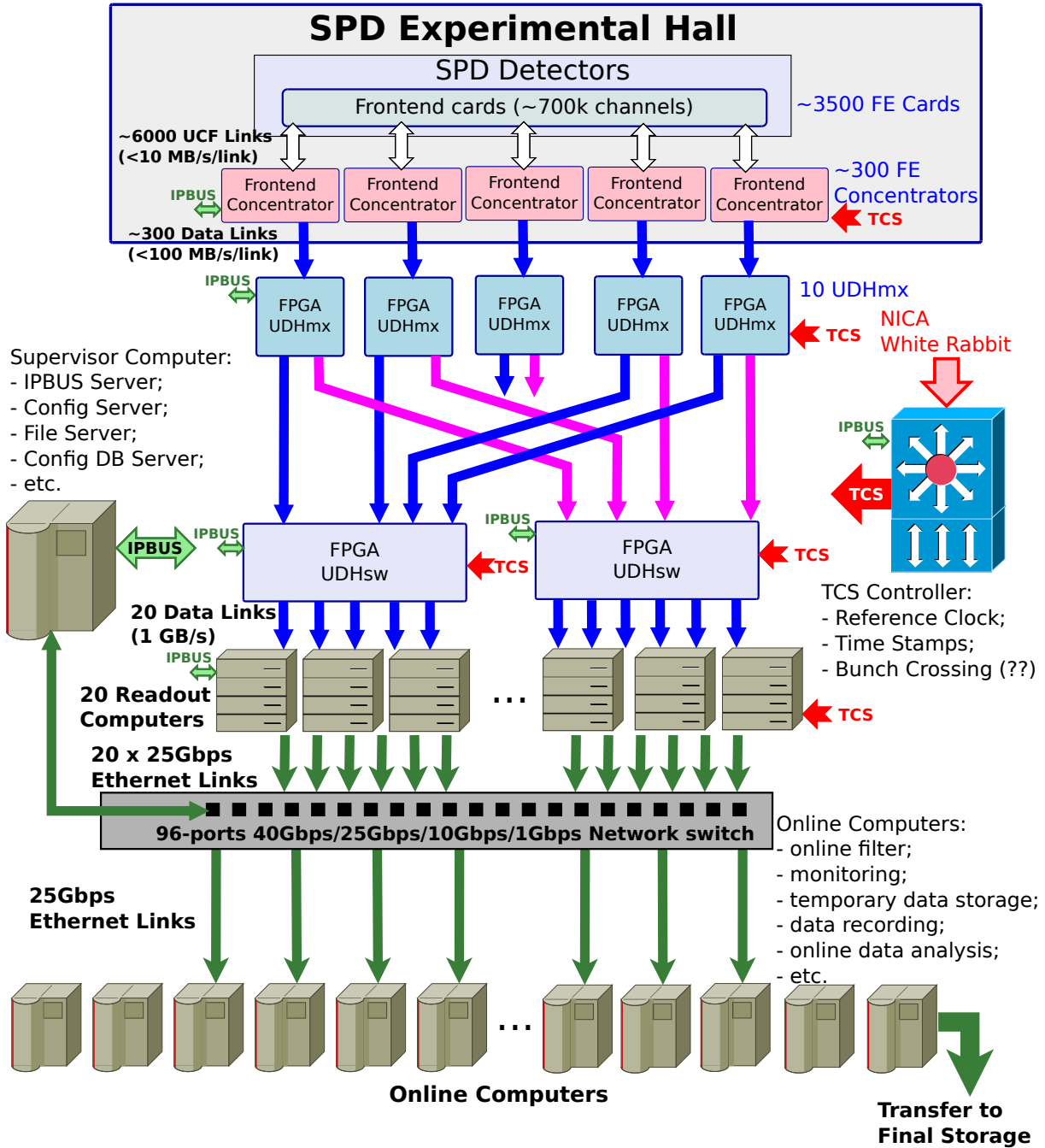


Figure 7.1: General structure of DAQ-SPD.

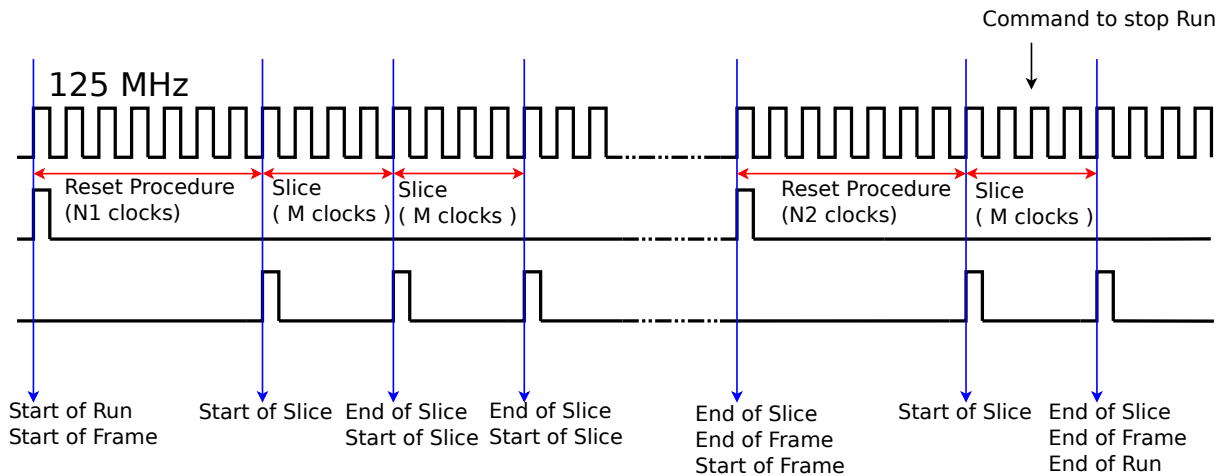


Figure 7.2: Time diagram of a sequence of clocks, Slices and Frames within the Run.

31	24 23	16 15	0
Start of Run	Run Number		
Start of Run Time in seconds since DATE			
Frame 0			
Frame 1			
...			
Frame K			
End of Run	LSB of Run Number	Run Number	
Start of Run	Run Number		
End of Run Time in seconds since DATE			

Figure 7.3: Data Format: Run structure.

31	24 23	16 15	0
Start of Frame	LSB of Run Number	Frame Number	
Start of Frame Time in seconds since DATE			
Slice 0			
Slice 1			
...			
Slice K			
End of Frame	LSB of Run Number	Frame Number	
End of Frame Time in seconds since DATE			

Figure 7.4: Data Format: Frame structure.

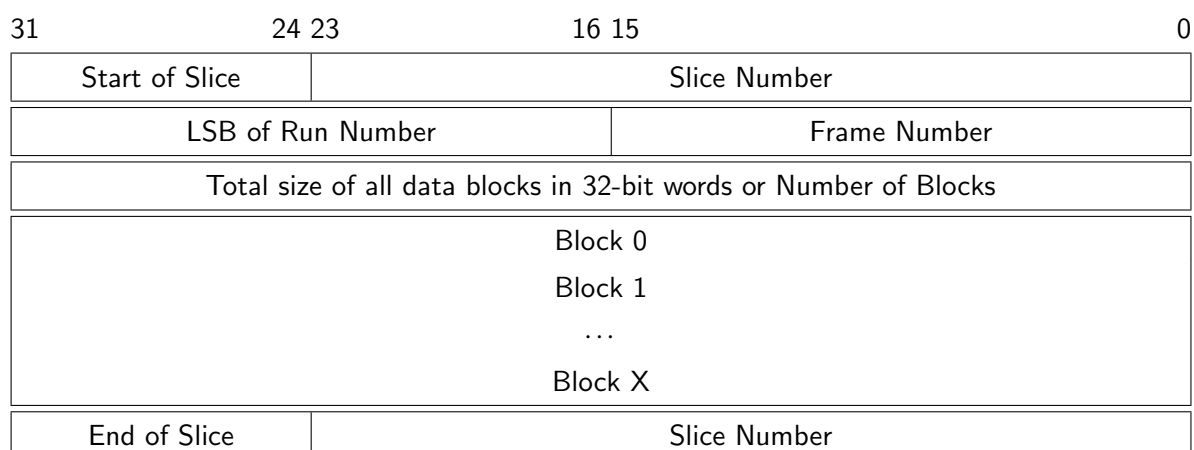


Figure 7.5: Data Format: Slice structure.

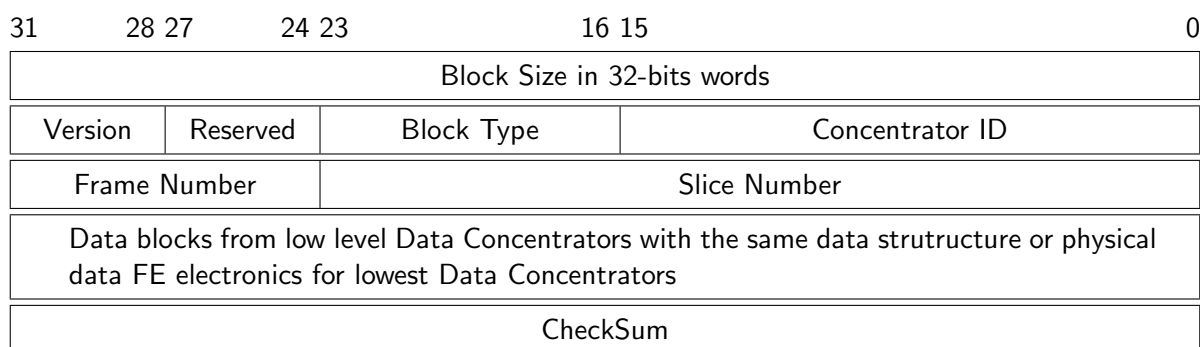


Figure 7.6: Data Format: structure of Data Blocks of High Level.

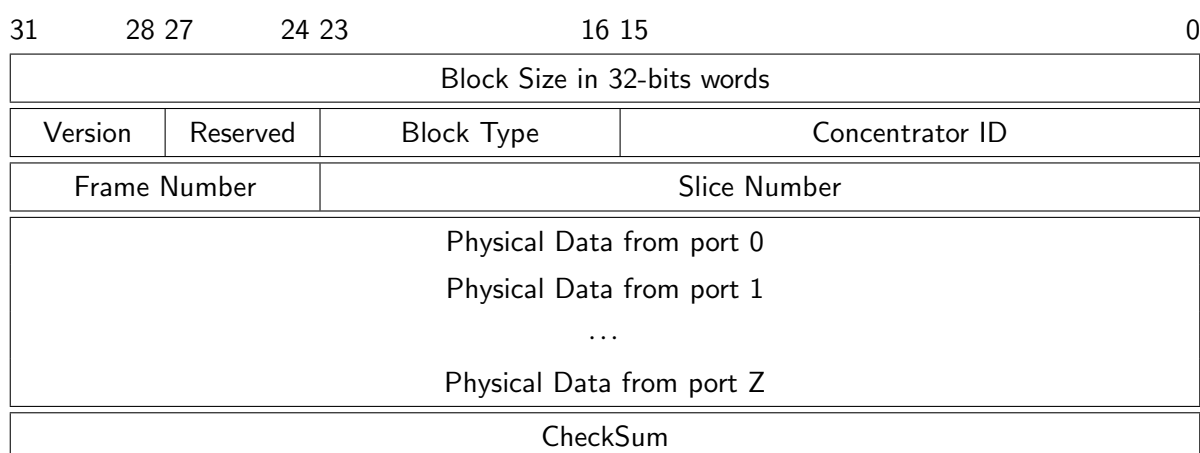


Figure 7.7: Data Format: structure of Low Level Data from FE Concentrators.

Table 7.2: Cost estimation of DAQ

	Number	Cost (k\$)	Total (k\$)
FE concentrators	180	3.5	630
UDHmx modules	12	17.5	210
UDHsw modules	3	17.5	52
Case for UDHmx modules	6	2.3	14
Time Distribution	1	35	35
Online Computers	20	12	240
VME crates	20	5.93	120
Consumables			100
Contingencies			≈200 (15%)
Total			1600

Chapter 8

Computing and Offline Software

1 SPD Computing Model

Expected event rate of the SPD experiment is about 3 MHz (pp collisions at $\sqrt{s} = 27$ GeV and 10^{32} $\text{cm}^{-2}\text{s}^{-1}$ design luminosity). This is equivalent to the raw data rate of 20 GB/s or 200 PB/year, assuming the detector duty cycle is 0.3, while the signal-to-background ratio is expected to be in order of 10^{-5} . Taking into account the bunch crossing rate of 12.5 MHz, one may conclude that pile-up probability will be sufficiently high.

The key challenge of the SPD Computing Model is the fact, that no simple selection of physics events is possible at the hardware level, because the trigger decision would depend on measurement of momentum and vertex position, which requires tracking. Moreover, the free-running DAQ provides a continuous data stream, which requires a sophisticated unscrambling prior building individual events. That is the reason why any reliable hardware-based trigger system turns out to be over-complicated and the computing system will have to cope with the full amount of data supplied by the DAQ system. This makes a medium-scale setup of SPD a large scale data factory.

The continuous data reduction is a key point in the SPD computing. While simple operations like noise removal can be done yet by DAQ, it is an online filter that is aimed at fast partial reconstruction of events and data selection, thus being a kind of a software trigger. The goal of the online filter is to decrease the data rate at least by a factor of 50 so that the annual upgrowth of data including the simulated samples stays within 10 PB. Then, data are transferred to the Tier-1 facility, where full reconstruction takes place and the data is stored permanently. Two reconstruction cycles are foreseen. The first cycle includes reconstruction of some fraction of each run necessary to study the detector performance and derive calibration constants, followed by the second cycle of reconstruction of full data sample for physics analysis. The data analysis and Monte-Carlo simulation will likely run at the remote computing centers (Tier-2s). Given the large data volume, a thorough optimization of the event model and performance of reconstruction and simulation algorithms are necessary.

Taking into account recent advances in the computing hardware and software, the investment in the research and development necessary to deploy software to acquire, manage, process, and analyze the data recorded is required along with the physics program elaboration and the detector design. While the core elements of the SPD computing system and offline software now exist as prototypes, the system as a whole with capabilities such as described above is in the conceptual design stage and information will be added to SPD planning documents as it is developed.

2739 **2 Online Filter**

2740 The SPD online filter facility will be a high-throughput system which will include heterogeneous com-
2741 puting platforms similar to many high performance computing clusters. The computing nodes will be
2742 equipped with hardware acceleration. The software framework will provide the necessary abstraction so
2743 that common code can deliver the selected functionality on different platforms.

2744 The main goal of the online filter is a fast reconstruction of the SPD events and suppression of the
2745 background ones at least by a factor of 50. This requires fast tracking and fast clustering in the electro-
2746 magnetic calorimeter, followed by reconstruction of event from a sequence of time slices and an event
2747 selection (software trigger). Several consecutive time slices shall be considered, tracker data unpacked
2748 and given for a fast tracking. The result of the fast track reconstruction is the number of tracks, an es-
2749 timate of their momentum and an estimate of primary vertex (to distinguish between tracks belonging
2750 to different collisions). Using this outcome, the online filter should combine information from the time
2751 slices into events and add a trigger mark. The events shall be separated in several data streams using the
2752 trigger mark and an individual prescale factor for each stream is applied.

2753 One of the most important aspects of this chain is the recognition of particle tracks. Traditional tracking
2754 algorithms, such as the combinatorial Kalman filter, are inherently sequential, which makes them rather
2755 slow and hard to parallelized on modern high-performance architectures (graphics processors). As a
2756 result, they do not scale well with the expected increase in the detector occupancy during the SPD data
2757 taking. This is especially important for the online event filter, which should be able to cope with the
2758 extremely high data rates and to fulfill the significant data reduction based on partial event reconstruction
2759 ‘on the fly’. The parallel resources like multicore CPU and GPU farms will likely be used as a computing
2760 platform, which requires the algorithms, capable of the effective parallelization, to be developed, as well
2761 as the overall cluster simulation and optimization.

2762 Machine learning algorithms are well suited for multi-track recognition problems because of their abil-
2763 ity to reveal effective representations of multidimensional data through learning and to model complex
2764 dynamics through computationally regular transformations, that scale linearly with the size of input data
2765 and are easily distributed across computing nodes. Moreover, these algorithms are based on the linear
2766 algebra operations and can be parallelized well using standard ML packages. This approach was already
2767 been applied successfully to recognize tracks in the BM@N experiment at JINR and in the BESIII ex-
2768 periment in IHEP CAS in China [386, 387]. In the course of the project an algorithm, based on recurrent
2769 neural networks of deep learning, will be developed to search for and reconstruct tracks of elementary
2770 particles in SPD data from the silicon vertex detector and the straw tube-based main tracker. The same
2771 approach will be applied to the clustering in the SPD electromagnetic calorimeter, and fast π^0 recon-
2772 struction. The caution is necessary, though, to avoid possible bias due to an inadequacy of the training
2773 data to the real ones, including possible machine background and the detector noise. A dedicated work-
2774 flow that includes continuous learning and re-learning of neuron network, deployment of new versions
2775 of network and the continuous monitoring of the performance of the neural networks used in the online
2776 filter is necessary and needs to be elaborated.

2777 Besides the high-level event filtering and corresponding data reduction, the online filter will provide input
2778 for the run monitoring by the shift team and the data quality assessment, as well as local polarimetry.

2779 **3 Computing System**

2780 The projected rate and amount of data produced by SPD prescribe to use high throughput computing
2781 solutions for the processing of collected data. It is the experience of a decade of the LHC computing that
2782 already developed a set of technologies mature enough for the building of distributed high-throughput

2783 computing systems for HEP.

2784 3.1 The Computing Model

2785 The 'online' part of computing systems for the SPD experiment, namely the online filter described above,
 2786 is an integral part of experimental facilities, connected with the 'offline' part using a high throughput
 2787 backbone network. The entry point to 'offline' facilities is a high capacity storage system, connected
 2788 with 'online facility' through a multilink high-speed network. Data from high capacity storage at the
 2789 Laboratory of Information Technologies will be copied to the tape-based mass storage system for long
 2790 term storage. At the same time, data from high capacity storage will be processed on different computing
 2791 facilities as in JINR as in other collaborative institutions.

2792 The hierarchy of offline processing facilities can be introduced:

- 2793 – Tier 1 level facilities should provide high capacity long term storage which will have enough
 2794 capacity to store a full copy of primary data and a significant amount of important derived data.
- 2795 – Tier 2 level facility should provide (transient) storage with capacity that will be enough for storing
 2796 of data associated with a period of data taking.
- 2797 – Optional Tier 3 level are opportunistic resources, that can be used to cope with a pile-up of pro-
 2798 cessing during some period of time or for special analysis.

2799 Offline data processing resources are heterogeneous as on hardware architecture level so by technolo-
 2800 gies and at JINR site it includes batch processing computing farms, high performance (supercomputer)
 2801 facilities, and cloud resources. A set of middleware services will be required to have unified access to
 2802 different resources.

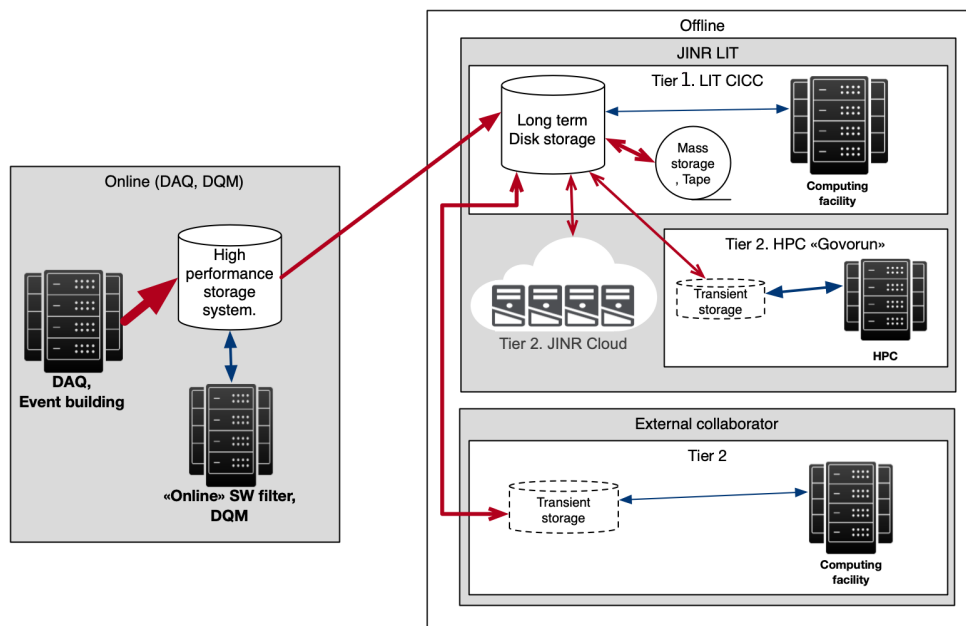


Figure 8.1: Scheme of the SPD computing system

2803 3.2 Computing services

2804 Computing systems for NICA at JINR are naturally distributed. Experimental facilities and main data
 2805 processing facilities placed across two JINR sites and, inter alia, managed by different teams. That causes
 2806 some heterogeneity not only on hardware systems but also on the level of basic software: different OSs,
 2807 different batch systems etc.

2808 Taking into account the distributed nature and heterogeneity of the existing infrastructure, and expected
 2809 data volumes, the experimental data processing system must be based on a set of low-level services that
 2810 have proven their reliability and performance.

2811 It is necessary to develop a high-level orchestrating system that will manage the low-level services.
 2812 The main task of that system will be to provide efficient, highly automated multi-step data processing
 2813 following the experimental data processing chain.

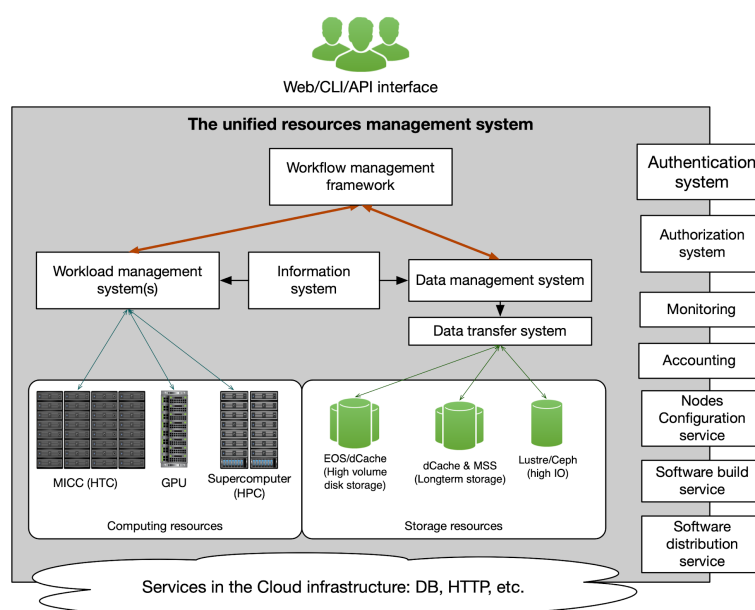


Figure 8.2: Distributed SPD computing services

2814 The Unified Resource Management System is a IT ecosystem composed from the set of subsystem and
 2815 services which should:

- 2816 – Unify of access to the data and compute resources in a heterogeneous distributed environment
- 2817 – Automate most of the operations related to massive data processing
- 2818 – Avoid duplication of basic functionality, through sharing of systems across different users (if it
 2819 possible)
- 2820 – As a result - reduce operational cost, increase the efficiency of usage of resources,
- 2821 – Transparent accounting of usage of resources

2822 Many distributed computing tools have already been developed for the LHC experiments and can be re-
 2823 used in SPD. For the task management one can use PANDA [388] or DIRAC [389] frameworks. For the

2824 distributed data management RUCIO [390] package has been developed. For the massive data transfer
2825 FTS [391] can be used. Evaluation of these tools for the SPD experiment and their implementation
2826 within the SPD Unified Resource Management System is planned in scope of the TDR preparation.

2827 **4 Offline Software**

2828 Offline software is a toolkit for event reconstruction, Monte-Carlo simulation and data analysis. Linux is
2829 chosen as a base operating system.

2830 Currently, the offline software of the SPD experiment – SpdRoot – is derived from the FairRoot soft-
2831 ware [392] and it is capable of Monte Carlo simulation, event reconstruction, and data analysis and visu-
2832 alization. The SPD detector description is flexible and based on the ROOT geometry package. Proton-
2833 proton collisions are simulated using a multipurpose generator Pythia8 [393]. Deuteron-deuteron colli-
2834 sions are simulated using a modern implementation of the FRITIOF model [394, 395], while UrQMD [396,
2835 397] generator is used to simulate nucleus-nucleus interactions. Transportation of secondary particles
2836 through the material of the SPD setup and the simulation of detector response is provided by Geant4
2837 toolkit [398–400]. Track reconstruction uses GenFit toolkit [401] and KFparticle package [402] is used
2838 to reconstruct primary and secondary vertices. The central database is going to be established to keep
2839 and distribute run information, slow control data and calibration constants.

2840 Recent developments in computing hardware resulted in the rapid increase in potential processing capac-
2841 ity from increases in the core count of CPUs and wide CPU registers. Alternative processing architectures
2842 have become more commonplace. These range from the many-core architecture based on x86_64 com-
2843 patible cores to numerous alternatives such as other CPU architectures (ARM, PowerPC) and special
2844 co-processors/accelerators: (GPUs, FPGA, etc). For GPUs, for instance, the processing model is very
2845 different, allowing a much greater fraction of the die to be dedicated to arithmetic calculations, but at a
2846 price in programming difficulty and memory handling for the developer that tends to be specific to each
2847 processor generation. Further developments may even see the use of FPGAs for more general-purpose
2848 tasks.

2849 The effective use of these computing resources may provide a significant improvement in offline data
2850 processing. However, the offline software should be capable to do it by taking advantage of concurrent
2851 programming techniques, such as vectorization and thread-based programming. Currently, the SPD
2852 software framework, SpdRoot, cannot use these techniques effectively. The studies of the concurrent-
2853 capable software frameworks (e.g. ALFA [403], Key4Hep [404]) are needed to provide input for the
2854 proper choice of the offline software for Day-1 of the SPD detector operation, as well as a dedicated
2855 R&D effort to find proper solutions for the development of efficient cross-platform code.

2856 A git-based infrastructure for the SPD software development already established at JINR [405].

2857 **5 Resource estimate**

2858 For the online filter we assume the CPU consumption of 1000 SPD events/core/second. This requires
2859 3000 cores simultaneously for the fast tracking. Taking into account additional expenditures to the event
2860 unscrambling and data packing and including a real efficiency of CPU which will be lower than 100%,
2861 one derives the CPU resources for the online filter as 6000 CPU cores. This number sets the upper limit
2862 and the required computing power may decrease substantially if an efficient way to use GPU cores is
2863 implemented for the event filtration. As for the data storage, a high performance disk buffer of 2 PB
2864 capable to keep data of about one day of data taking is needed.

2865 For the offline computing, the data storage is determined by the data rate after the online filter, or 4

Table 8.1: Required SPD computing resources

	CPU [cores]	Disk [PB]	Tape [PB]
Online filter	6000	2	none
Offline computing	30000	5	9 per year
Cost estimate [kUSD]	4000	8000	4500 per year

2866 PB/year of raw data. Besides that, we may expect the comparable amount of simulated data and estimate
 2867 the long term storage as 10 PB/year, assuming two cycles of data processing and possible optimization
 2868 of the data format and data objects to be stored permanently. We assume that a half of the annual data
 2869 sample (~ 5 PB) is kept on disk storage, and the rest is stored on tape. The CPU power necessary to
 2870 process the amount of data like this and to run Monte-Carlo simulation is estimated as many as 30000
 2871 CPU cores. The summary of computing resources is given in Table. 8.1. The cost estimate is conservative
 2872 and will be defined more exactly in the TDR, when detailed hardware solutions and their actual price in
 2873 the market will be considered.

2874 The burden of the SPD computing system operation is a subject of sharing between the computing centers
 2875 of the participating institutes.

Chapter 9

Physics performance

1 General performance of the SPD setup

1.1 Minimum bias events [A. Guskov]

The total cross-section of the p - p collisions in the full energy range of SPD operation is a constant and equals to about 40 mb. The main contributions to that cross-section i. e. the elastic scattering, the diffractive, and the non-diffractive processes are shown in Fig. 9.1. The cross-section of "hard" processes, the QCD processes with partonic $\hat{p}_T > 1$ GeV/ c , is also shown as a part of the non-diffractive cross-section. The beam particle collisions in the interaction point are the source of numerous secondary charged and neutral particles in the SPD setup that fully defines our experimental conditions (the load of the detector, radiation environment etc.). The fluxes of different kinds of the charged and neutral particles produced in the interaction point as a function of the polar angle are shown in Fig. 9.2(a) and (b) for $\sqrt{s} = 27$ and 13.5 GeV, respectively. Table 9.1 shows the total cross-section of the p - p collisions and the

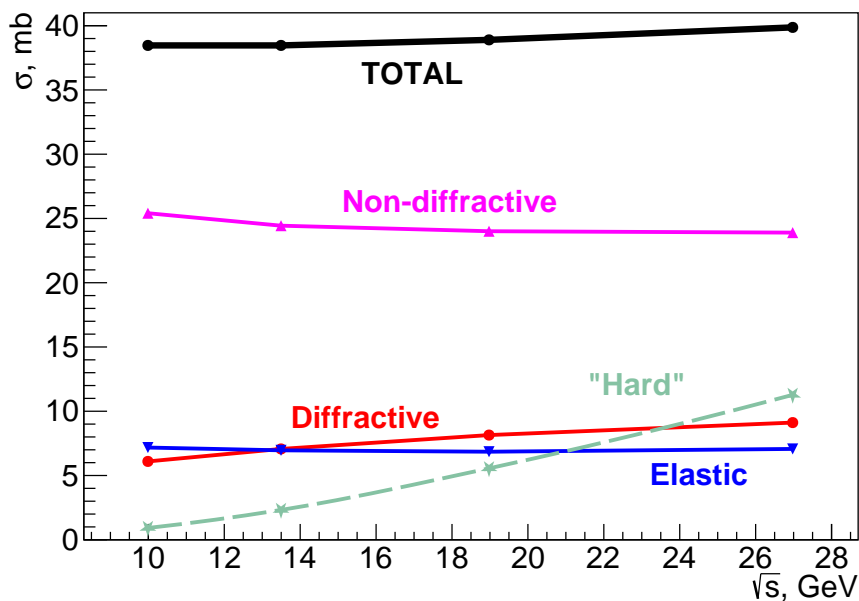


Figure 9.1: Main contributions to the total cross-section of p - p interaction as a function of \sqrt{s} . The "hard" cross-section is a part of the non-diffractive one.

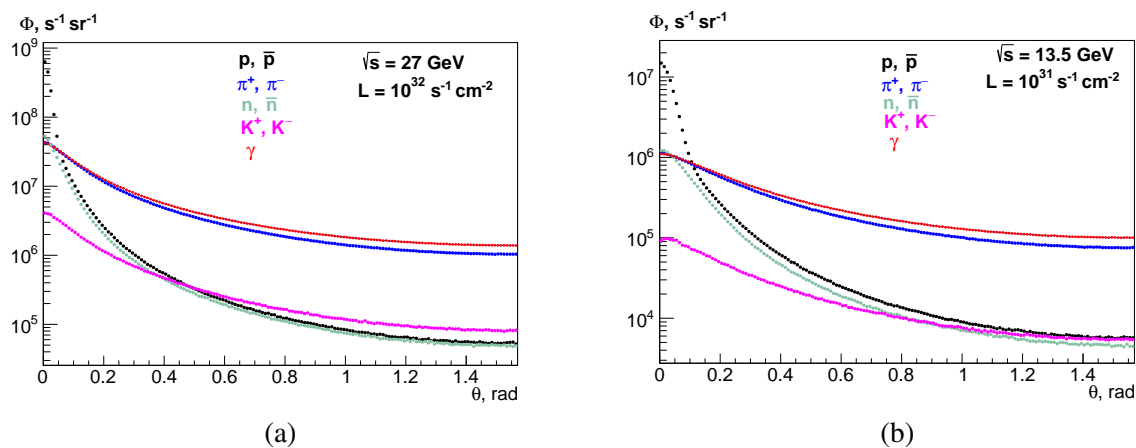


Figure 9.2: Fluxes of $p + \bar{p}$, π^\pm, K^\pm , $n + \bar{n}$ and γ as a functions of the polar angle θ for (a) $\sqrt{s} = 27$ GeV and (b) 13.5 GeV.

2889 multiplicity of charged and neutral particles for the different collision energies \sqrt{s} .

2890 The secondary interactions in the material of the setup, the multiple scattering, the decays of unstable
 2891 particles, and the influence of the magnetic field modify significantly the radiation environment inside
 2892 the SPD setup. All these factors are taken into account in the figure 9.3 that illustrates the fluxes of the
 2893 charged particles, the photons, and the neutrons at the different points of the SPD setup for $\sqrt{s} = 27$

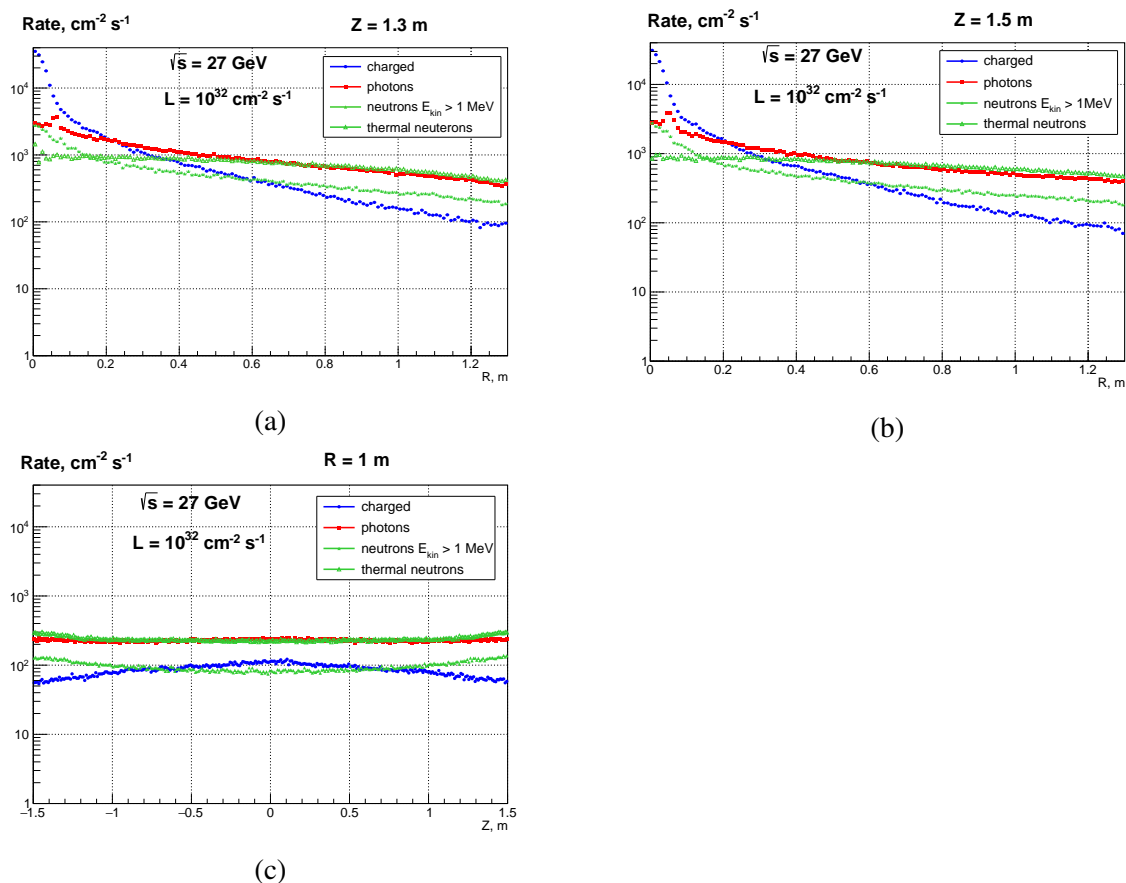


Figure 9.3: Flux of charged particles, photons, and neutrons in the radial direction at (a) $Z=1.3$ m, (b) $Z=1.5$ m, and (c) $R=1$ m.

2894 GeV and $L = 10^3 2 \text{ cm}^{-2} \text{ s}^{-1}$: $Z=1.3 \text{ m}$ (a), $Z=1.5 \text{ m}$ (b), and $R=1 \text{ m}$ (c).

Table 9.1: The total cross-section and the average multiplicity of the charged and neutral particles produced in the p - p collisions as a function of \sqrt{s} .

\sqrt{s} , GeV	σ_{tot} , mb	Charged multiplicity	Neutral (γ) multiplicity
13	38.4	5.9	4.6 (3.8)
20	38.9	7.2	6.0 (5.0)
26	39.7	7.8	6.5 (5.5)

2895 1.2 Tracking [A. Guskov]

2896 Traditionally the track reconstruction procedure is divided into two separate tasks: the track finding (or
2897 pattern recognition) and the track fitting. Since the track multiplicity in the p - p collisions is low enough
2898 (see Tab. 9.1) the occupancy of the coordinate detectors is not really a problem. So we hope to have the
2899 efficiency of the track finding not less than 90% in the most of our acceptance and do not pay too much
2900 attention to the pattern recognition algorithms now. However, the high multiplicity will limit the SPD
2901 performance in case of NICA operation with heavy-ion beams.

2902 The track fitting procedure uses measured hits in the tracking detectors (or simulated points for Monte
2903 Carlo events) as an input, and computes the most probable track parameters at any given point along the
2904 track, together with the corresponding covariance matrix. The fitting procedure takes also into consider-
2905 ation such effects related to the particle interaction in the material as the multiple scattering, and energy
2906 losses, the magnitude and configuration of the magnetic field. For the track fitting at SPD the well-known
2907 Kalman filter [406] implemented within the GenFit2 package [401] is used. The GenFit2 extrapolates
2908 tracks using the standard Runge-Kutta-Nyström method [407] modified by Bugge and Myrheim to carry
2909 along the Jacobian matrix [408, 409].

2910 The expected transverse momentum resolution σ_{p_T}/p_T for muons with different momenta for the max-
2911 imal magnetic field 1.0 T at the beam axis is shown in Fig. 9.4(a). The corresponding resolution for
2912 muons emitted at the polar angle $\theta = 90^\circ$ could be expressed as

$$\sigma_p/p|_{\theta=90^\circ} = 1.3\% + 0.1\% \times p + 0.003\% \times p^2. \quad (9.1)$$

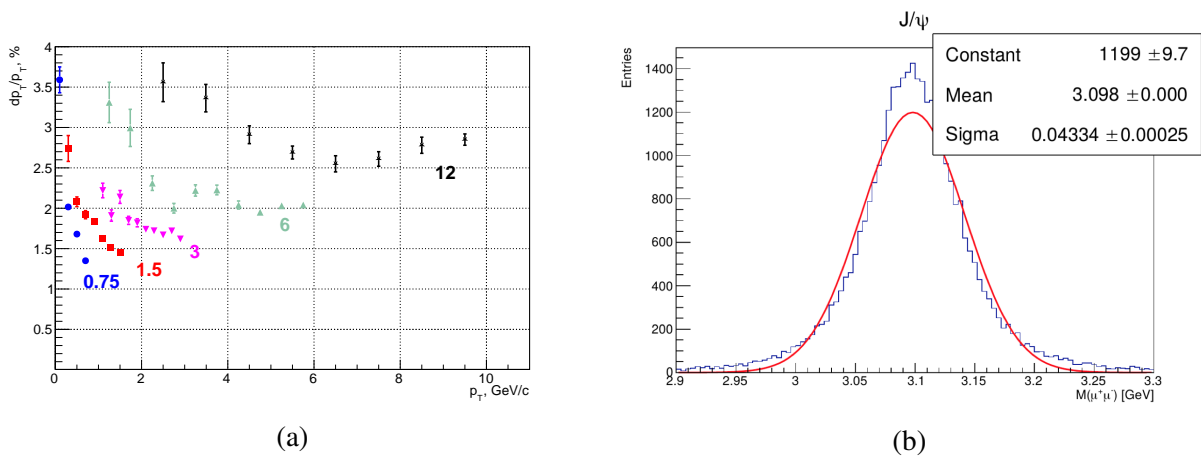


Figure 9.4: (a) The expected resolution for the transverse momentum σ_{p_T}/p_T of muons with momentum 0.75, 1.5, 3, 6 and 12 GeV/c. (b) The J/ψ peak from the dimuon decay.

2913 The width of the J/ψ peak shown in Fig. 9.4(b) is a good indicator of the tracking performance. The
 2914 SPD tracking system demonstrates the width on the level of 40 MeV. It is 1.5 times better than at the
 2915 fixed-target COMPASS experiment with the open setup (~ 60 MeV [410]) and much better than in the
 2916 fixed-target beam dump experiments like NA3 (80–120 MeV [411]), COMPASS (~ 200 MeV [179]),
 2917 SeaQuest (~ 150 MeV [412]) worked successfully on the study of the partonic structure of the nucleon
 2918 at the discussed energy range.

2919 1.3 Vertex reconstruction [A. Guskov, V. Andreev]

2920 The only subsystem that defines reconstruction of primary vertices is the silicon vertex detector. Its im-
 2921 pact to the accuracy of the vertex reconstruction depends on the baseline (the radial distance between
 2922 layers), the amount of passed material producing the multiple scattering effects and the spatial resolution
 2923 of the detector. The latter is a rather complex function of the number of fired strips (or pixels). We
 2924 estimate the effective spatial resolution of the DSSD layer as $\sigma_\phi = 11 \mu\text{m}$, $\sigma_z = 23 \mu\text{m}$ while the reso-
 2925 lution of the MAPS layer is $\sigma_{\phi,z} = 4 \mu\text{m}$. σ_ϕ here denotes the resolution in the direction perpendicular
 2926 to the beam line. The effective values are about two times smaller than a corresponding pitch divided
 2927 to $\sqrt{12}$. The amount of the material corresponds to $300 \mu\text{m}$ and $50 \mu\text{m}$ of silicon per one layer of the
 2928 DSSD and the MAPS, respectively. Figure 9.5(a) shows the accuracy of the primary vertex position
 2929 reconstruction as a function of the number of outgoing tracks for two configurations of the vertex de-
 2930 tector: (i) 5 layers of the DSSD, (ii) 3 layers of the MAPS and 2 layers of the DSSD. In both cases the
 2931 accuracy becomes better with increasing the number of outgoing tracks as expected. The DSSD+MAPS
 configuration demonstrates 1.5 times better precision.

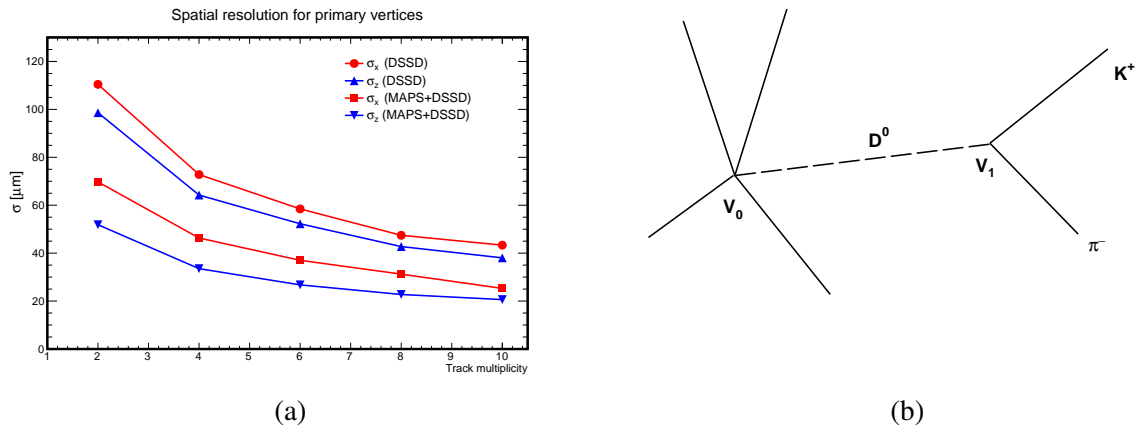


Figure 9.5: (a) Accuracy of the primary vertex position reconstruction as a function of the number of outgoing tracks for two configurations of the vertex detector. (b) A sketch of D^0 meson production and decay.

2932

2933 The silicon vertex detector is fully responsible also for reconstruction of the decay vertices of the short-
 2934 lived ($c\tau < 1$ cm) particles. We use the $D^0 \rightarrow K^+ \pi^-$ decay as an example (see sketch at Fig. 9.5(b))
 2935 but all the conclusions are valid qualitatively also for the decays like $D^+ \rightarrow K^- \pi^+ \pi^-$, $\Lambda_c^+ \rightarrow p \pi^+ K^-$
 2936 etc. Accuracy of the D^0 -decay vertex reconstruction as a function of the D^0 momentum is shown in
 2937 the Fig. 9.6(a). The gaussian width of the D^0 meson peak in the $K^+ \pi^-$ mass spectrum determined by
 2938 the tracking accuracy (mainly by the momentum resolution) is 27.2 and 25.0 MeV for the DSSD and
 2939 DSSD+MAPS configurations, respectively. The constrained fit of the D^0 decay where the angle between
 2940 the reconstructed D^0 momentum and the line connecting primary and secondary vertices is forced to be
 2941 zero and the found vertex is included to the track fitting, reduces the width to 21.4 and 18.0 MeV. That
 2942 improves, respectively, the signal-to-background ratio by the factor of 1.3 and 2.4. The D^0 peak width

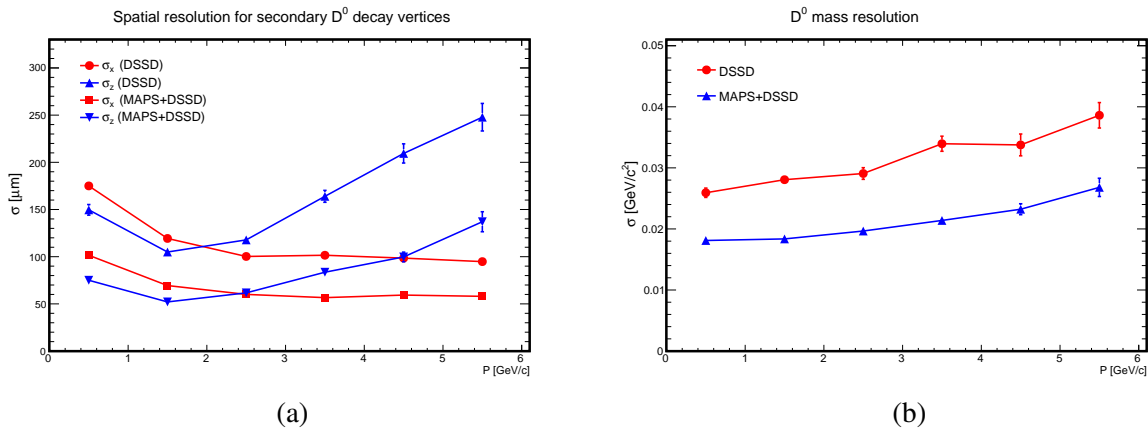
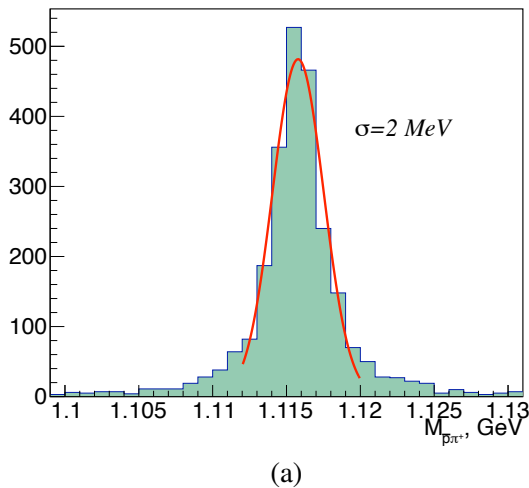


Figure 9.6: (a) Accuracy of the D^0 -decay vertex reconstruction as a function of the D^0 momentum. (b) D^0 peak width as a function of D^0 momentum.



Your ad
could be here

(a)

(b)

Figure 9.7: (a) Λ peak in the $p\pi$ mass spectrum.

2943 obtained from the constrained fit as a function of D^0 momentum is shown in Fig 9.6 (b). The impact of
 2944 the secondary vertex reconstruction procedure to our expectations for the asymmetries measurement is
 2945 discussed in Sec. 2.

2946 The decays of relatively long-lived unstable particles like Λ^0 , K^0 , Σ^- etc. occur mainly within the straw
 2947 tracker. The $\Lambda^0 \rightarrow p^+\pi^-$ peak is presented in Fig. 9.7(a) as an example.

2948 1.4 Calorimetry [A. Guskov]

2949 The electromagnetic calorimeter is one of the main detectors for the SPD gluon program. Its functions
 2950 are: (i) to measure the energy and the position of the hard prompt photons, and the photons from the
 2951 radiative decays of π^0 and η mesons; (ii) to reconstruct the soft photons ($\sim 0.5 \text{ GeV}$) from the decays
 2952 $\chi_{c1,2} \rightarrow J/\psi\gamma$; (iii) to provide identification of the electrons and positrons via the comparison of the
 2953 energy deposit in the ECAL and their momentum measured in the tracking system. The end-cup part
 2954 of the ECAL participates also in the online polarimetry with the inclusive π^0 production at high x_F (see
 2955 Sec. 2).

2956 Transparency of the SPD setup allows us to detect photons produced in the interaction point in the wide

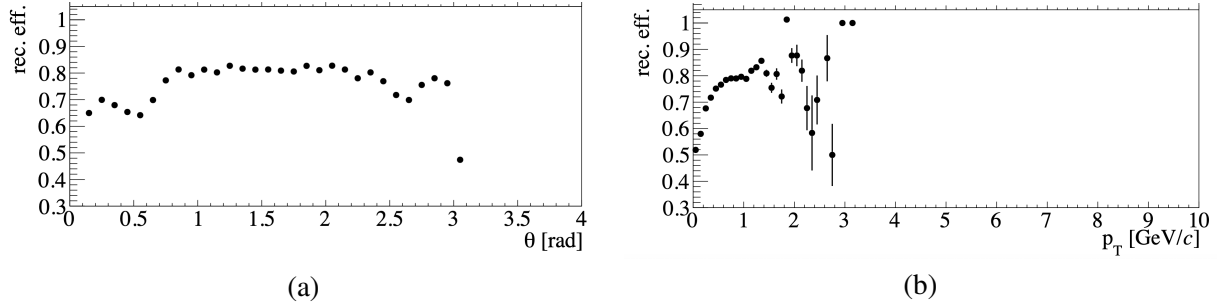


Figure 9.8: Efficiency of photon detection as a function of (a) θ and (b) p_T . **[Dummy now!]**

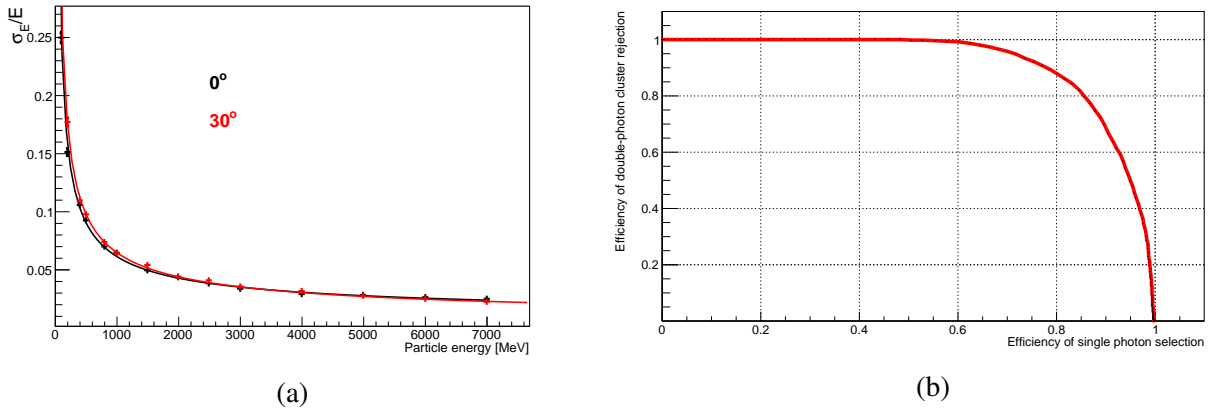


Figure 9.9: (a) Energy resolution of the ECAL for the normal incidence of photons and for the angle of 30° . (b) Purity of the double-photon clusters rejection vs. the efficiency of single photon reconstruction for 6 GeV photons and two 3 GeV photons separated by the distance of 4 cm basing on the cluster shape analysis.

2957 kinematic range. The efficiency of photon detection as a function of the production angle θ in respect
 2958 to the beam direction and as a function of the transverse momentum p_T is shown in Fig. 9.8(a) and (b),
 2959 respectively. The expected energy resolution of the ECAL obtained from the Geant4-based Monte Carlo
 2960 simulation for the normal incidence of photons and for the angle of 30° in respect to the normal line is
 2961 shown in Fig. 9.9(a). Such effects as the individual cell energy threshold on the level of 50 MeV, the
 2962 light absorption in the optic fibers and the fluctuation of the number of photons are taken into account.
 2963 The fitted curve has the shape:

$$\sigma_E/E = A \oplus \frac{B}{\sqrt{E/\text{GeV}}} \oplus \frac{C}{E/\text{GeV}}, \quad (9.2)$$

2964 were the parameters A , B and C are 0.9%, 5.9%, 1.7% and 0.0%, 6.0%, 2.2%, respectively, for 0° and 30°
 2965 of the incidence angle. The superconducting coils of the magnetic system (0.7 X_0 of material) placed in
 2966 front of the calorimeter practically do not reduce its acceptance for the hard photons and do not produce
 2967 any sizable impart to the energy resolution. For instance, the average resolution for the 1-GeV photons
 2968 passed through the coil changes from 6.1% to 6.3%.

2969 As soon as the internal longitudinal and transverse size of the ECAL is quite small, there is a proba-
 2970 bility for photons from the high-energy pions decay ($E_{\pi^0} \gtrsim 6$ GeV) to produce a single cluster and be
 2971 misidentified as a single high-energy photon. That is especially important for the prompt-photon part of
 2972 the physics program. But it is possible to identify such clusters with a certain precision performing the
 2973 cluster shape analysis. The cluster shape can be characterised using variables such as the dispersion, or

2974 the second-order moment (in one or two dimensions), the fourth-order moment, the ratio of the major
 2975 and the minor semiaxes of the ellipse of the cluster, etc. The machine learning classification techniques
 2976 are planned to be applied (the multilayer perceptron, the k-nearest neighbors, etc.) using these variables
 2977 as an input to classify between single and double-photon clusters. Figure 9.9(b) illustrates the purity of
 2978 double-photon rejection vs. the efficiency of single photon reconstruction for 6 GeV photons and two 3
 2979 GeV photons separated by the distance of 4 cm (exactly the ECAL cell size) basing on the cluster shape
 2980 analysis.

2981 The impact of the ECAL energy resolution to the reconstruction of such states as π^0 , η is shown in Fig.
 2982 9.10(a). The relative width of the π^0 and η peaks is 7.3% and 6.9%, respectively, for $E_\gamma > 0.5$ GeV. The
 2983 reconstruction of the charmonium states $\chi_{c,1,2}$ via their radiative decays is presented in Fig. 9.10(b). The
 2984 χ_{c1} and χ_{c2} peaks cannot be fully resolved ($\Delta M/\sigma_M \approx 1.5$) but nevertheless the relative contribution of
 2985 these states could be estimated basing on the detailed peak shape analysis.

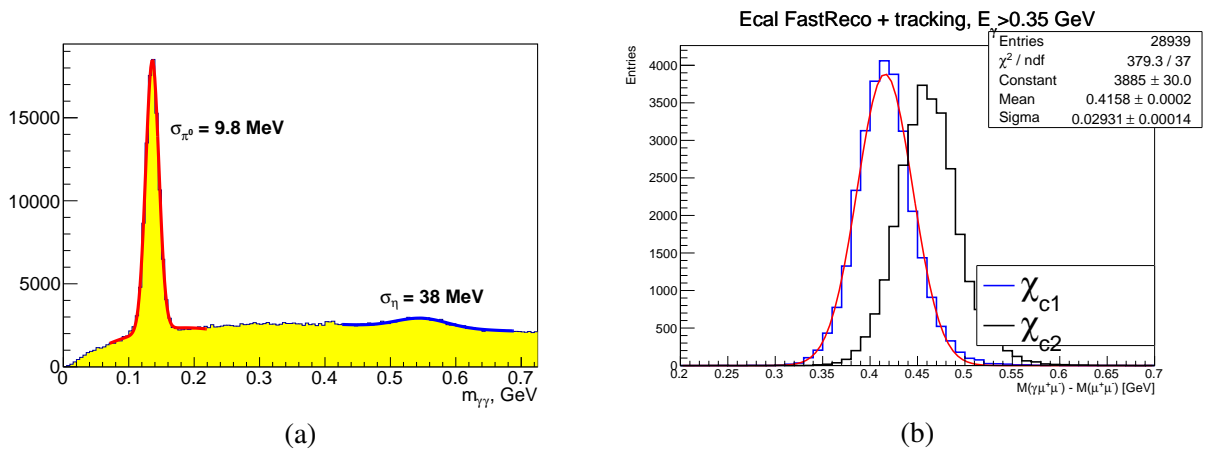


Figure 9.10: (a) π^0 peak in the $\gamma\gamma$ mass spectrum. (b) Mass resolution for $\chi_{c1,2}$ reconstructed via their decay into $J/\psi\gamma$ final state.

2986 1.5 Particle identification with TOF [A. Guskov]

2987 The particle identification with the TOF detector is based on the comparison between the time of flight
 2988 of the particle from the primary vertex to the TOF detector and the expected time under a given mass hypothesis.
 2989 Presence of only one plane of the TOF detector requires for particle identification the precision
 2990 knowledge of the event collision time t_0 . It can be estimated by the TOF detector on an event-by-event
 2991 basis using the χ^2 minimization procedure for events with two and more reconstructed tracks. Having in
 2992 the event N tracks matched to corresponding hits on the TOF plane it is possible to define certain combinations
 2993 of masses \vec{m}_i assigning independently for each track the π , K or p mass. The index i indicates
 2994 one of the possible combination $(m_1, m_2, \dots, m_{N \text{ tracks}})$ among the $3N$ tracks ones [413].

2995 For each track the following weight is attributed

$$W_i = \frac{1}{\sigma_{TOF}^2 + \sigma_{t_{exp. i}}^2}. \quad (9.3)$$

2996 Here σ_{TOF} and $\sigma_{t_{exp. i}}$ are the time resolution of the TOF detector and the uncertainty of the expected
 2997 time of flight under a given mass hypothesis $t_{exp. i}$, respectively. The latter is defined by the uncertainty
 2998 of the momentum and track length measurements.

2999 The following χ^2 function has to be minimized

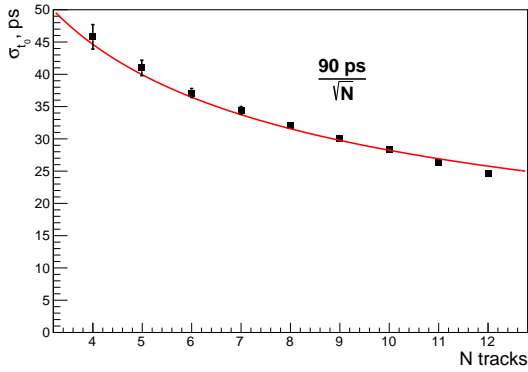
$$\chi^2(\vec{m}_i) = \sum_N W_i ((t_{TOF} - t_0(\vec{m}_i)) - t_{exp. i})^2. \quad (9.4)$$

3000 Here

$$t_0(\vec{m}_i) = \frac{\sum_N (t_{TOF} - t_{exp. i})}{\sum_N W_i}. \quad (9.5)$$

3001 The mass vector \vec{m}_i that minimizes χ^2 in Eq. 9.4 can be used in Eq. 9.5 for determination of the event
3002 collision time t_0 . For unbiased particle mass determination, each track has to be subsequently excluded
3003 from the t_0 calculation procedure.

3004 Figure 9.11(a) illustrates the accuracy of t_0 reconstruction as a function of the number of tracks for
3005 $\sigma_{TOF} = 70$ ps. One can see that σ_{t_0} is proportional to $1/\sqrt{N}$ and for the track multiplicity 10 (typical
3006 for hard interaction events) is about 30 ps. Pion, kaon and proton separation with the TOF detector is
3007 shown in Fig. 9.12. The π/K and K/p separation power as a function of the particle momenta and the
3008 emission angle θ in the primary vertex is presented in Fig. 9.13 (a) and (b), respectively, for the time of
3009 flight ($t_{TOF} - t_0$) resolution 80 ps. It is mostly defined by the time measurements while the accuracy of
3010 the momentum reconstruction becomes sizable only for $\theta < 10^\circ$.



(a)

Figure 9.11: Accuracy of t_0 reconstruction as a function of the number of tracks in the primary vertex.

3011 2 Accuracies of asymmetries measurement

3012 The single transverse (A_N) and the double longitudinal and transverse (A_{LL} and A_{TT}) spin asymmetries
3013 are the main observables to be accessed at SPD. The asymmetry A_N is denoted as

$$A_N = \frac{\sigma^\uparrow - \sigma^\downarrow}{\sigma^\uparrow + \sigma^\downarrow}, \quad (9.6)$$

3014 where σ^\uparrow and σ^\downarrow denote the inclusive production cross sections with opposite transverse polarization of
3015 one of the colliding particles. In practice, taking into account the 2π coverage of the SPD setup in the
3016 azimuthal angle ϕ , the A_N can be extracted from the azimuthal modulation amplitude of the differential
3017 cross-section $d\sigma/d\phi$

$$d\sigma/d\phi \propto 1 + PA_N \cos(\phi - \phi_0), \quad (9.7)$$

3018 where P and ϕ_0 are the beam polarization and its direction.

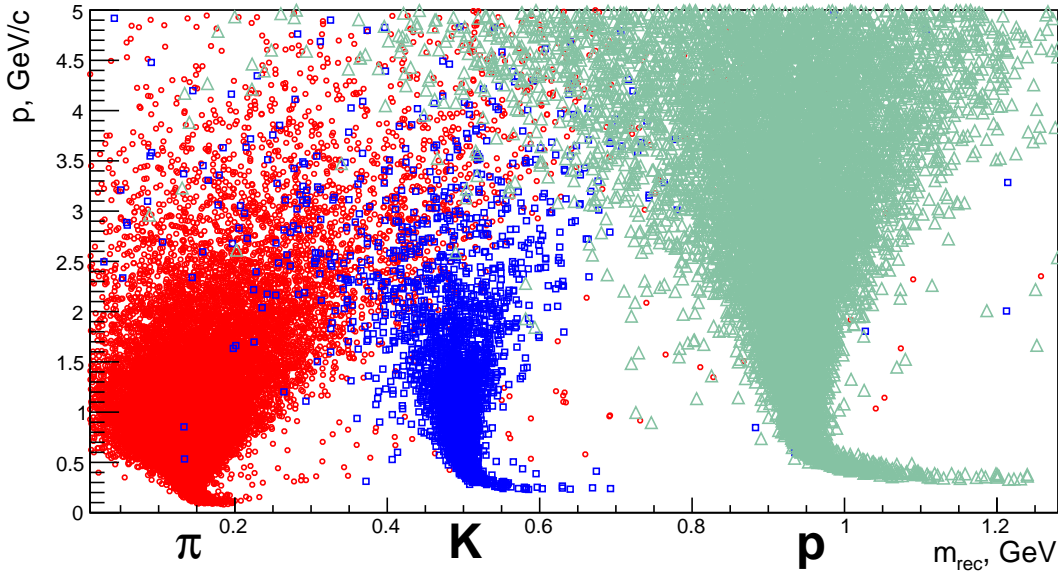


Figure 9.12: Reconstructed mass vs. particle momentum for pions, kaons and protons.

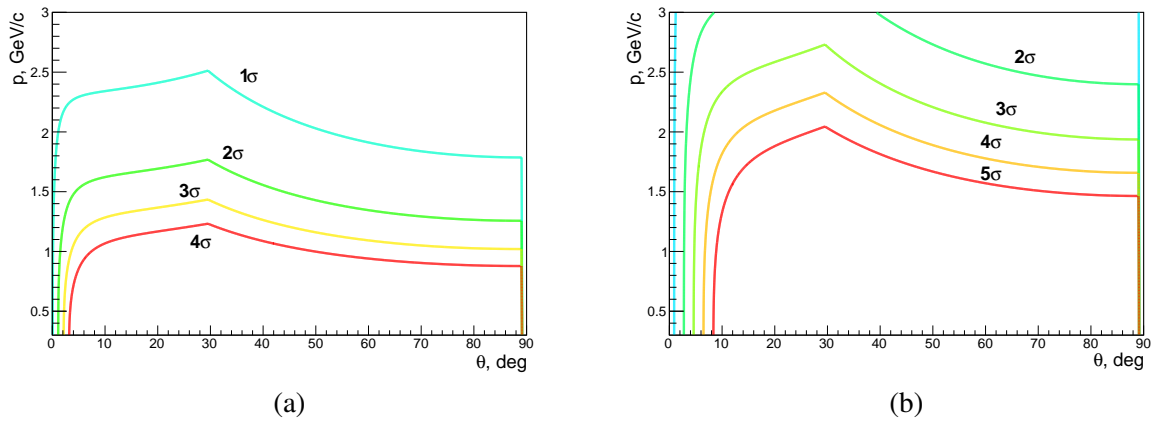


Figure 9.13: π/K (a) and K/p (b) separation power of the TOF system as a function of particle momenta and emission angle.

3019 The double longitudinal spin asymmetry can be expressed via the number of events for same (N^{++}) and
 3020 opposite (N^{+-}) spin orientations of colliding protons:

$$A_{LL} = \frac{\sigma^{++} - \sigma^{+-}}{\sigma^{++} + \sigma^{+-}} = \frac{1}{P_1 P_2} \times \frac{N^{++} - RN^{+-}}{N^{++} + RN^{+-}}. \quad (9.8)$$

3021 There σ^{++} and σ^{+-} denote the cross sections with the same and opposite proton helicity combinations,
 3022 respectively, P_1 and P_2 are the absolute values of proton beams polarizations and $R = L_{++}/L_{+-}$ is the
 3023 ratio of integrated luminosities for the samples with same and opposite spin orientations. Assuming the
 3024 same amount of data collected with both spin orientations the Eq. 9.8 can be rewritten as:

$$A_{LL} = \frac{1}{P_1 P_2} \times \frac{N^{++} - N^{+-}}{N^{++} + N^{+-}}. \quad (9.9)$$

3025 Aforesaid is also valid for the asymmetry A_{TT} .

3026 2.1 Charmonia production [I. Denisenko]

3027 According to the modern theoretical approaches, the charmonia production at the SPD energies ($10 \text{ GeV} \leq$
 3028 $\sqrt{s} \leq 27 \text{ GeV}$) is dominated by gluon-gluon fusion process. The inclusive J/ψ production has a large
 3029 cross-section ($200 - 250 \text{ nb}$ at the maximum energy) and clear experimental signature in the dimuon
 3030 decay mode, and thus is a powerful probe of internal structure of proton [and deuteron]. The distinct
 3031 J/ψ signal allows us to also reconstruct excited charmonia states in the decays $\chi_{c1,2} \rightarrow \gamma J/\psi$ and
 3032 $\psi(2S) \rightarrow \pi^+ \pi^- J/\psi$. There is also a possibility to reconstruct J/ψ from $e^+ e^-$ final state, but it look
 3033 less promising due larger background, a larger observed J/ψ width and more complicated shape of the
 3034 peak, which will significantly affect both statistical and systematic errors. The study of the η_c production
 3035 properties in the $p\bar{p}$ and $\Lambda\bar{\Lambda}$ decay modes may be also feasible.

3036 Muons are identified in the RS. The system is expected to separate showers from strongly interacted
 3037 pions and muon tracks (using standard or machine learning techniques.) The main background are
 3038 muons from pion decays and pions that passed large distance in the RS. The pion decays result in a small
 3039 kink of charged track (about 2°), and the decay muon retains from 60% to almost 100% of the initial pion
 3040 energy. There is a possibility that a fraction of decay muons can be suppressed by search of a kink in
 3041 the tracker or by considering correlation between particle momentum and amount of material it crossed.
 3042 But the results in this section are based on a simplified model (gives a lower performance boundary). A
 3043 particle is identified as a muon based on the amount of material it passes in the active part of the RS, this
 3044 amount is given as a number of proton nuclear lengths (n_λ). Two possibilities are considered: a particle
 3045 from the initial interaction and a muon from a pion decay (the pion must be from the initial interaction).
 3046 In the latter case, if pion decays in the RS, the amount of material is added for pion and muon.

3047 It is clear that higher running energies are preferable for physics with charmonia due to higher production
 3048 cross-section, stronger boost for pions and more energetic muons. All estimates in this section assume a
 3049 pp collision energy of 27 GeV , 10^7 s time of data taking (one year) with the maximum luminosity and a
 3050 polarization P of 0.7. At these conditions one expects about 12 million $J/\psi \rightarrow \mu^+ \mu^-$ decays in the SPD
 3051 detector.

3052 The J/ψ events are simulated using Pythia8 and their number normalized to the production cross-section
 3053 of 200 nb . For background minimum bias events generated with Pythia6 and Pythia8 are considered
 3054 (giving almost the same predictions around J/ψ peak). Approximately half of background events are
 3055 produced in the hard interaction, but a sizable fraction comes also from the diffraction processes. It
 3056 appears that significant amount of background events can be suppressed by a requirement on polar angle
 3057 of a muon candidate. The $\mu^+ \mu^-$ invariant mass spectrum for the muon candidates with $n_\lambda > 3$ and
 3058 satisfying $|\cos \theta| < 0.9$ after one year of data taking is shown in Fig 9.14 (a). Figure 9.14 (b) illustrates
 3059 the structure of the background: [.....]. The selection efficiency can be estimated to be around 35
 3060 – 45% depending on the cut on θ , resulting in 4 – 5 million selected events. The barrel part of the
 3061 RS is essential for reconstruction of approximately 90% of J/ψ events: for more than 50% of J/ψ
 3062 events one lepton is reconstructed in the barrel and the other one in end-caps, more than 35% of events
 3063 are reconstructed solely in the barrel part of the detector. The statistical errors for observables can be
 3064 estimated using a linear LSM fit [414]. As an example, the estimated statistical precision for the J/ψ
 3065 polarization λ as a function of the transverse momentum p_T is shown in Fig. 9.15 (a). The estimation
 3066 was done under the assumption $\lambda \ll 1$ basing on the angular modulation of the differential cross-section
 3067

$$d\sigma/d\cos\theta_\mu \propto 1 + \lambda \cos^2\theta_\mu, \quad (9.10)$$

3068 where θ_μ is the angle between the muon momentum and the J/ψ momentum in the helicity frame.

3069 The transverse single spin asymmetry A_N in J/ψ production probes the Sivers function. At $\sqrt{s} =$
 3070 200 GeV it was measured by the PHENIX Collaboration and found consistent with zero [17, 18]. To

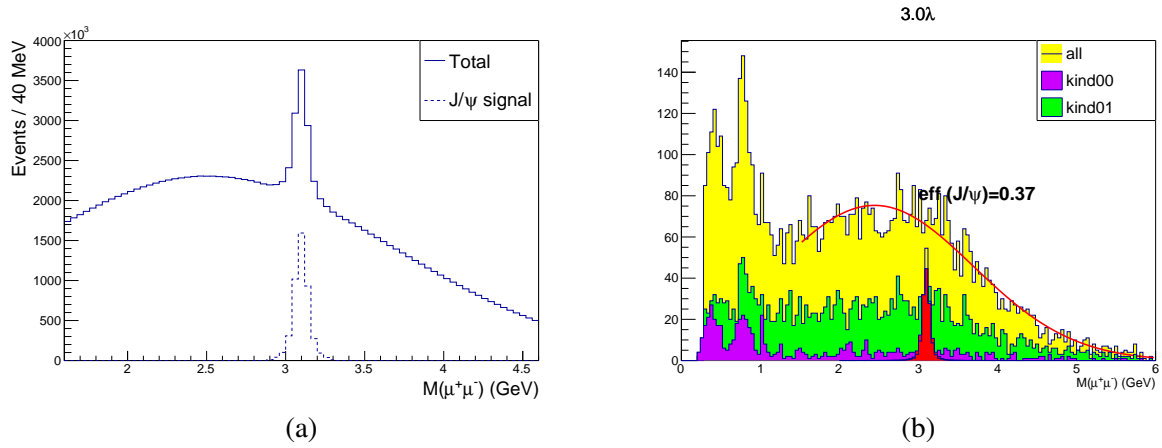


Figure 9.14: (a) Dimuon candidate spectrum and the J/ψ peak after one year of data taking. (b) The contributions to the background from ... are shown in

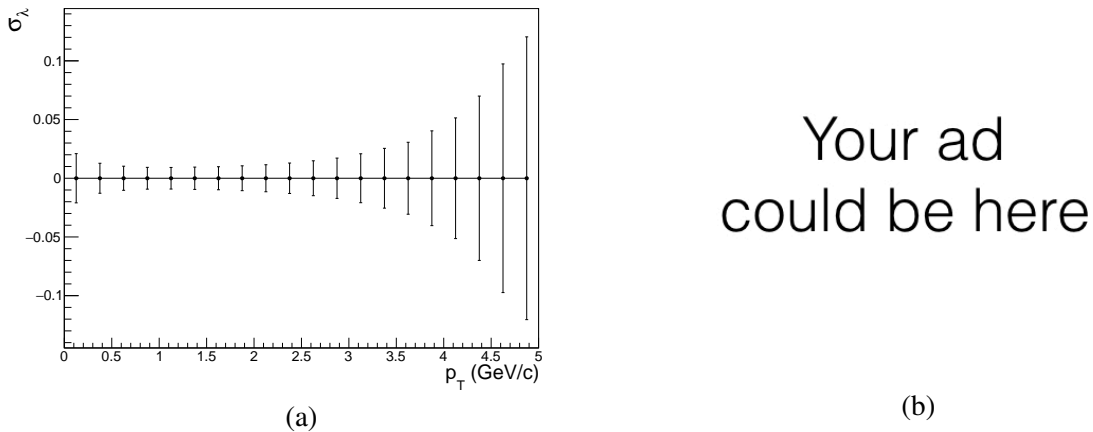


Figure 9.15: (a) Expected statistical precision for polarization as a function of J/ψ transverse momentum.

3071 estimate our statistical precision 8 bins in ϕ are considered (see Eq. 9.7). The same linear fit is used to
 3072 firstly estimate error in bins based on expected J/ψ number and secondly to extract A_N . The projected
 3073 statistical uncertainties for A_N as a function of x_F are compared to the GPM model predictions from
 3074 Ref. [415] in Fig. 9.16 (preliminary CGI-GPM calculations indicate lower asymmetries). Compared to
 3075 the PHENIX measurement, we expect much better precision and much wider kinematic range in x_F . Our
 3076 rapidity range is approximately $|y| < 2$.

3077 The statistical error of the longitudinal double spin asymmetry A_{LL} sensitive to the polarized gluon distri-
 3078 bution was estimated basing on Eq. 9.8 and 9.8. There we neglect the uncertainties of the measurement of
 3079 the relative integrated luminosities and the beam polarizations. The projection of statistical uncertainties
 3080 as functions of p_T and $|y|$ are shown in Fig 9.17. Compared to previous results obtained by the PHENIX
 3081 Collaboration at $\sqrt{s} = 510$ GeV [114], we have much better precision and probe wider kinematic range.

3082 The study of associated J/ψ production will be strongly restricted by the small expected statistics. The
 3083 double J/ψ production cross-section was measured by the NA3 Collaboration [416] and was found to
 3084 be 27 ± 10 pb in proton nucleus interaction at $\sqrt{s} \approx 27$ GeV. Optimistically, such cross-section would
 3085 result in 50 – 100 reconstructed events if both e^+e^- and $\mu^+\mu^-$ modes are used to reconstruct J/ψ . It
 3086 may be enough to determine low- p_T cross-section dependence, but the study of any angular modulation

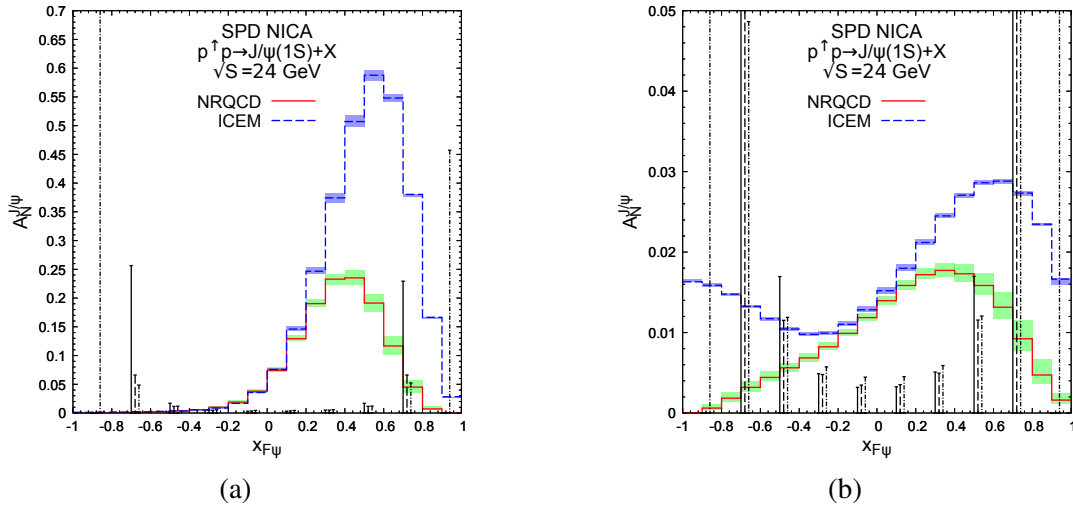


Figure 9.16: Projection of the estimated statistical uncertainties for A_N compared to GPM predictions from Ref. [415] for SIDIS (a) and D'Alesio PDF parameterizations (b).

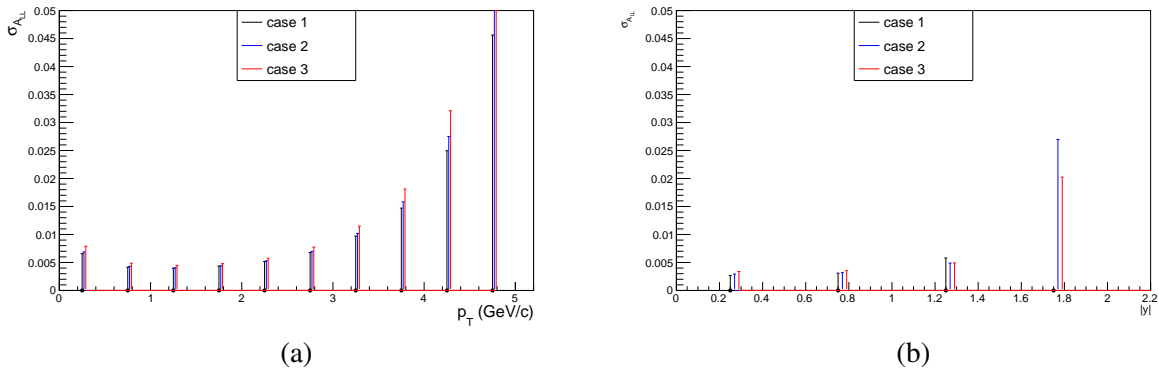


Figure 9.17: Estimated statistical precision of A_{LL} as a function of p_T (a) and rapidity (b).

3087 will not be possible. The study of $\gamma J/\psi$ production will be challenging experimentally due to both
 3088 lack of statistics and high expected background. The reasonable statistics might be expected for $J/\psi D$
 3089 production.

3090 The $\psi(2S) \rightarrow \mu^+ \mu^-$ decay is suppressed as compared to $J/\psi \rightarrow \mu^+ \mu^-$ by approximately a factor of 50
 3091 and its reliable extraction may not be feasible. At the same time the decay $\psi(2S) \rightarrow \pi^+ \pi^- J/\psi$ can
 3092 be reliably identified as a narrow (about $10 \text{ MeV}/c^2$ wide) peak in the $M_{\pi^+ \pi^- \mu^+ \mu^-} - M_{\mu^+ \mu^-}$ distribution.
 3093 This distribution is shown in Fig. 9.18 (a). The expected statistics is about 1×10^5 selected events.

3094 The χ_{c1} and χ_{c2} states have a large partial width of decay to $J/\psi \gamma$ and can be reconstructed using it. The
 3095 production properties of these states at low energies are poorly known (e.g. see review of the experimen-
 3096 tal results in Ref. [30]). The identification of these decays at SPD relies on the ECAL performance. The
 3097 result of MC simulation for $M_{\gamma \mu^+ \mu^-} - M_{\mu^+ \mu^-}$ is shown in Fig. 9.10(b). It will not be possible to separate
 3098 χ_{c1} from χ_{c2} , but their relative fractions should be well measurable. For the expected statistics of ap-
 3099 proximately 0.5 million reconstructed decays per year (for both states together) it should be possible to
 3100 measure cross-section kinematic dependencies of these states. The major difficulty in studying of these
 3101 states is the high expected background. Its very rough estimation is shown in Fig. 9.18 (b).

3102 The η_c production cross-section is highly uncertain. At $\sqrt{s} = 24$ GeV it is estimated that $\sigma_{\eta_c} \cdot B(\eta_c \rightarrow$

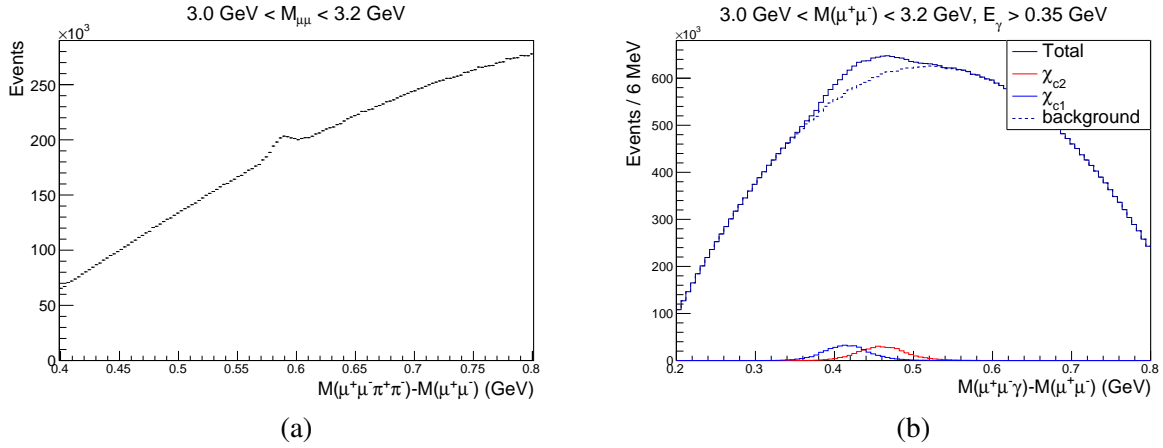


Figure 9.18: (a) $\psi(2S)$ signal in the $M_{\pi^+\pi^-\mu^+\mu^-} - M_{\mu^+\mu^-}$ distribution. (b) Very rough estimation of the background for the χ_{c1} and χ_{c2} reconstruction. For this plot feed-down fraction of 15% is assumed for both states.

3103 $p\bar{p}) = 0.6_{-0.4}^{+0.8}$ nb [Nefedov, SPD meeting, 28.10.2020] or 6×10^5 events per year. The typical mo-
 3104 menta of p and \bar{p} is $1.5 - 2$ GeV/ c , where these particles should be well identified by the TOF system
 3105 (see Fig. TOF_PERF). Feasibility of the differential cross-section measurements requires detailed MC-
 3106 simulations due to the high expected background. A very limited statistics, but a cleaner signal may be
 3107 also expected in the $\Lambda\bar{\Lambda}$ decay mode.

3108 2.2 Prompt photon production

3109 As it was already mentioned in the Sec. , the two hard processes determine the production of prompt
 3110 photons in p - p collisions in the leading order: gluon Compton scattering $gq(\bar{q}) \rightarrow \gamma q(\bar{q})$ and quark-
 3111 antiquark annihilation: $q\bar{q} \rightarrow g\gamma$. Contribution of the latter process to the total cross section does not
 3112 exceed 20% at the discussed energy range. That is what makes prompt photons a convenient probe
 3113 for gluons inside the nucleon. In ultrarelativistic approximation the minimal value of the longitudinal
 3114 momentum fraction of struck parton x_{min} accessible by detection of prompt photon with normalized
 3115 transverse momentum $x_T = 2p_T/\sqrt{s}$ and rapidity y could be expressed as [417]

$$x_{min} = \frac{x_T e^{-y}}{2 - x_T e^y}. \quad (9.11)$$

3116 For the fixed x_T the minimal $x_{min} = x_T^2$ is reached at $y_0 = -\ln(x_T)$. The value x_{min} as a function of rapidity
 3117 y and p_T of photon for $\sqrt{s} = 27$ GeV is shown in color in Fig. 9.19(a). One can see that possibility to
 3118 access low- x region is limited by our capability to detect prompt-photon signal at low p_T and angular
 3119 acceptance of the experimental apparatus. The latter is especially important for collider experiments like
 3120 SPD where large values of $|y|$ correspond to a blind area near beam pipes.

3121 Huge rate of decay photons makes rather difficult determination of the prompt photon production cross-
 3122 section. Main source of decay photons is the two-body decay $\pi^0 \rightarrow \gamma\gamma$. The second most important
 3123 source is the decay $\eta \rightarrow \gamma\gamma$. In the kinematic range $p_T > 3$ GeV/ c at $\sqrt{s} = 27$ GeV there are 0.18
 3124 photons from the η decay per one photon from the π decay. Relative contribution of all other decay
 3125 photons (ω, ρ, ϕ decays) does not exceed 0.03.

3126 The p_T spectra for prompt and decay photons expected at SPD after one year of running at $\sqrt{s} = 27$
 3127 GeV are presented in Fig. (b). The result was obtained using Pythia8 generator with parameters tuned to
 3128 reproduce high- p_T spectra of π^0 and prompt photons measured at similar energies by WA70 ($\sqrt{s} = 22.96$
 3129 GeV) [418, 419] and UA6 ($\sqrt{s} = 24.3$ GeV) [], respectively. One can see that the p_T spectrum of decay

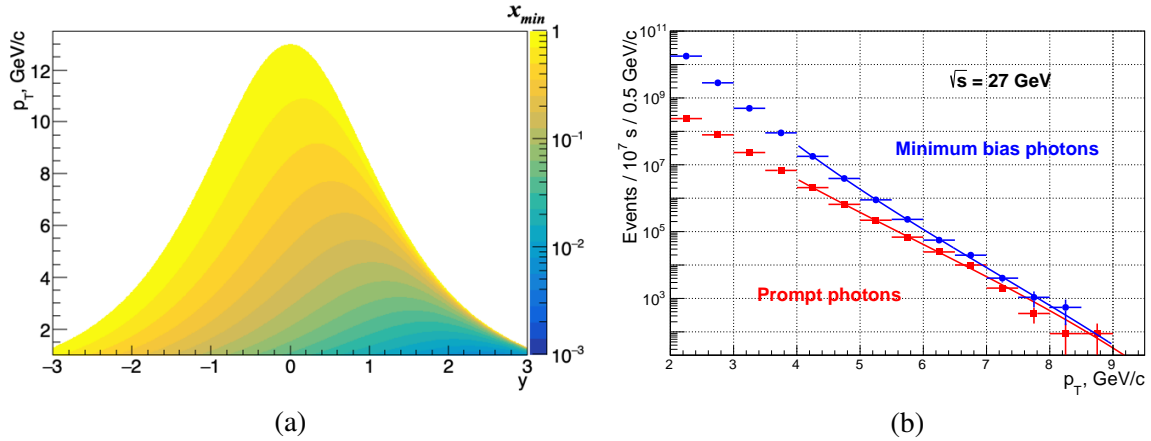


Figure 9.19: (a) A minimal value of gluon x accessible via registration of prompt photon with rapidity y and transverse momentum p_T at $\sqrt{s} = 27$ GeV. (b) p_T spectra of produced prompt (red) and decay or minimum bias (blue) photons in p - p collisions at $\sqrt{s} = 27$ GeV. Distributions are scaled to one year of data taking (10^7 s).

3130 photons goes down with grows of p_T faster that for prompt photons an their rates becomes comparable
 3131 at $p_T \approx 7$ GeV/c. The fitted functions presented on the plot have shape

$$N(p_T) = A(1 - x_T)^n (p/p_0)^{-m}. \quad (9.12)$$

3132 Each cluster of energy deposition in the ECAL with energy above the threshold $E_0 = 100$ MeV that is
 3133 not associated with any reconstructed tracks is treated as a prompt photon candidate. The momentum of
 3134 such photon is reconstructed under assumption of its production in the primary vertex. In order to reject
 3135 photons from the $\pi^0 \rightarrow \gamma\gamma$ decay the invariant mass of each to photons is calculated. If the difference
 3136 between the reconstructed mass and the nominal mass of π^0 is smaller than 10 MeV, both photons
 3137 are removed from the list of candidates. Nevertheless this procedure removes just about 40% of false
 3138 candidates. The photons from the $\pi^0 \rightarrow \gamma\gamma$ decay whose partner was not reconstructed due to conversion
 3139 in the material, too low energy or acceptance issue remain in the list of candidates. Photons from radiative
 3140 decays of other particles are also in the list. The list of candidates includes also photons associated with
 3141 two or more overlapping clusters, first of all clusters from the decay of energetic π^0 . Significant part of
 3142 such false candidates could be rejected by a sophisticated analysis of the cluster shape. Clusters produced
 3143 by charged particles whose tracks are lost, clusters deposited by photons originated from elements of the
 3144 setup and clusters induced by neutral hadrons are also taken into account as a background. Contributions
 3145 of each source of background mentioned above are presented as a function of p_T in Fig. 9.20(a).

3146 As one can see, photons from unreconstructed decays of neutral pions are the main source of background.
 3147 Fraction of such unreconstructed decays can be estimated from the Monte Carlo simulation and is about
 3148 50%. Basing on the number N_{π^0} of reconstructed $\pi^0 \rightarrow \gamma\gamma$ decays the corresponding number of remaining
 3149 background photons $k \times N_{\pi^0}$ should be subtracted from the number of prompt photon candidates N_γ in
 3150 order to get estimation of a true number of prompt photons:

$$N_{prompt} = N_\gamma - k \times N_{\pi^0}. \quad (9.13)$$

3151 Here $k \approx 0.3$ is a coefficient, calculated from the MC simulation and takes into account not only an
 3152 inefficiency of the $\pi^0 \rightarrow \gamma\gamma$ decay reconstruction but also overall contribution of all other background
 3153 photons including photons from radiative decays of η , ω , ρ , ϕ etc. The described subtraction procedure
 3154 has to be performed for each bin of p_T and x_F ranges. One should keep in mind that the background

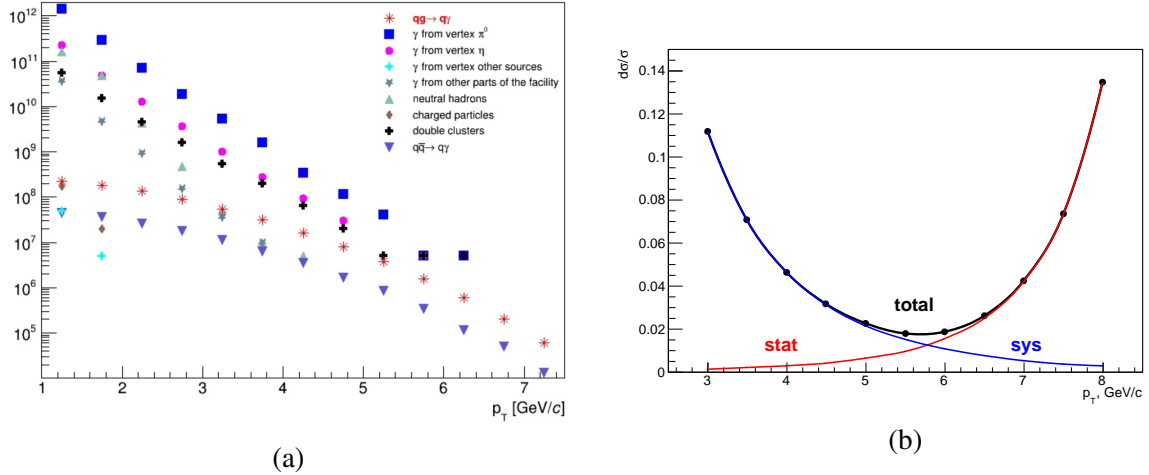


Figure 9.20: (a) Contributions of different background components for the prompt photon production in p - p collisions at $\sqrt{s} = 27$ GeV. (b) Expected uncertainty of the unpolarized cross section $Ed^3\sigma/dp^3$ measurement as a function of p_T .

3155 of decay photons is also spin-dependent: there is an indication of nonzero asymmetries A_{LL} and A_N in
 3156 inclusive π^0 and η production [].

3157 An expected accuracy of the unpolarized cross section $Ed^3\sigma/dp^3$ measurement after one year (10^7 s) of
 3158 data taking is shown in Fig. 9.20(b). At low- p_T the main contribution to the total uncertainty is coming
 3159 from the systematics of the π^0 background subtraction procedure while at high p_T statistical uncertainty
 3160 dominates. To estimate systematics $dk/k = 1\%$ is assumed.

3161 The accuracy of the A_{LL} spin asymmetry measurement is estimated basing on Eq. 9.8 and 9.8 and
 3162 neglecting the uncertainty of P_1, P_2 and R measurements.

3163 To estimate the A_N asymmetry the function

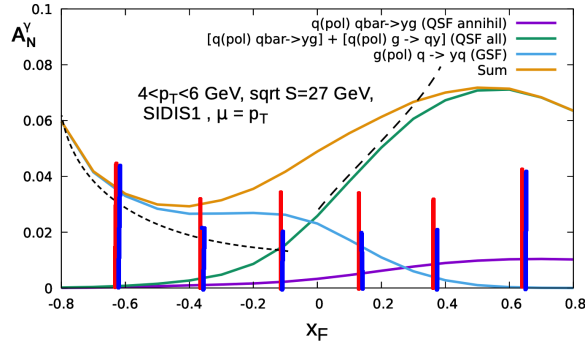
$$f(\phi) = C + P \times A_N \cos \phi \quad (9.14)$$

3164 is fitted to the expected acceptance-corrected azimuthal distribution of prompt-photon events. Here ϕ is
 3165 the azimuthal angle of produced photon in the lab. system in respect to the direction of the proton beam
 3166 polarization. The expected accuracy of A_{LL} and A_N measurement as a function of x_F is shown in Fig. . It
 3167 does not include uncertainties related with luminosity and beam polarization measurement.

3168 Systematic uncertainty related with background subtraction could be partially reduced by simultaneous
 3169 study of the asymmetries for prompt photons, π^0 and η mesons. ...

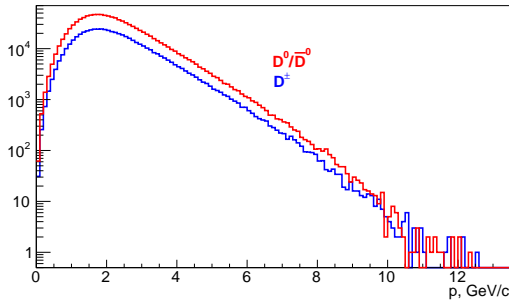
3170 2.3 Open charm production

3171 In spite of the relatively large cross-section of the open charm production, the most of the D -meson
 3172 decays cannot be reconstructed easily. The "golden" decay channels are: $D^0 \rightarrow K^- \pi^+$ and $D^+ \rightarrow K^- \pi^+$
 3173 π^+ (BF=3.95% and 9.38%, respectively). The momentum distributions for D^\pm and D^0/\bar{D}^0 produced in
 3174 p - p collisions at $\sqrt{s} = 27$ GeV are shown in Fig. 9.22(a). Difference between the red and blue curves
 3175 reflects the fact that probability for c quart to hadronize into the neutral D -meson is 2 times larger than
 3176 into the charged one. Since the decay length $c\tau$ is 311.8 and 122.9 μm , respectively, that is larger than
 3177 the spatial resolution of the vertex reconstruction (see ...), the Vertex Detector allowing to reconstruct
 3178 the secondary vertex of the D meson decay is the key detector for the open charm physics at SPD. The
 3179 spatial distance between the primary (production) and the secondary (decay) vertices for D mesons is
 3180 presented in Fig. 9.22(b).

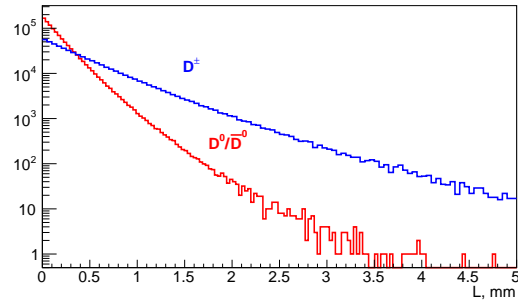


(a)

Figure 9.21: (a) Expected accuracy of the A_N measurement for prompt photons with $p_T > 4$ GeV/c at $\sqrt{s} = 27$ GeV as a function of x_F (**dummy at the moment**). Model predictions are also shown.



(a)



(b)

Figure 9.22: (a) Momentum distributions for D^\pm and D^0/\bar{D}^0 produced in p - p collisions at $\sqrt{s} = 27$ GeV. (b) Spatial distance between the production and the decay) vertices for D mesons.

3181 The accuracy of the spin asymmetries measurement was estimated for the D^0/\bar{D}^0 -meson production and
 3182 decay. The following selection criteria were applied in order to reduce combinatorial background under
 3183 the D^0 peak: i)...., ii)...., iii) Figure 9.23(a) illustrates the $K^\pm\pi^\mp$ invariant mass spectrum after
 3184 the selections. The signal-to-background ratio for D^0 is about X%. The statistical accuracy of the A_N
 3185 measurement as a function of x_F estimated using the approach described above is shown in Fig. 9.23(b)
 3186 together with the theory expectations.

Your ad
could be here

(a)

Your ad
could be here

(b)

Figure 9.23

3187 Another way to improve the signal-to-background ratio is the tagging the D -mesons by their origin from
3188 the decay of a higher state $D^* \rightarrow D\pi$. The complexity of this approach lies in the need to detect soft
3189 ($p_{\pi} \sim 0.1$ GeV) pion.

Chapter 10

Integration and services [OUT OF DATE]

According NICA TDR [420] the SPD is allocated in southern point of beams collision. The NICA SPD location is shown in Figure 10.1.



Figure 10.1: NICA layout with SPD.

The experimental hall is designed very close to MPD hall [421].

1 Hall facilities and services

The hall solid concrete floor is considered to have the bearing capacity to be able to perform the operation and assembly of the SPD. It would be quite enough:

1. to bear the weight of the assembled detector with needed services,
2. to keep the integrity of the detector in the process of its transportation on the rail guided carriage and its assembling,
3. to provide a stable detector position during operation cycles with high accuracy .

3202 A helium refrigerators has to be mounted in close to the detector to provide cryogenic fluids and gases for
 3203 toroidal and solenoidal magnets operation (see chapter 3.2). The crates of the data acquisition systems
 3204 and power supplies has to be placed in close the detector on special electronic platforms.

3205 2 SPD integration

3206 The SPD hall shown in Figures 10.2, 10.3, consists of the Production area and Experimental hall. The
 3207 experimental area is located on the right side of the Figure 10.2, below the level of the production area.
 3208 The production area will be used for the preparation and testing of the SPD detectors system and for
 3209 the installation and the final assembly for the data taking. Also, the Production area will be used for
 3210 technical work and maintenance of the set-up. It is assumed that the maximum for the power supply of
 3211 the SPD hall will be about 1.2 MWatts.

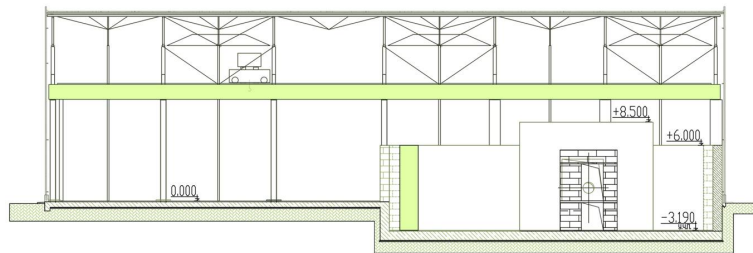


Figure 10.2: SPD experimental hall.

3212 The sizes of the SPD hall is as follows: the total area is more than 2000 m^2 , the main gate for trucks -
 3213 $4000 \text{ mm} \times 4000 \text{ mm}$, the dismantle part of wall for widest equipment - $8000 \text{ mm} \times 8000 \text{ mm}$.

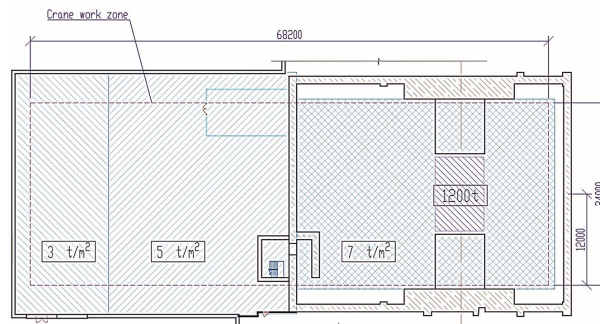


Figure 10.3: The view from the top of the SPD experimental hall.

3214 To provide access to the electronic racks and to sections of the detector, between the detector and the
 3215 electronics platform especial radiation shielding can be installed.

Table 10.1: Technical requirements.

Subsystem	Weight, t	Power, kW	Special requirements
VD	< 0.1	1-1.5	water cooling
ST	0.1	2-4	Ar
ECAL	60	63	
RS	800	>15	Ar+CO ₂
BBC			
Magnet	50	?	cryogenics
Supporting structure	200		
Total	1110+	81+	

Chapter 11

Beam test facilities [A. Baldin, A. Kovalenko]

Two dedicated beam test facilities are planned to operate for the benefit of the SPD project. The first one using secondary beams from the Nuclotron is organizing in the building 205 (LHEP). It will be used for testing and certification of detector elements, electronics, data acquisition and slow-control systems under conditions close to those anticipated at NICA. Some elements could be studied using the SPD straight section of NICA before the Spin Physics Detector construction at early phase of the collider running. Beam test facilities will be also used for education and training young specialists for the SPD project.

1 Test zone with extracted Nuclotron beams

Two specialized channels for secondary particles (electrons, muons, pions, kaons, protons, neutrons, light nuclei) will be organized: the Low Momentum Channel (LMC) and the High Momentum Channel (HMC) in the region of focus F4 of extracted beams of Nuclotron. The LMC is designated for secondary beams with a momentum range from 100 MeV/c to 2 GeV/c while a momentum range of secondary particles at HMC is from 1 GeV/c to 10 GeV/c. After upgrade the existing channel of the MARUSYA installation [422–425] will be used in the LMC construction. It is advantageous that there exists positive experience in working with extracted polarized beams at MARUSYA [426]. This would ensure physical measurements at extracted beams using the existing experimental installation and infrastructure. The installation MARUSYA is well suitable for applied studies with secondary beams at maximum possible intensity of the primary beam extracted to the building 205 up to 10^{11} protons per acceleration cycle. The development of HMC requires two new magnetic elements; therefore, it is considered as an independent installation to be put in operation at the second stage of upgrade in accordance with the existing regulations for commissioning of experimental facilities. Layout of the main elements of the SPD test zone are shown in Fig. 11.1.

It is planned to use the SP12 magnet of the VP1 extraction channel situated directly in front of F4 focus in order to turn the primary extracted beam toward HMC. Calculations show that the primary beam can be turned to the required angle in a proton momentum range of 1–7 GeV/c. For higher-energy particles, it is necessary to use a target in F4 focus. In this operation mode, secondary beams are formed at the LMC and HMC simultaneously. Note that this operation mode is possible with parallel operation of other installations at VP1 extraction channel in particular the BM&N setup. For primary 5 GeV/nucleon deuteron beam extracted to carbon targets with a thickness from 0.005 to 5 g/cm², typical intensities for different species available at LMC and HMC are shown in Tab. 11.1. There is also a possibility to

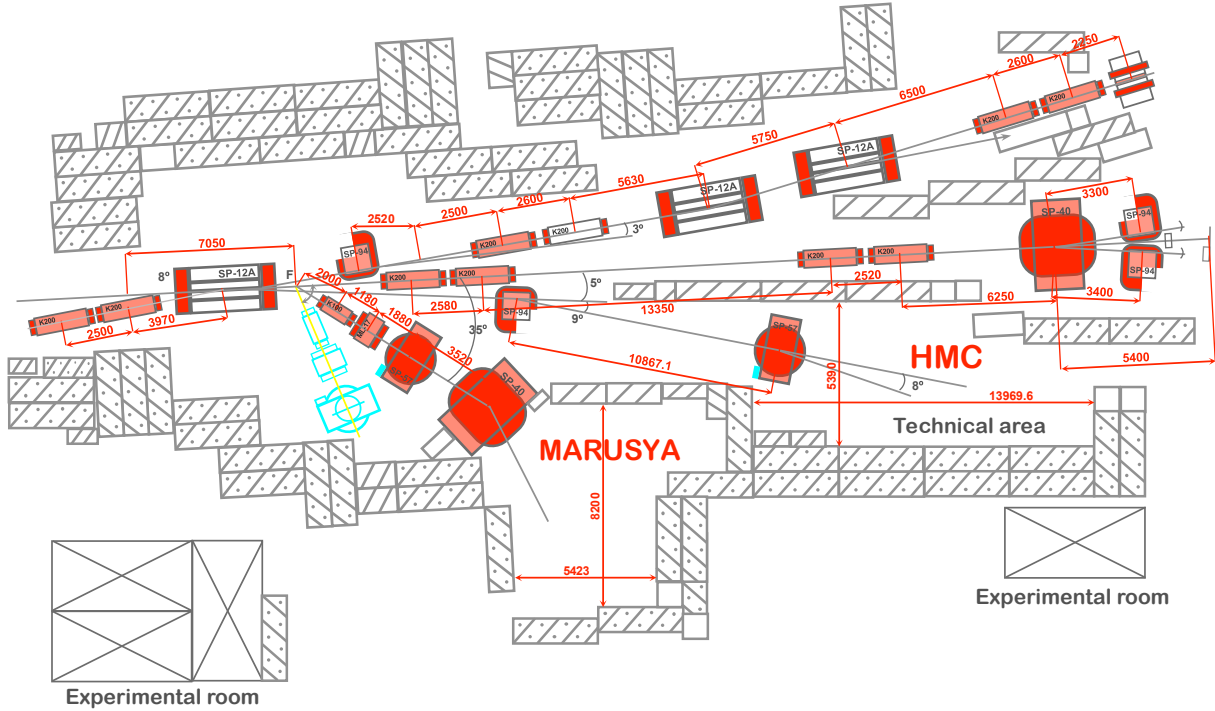


Figure 11.1: Layout of the main elements of the SPD test zone

3249 form a secondary quasi-monochromatic neutron beam via interaction of a deuteron beam in a target and
 3250 deflecting out the charged component.

Table 11.1: Beam intensities feasible at the channel of the LMC and the HMC.

Channel	p, MeV/c	d	p,n	π^\pm	K^+	K^-	μ^\pm	e^\pm
LMC	400	10^3	10^5	10^5	10^3	10^2	10^3	10^3
LMC	800	10^3	10^4	10^4	10^3	10^2	10^3	10^3
LMC	1500	10^2	10^4	10^4	10^3	10^2	10^2	10^2
HMC	2000	10^4	10^5	10^4	10^3	10^2	10^2	10^2
HMC	7000	10^4	10^6	10^3	10^3	10^2	10^2	10^2

3251 Each channel-spectrometer provides spatial registration, identification, and tagging of each particle hit-
 3252 ting the detector under the condition of matching of the electronic registration system of the installation
 3253 and the tested detector or data acquisition system element. A prototype time-of-flight system based on
 3254 scintillation hodoscopes demonstrated reliable identification of protons, pions, kaons in a momentum
 3255 range of 600-1200 MeV/c for LMC. TOF scintillation hodoscopes providing a momentum resolution of
 3256 0.5% and a time resolution on a level of 100 ps are capable of on-line detection and identification of
 3257 secondary pions, kaons and protons at HMC. In order to extend testing capabilities of the SPD test zone
 3258 it will be equipped with new coordinate detectors, Cherenkov counter and BGO-based electromagnetic
 3259 calorimeter.

3260 **2 Tests at the SPD straight section of the collider**

Chapter 12

Running strategy

1 Accelerator [A. Kovalenko]

We consider the strategy of SPD operation as successive chain of the experimental work with polarized proton and deuteron beam aimed at the obtaining of the ultimate polarized proton beam parameters at the collider and the use of the existing unique polarized deuteron beam for physics experiments from the early beginning of the collider putting into commissioning. Polarized deuterons $d\uparrow$ was first accelerated at the old LHEP proton accelerator Synchrophasotron in 1986 and much later at the new superconducting synchrotron- Nuclotron in 2002 (see Fig. 12.1).

Polarized protons $p\uparrow$ was first obtained in 2017. The first test was performed after analysis of the proton spin resonances in 2018. The first dangerous proton spin resonance in Nuclotron corresponds to the beam momentum of about 3.5 GeV/c, whereas in the deuteron case the spin resonance will be occurred at the particle kinetic energy of 5.6 GeV/nucleon. This limit is practically equal to the maximum achievable energy corresponding to the magnetic rigidity of the Nuclotron dipoles.



(a)

Figure 12.1: (a) View of the Nuclotron ring.

The existing polarized proton and deuteron ion source SPI provides up to 3 mA pulse current over $t \approx 100$ mks. Thus up to 1.5×10^{11} can be injected in the Nuclotron during the injection time (8 mks). The spin modes (pz, pzz): (0,0), (0,-2), (2/3, 0) and (-1/3,+1) were adjusted. Polarization degree of 80 % was achieved.

The existing pre-accelerator of RFQ-type put limit for the achievable proton energy in the next element of the injector chain - linac LU-20. We can obtain only 5 MeV at its output instead of 20 MeV that we

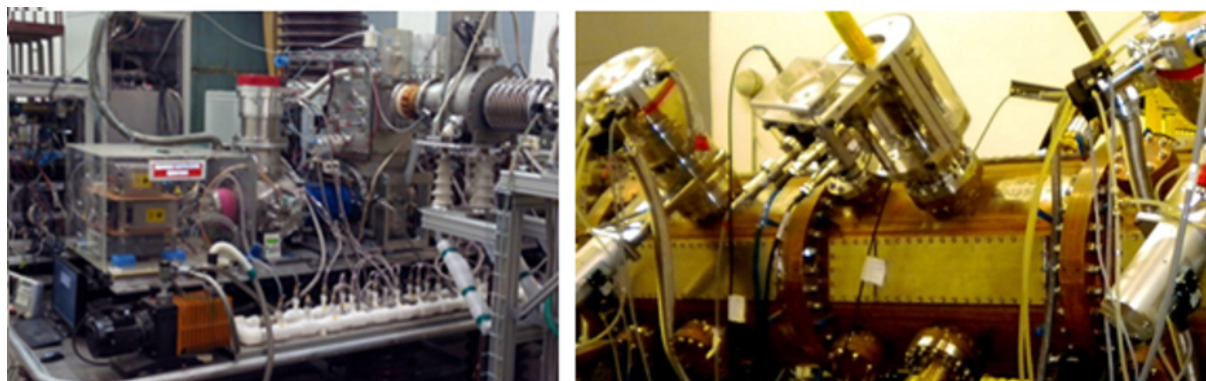


Figure 12.2: View of the SPI (left) and existing RFQ (right).

3281 have had in the past years. The new proton and light ion linac “LILAC” is now under manufacturing.
 3282 The LILAC output energy will be of 12 MeV. Commissioning is scheduled in 2015-2016. Photos of the
 3283 SPI and existing RFQ are presented in Fig. 12.2.

3284 The further tasks for the period of 2021-2025 are reasonable and necessary for the starting the SPD
 3285 operation at the ultimate beam parameters:

- 3286 – continuation of operation and further improvement of polarized ion source SPI, waiting beam time
 3287 at Nuclotron – 2021-2022;
- 3288 – upgrade of the polarimeters: linac output; coasting beam; extracted beam; new polarimeter for
 3289 proton energy above 6 GeV – 2020-2023;
- 3290 – manufacturing of the 6T SC-solenoid model; for the SPD test bench -2021-2022;
- 3291 – design and manufacturing equipment for the SPD test bench at the collider - 2020-2023;
- 3292 – LILAC manufacturing and tests – 2020-2025;
- 3293 – analysis of ^3He (2+) polarized ion source based on the SPI upgrade.

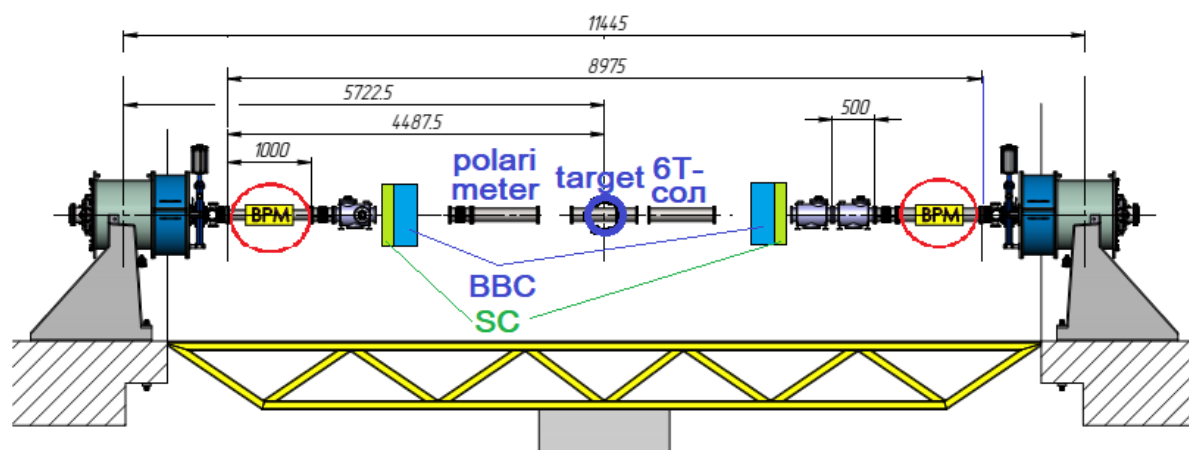


Figure 12.3: The SPD straight section equipped with the diagnostic and control units.

3294 We suppose also, the beam test experiments and preparation to getting the luminosity of $10^{32} \text{ cm}^{-2} \text{ s}^{-1}$ at
 3295 $\sqrt{s} = 27 \text{ GeV}$ including the proton polarization control will be demonstrated by the SPD commissioning.
 3296 For that reason we propose installation of the diagnostic and control equipment at the SPD straight
 3297 section (see Fig. 12.3).

3298 **2 Spin Physics Detector [A. Guskov]**

Table 12.1: Study of the gluon content in proton and deuteron at SPD.

Physics goal	Required time	Experimental conditions
Spin effects in p - p scattering dibaryon resonances	0.3 year	$p_{L,T}$ - $p_{L,T}$, $\sqrt{s} < 7.5$ GeV
Spin effects in p - d scattering, non-nucleonic structure of deuteron, \bar{p} yield	0.3 year	d_t - p , $\sqrt{s} < 7.5$ GeV
Spin effects in d - d scattering hypernuclei	0.3 year	d_t - d_t , $\sqrt{s} < 7.5$ GeV
Hyperon polarization, SRC, ... multiquarks	together with MPD	ions up to Ca
Gluon TMDs, SSA for light hadrons	1 year	p_T - p_T , $\sqrt{s} = 27$ GeV
TMD-factorization test, SSA, charm production near threshold, onset of deconfinement, \bar{p} yield	1 year	p_T - p_T , $7 \text{ GeV} < \sqrt{s} < 27 \text{ GeV}$ (scan)
Gluon helicity, ...	1 year	p_L - p_L , $\sqrt{s} = 27$ GeV
Gluon transversity, non-nucleonic structure of deuteron, "Tensor polarized" PDFs	1 year	d_t - d_T , $\sqrt{s_{NN}} = 13.5$ GeV or/and? d_t - p_T , $\sqrt{s_{NN}} = 19$ GeV

3299 Chapter 13

3300 Cost estimate

3301 The estimated cost of the Spin Physics Detector is XX M\$. This value does not include the construction
3302 of the SPD Test zone and possible R&D expanses. Any expanses related with development and con-
3303 struction of an infrastructure for polarized beams at NICA are also out of this estimation. The detailed
3304 contribution to the total cost is presented in Tab. 13.1.

Table 13.1: Preliminary cost estimate of the SPD setup.

	Subsystem	Cost, M\$
SPD setup	Vertex detector	?
	Straw tracker	2
	ToF system	?
	Electromagnetic calorimeter	21.1
	Range system	16.2
	Aerogel PID system	5
	ZDC	2
	BBC	0.4
	Magnetic system	10
	Beam pipe	?
General infrastructure		?
Data acquisition system		1.6
Computing		10
TOTAL COST		68.3+?

3305 **Chapter 14**

3306 **Participating institutions and author list**
3307 **[In progress]**

3308 **Institute of Applied Physics of the National Academy of Sciences of Belarus, Minsk,**
3309 **Belarus**
3310 Shulyakovsky R.

3311 **Research Institute for Nuclear Problems of Belarusian State University, Minsk, Belarus**
3312 Korjik M.V., Lobko A.S., Makarenko V.V., Solin A.A., Solin A.V.

3313 **Higher Institute of Technologies and Applied Sciences (InSTEC), Havana University,**
3314 **Havana, Cuba**
3315 Guzman F., Garsía Trapaga C.E.

3316 **Charles University, Prague, Czech Republic**
3317 Finger M., Finger M. (jr.), Prochazka I., Slunecka M., Sluneckova V.

3318 **Czech Technical University in Prague, Czech Republic**
3319 Havranek M., Jary V., Lednický D., Marcisovsky M., Neue G., Popule J., Tomasek L., Virius M., Vrba
3320 V.

3321 **University of Turin and INFN Section, Turin, Italy**
3322 Denisov O.Yu., Panzieri D., Rivetti A.

3323 **Joint Institute for Nuclear Research, JINR, Dubna, Russia**
3324 **Directorate**
3325 Lednický R.

3326 **Laboratory of High-Energy Physics**
3327 Anosov V.A., Akhunzyanov R.R., Azorskiy N.I., Baldin A.A., Baldina E.G., Barabanov M.Yu.,
3328 Beloborodov A.N., Belyaev A. V., Bleko V.V., Bogoslovsky D.N., Boguslavsky I.N., Burtsev V.E.,

3329 Dunin V.B., Enik T.L., Filatov Yu.N., Gavrishchuk O.P., Galoyan A.S., Glonti L., Golubykh S.M.,
3330 Grafov N.O., Gribovsky A.S., Gromov S.A., Gromov V.A., Gurchin Yu.V., Gusakov Yu.V., Ivanov
3331 A.V., Ivanov N.Ya., Isupov A.Yu., Kasianova E.A., Kekelidze G.D., Khabarov S.V., Kharusov P.R.,
3332 Khrenov A.N., Kokoulina E.S., Kopylov Yu.A., Korovkin P.S., Korzenev A. Yu., Kostukov E.V.,
3333 Kovalenko A.D., Kozhin M.A., Kramarenko V.A., Kruglov V.N., Ladygin V.P., Lysan V.M., Makankin
3334 A.M., Martovitsky E.V., Meshcheriakov G.V., Moshkovsky I.V., Nagorniy S.N., Nikitin V.A.,
3335 Parzhitsky S.S., Pavlov V.V., Perepelkin E.E., Peshekhonov D.V., Popov V.V., Reznikov S.G.,
3336 Rogachevsky O.V., Safonov A.B., Salamatin K.M., Savenkov A.A., Sheremeteva A.I., Shimanskii S.S.,
3337 Starikova S.Yu., Streletskaya E.A., Tarasov O.G., Terekhin A.A., Teryaev O.V., Tishevsky A.V., Topilin
3338 N.D., Topko B.L., Troyan. Yu.A., Usenko E.A., Vasilieva E.V., Volkov I.S., Volkov P.V., Yudin I.P.,
3339 Zamyatin N.I., Zhukov I.A., Zinin A.V., Zubarev E.V.

Laboratory of Nuclear Problems

3340
3341 Abazov V.M., Alexeev G.D., Afanasyev L.G., Belova A.P., Bobkov A.V., Boltushkin T.V., Brazhnikov
3342 E.V., Denisenko I.I., Duginov V.N., Frolov V.N., Golovanov G.A., Gridin A.O., Gritsay K. I., Guskov
3343 A.V., Kirichkov N.V., Komarov V.I., Kulikov A.V., Kurbatov V.S., Kutuzov S.A., Maltsev A.,
3344 Mitrofanov E.O., Nefedov Yu.A., Pavlova A.A., Parsamyan B., Piskun A.A., Prokhorov I.K., Romanov
3345 V.M., Rudenko A.I., Rumyantsev M.A., Rybakov N.A., Rymbekova A., Samartsev A.G., Semenov
3346 A.V., Shaikovsky V.N., Shtejer K., Sinita A.A., Skachkov N.B., Skachkova A.N., Tereschenko V.V.,
3347 Tkachenko A.V., Tokmenin V.V., Uzikov Yu.N., Verkheev A.Yu., Vertogradov L.S., Vertogradova
3348 Yu.L., Vesenkov V.A., Zhuravlev N.I.

Laboratory of Theoretical Physics

3349
3350 Anikin I.V., Efremov A.V., Goloskokov S.V., Klopot Ya., Strusik-Kotlozh D., Volchansky N.I.

Laboratory of Information Technologies

3351
3352 Goncharov P.V., Oleynik D.A., Ososkov G.A., Petrosyan A.Sh., Podgainy D.V., Polevanyuk I.S.,
3353 Polyakova R.V., Uzhinsky V.V., Zuev M.I.

St. Petersburg Nuclear Physics Institute, Gatchina, Russia

3354
3355 Kim V.T.

Lebedev Physical Institute of the Russian Academy of Sciences, Moscow, Russia

3356
3357 Andreev V.F., Baskov V.A., Dalkarov O.D., Demikhov E.I., Gerasimov S.G., L'vov A.I., Negodaev
3358 M.A., Nechaeva P.Yu., Polyansky V.V., Suchkov S.I., Terkulov A.R., Topchiev N.P.

Skobeltsin Institute of Nuclear Physics of the Moscow State University, Moscow, Russia

3359
3360 Boos E., Merkin M.

Institute for Theoretical and Experimental Physics, Moscow, Russia

3361
3362 Akindinov A.V., Alekseev, Golubev A., Kirin D.Yu., Lushevskaya E., Malkevich D.B., B. Morozov,
3363 Plotnikov V.V., Polozov P., Rusinov V., Stavinskiy A.V., Sultanov R.I., D. Svirida, Tarkovskiy E.I.,
3364 Zhigareva N.M.

Institute for High-Energy Physics, Protvino, Russia

3365
3366 Vorobiev A.

Samara National Research University, Samara, Russia

3367
3368 A.V. Karpishkov, M.A. Nefedov, V.A. Saleev, A.V. Shipilova

3369
3370

St. Petersburg Polytechnic University, St. Petersburg, Russia

Berdnikov Ya.

3371
3372

St. Petersburg State University, St. Petersburg, Russia

Feofilov G.A., V.Kovalenko V.N., Valiev F.F., Vechernin V.V., Zhrebchevsky V.Yo.

3373
3374
3375

Tomsk State University, Tomsk, Russia

Chumakov A., Dusaev R., Lyubovitskij V., Mamon S., Sharko K., Trifonov A., Vasilishin B., Zhevlakov A.

3376
3377

V.N. Karazin Kharkiv National University, Kharkiv, Ukraine

Kovtun V.E., Lyashchenko V.N., Malykhina T.V., Reva S.N., Sotnikov V.V.

3378
3379
3380
3381
3382

Individual contributors:

El-Kholy R. (Cairo University), Konorov I. (Technical University of Munich), Richard J.-M. (Université de Lyon), Strikman M. (Penn State University), Tomasi-Gustafson E. (DPhN, IRFU, CEA, Université Paris-Saclay), Tsenov R. (), Wang Q. (South China Normal University, Guangzhou), Zhao Q. (Institute of High Energy Physics CAS, Beijing)

3383 **Chapter 15**

3384 **Conclusion**

Bibliography

3385

- 3386 [1] A. Kotzinian, New quark distributions and semiinclusive electroproduction on the polarized nu-
3387 cleons, Nucl. Phys. B 441 (1995) 234–248.
- 3388 [2] P. J. Mulders, R. D. Tangerman, The Complete tree level result up to order $1/Q$ for po-
3389 larized deep inelastic leptonproduction, Nucl. Phys. B461 (1996) 197–237, [Erratum: Nucl.
3390 Phys.B484,538(1997)].
- 3391 [3] D. Boer, P. Mulders, Time reversal odd distribution functions in leptonproduction, Phys. Rev. D 57
3392 (1998) 5780–5786.
- 3393 [4] K. Goeke, A. Metz, M. Schlegel, Parameterization of the quark-quark correlator of a spin-1/2
3394 hadron, Phys. Lett. B 618 (2005) 90–96.
- 3395 [5] A. Bacchetta, M. Diehl, K. Goeke, A. Metz, P. J. Mulders, M. Schlegel, Semi-inclusive deep
3396 inelastic scattering at small transverse momentum, JHEP 02 (2007) 093.
- 3397 [6] R. Angeles-Martinez, et al., Transverse Momentum Dependent (TMD) parton distribution func-
3398 tions: status and prospects, Acta Phys. Polon. B 46 (12) (2015) 2501–2534.
- 3399 [7] S. Bastami, et al., Semi-Inclusive Deep Inelastic Scattering in Wandzura-Wilczek-type approxi-
3400 mation, JHEP 06 (2019) 007.
- 3401 [8] S. Arnold, A. Metz, M. Schlegel, Dilepton production from polarized hadron hadron collisions,
3402 Phys. Rev. D79 (2009) 034005.
- 3403 [9] S. Bastami, L. Gamberg, B. Parsamyan, B. Pasquini, A. Prokudin, P. Schweitzer, The Drell-Yan
3404 process with pions and polarized nucleons .
- 3405 [10] A. Metz, A. Vossen, Parton Fragmentation Functions, Prog. Part. Nucl. Phys. 91 (2016) 136–202.
- 3406 [11] M. Anselmino, A. Mukherjee, A. Vossen, Transverse spin effects in hard semi-inclusive collisions
3407 .
- 3408 [12] H. Avakian, B. Parsamyan, A. Prokudin, Spin orbit correlations and the structure of the nucleon,
3409 Riv. Nuovo Cim. 42 (1) (2019) 1–48.
- 3410 [13] M. Grosse Perdekamp, F. Yuan, Transverse Spin Structure of the Nucleon, Ann. Rev. Nucl. Part.
3411 Sci. 65 (2015) 429–456.
- 3412 [14] M. Boglione, A. Prokudin, Phenomenology of transverse spin: past, present and future, Eur. Phys.
3413 J. A 52 (6) (2016) 154.
- 3414 [15] C. A. Aidala, S. D. Bass, D. Hasch, G. K. Mallot, The Spin Structure of the Nucleon, Rev. Mod.
3415 Phys. 85 (2013) 655–691.

- 3416 [16] A. Adare, et al., Measurement of transverse-single-spin asymmetries for midrapidity and forward-
3417 rapidity production of hadrons in polarized p+p collisions at $\sqrt{s} = 200$ and 62.4 GeV, Phys. Rev.
3418 D 90 (1) (2014) 012006.
- 3419 [17] A. Adare, et al., Measurement of Transverse Single-Spin Asymmetries for J/ψ Production in Po-
3420 larized $p + p$ Collisions at $\sqrt{s} = 200$ GeV, Phys. Rev. D 82 (2010) 112008, [Erratum: Phys.Rev.D
3421 86, 099904 (2012)].
- 3422 [18] C. Aidala, et al., Single-spin asymmetry of J/ψ production in $p+p$, $p+Al$, and $p+Au$ collisions
3423 with transversely polarized proton beams at $\sqrt{s_{NN}} = 200$ GeV, Phys. Rev. D 98 (1) (2018) 012006.
- 3424 [19] C. Aidala, et al., Cross section and transverse single-spin asymmetry of muons from open heavy-
3425 flavor decays in polarized $p+p$ collisions at $\sqrt{s} = 200$ GeV, Phys. Rev. D 95 (11) (2017) 112001.
- 3426 [20] C. Adolph, et al., First measurement of the Sivers asymmetry for gluons using SIDIS data, Phys.
3427 Lett. B 772 (2017) 854–864.
- 3428 [21] A. Szabelski, The gluon Sivers asymmetry measurements at COMPASS, PoS DIS2016 (2016)
3429 219.
- 3430 [22] V. Barone, A. Drago, P. G. Ratcliffe, Transverse polarisation of quarks in hadrons, Phys. Rept.
3431 359 (2002) 1–168.
- 3432 [23] C. Hadjidakis, et al., A Fixed-Target Programme at the LHC: Physics Case and Projected Perfor-
3433 mances for Heavy-Ion, Hadron, Spin and Astroparticle Studies .
- 3434 [24] C. Aidala, et al., The LHCSpin Project (2020) 204–207.
- 3435 [25] A. Accardi, et al., Electron Ion Collider: The Next QCD Frontier: Understanding the glue that
3436 binds us all, Eur. Phys. J. A 52 (9) (2016) 268.
- 3437 [26] E. R. Nocera, R. D. Ball, S. Forte, G. Ridolfi, J. Rojo, A first unbiased global determination of
3438 polarized PDFs and their uncertainties, Nucl. Phys. B887 (2014) 276–308.
- 3439 [27] C. Brenner Mariotto, M. B. Gay Ducati, G. Ingelman, Soft and hard QCD dynamics in hadropro-
3440 duction of charmonium, Eur. Phys. J. C23 (2002) 527–538.
- 3441 [28] <https://www.agsrhichome.bnl.gov/RHIC/Runs/>, Run overview of the relativistic heavy ion
3442 collider .
- 3443 [29] I. N. Meshkov, Luminosity of an Ion Collider, Phys. Part. Nucl. 50 (6) (2019) 663–682.
- 3444 [30] I. Abt, et al., Production of the Charmonium States χ_{c1} and χ_{c2} in Proton Nucleus Interactions at
3445 $\sqrt{s} = 41.6$ -GeV, Phys. Rev. D 79 (2009) 012001.
- 3446 [31] C.-Y. Wong, H. Wang, Effects of parton intrinsic transverse momentum on photon production in
3447 hard scattering processes, Phys. Rev. C 58 (1998) 376–388.
- 3448 [32] W. Vogelsang, M. R. Whalley, A Compilation of data on single and double prompt photon pro-
3449 duction in hadron hadron interactions, J. Phys. G23 (1997) A1–A69.
- 3450 [33] P. Aurenche, M. Fontannaz, J.-P. Guillet, E. Pilon, M. Werlen, A New critical study of photon
3451 production in hadronic collisions, Phys. Rev. D73 (2006) 094007.
- 3452 [34] T. Binoth, J. Guillet, E. Pilon, M. Werlen, A Full next-to-leading order study of direct photon pair
3453 production in hadronic collisions, Eur. Phys. J. C 16 (2000) 311–330.

- 3454 [35] L. Apanasevich, et al., Evidence for parton k_T effects in high p_T particle production, Phys. Rev.
3455 Lett. 81 (1998) 2642–2645.
- 3456 [36] E. Anassontzis, et al., High $p(t)$ Direct Photon Production in p p Collisions, Z. Phys. C 13 (1982)
3457 277–289.
- 3458 [37] J. Badier, et al., Direct Photon Pair Production From Pions and Protons at 200-GeV/c, Phys. Lett.
3459 B 164 (1985) 184–188.
- 3460 [38] H.-L. Lai, M. Guzzi, J. Huston, Z. Li, P. M. Nadolsky, J. Pumplin, C.-P. Yuan, New parton distri-
3461 butions for collider physics, Phys. Rev. D 82 (2010) 074024.
- 3462 [39] S. J. Brodsky, K. Y.-J. Chiu, J.-P. Lansberg, N. Yamanaka, The gluon and charm content of the
3463 deuteron, Phys. Lett. B 783 (2018) 287–293.
- 3464 [40] I. Abt, et al., Study of proton parton distribution functions at high x using ZEUS data .
- 3465 [41] A. M. Sirunyan, et al., Measurement of double-differential cross sections for top quark pair pro-
3466 duction in pp collisions at $\sqrt{s} = 8$ TeV and impact on parton distribution functions, Eur. Phys. J.
3467 C 77 (7) (2017) 459.
- 3468 [42] H. Abdolmaleki, A. Khorramian, Parton distribution functions and constraints on the intrinsic
3469 charm content of the proton using the Brodsky-Hoyer-Peterson-Saka approach, Phys. Rev. D
3470 99 (11) (2019) 116019.
- 3471 [43] C. Lourenco, H. Wohri, Heavy flavour hadro-production from fixed-target to collider energies,
3472 Phys. Rept. 433 (2006) 127–180.
- 3473 [44] A. Accardi, et al., A Critical Appraisal and Evaluation of Modern PDFs, Eur. Phys. J. C 76 (8)
3474 (2016) 471.
- 3475 [45] G. Alves, et al., Forward cross-sections for production of D^+ , D^0 , $D(s)$, D^{*+} and Λ_c in 250-
3476 GeV π^\pm , K^\pm , and p - nucleon interactions, Phys. Rev. Lett. 77 (1996) 2388–2391, [Erratum:
3477 Phys.Rev.Lett. 81, 1537 (1998)].
- 3478 [46] G. F. Sterman, Summation of Large Corrections to Short Distance Hadronic Cross-Sections, Nucl.
3479 Phys. B 281 (1987) 310–364.
- 3480 [47] S. Catani, L. Trentadue, Resummation of the QCD Perturbative Series for Hard Processes, Nucl.
3481 Phys. B 327 (1989) 323–352.
- 3482 [48] H. Contopanagos, E. Laenen, G. F. Sterman, Sudakov factorization and resummation, Nucl. Phys.
3483 B 484 (1997) 303–330.
- 3484 [49] N. Kidonakis, G. Oderda, G. F. Sterman, Evolution of color exchange in QCD hard scattering,
3485 Nucl. Phys. B 531 (1998) 365–402.
- 3486 [50] N. Ivanov, Perturbative stability of the QCD predictions for single spin asymmetry in heavy quark
3487 photoproduction, Nucl. Phys. B 615 (2001) 266–284.
- 3488 [51] S. Catani, M. L. Mangano, P. Nason, L. Trentadue, The Resummation of soft gluons in hadronic
3489 collisions, Nucl. Phys. B 478 (1996) 273–310.
- 3490 [52] E. L. Berger, H. Contopanagos, The Perturbative resummed series for top quark production in
3491 hadron reactions, Phys. Rev. D 54 (1996) 3085–3113.

- 3492 [53] N. Kidonakis, High order corrections and subleading logarithms for top quark production, Phys.
3493 Rev. D 64 (2001) 014009.
- 3494 [54] S. Forte, G. Ridolfi, J. Rojo, M. Ubiali, Borel resummation of soft gluon radiation and higher
3495 twists, Phys. Lett. B 635 (2006) 313–319.
- 3496 [55] S. Brodsky, P. Hoyer, C. Peterson, N. Sakai, The Intrinsic Charm of the Proton, Phys. Lett. B 93
3497 (1980) 451–455.
- 3498 [56] S. J. Brodsky, C. Peterson, N. Sakai, Intrinsic Heavy Quark States, Phys. Rev. D 23 (1981) 2745.
- 3499 [57] L. Ananikyan, N. Ivanov, Azimuthal Asymmetries in DIS as a Probe of Intrinsic Charm Content
3500 of the Proton, Nucl. Phys. B 762 (2007) 256–283.
- 3501 [58] J. Collins, Foundations of perturbative QCD, Vol. 32, Cambridge University Press, 2013.
- 3502 [59] M. G. Echevarria, T. Kasemets, P. J. Mulders, C. Pisano, QCD evolution of (un)polarized gluon
3503 TMDPDFs and the Higgs q_T -distribution, JHEP 07 (2015) 158, [Erratum: JHEP 05, 073 (2017)].
- 3504 [60] M. G. Echevarria, Proper TMD factorization for quarkonia production: $pp \rightarrow \eta_{c,b}$ as a study case,
3505 JHEP 10 (2019) 144.
- 3506 [61] S. Fleming, Y. Makris, T. Mehen, An effective field theory approach to quarkonium at small
3507 transverse momentum, JHEP 04 (2020) 122.
- 3508 [62] P. Mulders, J. Rodrigues, Transverse momentum dependence in gluon distribution and fragmen-
3509 tation functions, Phys. Rev. D 63 (2001) 094021.
- 3510 [63] D. Boer, S. J. Brodsky, P. J. Mulders, C. Pisano, Direct Probes of Linearly Polarized Gluons inside
3511 Unpolarized Hadrons, Phys. Rev. Lett. 106 (2011) 132001.
- 3512 [64] C. Pisano, D. Boer, S. J. Brodsky, M. G. Buffing, P. J. Mulders, Linear polarization of gluons and
3513 photons in unpolarized collider experiments, JHEP 10 (2013) 024.
- 3514 [65] A. Efremov, N. Ivanov, O. Teryaev, QCD predictions for the azimuthal asymmetry in charm lep-
3515 toproduction for the COMPASS kinematics, Phys. Lett. B 772 (2017) 283–289.
- 3516 [66] N. Y. Ivanov, A. Efremov, O. Teryaev, How to measure the linear polarization of gluons in unpolarized
3517 proton using the heavy-quark pair production, EPJ Web Conf. 204 (2019) 02006.
- 3518 [67] A. Efremov, N. Y. Ivanov, O. Teryaev, The ratio $R = d\sigma_L/d\sigma_T$ in heavy-quark pair lepton production
3519 as a probe of linearly polarized gluons in unpolarized proton, Phys. Lett. B 780 (2018) 303–307.
- 3520 [68] D. Boer, C. Pisano, Polarized gluon studies with charmonium and bottomonium at LHCb and
3521 AFTER, Phys. Rev. D 86 (2012) 094007.
- 3522 [69] J.-W. Qiu, M. Schlegel, W. Vogelsang, Probing Gluonic Spin-Orbit Correlations in Photon Pair
3523 Production, Phys. Rev. Lett. 107 (2011) 062001.
- 3524 [70] J.-P. Lansberg, C. Pisano, F. Scarpa, M. Schlegel, Pinning down the linearly-polarised gluons
3525 inside unpolarised protons using quarkonium-pair production at the LHC, Phys. Lett. B 784 (2018)
3526 217–222, [Erratum: Phys.Lett.B 791, 420–421 (2019)].
- 3527 [71] G. T. Bodwin, E. Braaten, G. Lepage, Rigorous QCD analysis of inclusive annihilation and pro-
3528 duction of heavy quarkonium, Phys. Rev. D 51 (1995) 1125–1171, [Erratum: Phys.Rev.D 55,
3529 5853 (1997)].

- 3530 [72] V. D. Barger, W.-Y. Keung, R. Phillips, On psi and Upsilon Production via Gluons, Phys. Lett. B
3531 91 (1980) 253–258.
- 3532 [73] V. D. Barger, W.-Y. Keung, R. Phillips, Hadroproduction of ψ and Υ , Z. Phys. C 6 (1980) 169.
- 3533 [74] R. Gvai, D. Kharzeev, H. Satz, G. Schuler, K. Sridhar, R. Vogt, Quarkonium production in
3534 hadronic collisions, Int. J. Mod. Phys. A 10 (1995) 3043–3070.
- 3535 [75] Y.-Q. Ma, R. Vogt, Quarkonium Production in an Improved Color Evaporation Model, Phys. Rev.
3536 D 94 (11) (2016) 114029.
- 3537 [76] N. Brambilla, et al., Heavy Quarkonium: Progress, Puzzles, and Opportunities, Eur. Phys. J. C 71
3538 (2011) 1534.
- 3539 [77] J.-P. Lansberg, New Observables in Inclusive Production of Quarkonia .
- 3540 [78] M. Butenschoen, B. A. Kniehl, J/ψ polarization at Tevatron and LHC: Nonrelativistic-QCD fac-
3541 torization at the crossroads, Phys. Rev. Lett. 108 (2012) 172002.
- 3542 [79] M. Butenschoen, B. A. Kniehl, Next-to-leading-order tests of NRQCD factorization with J/ψ
3543 yield and polarization, Mod. Phys. Lett. A 28 (2013) 1350027.
- 3544 [80] M. Butenschoen, Z.-G. He, B. A. Kniehl, η_c production at the LHC challenges nonrelativistic-
3545 QCD factorization, Phys. Rev. Lett. 114 (9) (2015) 092004.
- 3546 [81] L.-P. Sun, H. Han, K.-T. Chao, Impact of J/ψ pair production at the LHC and predictions in
3547 nonrelativistic QCD, Phys. Rev. D 94 (7) (2016) 074033.
- 3548 [82] Z.-G. He, B. A. Kniehl, M. A. Nefedov, V. A. Saleev, Double Prompt J/ψ Hadroproduction in the
3549 Parton Reggeization Approach with High-Energy Resummation, Phys. Rev. Lett. 123 (16) (2019)
3550 162002.
- 3551 [83] J.-P. Lansberg, H.-S. Shao, N. Yamanaka, Y.-J. Zhang, C. Noûs, Complete NLO QCD study of
3552 single- and double-quarkonium hadroproduction in the colour-evaporation model at the Tevatron
3553 and the LHC .
- 3554 [84] Z.-B. Kang, J.-W. Qiu, G. Sterman, Heavy quarkonium production and polarization, Phys. Rev.
3555 Lett. 108 (2012) 102002.
- 3556 [85] Y.-Q. Ma, K.-T. Chao, New factorization theory for heavy quarkonium production and decay,
3557 Phys. Rev. D 100 (9) (2019) 094007.
- 3558 [86] R. Li, Y. Feng, Y.-Q. Ma, Exclusive quarkonium production or decay in soft gluon factorization,
3559 JHEP 05 (2020) 009.
- 3560 [87] A.-P. Chen, Y.-Q. Ma, Theory for quarkonium: from NRQCD factorization to soft gluon factor-
3561 ization .
- 3562 [88] M. Butenschoen, B. A. Kniehl, Reconciling J/ψ production at HERA, RHIC, Tevatron, and LHC
3563 with NRQCD factorization at next-to-leading order, Phys. Rev. Lett. 106 (2011) 022003.
- 3564 [89] M. Butenschoen, B. A. Kniehl, World data of J/ψ production consolidate NRQCD factorization
3565 at NLO, Phys. Rev. D 84 (2011) 051501.

- 3566 [90] A. V. Karpishkov, M. A. Nefedov, V. A. Saleev, $B\bar{B}$ angular correlations at the LHC in parton
3567 Reggeization approach merged with higher-order matrix elements, Phys. Rev. D 96 (9) (2017)
3568 096019.
- 3569 [91] V. Saleev, M. Nefedov, A. Shipilova, Prompt J/ψ production in the Regge limit of QCD: From
3570 Tevatron to LHC, Phys. Rev. D 85 (2012) 074013.
- 3571 [92] A. Karpishkov, M. Nefedov, V. Saleev, Spectra and polarizations of prompt J/ψ at the NICA
3572 within collinear parton model and parton Reggeization approach, J. Phys. Conf. Ser. 1435 (1)
3573 (2020) 012015.
- 3574 [93] V. Cheung, R. Vogt, Production and polarization of prompt J/ψ in the improved color evaporation
3575 model using the k_T -factorization approach, Phys. Rev. D 98 (11) (2018) 114029.
- 3576 [94] A. Airapetian, et al., First measurement of the tensor structure function $b(1)$ of the deuteron, Phys.
3577 Rev. Lett. 95 (2005) 242001.
- 3578 [95] M. Harvey, On the Fractional Parentage Expansions of Color Singlet Six Quark States in a Cluster
3579 Model, Nucl. Phys. A 352 (1981) 301, [Erratum: Nucl.Phys.A 481, 834 (1988)].
- 3580 [96] G. A. Miller, Pionic and Hidden-Color, Six-Quark Contributions to the Deuteron b_1 Structure
3581 Function, Phys. Rev. C 89 (4) (2014) 045203.
- 3582 [97] P. Hoyer, D. Roy, The Intrinsic gluon component of the nucleon, Phys. Lett. B 410 (1997) 63–66.
- 3583 [98] H. Mäntysaari, B. Schenke, Accessing the gluonic structure of light nuclei at a future electron-ion
3584 collider, Phys. Rev. C 101 (1) (2020) 015203.
- 3585 [99] F. Winter, W. Detmold, A. S. Gambhir, K. Orginos, M. J. Savage, P. E. Shanahan, M. L. Wagman,
3586 First lattice QCD study of the gluonic structure of light nuclei, Phys. Rev. D 96 (9) (2017) 094512.
- 3587 [100] J. Ashman, et al., An Investigation of the Spin Structure of the Proton in Deep Inelastic Scattering
3588 of Polarized Muons on Polarized Protons, Nucl. Phys. B 328 (1989) 1.
- 3589 [101] D. L. Adams, et al., Measurement of the double spin asymmetry A_{LL} for inclusive multi gamma
3590 pair production with 200-GeV/c polarized proton beam and polarized proton target, Phys. Lett.
3591 B336 (1994) 269–274.
- 3592 [102] A. Airapetian, et al., Leading-Order Determination of the Gluon Polarization from high-p(T)
3593 Hadron Electroproduction, JHEP 08 (2010) 130.
- 3594 [103] B. Adeva, et al., Spin asymmetries for events with high p(T) hadrons in DIS and an evaluation of
3595 the gluon polarization, Phys. Rev. D70 (2004) 012002.
- 3596 [104] E. S. Ageev, et al., Gluon polarization in the nucleon from quasi-real photoproduction of high-p(T)
3597 hadron pairs, Phys. Lett. B633 (2006) 25–32.
- 3598 [105] M. Alekseev, et al., Gluon polarisation in the nucleon and longitudinal double spin asymmetries
3599 from open charm muoproduction, Phys. Lett. B676 (2009) 31–38.
- 3600 [106] C. Adolph, et al., Leading order determination of the gluon polarisation from DIS events with
3601 high- p_T hadron pairs, Phys. Lett. B718 (2013) 922–930.
- 3602 [107] C. Adolph, et al., Leading and Next-to-Leading Order Gluon Polarization in the Nucleon and
3603 Longitudinal Double Spin Asymmetries from Open Charm Muoproduction, Phys. Rev. D87 (5)
3604 (2013) 052018.

- 3605 [108] C. Adolph, et al., Leading-order determination of the gluon polarisation from semi-inclusive deep
3606 inelastic scattering data, *Eur. Phys. J. C* 77 (4) (2017) 209.
- 3607 [109] A. Adare, et al., Inclusive double-helicity asymmetries in neutral-pion and eta-meson production
3608 in $\vec{p} + \vec{p}$ collisions at $\sqrt{s} = 200$ GeV, *Phys. Rev. D* 90 (1) (2014) 012007.
- 3609 [110] A. Adare, et al., The Polarized gluon contribution to the proton spin from the double helicity
3610 asymmetry in inclusive π^0 production in polarized $p + p$ collisions at $\sqrt{s} = 200$ -GeV, *Phys. Rev.*
3611 *Lett.* 103 (2009) 012003.
- 3612 [111] A. Adare, et al., Inclusive cross section and double helicity asymmetry for π^0 production in $p^+ p$
3613 collisions at $\sqrt{s} = 62.4$ GeV, *Phys. Rev. D* 79 (2009) 012003.
- 3614 [112] P. Djawotho, Gluon polarization and jet production at STAR, *Nuovo Cim.* C036 (05) (2013) 35–
3615 38.
- 3616 [113] A. Adare, et al., Double Spin Asymmetry of Electrons from Heavy Flavor Decays in $p + p$ Colli-
3617 sions at $\sqrt{s} = 200$ GeV, *Phys. Rev. D* 87 (1) (2013) 012011.
- 3618 [114] A. Adare, et al., Measurements of double-helicity asymmetries in inclusive J/ψ production in
3619 longitudinally polarized $p + p$ collisions at $\sqrt{s} = 510$ GeV, *Phys. Rev. D* 94 (11) (2016) 112008.
- 3620 [115] E. Leader, A. V. Sidorov, D. B. Stamenov, New analysis concerning the strange quark polarization
3621 puzzle, *Phys. Rev. D* 91 (5) (2015) 054017.
- 3622 [116] D. de Florian, R. Sassot, M. Stratmann, W. Vogelsang, Evidence for polarization of gluons in the
3623 proton, *Phys. Rev. Lett.* 113 (1) (2014) 012001.
- 3624 [117] D. De Florian, G. A. Lucero, R. Sassot, M. Stratmann, W. Vogelsang, Monte Carlo sampling
3625 variant of the DSSV14 set of helicity parton densities, *Phys. Rev. D* 100 (11) (2019) 114027.
- 3626 [118] J. J. Ethier, N. Sato, W. Melnitchouk, First simultaneous extraction of spin-dependent parton dis-
3627 tributions and fragmentation functions from a global QCD analysis, *Phys. Rev. Lett.* 119 (13)
3628 (2017) 132001.
- 3629 [119] J. J. Ethier, E. R. Nocera, Parton Distributions in Nucleons and Nuclei, *Ann. Rev. Nucl. Part. Sci.*
3630 (70) (2020) 1–34.
- 3631 [120] D. de Florian, R. Sassot, M. Stratmann, W. Vogelsang, Global Analysis of Helicity Parton Densi-
3632 ties and Their Uncertainties, *Phys. Rev. Lett.* 101 (2008) 072001.
- 3633 [121] C. AIDALA, G. BUNCE, E. AL., Research plan for spin physics at rhic. .
- 3634 [122] M. Anselmino, E. Andreeva, V. Korotkov, F. Murgia, W. D. Nowak, S. Nurushev, O. Teryaev,
3635 A. Tkabladze, On the physics potential of polarized nucleon-nucleon collisions at HERA, in:
3636 Future physics at HERA. Proceedings, Workshop, Hamburg, Germany, September 25, 1995-May
3637 31, 1996. Vol. 1, 2, 1996.
- 3638 [123] E. Leader, Spin in particle physics, Cambridge University Press (2011).
- 3639 [124] Y. Feng, H.-F. Zhang, Double longitudinal-spin asymmetries in J/ψ production at RHIC, *JHEP*
3640 11 (2018) 136.
- 3641 [125] W. Vogelsang, Prompt photon production in polarized hadron collisions, in: Deep inelastic scat-
3642 tering. Proceedings, 8th International Workshop, DIS 2000, Liverpool, UK, April 25-30, 2000,
3643 2000, pp. 253–254.

- 3644 [126] L. E. Gordon, W. Vogelsang, Inclusive prompt photon production in polarized p p collisions at
3645 HERA-N(polarized), Phys. Lett. B387 (1996) 629–636.
- 3646 [127] L. E. Gordon, Constraints on Delta G from prompt photon plus jet production at HERA-N (polar-
3647 ized), Phys. Lett. B406 (1997) 184–192.
- 3648 [128] Q.-h. Xu, Z.-t. Liang, Probing gluon helicity distribution and quark transversity through hyperon
3649 polarization in singly polarized pp collisions, Phys. Rev. D70 (2004) 034015.
- 3650 [129] A. Efremov, O. Teryaev, On Spin Effects in Quantum Chromodynamics, Sov. J. Nucl. Phys. 36
3651 (1982) 140.
- 3652 [130] A. Efremov, O. Teryaev, QCD Asymmetry and Polarized Hadron Structure Functions, Phys. Lett.
3653 B 150 (1985) 383.
- 3654 [131] J.-w. Qiu, G. F. Sterman, Single transverse spin asymmetries, Phys. Rev. Lett. 67 (1991) 2264–
3655 2267.
- 3656 [132] A. Efremov, V. Korotkiian, O. Teryaev, The twist - three single spin asymmetries of pion produc-
3657 tion, Phys. Lett. B 348 (1995) 577–581.
- 3658 [133] D. W. Sivers, Single Spin Production Asymmetries from the Hard Scattering of Point-Like Con-
3659 stituents, Phys. Rev. D 41 (1990) 83.
- 3660 [134] D. Boer, C. Lorcé, C. Pisano, J. Zhou, The gluon Sivers distribution: status and future prospects,
3661 Adv. High Energy Phys. 2015 (2015) 371396.
- 3662 [135] U. D’Alesio, F. Murgia, C. Pisano, Towards a first estimate of the gluon Sivers function from A_N
3663 data in pp collisions at RHIC, JHEP 09 (2015) 119.
- 3664 [136] M. Anselmino, M. Boglione, U. D’Alesio, A. Kotzinian, F. Murgia, A. Prokudin, Extracting
3665 the Sivers function from polarized SIDIS data and making predictions, Phys. Rev. D 72 (2005)
3666 094007, [Erratum: Phys.Rev.D 72, 099903 (2005)].
- 3667 [137] M. Anselmino, M. Boglione, U. D’Alesio, A. Kotzinian, S. Melis, F. Murgia, A. Prokudin,
3668 C. Turk, Sivers Effect for Pion and Kaon Production in Semi-Inclusive Deep Inelastic Scatter-
3669 ing, Eur. Phys. J. A 39 (2009) 89–100.
- 3670 [138] S. Kretzer, Fragmentation functions from flavor inclusive and flavor tagged $e^+ e^-$ annihilations,
3671 Phys. Rev. D 62 (2000) 054001.
- 3672 [139] D. de Florian, R. Sassot, M. Stratmann, Global analysis of fragmentation functions for pions and
3673 kaons and their uncertainties, Phys. Rev. D 75 (2007) 114010.
- 3674 [140] R. M. Godbole, A. Kaushik, A. Misra, V. Rawoot, B. Sonawane, Transverse single spin asymmetry
3675 in $p + p^\uparrow \rightarrow J/\psi + X$, Phys. Rev. D 96 (9) (2017) 096025.
- 3676 [141] M. Anselmino, M. Boglione, U. D’Alesio, E. Leader, F. Murgia, Accessing Sivers gluon distribu-
3677 tion via transverse single spin asymmetries in p(transv. polarized) p \rightarrow j D X processes at RHIC,
3678 Phys. Rev. D 70 (2004) 074025.
- 3679 [142] Y. Koike, S. Yoshida, Probing the three-gluon correlation functions by the single spin asymmetry
3680 in $p^\uparrow p \rightarrow DX$, Phys. Rev. D 84 (2011) 014026.
- 3681 [143] Z.-B. Kang, J.-W. Qiu, W. Vogelsang, F. Yuan, Accessing tri-gluon correlations in the nucleon via
3682 the single spin asymmetry in open charm production, Phys. Rev. D78 (2008) 114013.

- 3683 [144] R. M. Godbole, A. Kaushik, A. Misra, Transverse single spin asymmetry in $p + p^\uparrow \rightarrow D^+ X$, Phys. Rev. D94 (11) (2016) 114022.
3684
- 3685 [145] N. Hammon, B. Ehrnsperger, A. Schaefer, Single-transverse spin asymmetry in prompt photon production, J. Phys. G24 (1998) 991–1001.
3686
- 3687 [146] K. Kanazawa, Y. Koike, Single transverse-spin asymmetry for direct-photon and single-jet productions at RHIC, Phys. Lett. B720 (2013) 161–165.
3688
- 3689 [147] D. Boer, W. Vogelsang, Asymmetric jet correlations in p p uparrow scattering, Phys. Rev. D69 (2004) 094025.
3690
- 3691 [148] U. D’Alesio, F. Murgia, C. Pisano, P. Taelis, Probing the gluon Sivers function in $p^\uparrow p \rightarrow J/\psi X$ and $p^\uparrow p \rightarrow DX$, Phys. Rev. D 96 (3) (2017) 036011.
3692
- 3693 [149] U. D’Alesio, F. Murgia, C. Pisano, S. Rajesh, Single-spin asymmetries in $p^\uparrow p \rightarrow J/\psi + X$ within a TMD approach: role of the color octet mechanism, Eur. Phys. J. C 79 (12) (2019) 1029.
3694
- 3695 [150] D. L. Adams, et al., Measurement of single spin asymmetry for direct photon production in p p collisions at 200-GeV/c, Phys. Lett. B345 (1995) 569–575.
3696
- 3697 [151] S. Kumano, Q.-T. Song, Gluon transversity in polarized proton-deuteron Drell-Yan process, Phys. Rev. D 101 (5) (2020) 054011.
3698
- 3699 [152] J. Soffer, M. Stratmann, W. Vogelsang, Accessing transversity in double-spin asymmetries at the BNL-RHIC, Phys. Rev. D 65 (2002) 114024.
3700
- 3701 [153] A. Mukherjee, M. Stratmann, W. Vogelsang, Next-to-leading order QCD corrections to A(TT) for prompt photon production, Phys. Rev. D 67 (2003) 114006.
3702
- 3703 [154] R. Jaffe, A. Manohar, NUCLEAR GLUONOMETRY, Phys. Lett. B 223 (1989) 218–224.
- 3704 [155] O. Teryaev, Shear forces and tensor polarization, PoS DIS2019 (2019) 240.
- 3705 [156] P. Hoodbhoy, R. Jaffe, A. Manohar, Novel Effects in Deep Inelastic Scattering from Spin 1 Hadrons, Nucl. Phys. B 312 (1989) 571–588.
3706
- 3707 [157] F. Close, S. Kumano, A sum rule for the spin dependent structure function b-1(x) for spin one hadrons, Phys. Rev. D 42 (1990) 2377–2379.
3708
- 3709 [158] A. Efremov, O. Teryaev, ON HIGH P(T) VECTOR MESONS SPIN ALIGNMENT, Sov. J. Nucl. Phys. 36 (1982) 557.
3710
- 3711 [159] A. Efremov, O. Teryaev, On the oscillations of the tensor spin structure function, in: International Symposium: Dubna Deuteron 93, 1994.
3712
- 3713 [160] O. Teryaev, Nucleon spin and orbital structure: 20 years later, Mod. Phys. Lett. A 24 (2009) 2831–2837.
3714
- 3715 [161] O. Teryaev, Spin structure of nucleon and equivalence principle .
- 3716 [162] O. Teryaev, Sources of time reversal odd spin asymmetries in QCD, Czech. J. Phys. 53 (2003) 47–58A.
3717
- 3718 [163] O. Teryaev, Equivalence principle and partition of angular momenta in the nucleon, AIP Conf. Proc. 915 (1) (2007) 260–263.
3719

- 3720 [164] O. Teryaev, Gravitational form factors and nucleon spin structure, *Front. Phys. (Beijing)* 11 (5)
3721 (2016) 111207.
- 3722 [165] G. Y. Prokhorov, O. V. Teryaev, V. I. Zakharov, Unruh effect for fermions from the Zubarev density
3723 operator, *Phys. Rev. D* 99 (7) (2019) 071901.
- 3724 [166] M. V. Polyakov, H.-D. Son, Nucleon gravitational form factors from instantons: forces between
3725 quark and gluon subsystems, *JHEP* 09 (2018) 156.
- 3726 [167] S. Kumano, Q.-T. Song, Spin asymmetry for proton-deuteron Drell-Yan process with tensor-
3727 polarized deuteron, in: 22nd International Symposium on Spin Physics, 2017.
- 3728 [168] D. L. Adams, et al., Comparison of spin asymmetries and cross-sections in π^0 production by 200
3729 GeV polarized anti-protons and protons, *Phys. Lett. B* 261 (1991) 201–206.
- 3730 [169] D. L. Adams, et al., Analyzing power in inclusive π^+ and π^- production at high $x(F)$ with a
3731 200-GeV polarized proton beam, *Phys. Lett. B* 264 (1991) 462–466.
- 3732 [170] A. Bravar, et al., Single spin asymmetries in inclusive charged pion production by transversely
3733 polarized anti-protons, *Phys. Rev. Lett.* 77 (1996) 2626–2629.
- 3734 [171] D. Adams, et al., Measurement of single spin asymmetry in eta meson production in p (polarized)
3735 p and anti-p (polarized) p interactions in the beam fragmentation region at 200-GeV/c, *Nucl. Phys.*
3736 *B* 510 (1998) 3–11.
- 3737 [172] S. Heppelmann, Measurement of Transverse Single Spin Asymmetry $A(N)$ in Eta Mass Region at
3738 Large Feynman $X(F)$ with the STAR Forward Pion Detector, in: 18th International Conference on
3739 Particles and Nuclei, 2009, pp. 273–275.
- 3740 [173] I. Arsene, et al., Single Transverse Spin Asymmetries of Identified Charged Hadrons in Polarized
3741 p+p Collisions at $\sqrt{s^{**}}(1/2) = 62.4$ -GeV, *Phys. Rev. Lett.* 101 (2008) 042001.
- 3742 [174] B. Abelev, et al., Forward Neutral Pion Transverse Single Spin Asymmetries in p+p Collisions at
3743 $\sqrt{s^{**}}(1/2) = 200$ -GeV, *Phys. Rev. Lett.* 101 (2008) 222001.
- 3744 [175] S. Adler, et al., Measurement of transverse single-spin asymmetries for mid-rapidity production
3745 of neutral pions and charged hadrons in polarized p+p collisions at $\sqrt{s^{**}}(1/2) = 200$ -GeV, *Phys.*
3746 *Rev. Lett.* 95 (2005) 202001.
- 3747 [176] J. Adams, et al., Cross-sections and transverse single spin asymmetries in forward neutral pion
3748 production from proton collisions at $\sqrt{s^{**}}(1/2) = 200$ - GeV, *Phys. Rev. Lett.* 92 (2004) 171801.
- 3749 [177] J. Cammarota, L. Gamberg, Z.-B. Kang, J. A. Miller, D. Pitonyak, A. Prokudin, T. C. Rogers,
3750 N. Sato, Origin of single transverse-spin asymmetries in high-energy collisions, *Phys. Rev. D*
3751 102 (5) (2020) 054002.
- 3752 [178] Prokudin A., private communication.
- 3753 [179] M. Aghasyan, et al., First measurement of transverse-spin-dependent azimuthal asymmetries in
3754 the Drell-Yan process, *Phys. Rev. Lett.* 119 (11) (2017) 112002.
- 3755 [180] B. Parsamyan, Transversely polarized Drell-Yan measurements at COMPASS, *PoS DIS2019*
3756 (2019) 195.
- 3757 [181] C. Brown, et al., Letter of Intent for a Drell-Yan Experiment with a Polarized Proton Target .

- 3758 [182] A. Chen, et al., Probing nucleon spin structures with polarized Drell-Yan in the Fermilab Spin-
3759 Quest experiment, PoS SPIN2018 (2019) 164.
- 3760 [183] J. C. Collins, A. V. Efremov, K. Goeke, S. Menzel, A. Metz, P. Schweitzer, Sivers effect in semi-
3761 inclusive deeply inelastic scattering, Phys. Rev. D73 (2006) 014021.
- 3762 [184] S. V. Goloskokov, P. Kroll, The Longitudinal cross-section of vector meson electroproduction,
3763 Eur. Phys. J. C50 (2007) 829–842.
- 3764 [185] S. V. Goloskokov, P. Kroll, The Role of the quark and gluon GPDs in hard vector-meson electro-
3765 production, Eur. Phys. J. C53 (2008) 367–384.
- 3766 [186] Y. Hagiwara, Y. Hatta, R. Pasechnik, M. Tasevsky, O. Teryaev, Accessing the gluon Wigner dis-
3767 tribution in ultraperipheral pA collisions, Phys. Rev. D96 (3) (2017) 034009.
- 3768 [187] O. V. Teryaev, Analytic properties of hard exclusive amplitudes, in: 11th International Conference
3769 on Elastic and Diffractive Scattering: Towards High Energy Frontiers: The 20th Anniversary of
3770 the Blois Workshops, 17th Rencontre de Blois (EDS 05) Chateau de Blois, Blois, France, May
3771 15-20, 2005, 2005.
- 3772 [188] P. Kroll, P. Kroll, O. Teryaev, Lepton-pair production in hard exclusive hadron-hadron collisions .
- 3773 [189] The MultiPurpose Detector – MPD. Conceptual Design Report, 2016.
- 3774 [190] Exploring strongly interacting matter at high densities - NICA White Paper, EPJA, 2016.
- 3775 [191] MPD web site.
3776 URL `mpd.jinr.ru`
- 3777 [192] R. Arndt, W. Briscoe, I. Strakovsky, R. Workman, Updated analysis of NN elastic scattering to
3778 3-GeV, Phys. Rev. C 76 (2007) 025209.
- 3779 [193] M. Sawamoto, S. Wakaizumi, ANALYSIS OF ELASTIC P P SCATTERING AT 6-GEV/C WITH
3780 SPIN ORBIT AND SPIN SPIN COUPLING EIKONALS, Prog. Theor. Phys. 62 (1979) 563–565.
- 3781 [194] O. Selyugin, O. Teryaev, Generalized Parton Distributions and Description of Electromagnetic
3782 and Graviton form factors of nucleon, Phys. Rev. D 79 (2009) 033003.
- 3783 [195] A. Sibirtsev, J. Haidenbauer, H.-W. Hammer, S. Krewald, U.-G. Meissner, Proton-proton scatter-
3784 ing above 3 GeV/c, Eur. Phys. J. A 45 (2010) 357–372.
- 3785 [196] W. P. Ford, J. Van Orden, Regge model for nucleon-nucleon spin-dependent amplitudes, Phys.
3786 Rev. C 87 (1) (2013) 014004.
- 3787 [197] M. Platonova, V. Kukulín, Refined Glauber model versus Faddeev calculations and experimental
3788 data for pd spin observables, Phys. Rev. C 81 (2010) 014004, [Erratum: Phys.Rev.C 94, 069902
3789 (2016)].
- 3790 [198] A. Temerbayev, Y. Uzikov, Spin observables in proton-deuteron scattering and T-invariance test,
3791 Phys. Atom. Nucl. 78 (1) (2015) 35–42.
- 3792 [199] D. Mchedlishvili, et al., Deuteron analysing powers in deuteron–proton elastic scattering at 1.2
3793 and 2.27 GeV, Nucl. Phys. A 977 (2018) 14–22.
- 3794 [200] M. N. Platonova, V. I. Kukulín, Theoretical study of spin observables in pd elastic scattering at
3795 energies $T_p = 800\text{-}1000$ MeV, Eur. Phys. J. A 56 (5) (2020) 132.

- 3796 [201] Y. Uzikov, J. Haidenbauer, A. Bazarova, A. Temerbayev, Spin observables of proton-deuteron
3797 elastic scattering at SPD NICA energies within the Glauber model and pN amplitudes, Talk at
3798 NUCLEUS-2020, (11-17 October, 2020; S-Petersburg, Russia).
- 3799 [202] Y. Uzikov, J. Haidenbauer, A. Bazarova, A. Temerbayev, Spin observables of proton-deuteron
3800 elastic scattering at SPD NICA energies within the Glauber model and pN amplitudes, 2020.
- 3801 [203] G. G. Ohlsen, Polarization transfer and spin correlation experiments in nuclear physics, Rept.
3802 Prog. Phys. 35 (1972) 717–801.
- 3803 [204] Y. Uzikov, C. Wilkin, The analysing powers in proton-deuteron elastic scattering, Phys. Lett. B
3804 793 (2019) 224–226.
- 3805 [205] Y. N. Uzikov, A. Temerbayev, Null-test signal for T -invariance violation in pd scattering, Phys.
3806 Rev. C 92 (1) (2015) 014002.
- 3807 [206] Y. N. Uzikov, J. Haidenbauer, Polarized proton-deuteron scattering as a test of time-reversal in-
3808 variance, Phys. Rev. C 94 (3) (2016) 035501.
- 3809 [207] O. Selyugin, Gravitation form-factors and spin asymmetries in hadron elastic scattering .
- 3810 [208] U. Amaldi, K. R. Schubert, Impact Parameter Interpretation of Proton Proton Scattering from a
3811 Critical Review of All ISR Data, Nucl. Phys. B 166 (1980) 301–320.
- 3812 [209] A. Anselm, V. Gribov, Zero pion mass limit in interactions at very high-energies, Phys. Lett. B 40
3813 (1972) 487–490.
- 3814 [210] V. Khoze, A. Martin, M. Ryskin, t dependence of the slope of the high energy elastic pp cross
3815 section, J. Phys. G 42 (2) (2015) 025003.
- 3816 [211] L. Jenkovszky, I. Szanyi, C.-I. Tan, Shape of Proton and the Pion Cloud, Eur. Phys. J. A 54 (7)
3817 (2018) 116.
- 3818 [212] O. Selyugin, New feature in the differential cross sections at 13 TeV measured at the LHC, Phys.
3819 Lett. B 797 (2019) 134870.
- 3820 [213] O. Selyugin, Anomaly in the differential cross sections at 13 TeV .
- 3821 [214] V. Baskov, O. Dalkarov, A. L'vov, V. Polyanskiy, Studying periphery of the nucleon in diffrac-
3822 tive scattering at SPD. Talk at NUCLEUS-2020, (11-17 October, 2020; S-Petersburg, Russia) .
3823 Submitted to PEPAN .
- 3824 [215] V. Abramov, Phenomenology of single-spin effects in hadron production at high energies, Phys.
3825 Atom. Nucl. 72 (2009) 1872–1888.
- 3826 [216] L. Frankfurt, E. Piasetsky, M. Sargsian, M. Strikman, Probing short range nucleon correlations in
3827 high-energy hard quasielastic p d reactions, Phys. Rev. C 51 (1995) 890–900.
- 3828 [217] L. Frankfurt, E. Piasetzky, M. Sargsian, M. Strikman, On the possibility to study color trans-
3829 parency in the large momentum transfer exclusive d (p, 2 p) n reaction, Phys. Rev. C 56 (1997)
3830 2752–2766.
- 3831 [218] L. Frankfurt, M. Sargsian, M. Strikman, Feynman graphs and Gribov-Glauber approach to high-
3832 energy knockout processes, Phys. Rev. C 56 (1997) 1124–1137.

- 3833 [219] A. Mueller, Proceedings of 17th rencontre de Moriond, Moriond, 1982 Van (Editions Frontieres,
3834 Gif-sur-Yvette, France, 1982) Vol. I p.13.
- 3835 [220] S. Brodsky, Proceedings. of the 13th Int. Symposium on Multiparticle Dynamics, W. Kittel, W.
3836 Metzger and A. Stergiou (eds.) Singapore 1982,) p.963.
- 3837 [221] G. Farrar, H. Liu, L. Frankfurt, M. Strikman, Transparency in Nuclear Quasiexclusive Processes
3838 with Large Momentum Transfer, Phys. Rev. Lett. 61 (1988) 686–689.
- 3839 [222] L. Frankfurt, M. Strikman, Hard Nuclear Processes and Microscopic Nuclear Structure, Phys.
3840 Rept. 160 (1988) 235–427.
- 3841 [223] C. G. Granados, M. M. Sargsian, Quark Structure of the Nucleon and Angular Asymmetry of
3842 Proton-Neutron Hard Elastic Scattering, Phys. Rev. Lett. 103 (2009) 212001.
- 3843 [224] D. G. Crabb, et al., Spin Dependence of High p-Transverse**2 Elastic p p Scattering, Phys. Rev.
3844 Lett. 41 (1978) 1257.
- 3845 [225] L. Frankfurt, T. Lee, G. Miller, M. Strikman, Chiral transparency, Phys. Rev. C 55 (1997) 909–
3846 916.
- 3847 [226] L. Frankfurt, M. Sargsian, M. Strikman, Recent observation of short range nucleon correlations in
3848 nuclei and their implications for the structure of nuclei and neutron stars, Int. J. Mod. Phys. A 23
3849 (2008) 2991–3055.
- 3850 [227] O. Hen, G. Miller, E. Piasetzky, L. Weinstein, Nucleon-Nucleon Correlations, Short-lived Excita-
3851 tions, and the Quarks Within, Rev. Mod. Phys. 89 (4) (2017) 045002.
- 3852 [228] V. Matveev, R. Muradian, A. Tavkhelidze, Automodellism in the large - angle elastic scattering
3853 and structure of hadrons, Lett. Nuovo Cim. 7 (1973) 719–723.
- 3854 [229] S. J. Brodsky, G. R. Farrar, Scaling Laws at Large Transverse Momentum, Phys. Rev. Lett. 31
3855 (1973) 1153–1156.
- 3856 [230] G. Bizard, et al., EXPERIMENTAL STUDY AND BARYONIC EXCHANGE INTERPRETA-
3857 TION OF THE REACTION H-2 (D, N) HE-3 IN THE INTERMEDIATE-ENERGY REGION,
3858 Phys. Rev. C 22 (1980) 1632–1637.
- 3859 [231] Y. Uzikov, Indication of asymptotic scaling in the reactions $dd \rightarrow p\ ^3\text{H}$, $dd \rightarrow n\ ^3\text{He}$ and pd
3860 $\rightarrow pd$, JETP Lett. 81 (2005) 303–306.
- 3861 [232] A. Terekhin, V. Ladygin, Y. Gurchin, A. Isupov, A. Kurilkin, P. Kurilkin, N. Ladygina, S. Piyadin,
3862 S. Reznikov, A. Khrenov, Differential Cross Section for Elastic Deuteron–Proton Scattering at the
3863 Energy of 700 MeV per Nucleon, Phys. Atom. Nucl. 80 (6) (2017) 1061–1072.
- 3864 [233] A. Terekhin, et al., The differential cross section in deuteron-proton elastic scattering at 500, 750
3865 and 900 MeV/nucleon, Eur. Phys. J. A 55 (8) (2019) 129.
- 3866 [234] Y. N. Uzikov, Search for scaling onset in exclusive reactions with the lightest nuclei, Eur. Phys. J.
3867 A 52 (8) (2016) 243.
- 3868 [235] P. Kurilkin, et al., Measurement of the vector and tensor analyzing powers for dp- elastic scattering
3869 at 880 MeV, Phys. Lett. B 715 (2012) 61–65.
- 3870 [236] P. Kurilkin, et al., Investigation of the angular dependence of the analyzing powers in the deuteron-
3871 proton elastic scattering at the nuclotron, Phys. Part. Nucl. Lett. 8 (2011) 1081–1083.

- 3872 [237] V. Ladygin, et al., Tensor analyzing power $A(\text{yy})$ in deuteron inclusive breakup on hydrogen and
3873 carbon at 9-GeV/c and large proton transverse momenta, Phys. Lett. B 629 (2005) 60–67.
- 3874 [238] S. Afanasiev, et al., Phys. Lett. B 434 (1998) 21–25.
- 3875 [239] R. Vogt, J/ψ production and suppression, Phys. Rept. 310 (1999) 197–260.
- 3876 [240] F. Maltoni, et al., Analysis of charmonium production at fixed-target experiments in the NRQCD
3877 approach, Phys. Lett. B638 (2006) 202–208.
- 3878 [241] S. Brodsky, E. Chudakov, P. Hoyer, J. Laget, Photoproduction of charm near threshold, Phys. Lett.
3879 B 498 (2001) 23–28.
- 3880 [242] M. P. Rekalo, E. Tomasi-Gustafsson, Threshold J/ψ production in nucleon-nucleon collisions,
3881 New J. Phys. 4 (2002) 68.
- 3882 [243] N. Craigie, Lepton and Photon Production in Hadron Collisions, Phys. Rept. 47 (1978) 1–108.
- 3883 [244] Y. Antipov, V. Bessubov, N. Budanov, Y. Bushnin, S. Denisov, Y. Gorin, A. Lebedev, A. Lednev,
3884 Y. Mikhailov, A. Petrukhin, S. Polovnikov, V. Roinishvili, V. Selesnev, V. Sergienko, D. Stoy-
3885 onova, A. Sytin, Y. Vazdik, F. Yotch, j/ψ particle production by 70 gev/c protons, Physics Letters
3886 B 60 (3) (1976) 309 – 312.
3887 URL <http://www.sciencedirect.com/science/article/pii/0370269376903087>
- 3888 [245] C. Lourenço, H. Wöhri, Heavy-flavour hadro-production from fixed-target to collider energies,
3889 Physics Reports 433 (3) (2006) 127–180.
3890 URL <http://dx.doi.org/10.1016/j.physrep.2006.05.005>
- 3891 [246] A. Rustamov, Inclusive meson production in 3.5-GeV p p collisions studied with the HADES
3892 spectrometer, AIP Conf. Proc. 1257 (1) (2010) 736–740.
- 3893 [247] M. Albrow, et al., Inclusive ρ^0 Production in pp Collisions at the CERN ISR, Nucl. Phys. B 155
3894 (1979) 39–51.
- 3895 [248] M. P. Rekalo, E. Tomasi-Gustafsson, Threshold open charm production in nucleon-nucleon colli-
3896 sions, Eur. Phys. J. A16 (2003) 575–581.
- 3897 [249] A. Sibirtsev, W. Cassing, Rho meson production and decay in proton nucleus collisions, Nucl.
3898 Phys. A 629 (1998) 717–738.
- 3899 [250] V. Blobel, et al., Observation of Vector Meson Production in Inclusive p p Reactions, Phys. Lett.
3900 B 48 (1974) 73–76.
- 3901 [251] E. A. Kuraev, E. S. Kokoulina, E. Tomasi-Gustafsson, Hard light meson production in
3902 (anti)proton-hadron collisions and charge-exchange reactions, Phys. Part. Nucl. Lett. 12 (1) (2015)
3903 1–7.
- 3904 [252] V. Baier, V. S. Fadin, V. A. Khoze, Quasireal electron method in high-energy quantum electrody-
3905 namics, Nucl. Phys. B 65 (1973) 381–396.
- 3906 [253] E. V. Shuryak, Two Scales and Phase Transitions in Quantum Chromodynamics, Phys. Lett. B 107
3907 (1981) 103–105.
- 3908 [254] A. Manohar, H. Georgi, Chiral Quarks and the Nonrelativistic Quark Model, Nucl. Phys. B 234
3909 (1984) 189–212.

- 3910 [255] V. Komarov, On the possibility of revealing the transition of a baryon pair state to a six-quark
3911 confinement state, Phys. Part. Nucl. Lett. 15 (1) (2018) 69–75.
- 3912 [256] V. Komarov, B. Baimurzinova, A. Kunsafina, D. Tsirkov, Centrality criteria of inelastic nucleon-
3913 nucleon collisions .
- 3914 [257] A. Faessler, V. Kukulín, M. Shikhalev, Description of intermediate- and short-range NN nuclear
3915 force within a covariant effective field theory, Annals Phys. 320 (2005) 71–107.
- 3916 [258] T. Hatsuda, T. Kunihiro, POSSIBLE CRITICAL PHENOMENA ASSOCIATED WITH THE
3917 CHIRAL SYMMETRY BREAKING, Phys. Lett. B 145 (1984) 7–10.
- 3918 [259] D. Blaschke, Y. Kalinovsky, A. Radzhabov, M. Volkov, Scalar sigma meson at a finite temperature
3919 in a nonlocal quark model, Phys. Part. Nucl. Lett. 3 (2006) 327–330.
- 3920 [260] A. Aduszkiewicz, et al., Proton-Proton Interactions and Onset of Deconfinement, Phys. Rev. C
3921 102 (1) (2020) 011901.
- 3922 [261] B. Andersson, G. Gustafson, G. Ingelman, T. Sjostrand, Parton Fragmentation and String Dynam-
3923 ics, Phys. Rept. 97 (1983) 31–145.
- 3924 [262] H. Garcilazo, A. Valcarce, Strangeness -2 Hypertriton, Phys. Rev. Lett. 110 (1) (2013) 012503.
- 3925 [263] A. Gal, Comment on recent Strangeness -2 predictions, Phys. Rev. Lett. 110 (2013) 179201.
- 3926 [264] H. Garcilazo, A. Valcarce, Reply to "Comment on Strangeness -2 hypertriton", Phys. Rev. Lett.
3927 110 (2013) 179202.
- 3928 [265] I. Filikhin, A. Gal, Faddeev-Yakubovsky search for (Λ - Λ) H-4, Phys. Rev. Lett. 89
3929 (2002) 172502.
- 3930 [266] H. Nemura, Y. Akaishi, K. S. Myint, Stochastic variational search for H-4(Λ - Λ),
3931 Phys. Rev. C 67 (2003) 051001.
- 3932 [267] H. Garcilazo, A. Valcarce, Nonexistence of a Λnn bound state, Phys. Rev. C 89 (5) (2014) 057001.
- 3933 [268] E. Hiyama, S. Ohnishi, B. Gibson, T. A. Rijken, Three-body structure of the $nn\Lambda$ system with
3934 $\Lambda N - \Sigma N$ coupling, Phys. Rev. C 89 (6) (2014) 061302.
- 3935 [269] J.-M. Richard, Q. Wang, Q. Zhao, Lightest neutral hypernuclei with strangeness -1 and -2 , Phys.
3936 Rev. C 91 (1) (2015) 014003.
- 3937 [270] J.-M. Richard, Q. Wang, Q. Zhao, Possibility of a new neutral hypernucleus ${}_{\Lambda\Lambda}^4n = (n, n, \Lambda, \Lambda)$,
3938 J. Phys. Conf. Ser. 569 (1) (2014) 012079.
- 3939 [271] T. A. Rijken, M. Nagels, Y. Yamamoto, Baryon-baryon interactions: Nijmegen extended-soft-core
3940 models, Prog. Theor. Phys. Suppl. 185 (2010) 14–71.
- 3941 [272] H. Polinder, J. Haidenbauer, U.-G. Meissner, Strangeness $S = -2$ baryon-baryon interactions using
3942 chiral effective field theory, Phys. Lett. B 653 (2007) 29–37.
- 3943 [273] J. Haidenbauer, S. Petschauer, N. Kaiser, U.-G. Meissner, A. Nogga, W. Weise, Hyperon-nucleon
3944 interaction at next-to-leading order in chiral effective field theory, Nucl. Phys. A 915 (2013) 24–
3945 58.

- 3946 [274] J. Haidenbauer, U.-G. Meißner, S. Petschauer, Strangeness $S = -2$ baryon–baryon interaction at
3947 next-to-leading order in chiral effective field theory, Nucl. Phys. A 954 (2016) 273–293.
- 3948 [275] S. Acharya, et al., Study of the Λ - Λ interaction with femtoscopy correlations in pp and p-Pb
3949 collisions at the LHC, Phys. Lett. B 797 (2019) 134822.
- 3950 [276] D. Lonardoni, S. Gandolfi, F. Pederiva, Effects of the two-body and three-body hyperon-nucleon
3951 interactions in Λ -hypernuclei, Phys. Rev. C 87 (2013) 041303.
- 3952 [277] A. Efremov, QUARK - PARTON PICTURE OF THE CUMULATIVE PRODUCTION, Fiz. Elem.
3953 Chast. Atom. Yadra 13 (1982) 613–634.
- 3954 [278] A. Andrianov, V. Andrianov, D. Espriu, Chiral Imbalance in QCD and its consequences, EPJ Web
3955 Conf. 125 (2016) 01009.
- 3956 [279] A. *et al.*, Baldin, The Observation of High Energy Pions in Interactions of Relativistic Deuterons
3957 with Nuclei, AIP Conf. Proc. 2 (1971) 131–139.
- 3958 [280] A. Baldin, N. Giordenescu, L. Ivanova, N. Moroz, A. Povtoreiko, V. Radomanov, V. Stavinsky,
3959 V. Zubarev, An Experimental Investigation of Cumulative Meson Production, Sov. J. Nucl. Phys.
3960 20 (1975) 629–634.
- 3961 [281] A. Efremov, A. Kaidalov, V. Kim, G. Lykasov, N. Slavin, Cumulative Hadron Production in Quark
3962 Models of Flucton Fragmentation, Sov. J. Nucl. Phys. 47 (1988) 868.
- 3963 [282] V. Kim, QCD Evolution of Nuclear Structure Functions at Large X: EMC Effect and Cumulative
3964 Processes, Phys. Part. Nucl. Lett. 15 (4) (2018) 384–386.
- 3965 [283] S. Boyarinov, et al., Production of Cumulative K^- Mesons on Protons at 10- $\{\text{GeV}\}$ Energy, Sov.
3966 J. Nucl. Phys. 50 (1989) 996–1000.
- 3967 [284] S. Boyarinov, et al., The Cumulative production of anti-protons by 10 GeV protons bombarding
3968 nuclear targets, Sov. J. Nucl. Phys. 54 (1991) 71–74.
- 3969 [285] A. Efremov, V. Kim, G. Lykasov, Hard Hadron - Nucleus Processes and Multi - Quark Configura-
3970 tions in Nuclei, Sov. J. Nucl. Phys. 44 (1986) 151.
- 3971 [286] M. Braun, V. Vechernin, Nuclear structure functions and particle production in the cumulative
3972 region in the parton model, Nucl. Phys. B 427 (1994) 614–640.
- 3973 [287] M. Anselmino, E. Predazzi, S. Ekelin, S. Fredriksson, D. Lichtenberg, Diquarks, Rev. Mod. Phys.
3974 65 (1993) 1199–1234.
- 3975 [288] A. Breakstone, et al., A Diquark Scattering Model for High p_T Proton Production in pp Collisions
3976 at the $\{\text{ISR}\}$, Z. Phys. C 28 (1985) 335.
- 3977 [289] V. Kim, Diquarks as a Source of Large p_T Baryons in Hard Nucleon Collisions, JINR-E2-87-75
3978 (1987) Dubna .
- 3979 [290] V. Kim, Diquarks and Dynamics of Large p_T Baryon Pproduction, Mod. Phys. Lett. A 3 (1988)
3980 909–916.
- 3981 [291] V. t. Kim, A. A. Shavrin, A. V. Zelenov, Diquark Dynamics in Large p_T Baryon Production, Phys.
3982 Part. Nucl. Lett. .

- 3983 [292] A. Efremov, V. Kim, Diquarks Role in Large p_T Deuteron and H-dihyperon Production in hard
3984 nucleon Collisions, JINR-E2-87-74 (1987) Dubna .
- 3985 [293] Y. I. Azimov, Unexpected Mesons X, Y, Z, ... (tetraquarks? hadron molecules? ...) .
- 3986 [294] M. Barabanov, A. Vodopyanov, S. Olsen, New research of charmonium over $D\bar{D}$ threshold using
3987 the antiproton beam with momentum ranging from 1 to 15 GeV/c, Phys. Atom. Nucl. 77 (2014)
3988 126–130.
- 3989 [295] M. Barabanov, A. Vodopyanov, A. Zinchenko, S. Olsen, Perspective Study of Charmonium and
3990 Exotics above the $D\bar{D}$ Threshold, Phys. Atom. Nucl. 79 (1) (2016) 126–129.
- 3991 [296] R. L. Jaffe, F. Wilczek, Diquarks and exotic spectroscopy, Phys. Rev. Lett. 91 (2003) 232003.
- 3992 [297] J. R. West, S. J. Brodsky, G. F. de Teramond, A. S. Goldhaber, I. Schmidt, QCD Hidden-Color
3993 Hexa-diquark in the Central Core of Nuclei .
- 3994 [298] S. J. Brodsky, I. Schmidt, G. de Teramond, NUCLEAR BOUND QUARKONIUM, Phys. Rev.
3995 Lett. 64 (1990) 1011.
- 3996 [299] S. Brodsky, A. Hoang, J. H. Kuhn, T. Teubner, Angular distributions of massive quarks and leptons
3997 close to threshold, Phys. Lett. B 359 (1995) 355–361.
- 3998 [300] K. Tsushima, D. Lu, G. Krein, A. Thomas, J/Ψ -nuclear bound states, Phys. Rev. C 83 (2011)
3999 065208.
- 4000 [301] S. J. Brodsky, Novel QCD physics at NICA, Eur. Phys. J. A 52 (8) (2016) 220.
- 4001 [302] R. Aaij, et al., Observation of $J/\psi p$ Resonances Consistent with Pentaquark States in $\Lambda_b^0 \rightarrow$
4002 $J/\psi K^- p$ Decays, Phys. Rev. Lett. 115 (2015) 072001.
- 4003 [303] R. Aaij, et al., Observation of a narrow pentaquark state, $P_c(4312)^+$, and of two-peak structure of
4004 the $P_c(4450)^+$, Phys. Rev. Lett. 122 (22) (2019) 222001.
- 4005 [304] R. Baldini, S. Pacetti, A. Zallo, A. Zichichi, Unexpected features of $e^+ e^- \rightarrow p \text{ anti-}p$ and $e^+ e^-$
4006 $\rightarrow \Lambda \text{ anti-}\Lambda$ cross sections near threshold, Eur. Phys. J. A 39 (2009) 315–321.
- 4007 [305] R. Baldini Ferroli, S. Pacetti, A. Zallo, Time-like baryon form factors near threshold: Status and
4008 perspectives, Nucl. Phys. B Proc. Suppl. 219-220 (2011) 32–38.
- 4009 [306] G. Court, et al., Energy Dependence of Spin Effects in p (Polarized) p (Polarized) $\rightarrow pp$, Phys.
4010 Rev. Lett. 57 (1986) 507.
- 4011 [307] S. J. Brodsky, G. de Teramond, Spin Correlations, QCD Color Transparency and Heavy Quark
4012 Thresholds in Proton Proton Scattering, Phys. Rev. Lett. 60 (1988) 1924.
- 4013 [308] P. A. R. Ade, et al., Planck 2013 results. i. overview of products and scientific results, Astronomy
4014 & Astrophysics 571 (2014) A1.
- 4015 [309] D. Majumdar, Dark Matter: An Introduction, CRC Press, 2014.
- 4016 [310] O. Buchmueller, C. Doglioni, L.-T. Wang, Search for dark matter at colliders, Nature Physics
4017 13 (3) (2017) 217–223.
- 4018 [311] M. Aguilar, et al., First result from the alpha magnetic spectrometer on the international space
4019 station: Precision measurement of the positron fraction in primary cosmic rays of 0.5–350 GeV,
4020 Physical Review Letters 110 (14).

- 4021 [312] M. Aguilar, et al., Antiproton flux, antiproton-to-proton flux ratio, and properties of elementary
4022 particle fluxes in primary cosmic rays measured with the alpha magnetic spectrometer on the
4023 international space station, *Physical Review Letters* 117 (9).
- 4024 [313] G. Giesen, M. Boudaud, Y. Génolini, V. Poulin, M. Cirelli, P. Salati, P. D. Serpico, AMS-02
4025 antiprotons, at last! secondary astrophysical component and immediate implications for dark
4026 matter, *Journal of Cosmology and Astroparticle Physics* 2015 (09) (2015) 023–023.
- 4027 [314] M. di Mauro, F. Donato, A. Goudelis, P. D. Serpico, New evaluation of the antiproton production
4028 cross section for cosmic ray studies, *Physical Review D* 90 (8).
- 4029 [315] F. Donato, M. Korsmeier, M. D. Mauro, Prescriptions on antiproton cross section data for precise
4030 theoretical antiproton flux predictions, *Physical Review D* 96 (4).
- 4031 [316] A. Guskov, R. El-Kholy, On the possibility to study antiproton production at the SPD detector at
4032 NICA collider for dark matter search in astrophysical experiments, *Physics of Particles and Nuclei*
4033 *Letters* 16 (3) (2019) 216–223.
- 4034 [317] V. Alexakhin, A. Guskov, Z. Hayman, R. El-Kholy, A. Tkachenko, On the study of antiprotons
4035 yield in hadronic collisions at nica spd (2020).
4036 URL <https://arxiv.org/abs/2008.04136v1>
- 4037 [318] A. D. Kovalenko, Y. N. Filatov, A. M. Kondratenko, M. A. Kondratenko, V. A. Mikhaylov, Polar-
4038 ized deuterons and protons at nica@jinr, *Physics of Particles and Nuclei* 45 (1) (2014) 325–326.
- 4039 [319] A. Kovalenko, et al., The nica facility in polarized proton operation mode, IPAC11, San Sebastian,
4040 Spain, 4-9 Sept, TUPZ004 .
- 4041 [320] Y. S. Derbenev, et al., Spin-flipping systems for storage rings, *Proceedings of XIV Advanced*
4042 *Research Workshop on High Energy Spin Physics (DSPIN-11)* (2011) 377–384.
- 4043 [321] A. D. Kovalenko, A. V. Butenko, V. D. Kekelidze, V. A. Mikhaylov, A. M. Kondratenko, M. A.
4044 Kondratenko, Y. N. Filatov, Nica facility in polarized proton and deuteron mode, *International*
4045 *Journal of Modern Physics: Conference Series* 40 (2016) 1660096.
4046 URL <https://doi.org/10.1142/S201019451660096X>
- 4047 [322] Y. N. Filatov, A. D. Kovalenko, A. V. Butenko, A. M. Kondratenko, M. A. Kondratenko, V. A.
4048 Mikhaylov, Polarized proton beam acceleration at the nuclotron with the use of the solenoid
4049 siberian snake, *Physics of Particles and Nuclei* 45 (1) (2014) 262–264.
4050 URL <https://doi.org/10.1134/S1063779614010274>
- 4051 [323] Y. Filatov, et al., Orbital parameters of proton beam in nuclotron with solenoid siberian snake,
4052 *Proceedings of XV Advanced Research Workshop on High Energy Spin Physics (DSPIN-13)*
4053 (2013) 371–374.
- 4054 [324] A. D. Kovalenko, A. V. Butenko, V. D. Kekelidze, V. A. Mikhaylov, M. A. Kondratenko, A. M.
4055 Kondratenko, Y. N. Filatov, Numerical calculation of ion polarization in the nica collider, *Journal*
4056 *of Physics: Conference Series* 678 (1) (2016) 012023.
4057 URL <http://stacks.iop.org/1742-6596/678/i=1/a=012023>
- 4058 [325] A. D. Kovalenko, A. V. Butenko, V. A. Mikhaylov, M. A. Kondratenko, A. M. Kondratenko, Y. N.
4059 Filatov, Spin transparency mode in the nica collider with solenoid siberian snakes for proton and
4060 deuteron beam, *Journal of Physics: Conference Series* 938 (1) (2017) 012025.
4061 URL <http://stacks.iop.org/1742-6596/938/i=1/a=012025>

- 4062 [326] A. D. Kovalenko, A. V. Butenko, V. A. Mikhaylov, M. A. Kondratenko, A. M. Kondratenko,
4063 Y. N. Filatov, Acceleration of polarized protons up to 3.4 gev/c in the nuclotron at jinr, Journal of
4064 Physics: Conference Series 938 (1) (2017) 012018.
4065 URL <http://stacks.iop.org/1742-6596/938/i=1/a=012018>
- 4066 [327] A. Sergi, NA62 Spectrometer: A Low Mass Straw Tracker, Phys. Procedia 37 (2012) 530–534.
- 4067 [328] H. Nishiguchi, et al., Development of an extremely thin-wall straw tracker operational in vacuum
4068 – The COMET straw tracker system, Nucl. Instrum. Meth. A 845 (2017) 269–272.
- 4069 [329] M. Lee, The Straw-tube Tracker for the Mu2e Experiment, Nucl. Part. Phys. Proc. 273-275 (2016)
4070 2530–2532.
- 4071 [330] V. Bychkov, et al., Construction and manufacture of large size straw-chambers of the COMPASS
4072 spectrometer tracking system, Part. Nucl. Lett. 111 (2002) 64–73.
- 4073 [331] K. Platzer, W. Dunnweber, N. Dedek, M. Faessler, R. Geyer, C. Ilgner, V. Peshekhonov, H. Wellen-
4074 stein, Mapping the large area straw detectors of the COMPASS experiment with X-rays, IEEE
4075 Trans. Nucl. Sci. 52 (2005) 793–798.
- 4076 [332] V. Volkov, P. Volkov, T. Enik, G. Kekelidze, V. Kramarenko, V. Lysan, D. Peshekhonov, A. Solin,
4077 A. Solin, Straw Chambers for the NA64 Experiment, Phys. Part. Nucl. Lett. 16 (6) (2019) 847–
4078 858.
- 4079 [333] E. Abat, et al., The ATLAS Transition Radiation Tracker (TRT) proportional drift tube: Design
4080 and performance, JINST 3 (2008) P02013.
- 4081 [334] E. Abat, et al., The ATLAS TRT end-cap detectors, JINST 3 (2008) P10003.
- 4082 [335] P. Gianotti, et al., The Straw Tube Trackers of the PANDA Experiment, in: 3rd International
4083 Conference on Advancements in Nuclear Instrumentation Measurement Methods and their Appli-
4084 cations, 2013.
- 4085 [336] L. Glonti, T. Enik, V. Kekelidze, A. Kolesnikov, D. Madigozhin, N. Molokanova, S. Movchan,
4086 Y. Potrebenikov, S. Shkarovskiy, Longitudinal tension and mechanical stability of a pressurized
4087 straw tube, Instruments 2 (4) (2018) 27.
- 4088 [337] IHEP Web Page.
4089 URL <http://exwww.ihep.su/scint/mold/product.htm>
- 4090 [338] Kuraray web site.
4091 URL <http://kuraraypsf.jp/psf/ws.html>
- 4092 [339] Hamamatsu web site.
4093 URL [https://www.hamamatsu.com/eu/en/product/optical-sensors/mppc/index.](https://www.hamamatsu.com/eu/en/product/optical-sensors/mppc/index.html)
4094 [html](https://www.hamamatsu.com/eu/en/product/optical-sensors/mppc/index.html)
- 4095 [340] HVSys Web Site.
4096 URL <http://hvsys.ru/>
- 4097 [341] Afi electronics web site.
4098 URL <https://afi.jinr.ru/ADC64>
- 4099 [342] V. M. Abazov, G. D. Alexeev, Y. I. Davydov, V. L. Malyshev, V. V. Tokmenin, A. A. Piskun,
4100 Comparative analysis of the performance characteristics of mini-drift tubes with different design,
4101 Instruments and Experimental Techniques 53 (3) (2010) 356–361.

- 4102 [343] V. M. Abazov, G. D. Alexeev, Y. I. Davydov, V. L. Malyshev, A. A. Piskun, V. V. Tokmenin,
4103 Coordinate accuracy of mini-drift tubes in detection of an induced signal, *Instruments and Exper-*
4104 *imental Techniques* 53 (5) (2010) 648–652.
- 4105 [344] V. M. Abazov, et al., The Muon system of the run II D0 detector, *Nucl. Instrum. Meth.* A552
4106 (2005) 372–398.
- 4107 [345] P. Abbon, et al., The COMPASS experiment at CERN, *Nucl. Instrum. Meth.* A577 (2007) 455–
4108 518.
- 4109 [346] G. D. Alekseev, M. A. Baturitsky, O. V. Dvornikov, A. I. Khokhlov, V. A. Mikhailov, I. A. Odnok-
4110 loubov, V. V. Tokmenin, The eight-channel ASIC bipolar transresistance amplifier DOM AMPL-
4111 8.3, *Nucl. Instrum. Meth.* A462 (2001) 494–505.
- 4112 [347] G. Alexeev, M. Baturitsky, O. Dvornikov, V. Mikhailov, I. Odnokloubov, V. Tokmenin, The eight-
4113 channel fast comparator ic1the research described in this publication was partly funded by award
4114 no. rp1-189 of the us civilian research and development foundation for the independent states of
4115 the former soviet union (crdf).1, *Nuclear Instruments and Methods in Physics Research Section*
4116 *A: Accelerators, Spectrometers, Detectors and Associated Equipment* 423 (1) (1999) 157 – 162.
4117 URL <http://www.sciencedirect.com/science/article/pii/S0168900298011851>
- 4118 [348] G. D. Alekseev, M. A. Baturitsky, O. V. Dvornikov, A. I. Khokhlov, V. A. Mikhailov, I. A. Odnok-
4119 loubov, A. A. Shishkin, V. V. Tokmenin, S. F. Zhirikov, The D0 forward angle muon system
4120 front-end electronics design, *Nucl. Instrum. Meth.* A473 (2001) 269–282.
- 4121 [349] V. Babkin, et al., MPD NICA, Technical Design Report of the Time of Flight System (TOF) .
- 4122 [350] B. Singh, et al., Technical Design Report for the: Strong Interaction Studies with Antiprotons .
- 4123 [351] M. Nishimura, et al., Pixelated Positron Timing Counter with SiPM-readout Scintillator for MEG
4124 II experiment, *PoS PhotoDet2015* 011.
- 4125 [352] V.V. Anashin et al. PEPAN v.44, (2013) 1263 (in Russian).
- 4126 [353] I.V.Ovtin et al. "Aerogel Cherenkov Counters of the KEDR Detector", CERN-BINP Workshop for
4127 Young Scientists in e^+e^- Colliders 2016, Geneva; CERN-Proceedings-2017-001 (CERN, Geneva,
4128 2017).
- 4129 [354] A. Abashian, et al., The Belle Detector, *Nucl. Instrum. Meth.* A 479 (2002) 117–232.
- 4130 [355] Hamamatsu S12572-010P Datasheet.
4131 URL <http://www.hamamatsu.com/jp/en/S12572-010P.html>
- 4132 [356] A.V.Tishevsky et al., talk at ICAPP2020, submitted to *J.Phys.:Conf.Ser.*
- 4133 [357] A. Adare, et al., Inclusive cross section and single transverse spin asymmetry for very forward
4134 neutron production in polarized p+p collisions at s=200 GeV, *Phys. Rev. D*88 (3) (2013) 032006.
- 4135 [358] C. Adloff, et al., Construction and Commissioning of the CALICE Analog Hadron Calorimeter
4136 Prototype, *JINST* 5 (2010) P05004.
- 4137 [359] I. G. Alekseev, et al., RHIC p C CNI polarimeter: Experimental setup and physics results, *AIP*
4138 *Conf. Proc.* 675 (2003) 812–816, [812(2003)].
- 4139 [360] S. Trentalange, talk "STAR Spin Analysis Update", 2004 .

- 4140 [361] C. E. Allgower, et al., Measurement of analyzing powers of π^+ and π^- produced on a hydrogen
4141 and a carbon target with a 22-GeV/c incident polarized proton beam, Phys. Rev. D65 (2002)
4142 092008.
- 4143 [362] B. Z. Kopeliovich, I. K. Potashnikova, I. Schmidt, J. Soffer, Single transverse spin asymmetry of
4144 forward neutrons, Phys. Rev. D84 (2011) 114012.
- 4145 [363] C. Adler, A. Denisov, E. Garcia, M. J. Murray, H. Strobele, S. N. White, The RHIC zero degree
4146 calorimeter, Nucl. Instrum. Meth. A470 (2001) 488–499.
- 4147 [364] B. Michelson, Event-Driven Architecture Overview. Patricia Seybold Group / Business-Driven
4148 ArchitectureSM, February 2, pp. 1–8 (2006).
4149 URL <http://soa.omg.org/Uploaded%20Docs/EDA/bda2-2-06cc.pdf>
- 4150 [365] Etschberger, K, IXXAT Automation GmbH. Controller Area Network (CAN) Basics, Protocols,
4151 Chips and Applications. IXXAT Press, 2001. ISBN3-00-007376-0.
- 4152 [366] J. Chaize, A. Götz, W. Klotz, J. Meyer, M. Perez, E. Taurel, and P. Verdier, TANGO, 8th Inter-
4153 national Conference on Accelerator & Large Experimental Physics Control Systems, 2001, San
4154 Jose, California (JACoW, 2001).
- 4155 [367] E. Gorbachev, V. Andreev, A. Kirichenko, D. Monakhov, S. Romanov, T. Rukoyatkina, G. Sedykh,
4156 V. Volkov, The Nuclotron and Nica control system development status, Phys. Part. Nucl. Lett.
4157 13 (5) (2016) 573–578.
- 4158 [368] WinCC-OA: Introduction for Newcomers .
4159 URL <https://lhcb-online.web.cern.ch/ecs/PVSSIntro.htm>
- 4160 [369] H. Boterenbrood, H. J. Burckhart, J. Cook, V. Filimonov, B. I. Hallgren, F. Varela, Vertical Slice
4161 of the ATLAS Detector Control System .
4162 URL <http://cds.cern.ch/record/530680>
- 4163 [370] D. Steffen, et al., Overview and Future Developments of the intelligent, FPGA-based DAQ (iF-
4164 DAQ) of COMPASS, PoS ICHEP2016 (2016) 912.
- 4165 [371] M. Bodlak, V. Frolov, V. Jary, S. Huber, I. Konorov, D. Levit, J. Novy, R. Salac, M. Virius, De-
4166 velopment of new data acquisition system for compass experiment, Nuclear and Particle Physics
4167 Proceedings 273-275 (2016) 976 – 981, 37th International Conference on High Energy Physics
4168 (ICHEP).
- 4169 [372] I. Konorov, Data acquisition system for the spin physics detector, 2018 .
- 4170 [373] I. Konorov, Compass front-end, trigger and daq workshop, cern 02–03 march 2020, [https://](https://indico.cern.ch/event/863068/)
4171 indico.cern.ch/event/863068/ .
- 4172 [374] B.M.Veit, COMPASS Front-End, Trigger and DAQ Workshop, CERN 02–03 March 2020,
4173 <https://indico.cern.ch/event/863068/> .
- 4174 [375] S. Huber, Compass front-end, trigger and daq workshop, cern 02–03 march 2020, [https://](https://indico.cern.ch/event/863068/)
4175 indico.cern.ch/event/863068/ .
- 4176 [376] V. Frolov, Compass front-end, trigger and daq workshop, cern 02–03 march 2020, [https://](https://indico.cern.ch/event/863068/)
4177 indico.cern.ch/event/863068/ .

- 4178 [377] M. Kavatsyuk, E. Guliyev, P. Lemmens, H. Löhner, G. Tambave, VHDL implementation of
4179 feature-extraction algorithm for the PANDA electromagnetic calorimeter, in: 2010 IEEE Nuclear
4180 Science Symposium, Medical Imaging Conference, and 17th Room Temperature Semiconductor
4181 Detectors Workshop, 2010, pp. 785–788.
- 4182 [378] M.Ziembicki, Workshop feetdaq2019, munchen 11–13 feb 2019, [https://indico.cern.ch/
4183 event/783347](https://indico.cern.ch/event/783347) .
- 4184 [379] M.Suchenek, Workshop feetdaq2019, munchen 11–13 feb 2019, [https://indico.cern.ch/
4185 event/783347](https://indico.cern.ch/event/783347) .
- 4186 [380] I.Konorov, Workshop feetdaq2019, munchen 11–13 feb 2019, [https://indico.cern.ch/
4187 event/783347](https://indico.cern.ch/event/783347) .
- 4188 [381] C. Ghabrous Larrea, K. Harder, D. Newbold, D. Sankey, A. Rose, A. Thea, T. Williams, IPbus: a
4189 flexible Ethernet-based control system for xTCA hardware, JINST 10 (02) (2015) C02019.
- 4190 [382] D. Gaisbauer, Y. Bai, S. Huber, I. Konorov, D. Levit, S. Paul, D. Steffen, Unified communication
4191 framework, in: 20th IEEE-NPSS Real Time Conference, 2016.
- 4192 [383] J. Serrano, P. Alvarez, M. Cattin, E. Garcia Cota, J. Lewis, P. Moreira, T. Wlostowski, G. Gaderer,
4193 P. Loschmidt, J. Dedic, R. Bär, T. Fleck, M. Kreider, C. Prados, S. Rauch, The White Rabbit
4194 Project, Tech. Rep. CERN-ATS-2009-096, CERN, Geneva (Nov 2009).
4195 URL <https://cds.cern.ch/record/1215571>
- 4196 [384] White Rabbit .
4197 URL <https://ohwr.org/project/white-rabbit>
- 4198 [385] I. Konorov, L. Schmitt, B. Grube, Compass tcs documentation, compass note, date: 20 june 2001
4199 .
- 4200 [386] D. Baranov, S. Mitsyn, P. Goncharov, G. Ososkov, The Particle Track Reconstruction based on
4201 deep Neural networks, EPJ Web Conf. 214 (2019) 06018.
- 4202 [387] G. Ososkov, et al., Tracking on the BESIII CGEM inner detector using deep learning, Computer
4203 Research and Modeling 10 (20) 1–24.
- 4204 [388] F. B. Megino, et al., PanDA: Evolution and Recent Trends in LHC Computing, Procedia Comput.
4205 Sci. 66 (2015) 439–447.
- 4206 [389] F. Stagni, A. Tsaregorodtsev, L. Arrabito, A. Sailer, T. Hara, X. Zhang, DIRAC in Large Particle
4207 Physics Experiments, J. Phys. Conf. Ser. 898 (9) (2017) 092020.
- 4208 [390] M. Barisits, T. Beermann, F. Berghaus, et al., Rucio: Scientific data management., Comput. Softw.
4209 Big Sci. 3 (2019) 11.
- 4210 [391] A. Frohner, J.-P. Baud, R. M. Garcia Rioja, G. Grosdidier, R. Mollon, D. Smith, P. Tedesco, Data
4211 management in EGEE, J. Phys. Conf. Ser. 219 (2010) 062012.
- 4212 [392] M. Al-Turany, D. Bertini, R. Karabowicz, D. Kresan, P. Malzacher, T. Stockmanns, F. Uhlig, The
4213 FairRoot framework, J. Phys. Conf. Ser. 396 (2012) 022001.
- 4214 [393] T. Sjostrand, S. Ask, J. R. Christiansen, R. Corke, N. Desai, P. Ilten, S. Mrenna, S. Prestel, C. O.
4215 Rasmussen, P. Z. Skands, An Introduction to PYTHIA 8.2, Comput. Phys. Commun. 191 (2015)
4216 159–177.

- 4217 [394] B. Andersson, G. Gustafson, B. Nilsson-Almqvist, A Model for Low $p(t)$ Hadronic Reactions,
4218 with Generalizations to Hadron - Nucleus and Nucleus-Nucleus Collisions, Nucl. Phys. B 281
4219 (1987) 289–309.
- 4220 [395] B. Nilsson-Almqvist, E. Stenlund, Interactions Between Hadrons and Nuclei: The Lund Monte
4221 Carlo, Fritiof Version 1.6, Comput. Phys. Commun. 43 (1987) 387.
- 4222 [396] S. Bass, et al., Microscopic models for ultrarelativistic heavy ion collisions, Prog. Part. Nucl. Phys.
4223 41 (1998) 255–369.
- 4224 [397] M. Bleicher, et al., Relativistic hadron hadron collisions in the ultrarelativistic quantum molecular
4225 dynamics model, J. Phys. G 25 (1999) 1859–1896.
- 4226 [398] S. Agostinelli, et al., GEANT4—a simulation toolkit, Nucl. Instrum. Meth. A 506 (2003) 250–303.
- 4227 [399] J. Allison, et al., Geant4 developments and applications, IEEE Trans. Nucl. Sci. 53 (2006) 270.
- 4228 [400] J. Allison, et al., Recent developments in Geant4, Nucl. Instrum. Meth. A 835 (2016) 186–225.
- 4229 [401] J. Rauch, T. Schlüter, GENFIT — a Generic Track-Fitting Toolkit, J. Phys. Conf. Ser. 608 (1)
4230 (2015) 012042.
4231 URL <https://github.com/GenFit/GenFit>
- 4232 [402] S. Gorbunov, I. Kisel, Reconstruction of decayed particles based on the kalman filter, Tech. Rep.
4233 CBM-SOFT-note-2007-003, CBM Collaboration (2007).
- 4234 [403] M. Al-Turany, et al., ALFA: The new ALICE-FAIR software framework, J. Phys. Conf. Ser.
4235 664 (7) (2015) 072001.
- 4236 [404] Key4hep software.
4237 URL <https://key4hep.github.io/key4hep-doc/index.html>
- 4238 [405] Offline framework for the spd experiment.
4239 URL <https://git.jinr.ru/nica/spdroot>
- 4240 [406] Kalman, Rudolph Emil, A New Approach to Linear Filtering and Prediction Problems, Transac-
4241 tions of the ASME—Journal of Basic Engineering 82 (Series D) (1960) 35–45.
- 4242 [407] M. Abramowitz, I. A. Stegun, Handbook of Mathematical Functions with Formulas, Graphs, and
4243 Mathematical Tables, ninth dover printing, tenth gpo printing Edition, Dover, New York, 1964.
- 4244 [408] J. Myrheim, L. Bugge, A FAST RUNGE-KUTTA METHOD FOR FITTING TRACKS IN A
4245 MAGNETIC FIELD, Nucl. Instrum. Meth. 160 (1979) 43–48.
- 4246 [409] L. Bugge, J. Myrheim, TRACKING AND TRACK FITTING, Nucl. Instrum. Meth. 179 (1981)
4247 365–381.
- 4248 [410] C. Adolph, et al., Search for exclusive photoproduction of $Z_c^\pm(3900)$ at COMPASS, Phys. Lett. B
4249 742 (2015) 330–334.
- 4250 [411] J. Badier, et al., Experimental J/ψ Hadronic Production from 150-GeV/c to 280-GeV/c, Z. Phys.
4251 C20 (1983) 101.
- 4252 [412] Ayuso, Catherine. Nuclear modification of J/ψ and Drell-Yan production at the E906/SeaQuest
4253 experiment. United States: N. p., 2020. Web. doi:10.2172/1637630.

- 4254 [413] J. Adam, et al., Determination of the event collision time with the ALICE detector at the LHC,
4255 Eur. Phys. J. Plus 132 (2) (2017) 99.
- 4256 [414] P. Zyla, et al., Review of Particle Physics, PTEP 2020 (8) (2020) 083C01.
- 4257 [415] A. Karpishkov, V. Saleev, M. Nefedov, Estimates for the single-spin asymmetries in $p^\uparrow p \rightarrow J/\psi X$
4258 process at PHENIX RHIC and SPD NICA .
- 4259 [416] J. Badier, et al., $\psi\psi$ Production and Limits on Beauty Meson Production From 400- $\{GeV\}/c$
4260 Protons (1985) 401–408.
- 4261 [417] P. Aurenche, R. Baier, M. Fontannaz, Prompt Photon Production at Colliders, Phys. Rev. D42
4262 (1990) 1440–1449.
- 4263 [418] M. Bonesini, et al., High Transverse Momentum π^0 Production by π^- and π^+ on Protons at
4264 280-GeV/c, Z. Phys. C37 (1987) 39–50.
- 4265 [419] M. Bonesini, et al., Production of High Transverse Momentum Prompt Photons and Neutral Pions
4266 in Proton Proton Interactions at 280-GeV/c, Z. Phys. C38 (1988) 371.
- 4267 [420] I. N. Meshkov, G. V. o. Trubnikov, NICA Technical Desigh Report, Dubna, (2015) .
- 4268 [421] A. N. Sissakian, A. S. Sorin, V. D. Kekelidze, et al., The MultiPurpose Detector – MPD to study
4269 Heavy Ion Collisions at NICA (Conceptual Design Report), Dubna, (2014) .
- 4270 [422] A. A. Baldin, I. G. Voloshina, E. E. Perepelkin, R. V. Polyakova, N. S. Rossiyskaya, T. V. Shavrina,
4271 I. P. Yudin, Numerical simulation of the field distribution produced by the SP-40 magnet of the
4272 MARUSYA setup and comparison of simulation results with experimental data, Technical Physics,
4273 52 (2007) 1397-1406 52 (11) (2007) 1397–1406.
- 4274 [423] A. A. Baldin, et al., Measurement of the spatial magnetic field distribution of MARUSYA spec-
4275 trometer, JINR Preprint P13-2006-67 .
- 4276 [424] A. A. Baldin, et al., Magnet for Marusya Experiment, Phys. Part. Nucl. Lett. 7 (1 (157)).
- 4277 [425] A. A. Baldin, Polarization Studies at MARUSYA Setup, Proceedings of International Workshop
4278 ”Relativistic Nuclear Physics from Hundreds MeV to TeV, (2008) .
- 4279 [426] A. A. Baldin, et al., Experimental Study of Asymmetries in Inclusive π^+ , p, d Spectra in Interac-
4280 tion of Polarized Protons and Deuterons with Carbon Targets at MARUSYA Setup, JINR Preprint
4281 P1-2007-180 .